E 313

MEASUREMENT OF THE POLARIZATION PARAMETER IN PROTON-PROTON ELASTIC SCATTERING FOR BEAM MOMENTA RANGING FROM 20 GeV/c TO 200 GeV/c

by

Marjorie Blasius Corcoran

Submitted to the Faculty of the Graduate School
in partial fulfillment of the requirements
for the degree Doctor of Philosophy
in the Department of Physics
Indiana University

September 1977

September 12, 1977

The Thesis entitled "Measurement of the Polarization Parameter in Proton-Proton Elastic Scattering for Beam Momenta Ranging from 20 GeV/c to 200 GeV/c", which has been submitted by Marjorie Blasius Corcoran, has been read and found acceptable by the members of the Ph. D. Committee, whose signatures appear below.

H. A. Neal

H. A. Neal, Chairman

R. M. Heinz

R. M. Heinz

A. W. Hendry

A. W. Hendry

M. Lowengrub

M. Lowengrub

ACKNOWLEDGEMENT

I am very fortunate to have had Professor Homer Neal as my thesis advisor and friend. Many people contributed to E313, but he was the person who conceived the experiment, brought all the pieces together, and made them work. I was often amazed at his insight into the physics of the experiment and the various problems we encountered, and I am grateful for his advice, guidance, and encouragement through all phases of my graduate career.

Every experiment in high energy physics draws on the talents and energies of many people. I would like to express my gratitude to all those involved in E313. Very special thanks goes to Dr. Jon Saur for his tireless efforts both in running the experiment and analyzing the data. I would also like to thank Jon for sharing with me his knowledge of computers and data analysis. Others whose special talents and experience were instrumental in making the experiment work were Drs. Dave Rust, Steve Ems, Steve Gray and Harold Ogren. The experiment would never have been run without the many hours of hard work put in by Brian Martin and Paul Smith. Thanks also goes to John Krider and Professor Ray Crittenden for their advice and help in the construction of the proportional chambers, and to Bob Polvado for assistance during the data taking and for helpful discussions.

I would also like to thank the families of everyone involved, especially Patricia Saur, for their patience and understanding during the course of this experiment. High energy physics is often a lonely profession—not just for those working long hours on an experiment, but also for their families. And I would like to thank Alexis Saur (age two)

for keeping the experimenters entertained during the long weeks of data taking.

I would also like to express my gratitude to Professor Richard Heinz for his guidance during the first two years of my graduate career (especially through Buckner's cave).

My deepest thanks and much love go to my husband Chris, for his infinite patience, constant encouragement, and beautiful plots.

TABLE OF CONTENTS

	Page
Acknowledgement	iii
Abstract	vi
Introduction	viii
Chapter I	
Formalism and Theory	1
Figures	44
Chapter II	
Description of Apparatus	52
Figures	75
Chapter III	
Analysis	88
Figures	107
Chapter IV	
Results	148
Figures	155
Vita	168

Abstract of Dissertation

Measurement of the Polarization Parameter in Proton-Proton Elastic Scattering for Beam Momenta Ranging From 20 GeV/c to 200 GeV/c

by

Marjorie Blasius Corcoran

Doctor of Philosophy in Physics

Indiana University, 1977

The polarization parameter in proton-proton elastic scattering has been measured for fixed t (the square of the four-momentum transfer) as a function of s (the square of the total center of mass energy) for $t = -.3, -.6, -.8$ and -1.0 $(GeV/c)^2$ and for beam momenta ranging from 20 GeV/c to 200 GeV/c. These results are among the first pp polarization measurements above a beam momentum of 17.5 GeV/c and represent the first systematic study of the fixed-t s-dependence of the polarization at high energies.

The formalism used to describe proton-proton scattering is discussed, and the polarization and other spin parameters are presented in terms of helicity amplitudes. Theoretical ideas about polarizations are discussed in terms of both Regge models and optical models.

The experiment was done at the Internal Target Area of the Fermi National Accelerator Laboratory. Hydrogen from a gas jet target was sprayed into the accelerator's main ring, where interactions occurred. The momentum and production angle of the recoil proton were measured by the Internal Target Spectrometer. The spin of the proton was analyzed in a carbon re-scattering polarimeter.

At $t = -.3$ $(GeV/c)^2$ the polarization was found to fall from a small positive value at $s = 40$ $(GeV/c)^2$ to near zero around $s = 210$. At higher energies the polarization appears to be rising again. At both $t = -.6$ and $t = -.8$ the polarization was found to be a few percent positive at $s = 40$ and to become a few percent negative by $s = 86$. The polarization either remains a few percent negative or returns to zero for higher energies. At $t = -1.0$ the polarization was measured to be small and positive at $s = 40$, then was found to be fairly large and positive at $s = 86$. At higher s values, up to $s = 210$, the polarization was measured to be fairly large and negative.

INTRODUCTION

After many years of experimental and theoretical work, much still remains to be learned about the nature of strong interactions. The proton-proton (pp) system provides one of natures most basic opportunities for studying the strong interactions, and one cannot expect to understand more complicated many particle systems without first understanding this two particle system. pp scattering can be fully described in terms of five complex amplitudes which are functions of s and t. (The Mandelstam variable s is the square of the total four-momentum, $s = (p_1 + p_2)^2$, and t is the square of the four-momentum transfer, $t = (p_1 - p_3)^2$.) The polarization arises from the interference between the "helicity-flip" amplitudes and the "helicity non-flip" amplitudes, and is therefore a sensitive tool for determining their structure.

Until recently, many investigators believed that high energy polarization measurements would be uninteresting since standard Regge theory predicts that for $s \to \infty$, fixed-t polarizations should fall to zero as some negative power of s. The low energy polarization data seemed to support this view.[1-4] Within the past few years, however, some new measurements have been made which suggest a more interesting behavior of the polarization at high energies. In a polarized target experiment at Serpukhov, Gaidot et. al.[5] measured pp polarizations which were negative for $|t| > .5\ (\mathrm{GeV}/c)^2$ and seemed to become more negative with increasing $|t|$. This result was quite surprising, since the low

energy results had shown positive polarizations. The estimated errors in Serpukhov data were large, however, so the situation remained unclear. Also, in an experiment at Fermilab, Bunce et. al.[6] measured very large (up to .28) polarizations in Λ^0 particles inclusively produced by protons on a berillium target. This sparked increased interest in the polarization of inclusive processes.

New theoretical results have also indicated that polarizations may not be zero at high energies. A model proposed by Pumplin and Kane[7] predicted that pp polarizations would remain non-zero up to asymptotic energies and would change sign at high energies. An optical model due to Durand and Halzen[8] related the polarization to the derivative of the differential cross section; such a relationship would give very interesting structure to pp polarizations in the region of the dip in $d\sigma/dt$. (At $s = 500\ (\mathrm{GeV}/c)^2$ the dip occurs at about $t = -1.4\ (\mathrm{GeV}/c)^2$.) All of these factors have led to increased interest in polarization measurements at high energies.

The experiment reported upon here measured the polarization parameter in pp elastic scattering for fixed t as a function of s. The measurements were made at the Internal Target Area of the Fermi National Accelerator Laboratory. Interactions occurred between protons from a gas jet target and the circulating proton beam in the accelerator's main ring. The momentum of the recoil proton was measured by the Internal Target Area's Large Angle Recoil Spectrometer. The spin of the proton was analyzed in a carbon re-scattering polarimeter. In the kinematic region studied, a fixed laboratory angle of the recoil proton corresponded

very accurately to fixed-t. So the fixed-t s-dependence could be easily studied by setting the spectrometer at the proper laboratory angle and pulsing the gas jet target during the acceleration of the beam. Data was taken at t values of -.3, -.6, -.8, and -1.0 $(GeV/c)^2$ for beam momenta ranging from 20 GeV/c to 200 GeV/c. This data is among the first proton-proton polarization data above a beam momentum of 17.5 GeV/c, and is the first systematic study of fixed-t s-dependence at high energies.

The first chapter discusses the formalism used to describe pp scattering and some of the theoretical ideas concerning polarizations. Details of the experimental apparatus and data acquisition are described in the second chapter. The third chapter discusses the method of data analysis, and the results are presented in the fourth chapter.

REFERENCES

1. J. H. Parry et. al., Phys. Rev., D8, 45 (1973).
2. M. Borghini et. al., Phys. Letters, 31B, 405 (1970).
3. M. Borghini et. al., Phys. Letters, 36B, 501 (1971).
4. C. W. Abshire et. al., Phys. Rev. Letters, 32, 1261 (1974).
5. A. Caldot et. al., Phys. Letters, 61B, 103 (1976).
6. C. Bunce et. al., Phys. Rev. Letters, 36, 1113 (1976).
7. J. Humplin and G. Kane, Phys. Rev., D11, 1183 (1975).
8. L. Durand and F. Halzen, Nuc. Phys., B104, 317 (1976).

CHAPTER I

FORMALISM AND THEORY

This chapter summarizes the formalism used to describe proton-proton scattering and discusses some of the theoretical ideas about polarizations. In the first section, the helicity amplitudes of Jacob and Wick are described, and their relation to experimental observables is given. The (older and non-relativistic) formalism of Wolfenstein is also given. The density matrix and its use in calculating experimental observables is discussed. Then this experiment's particular method of measuring the polarization is described. The second section deals with theoretical models of pp interactions. The simple Regge model is treated, and then a Regge model with absorption corrections, due primarily to Kane, is discussed. Two optical models, one due to Chu, Hendry, and Abshire, and the second to Durand and Halzen, are also discussed.

Formalism

Proton-proton scattering can be completely described in terms of five complex amplitudes which are functions of the Mandelstam variables s and t.* If these amplitudes were known for all values of s and t, one would calculate any desired quantity involving pp scattering. A number of different ways of defining these amplitudes have been used by various authors. In 1952-54 Wolfenstein and Ashkin[1,2] expressed the scattering matrix for the pp system in terms of five complex parameters and showed the relationship of these parameters to experimentally measurable quantities. Wolfenstein's development was not relativistically correct, however. Stapp[3] and Bilenkii, Lapidus, and Ryndin[4] have given the

---

*Because the pp system is pure I=1, only the five I=1 amplitudes are needed. There are also five I=0 amplitudes which must be known to describe pn scattering.

relativistic generalization of Wolfenstein's formalism. A parameterization more commonly used today involves the relativistically correct helicity amplitudes introduced by Jacob and Wick[5] in 1959. The helicity amplitudes are discussed first.

1. Helicity Amplitudes

Let the wave function of a single particle, at rest and with helicity λ, be represented by $\psi_{o\lambda}$. Here the z-axis is chosen as the axis of quantization of the spin, and λ is the spin component along that axis. To obtain a plane wave state with momentum $\underset{\sim}{p}$ along the z-axis and still with helicity λ, apply a Lorentz transformation without rotation along the z-axis:

$$\psi_{p\lambda} = L_z(p)\psi_{o\lambda} \quad .$$

The helicity is not changed by this transformation. To obtain a state with momentum $\underset{\sim}{p}$ in the direction specified by the angles θ and φ, the state $\psi_{p\lambda}$ can be rotated

$$|p\theta\varphi;\lambda\rangle = R(\varphi\,\theta-\varphi)\psi_{p\lambda}$$

where $R(\varphi\theta-\varphi) = e^{-iJ_z\varphi}\, e^{-iJ_y\theta}\, e^{+iJ_z\varphi}$ is the rotation operator, and J_z, J_y are the angular momentum operators for the particle. The helicity of a plane wave state is not changed by either a rotation or a Lorentz velocity transformation along the direction of $\underset{\sim}{p}$.

Two particle states can be constructed as direct products of single particle states:

$$R(\varphi_1,\theta_1,-\varphi_1)\psi_{p_1\lambda_1}\; R(\varphi_2,\theta_2,-\varphi_2)\psi_{p_2\lambda_2} \quad .$$

For states of zero linear momentum (i.e. two particle states in the center of mass), where $\underset{\sim}{p}_2 = -\underset{\sim}{p}_1$, $\theta_2 = \pi - \theta_1$ and $\varphi_2 = \varphi_1 \pm \pi$, the wave function can be written in a form involving only one pair of angles θ, φ. Following Jacob and Wick, define

$$\chi_{p\lambda} = (-1)^{s-\lambda} e^{-i\pi J_y} \psi_{p\lambda} ,$$

which is a state with momentum $\underset{\sim}{p}$ in the negative z-direction with helicity λ. (s is the particle's spin, and the factor $(-1)^{s-\lambda}$ is a convenient phase factor following the convention of Jacob and Wick). Then the two-particle center of mass state is

$$|p\lambda_1\lambda_2\rangle = \psi_{p\lambda_1} \chi_{p\lambda_2} .$$

This represents a state with one particle having momentum $\underset{\sim}{p}$ in the positive z direction and one having momentum $\underset{\sim}{p}$ in the negative z direction. A state with momentum in an arbitrary direction can be obtained by a rotation involving $J = J_1 + J_2$:

$$|p\theta\varphi;\lambda_1\lambda_2\rangle = R(\varphi\theta-\varphi)\psi_{p\lambda_1} \chi_{p\lambda_2} .$$

Plane wave helicity states can be expanded in terms of states of definite angular momentum, $|pJM;\lambda_1\lambda_2\rangle$:[6]

$$|p\theta\varphi;\lambda_1\lambda_2\rangle = \sum_{JM} \left(\frac{2J+1}{4\pi}\right)^{\frac{1}{2}} D^J_{M\lambda}(\varphi\theta-\varphi)\, |pJM;\lambda_1\lambda_2\rangle$$

where $\lambda = \lambda_1 - \lambda_2$ and $D^J_{M\lambda}(\varphi\theta-\varphi)$ is the matrix corresponding to the rotation operator $R(\varphi\theta-\varphi)$ in the irreducible representation of order J. This is analogous to the partial wave expansion in non-relativistic scattering. A state of definite J can also be expanded as a superposition of plane wave states:[5]

$$|pJM;\lambda_1\lambda_2\rangle = \int_0^{2\pi}\int_0^{\pi} \left(\frac{2J+1}{4\pi}\right)^{\frac{1}{2}} D^{J*}_{M\lambda}(\varphi\theta-\varphi)|p\theta\varphi;\lambda_1\lambda_2\rangle \sin\theta d\theta d\varphi \ .$$

Helicity amplitudes are elements of the scattering matrix S between two particle plane wave helicity states. The initial beam direction is taken as the z axis, and θ,φ give the direction of the scattered beam in the center of mass. A helicity amplitude, then, is

$$\langle p\theta\varphi;\lambda_1'\lambda_2'|S|p00;\lambda_1\lambda_2\rangle \ ,$$

which can be written more simply as

$$\langle\lambda_1'\lambda_2'|S|\lambda_1\lambda_2\rangle \ ,$$

remembering that the amplitudes are functions of s and t.

Since each proton has two possible values of $\lambda, \pm\frac{1}{2}$, there are 16 possible amplitudes for pp scattering. However, invariance principles can be used to reduce the number of independent amplitudes to five. Parity conservation requires[7]

$$\langle-\lambda_1'-\lambda_2'|S|-\lambda_1-\lambda_2\rangle = (-1)^{\lambda-\lambda'}\langle\lambda_1'\lambda_2'|S|\lambda_1\lambda_2\rangle$$

where $\lambda = \lambda_1-\lambda_2$ and $\lambda' = \lambda_1'-\lambda_2'$. This reduces the number of independent amplitudes by a factor of two. Likewise, time reversal invariance requires

$$\langle\lambda_1'\lambda'_2|S|\lambda_1\lambda_2\rangle = (-1)^{\lambda-\lambda'}\langle\lambda_1\lambda_2|S|\lambda_1'\lambda_2'\rangle$$

which reduces the number of amplitudes from eight to six. For two nucleons in a definite isospin state, the requirements of Fermi statistics give

$$\langle\lambda_1'\lambda_2'|S|\lambda_1\lambda_2\rangle = (-1)^{\lambda-\lambda'}\langle\lambda_2'\lambda_1'|S|\lambda_2\lambda_1\rangle$$

which reduces the number of independent amplitudes to five. The conventional amplitudes are those defined by Goldberger et.al.[7]

$$\phi_1 = \langle ++|S|++\rangle$$
$$\phi_2 = \langle ++|S|--\rangle$$
$$\phi_3 = \langle +-|S|+-\rangle$$
$$\phi_4 = \langle +-|S|-+\rangle$$
$$\phi_5 = \langle ++|S|+-\rangle ,$$

where + means helicity $+\frac{1}{2}$ and - means helicity $-\frac{1}{2}$. (For elastic scattering, S is usually replaced by $T = -i(S-1)$, so that the unscattered wave is subtracted out.) These amplitudes have the expansion[5]

$$\langle \lambda_1' \lambda_2' |S| \lambda_1 \lambda_2 \rangle = \frac{1}{2p} \sum_J (2J+1) \langle \lambda_1' \lambda_2' |S^J| \lambda_1 \lambda_2 \rangle D^J_{\lambda\lambda'}(\theta)$$

where S^J is the part of the S matrix which acts on the Jth partial wave. In section I-4, the amplitudes are related to experimental quantities, which are bilinear combinations of the amplitudes of the form Re $\phi_\alpha \phi^*_\beta$ and Im $\phi_\alpha \phi^*_\beta$. The scattering matrix, which transforms an initial state into its final state is given by

$$S = \begin{pmatrix} \phi_1 & \phi_5 & -\phi_5 & \phi_2 \\ -\phi_5 & \phi_3 & \phi_4 & -\phi_5 \\ \phi_5 & \phi_4 & \phi_3 & \phi_5 \\ \phi_2 & \phi_5 & -\phi_5 & \phi_1 \end{pmatrix} = \begin{pmatrix} \langle ++|S|++\rangle & \langle ++|S|+-\rangle & \langle ++|S|-+\rangle & \langle ++|S|--\rangle \\ \langle +-|S|++\rangle & \langle +-|S|+-\rangle & \langle +-|S|-+\rangle & \langle +-|S|--\rangle \\ \langle -+|S|++\rangle & \langle -+|S|+-\rangle & \langle -+|S|-+\rangle & \langle -+|S|--\rangle \\ \langle --|S|++\rangle & \langle --|S|+-\rangle & \langle --|S|-+\rangle & \langle --|S|--\rangle \end{pmatrix}.$$

2. Wolfenstein Parameters

In the early 1950's Wolfenstein[1,2] derived an expression for the scattering matrix for two spin $\frac{1}{2}$ particles in terms of their spin operators and momenta. Following Wolfenstein, the 16 independent combinations of the spin operators which are available to construct

S are

$\underset{\approx}{1}$	scalar
$\underset{\approx}{\sigma}_1 : \underset{\approx}{\sigma}_2 - 1$	scalar
$\underset{\approx}{\sigma}_1 + \underset{\approx}{\sigma}_2$	axial vector
$\underset{\approx}{\sigma}_1 - \underset{\approx}{\sigma}_2$	axial vector
$\underset{\approx}{\sigma}_1 \times \underset{\approx}{\sigma}_2$	axial vector
$t_{\alpha\beta} = \sigma_{1\alpha}\sigma_{2\beta} + \sigma_{1\beta}\sigma_{2\alpha}$	symmetric tensor .

The subscripts 1 and 2 refer to particles 1 and 2. The operators of particle 1 do not operate on those of particle 2, and vice versa. These terms are to be combined with the following functions of the momenta to obtain scalars:

1	scalar	$K_\alpha K_\beta$, $N_\alpha N_\beta$, $P_\alpha P_\beta$	symmetric tensors
$\underset{\sim}{k}_f - \underset{\sim}{k}_i = \underset{\sim}{K}$	vector	$K_\alpha P_\beta + K_\beta P_\alpha$	
$\underset{\sim}{k}_f \times \underset{\sim}{k}_i = \underset{\sim}{N}$	axial vector	$K_\alpha N_\beta + K_\beta N_\alpha$	
$\underset{\sim}{N} \times \underset{\sim}{K} = \underset{\sim}{P}$	vector	$P_\alpha N_\beta + P_\beta N_\alpha$	.

Here $\underset{\sim}{k}_f$ and $\underset{\sim}{k}_i$ are the final and initial momenta of particle 1 in the center of mass. The possible combinations are restricted by invariance considerations. S must be invariant under both the parity transformation and time reversal. Under parity, $\underset{\approx}{\sigma} \to \underset{\approx}{\sigma}$, $\underset{\sim}{N} \to +\underset{\sim}{N}$, $\underset{\sim}{K} \to -\underset{\sim}{K}$, and $\underset{\sim}{P} \to -\underset{\sim}{P}$, and, for example, the term $(\underset{\approx}{\sigma}_1 - \underset{\approx}{\sigma}_2)\cdot\underset{\sim}{K}$ changes sign and must be excluded. Under time reversal, $\underset{\approx}{\sigma} \to -\underset{\approx}{\sigma}$, $\underset{\sim}{K} \to \underset{\sim}{K}$, $\underset{\sim}{P} \to -\underset{\sim}{P}$, and $\underset{\sim}{N} \to -\underset{\sim}{N}$. The terms $t_{\alpha\beta}(K_\alpha P_\alpha + K_\beta P_\alpha)$ and $(\underset{\sim}{\sigma}_1 \times \underset{\sim}{\sigma}_2)\cdot\underset{\sim}{N}$ are excluded by time reversal invariance. The terms that survive are

was non-relativistic. Stapp[3] and Bilenkii, Lapidus, and Ryndin[4] have given the relativistic generalization of this formalism. The Wolfenstein parameters can be written in terms of the helicity amplitudes defined earlier.[11]

3. Density Matrices

The problem of relating the helicity amplitudes or the Wolfenstein parameters to experimental observables is most easily done by means of spin density matrices. A thorough discussion of density matrices has been given by Fano.[8]

Suppose a system is in a "pure" state. Then its wave function can be expressed as a coherent sum over a complete set of states:

$$\psi = \sum_n a_n X_n$$

The expectation value of an operator $\underset{\approx}{Q}$ is given by

$$\langle \underset{\approx}{Q} \rangle = \langle \psi | \underset{\approx}{Q} | \psi \rangle = \sum_{m,n} a_m^* a_n \langle X_m | \underset{\approx}{Q} | X_n \rangle$$

$$= \sum_{m,n} a_m^* a_n Q_{mn}$$

$$= \sum_{m,n} \rho_{nm} Q_{mn} = \sum_n (\rho Q)_{nm} = \mathrm{Tr}(\underset{\approx}{\rho}\, \underset{\approx}{Q})$$

where $\rho_{nm} \equiv a_n a_m^*$ and $Q_{mn} = \langle X_m | Q | X_n \rangle$. If $\langle \psi | \psi \rangle = \mathrm{Tr}\rho$ is not normalized to 1, then

$$\langle \underset{\approx}{Q} \rangle = \frac{\langle \psi | \underset{\approx}{Q} | \psi \rangle}{\langle \psi | \psi \rangle} = \frac{\mathrm{Tr}(\underset{\approx}{\rho}\, \underset{\approx}{Q})}{\mathrm{Tr}\underset{\approx}{\rho}} .$$

A real system is generally an incoherent superposition of two or more pure states, each with weight w^j. Then

$$\langle \underset{\approx}{Q} \rangle = \sum_j w^j \langle \underset{\approx}{Q}^j \rangle$$

$$= \sum_j w^j \sum_{nm} a_n^j a_m^{j*} Q_{mn}$$

$$= \sum_{nm} [\sum_j w^j a_n^j a_m^{j*}] Q_{mn}$$

$$= \sum_{nm} \rho_{nm} Q_{mn} = Tr(\underset{\approx}{\rho} \underset{\approx}{Q})$$

where now $\rho_{nm} = \sum_j w^j a_n^j a_m^{j*}$. It is easy to find an expression for the final state density matrix ρ_f in terms of the initial density matrix, ρ_i, and the scattering matrix. If the operator $\underset{\approx}{S}$ transforms the initial states X_{ni} into the final states X_{nf}, then

$$\psi_f = \sum_n a_n \underset{\approx}{S} X_{ni}$$

and

$$\langle \psi_f | \psi_f \rangle \langle \underset{\approx}{Q} \rangle_f = \langle \psi_f | \underset{\approx}{Q} | \psi_f \rangle = \sum_{mn} a_m^* a_n \langle \underset{\approx}{S} X_{mi} | \underset{\approx}{Q} | \underset{\approx}{S} X_{ni} \rangle$$

$$= \sum_{mn} a_n a_m^* \langle X_{mi} | \underset{\approx}{S}^\dagger \underset{\approx}{Q} \underset{\approx}{S} | X_{ni} \rangle$$

$$= Tr(\underset{\approx}{\rho}_i \underset{\approx}{S}^\dagger \underset{\approx}{Q} \underset{\approx}{S}) = Tr(\underset{\approx}{S} \underset{\approx}{\rho}_i \underset{\approx}{S}^\dagger \underset{\approx}{Q})$$

$$= Tr(\underset{\approx}{\rho}_f \underset{\approx}{Q})$$

where $\underset{\approx}{\rho}_f = \underset{\approx}{S} \underset{\approx}{\rho}_i \underset{\approx}{S}^\dagger$ is the final state density matrix. Final state expectation values are given by

$$\langle \underset{\approx}{Q} \rangle_f = \frac{Tr(\underset{\approx}{\rho}_f \underset{\approx}{Q})}{Tr \underset{\approx}{\rho}_f} .$$

Note that the density matrix is hermitian, since

$$\rho_{nm}^* = \sum_j w^j (a_n a_m^*)^*$$

$$= \sum_j w^j (a_m a_n^*) = \rho_{mn} .$$

For a single particle of spin $\frac{1}{2}$, $\underset{\approx}{\rho}$ is a 2 x 2 matrix, since there are two possible spin states. Any 2 x 2 matrix can be expressed as a sum over the matrices $\underset{\approx}{1}$, $\underset{\approx}{\sigma}_x$, $\underset{\approx}{\sigma}_y$, and $\underset{\approx}{\sigma}_z$, where the $\underset{\approx}{\sigma}$'s are the Pauli matrices. So,

$$\underset{\approx}{\rho} = P_o \underset{\approx}{1} + P_x \underset{\approx}{\sigma}_x + P_y \underset{\approx}{\sigma}_y + P_z \underset{\approx}{\sigma}_z$$

$$= P_o \underset{\approx}{1} + \underset{\sim}{P}\cdot\underset{\approx}{\sigma} . \quad \text{where } \underset{\approx}{\sigma} = (\underset{\approx}{\sigma}_x, \underset{\approx}{\sigma}_y, \underset{\approx}{\sigma}_z)$$

Then

$$\langle \underset{\approx}{\sigma}_x \rangle = \mathrm{Tr}(\underset{\approx}{\rho}\, \underset{\approx}{\sigma}_x)$$

$$= \mathrm{Tr}(P_o \underset{\approx}{\sigma}_x + P_x \underset{\approx}{\sigma}_x^{\,2} + P_y \underset{\approx}{\sigma}_x \underset{\approx}{\sigma}_y + P_z \underset{\approx}{\sigma}_x \underset{\approx}{\sigma}_z)$$

$$= P_x$$

using the familiar properties of the $\underset{\approx}{\sigma}$'s. Similarly,

$$\langle \underset{\approx}{\sigma}_y \rangle = P_y \text{ and } \langle \underset{\approx}{\sigma}_z \rangle = P_z .$$

The vector $\underset{\sim}{P} = \langle \underset{\approx}{\sigma} \rangle$ is called the polarization vector of the particle. Using the normalization $\mathrm{Tr}\underset{\approx}{\rho} = 1$,

$$\underset{\approx}{\rho} = \tfrac{1}{2}[\underset{\approx}{1} + \underset{\sim}{P}\cdot\underset{\approx}{\sigma}]$$

for a spin $\frac{1}{2}$ particle. If the partilce is unpolarized, $\langle \underset{\approx}{\sigma} \rangle = \underset{\sim}{P} = 0$, and $\underset{\approx}{\rho} = \frac{1}{2}(\underset{\approx}{1})$.

For a two particle state, the composite density matrix is a 4 x 4 matrix with elements[8]

$$\rho_{ab,a'b'}$$

where a,a′ refer to particle 1 and b,b′ refer to particle 2. If the two systems are uncorrelated (as in the case of an initially polarized?.

beam and target), the composite density matrix element can be written (8)

$$\rho_{ab,a'b'} = \rho^1_{aa'}\ \rho^2_{bb'}$$

An operator $\underset{\approx}{Q}^1$ which acts only on particle 1 can be considered to be an operator of the entire system if it is multiplied by the unit operator of particle 2, $(\underset{\approx}{1})^2$. Then

$$\begin{aligned}
\langle \underset{\approx}{Q}^1 \rangle &= \mathrm{Tr}(\underset{\approx}{Q}^1\ \underset{\approx}{1}^2 \underset{\approx}{\rho}) \\
&= \sum_{\substack{aa' \\ bb'}} Q^1_{a'a}\ \delta_{bb'}\ \rho_{ab,a'b'} \\
&= \sum_{\substack{aa' \\ b}} Q^1_{a'a}\ \rho_{ab,a'b} \\
&= \sum_{aa'} Q^1_{a'a}\ \rho^1_{aa'} \\
&= \mathrm{Tr}(\underset{\approx}{Q}^1\ \underset{\approx}{\rho}^1)
\end{aligned}$$

where $\rho^1_{aa'} = \sum_b \rho_{ab,a'b} = \mathrm{Tr}_2(\rho)$. The density matrix for particle 1, $\underset{\approx}{\rho}^1$, can be obtained by taking the trace with respect to particle 2, that is, summing over elements with the same index for particle 2.

A notation which is perhaps more transparent involves direct products of matrices. The composite matrix for a two particle system can be written (assuming the systems are uncorrelated)

$$\underset{\approx}{\rho} = \underset{\approx}{\rho}^1 \otimes \underset{\approx}{\rho}^2$$

where $\otimes$ denotes the direct product. An operator which acts on particle 1 can be considered to be an operator of the system if its direct product with the unit operator of particle 2 is taken:

$$\underset{\approx}{Q} = \underset{\approx}{Q}^1 \otimes \underset{\approx}{1}^2 \quad .$$

For example, if

$$\underset{\approx}{Q}^1 = \begin{pmatrix} q_{11} & q_{12} \\ q_{21} & q_{22} \end{pmatrix}$$

then

$$\underset{\approx}{Q} = \begin{pmatrix} q_{11} & q_{12} \\ q_{21} & q_{22} \end{pmatrix} \otimes \begin{pmatrix} 1 & 0 \\ 0 & 1 \end{pmatrix} = \begin{pmatrix} q_{11} & 0 & q_{12} & 0 \\ 0 & q_{11} & 0 & q_{12} \\ q_{21} & 0 & q_{22} & 0 \\ 0 & q_{21} & 0 & q_{22} \end{pmatrix}.$$

Note that the order is important. That is, if $\underset{\approx}{\rho} = \underset{\approx}{\rho}^1 \otimes \underset{\approx}{\rho}^2$, then

$$\underset{\approx}{Q} = \underset{\approx}{Q}^1 \otimes \underset{\approx}{1}^2$$

If an operator acts only on particle 2, then $\underset{\approx}{Q} = \underset{\approx}{1}^1 \otimes \underset{\approx}{Q}^2 \neq \underset{\approx}{Q}^2 \otimes \underset{\approx}{1}$.

4. Experimental Observables

The most general spin experiment fixes the spins of the initial particles and measures the expectation value of spin operators for the final state particles. To find these expectation values we need to know $\underset{\approx}{\rho}_i$, the initial density matrix, and $\underset{\approx}{S}$, the scattering matrix which transforms $\underset{\approx}{\rho}_i$ into $\underset{\approx}{\rho}_f$, the final state density matrix. For two spin $\frac{1}{2}$ particles, the most general form of the density matrix for the incident particles is

$$\underset{\approx}{\rho}_i = (\underset{\approx}{1}^1 + \underset{\approx}{\sigma}^1 \cdot \underset{\sim}{P}_b) \otimes (\underset{\approx}{1}^2 + \underset{\approx}{\sigma}^2 \cdot \underset{\sim}{P}_t)$$

where $\underset{\sim}{P}_b$ is the polarization of the beam and $\underset{\sim}{P}_t$ is the polarization of the target. In the helicity formalism, let $\underset{\approx}{S}$ be the operator which transforms an initial state into its final state. Then for a single

particle, the scattering matrix is

$$\underset{\approx}{S} = \begin{pmatrix} \langle +|S|+\rangle & \langle +|S|-\rangle \\ \langle -|S|+\rangle & \langle -|S|-\rangle \end{pmatrix} .$$

For a two-particle state, $\underset{\approx}{S} = \underset{\approx}{S}^1 \otimes \underset{\approx}{S}^2$:

$$\underset{\approx}{S} = \begin{pmatrix} \langle ++|S|++\rangle & \langle ++|S|+-\rangle & \langle ++|S|-+\rangle & \langle ++|S|--\rangle \\ \langle +-|S|++\rangle & \langle +-|S|+-\rangle & \langle +-|S|-+\rangle & \langle +-|S|--\rangle \\ \langle -+|S|++\rangle & \langle -+|S|+-\rangle & \langle -+|S|-+\rangle & \langle -+|S|--\rangle \\ \langle --|S|++\rangle & \langle --|S|+-\rangle & \langle --|S|-+\rangle & \langle --|S|--\rangle \end{pmatrix}$$

$$= \begin{pmatrix} \phi_1 & \phi_5 & -\phi_5 & \phi_2 \\ -\phi_5 & \phi_3 & \phi_4 & -\phi_5 \\ \phi_5 & \phi_4 & \phi_3 & \phi_5 \\ \phi_2 & \phi_5 & -\phi_5 & \phi_1 \end{pmatrix} ,$$

using the definitions of the ϕ's from Goldberger, and the relations between the amplitudes due to parity, time reversal, and Fermi statistics. The density matrix for the final state is given by

$$\underset{\approx}{\rho}_f = \underset{\approx}{S}\, \underset{\approx}{\rho}_i\, \underset{\approx}{S}^\dagger ,$$

the expectation value of any final state operator is given by

$$\langle \underset{\approx}{\sigma} \rangle_f = \mathrm{Tr}(\underset{\approx}{\rho}_f \underset{\approx}{\sigma})/\mathrm{Tr}\, \underset{\approx}{\rho}_f ,$$

and the differential cross section is given by

$$I = \mathrm{Tr}\, \underset{\approx}{\rho}_f / \mathrm{Tr}\, \underset{\approx}{\rho}_i .$$

In the helicity formalism, expectation values of spin operators are referred to the helicity rest frames of each particle, which are shown in Fig. I-1. The z-axis for each particle is along its direction of motion in the center of mass frame; the y-axis is taken as the normal to the scattering plane,

$$\hat{y} = \hat{n} = (\underset{\sim}{k}_f \times \underset{\sim}{k}_i)/|k_i \times k_f| \quad .$$

(For the target and recoil particles, some authors choose $\hat{y}$ as antiparallel to $\hat{n}$.) For all particles, $\hat{x} = \hat{y} \times \hat{z}$.

As an example, suppose the beam is intially polarized the +y direction in its helicity rest frame. Then the density matrix for the single particle is

$$\underset{\approx}{\rho}_i^1 = \tfrac{1}{2}(\underset{\approx}{1}^1 + P_b \, \underset{\approx}{\sigma}_y^1)$$

The composite density matrix for the beam-target system is

$$\underset{\approx}{\rho}_i = \underset{\approx}{\rho}^1 \otimes \underset{\approx}{\rho}^2 = \tfrac{1}{4}[\underset{\approx}{1} + P_b \, \underset{\approx}{\sigma}_y) \otimes \underset{\approx}{1}]$$

$$= \tfrac{1}{4}\begin{pmatrix} 1 & -iP_b \\ iP_b & 1 \end{pmatrix} \times \begin{pmatrix} 1 & 0 \\ 0 & 1 \end{pmatrix}$$

$$= \tfrac{1}{4}\begin{pmatrix} 1 & 0 & -iP_b & 0 \\ 0 & 1 & 0 & -iP_b \\ iP_b & 0 & 1 & 0 \\ 0 & iP_b & 0 & 1 \end{pmatrix} \quad .$$

The final density matrix is

$$\underset{\approx}{\rho}_f = \underset{\approx}{S} \, \underset{\approx}{\rho}_i \, \underset{\approx}{S}^+ \quad \text{, or explicitly,}$$

$$\underset{\approx}{\rho}_f = \begin{pmatrix} \phi_1 & \phi_5 & -\phi_5 & \phi_2 \\ -\phi_5 & \phi_3 & \phi_4 & -\phi_5 \\ \phi_5 & \phi_4 & \phi_3 & \phi_5 \\ \phi_2 & \phi_5 & -\phi_5 & \phi_1 \end{pmatrix} \begin{pmatrix} 1 & 0 & -iP_b & 0 \\ 0 & 1 & 0 & -iP_b \\ iP_b & 0 & 1 & 0 \\ 0 & iP_b & 0 & 1 \end{pmatrix} \begin{pmatrix} \phi_1 & -\phi_5 & \phi_5 & \phi_2 \\ \phi_5 & \phi_3 & \phi_4 & \phi_5 \\ -\phi_5 & \phi_4 & \phi_3 & -\phi_5 \\ \phi_2 & -\phi_5 & \phi_5 & \phi_1 \end{pmatrix}^*$$

Then the differential cross section is given by

$$\frac{d\sigma}{d\Omega} = \mathrm{Tr}\ \underset{\approx}{\rho}_f / \mathrm{Tr}\ \underset{\approx}{\rho}_i$$

Carrying out the matrix multiplication and taking the trace, we have

$$\begin{aligned} \frac{\mathrm{Tr}(\rho_f)}{\mathrm{Tr}(\rho_i)} &= \tfrac{1}{4}[2\ |\phi_1|^2 + 2|\phi_2|^2 + 2|\phi_3|^2 + 2|\phi_4|^2 + 8|\phi_5|^2 \\ &\qquad + 2iP_b\ \phi_5^*(\phi_1+\phi_2+\phi_3-\phi_4) - 2iP_b\ \phi_5(\phi_1+\phi_2+\phi_3-\phi_4)^*] \\ &= \tfrac{1}{2}[|\phi_1|^2 + |\phi_2|^2 + |\phi_3|^2 + |\phi_4|^2 + 4|\phi_5|^2 + \\ &\qquad P_b\ \mathrm{Im}\ \phi_5(\phi_1+\phi_2+\phi_3-\phi_4)^*] \\ &= I_o + P_b\ PI_o \end{aligned}$$

where $I_o = \frac{1}{2}[|\phi_1|^2+|\phi_2|^2+|\phi_3|^2+|\phi_4|^2+4|\phi_5|^2]$, the cross section for an initially unpolarized state, and

$$PI_o = \mathrm{Im}\ \phi_5(\phi_1 + \phi_2 + \phi_3 - \phi_4)^*$$

defines the polarization parameter P.

Suppose instead the initial state is unpolarized and the expectation value of $\underset{\approx}{\sigma}_y$ is measured for the recoil particle along its y-axis in the helicity rest frame. (This is just the quantity measured in this experiment). If the scattered particle is particle 3, and the recoil particle is particle 4,

$$\langle \underset{\approx}{\sigma}_y^{\,4} \rangle_f = \mathrm{Tr}(\underset{\approx}{1}^3 \otimes \underset{\approx}{\sigma}_y^{\,4}\ \underset{\approx}{\rho}_f)/\mathrm{Tr}\ \underset{\approx}{\rho}_f\ .$$

Since the initial state is unpolarized, $\underset{\approx}{\rho}_i = \underset{\approx}{1}$, and $\underset{\approx}{\rho}_f = \underset{\approx}{S}\underset{\approx}{S}^\dagger$. The operator for $\underset{\approx}{\sigma}^4_y$ in the composite spin space is

$$\underset{\approx}{1} \otimes \underset{\approx}{\sigma}_y = \begin{pmatrix} 1 & 0 \\ 0 & 1 \end{pmatrix} \otimes \begin{pmatrix} 0 & -i \\ i & 0 \end{pmatrix}$$

$$= \begin{pmatrix} 0 & -i & 0 & 0 \\ i & 0 & 0 & 0 \\ 0 & 0 & 0 & -i \\ 0 & 0 & i & 0 \end{pmatrix} .$$

Then

$$\mathrm{Tr}\, \underset{\approx}{\rho}_f \langle \underset{\approx}{\sigma}^4_y \rangle = \mathrm{Tr} \begin{pmatrix} 0 & -i & 0 & 0 \\ i & 0 & 0 & 0 \\ 0 & 0 & 0 & -i \\ 0 & 0 & i & 0 \end{pmatrix} \begin{pmatrix} \phi_1 & \phi_5 & -\phi_5 & \phi_2 \\ -\phi_5 & \phi_3 & \phi_4 & -\phi_5 \\ \phi_5 & \phi_4 & \phi_3 & \phi_5 \\ \phi_2 & \phi_5 & -\phi_5 & \phi_1 \end{pmatrix} \begin{pmatrix} \phi_1 & -\phi_5 & \phi_5 & \phi_2 \\ \phi_5 & \phi_3 & \phi_4 & \phi_5 \\ -\phi_5 & \phi_4 & \phi_3 & -\phi_5 \\ \phi_2 & -\phi_5 & \phi_5 & \phi_1 \end{pmatrix}^* .$$

Carrying out the multiplication, we have

$$I_o \langle \underset{\approx}{\sigma}^4_y \rangle = - \mathrm{Im}\, [\phi_5(\phi_1 + \phi_2 + \phi_3 - \phi_4)^*]$$

$$= - P I_o \quad .$$

Here P is the same expression obtained in the scattering from a polarized beam. In fact, Wolfenstein[1] showed that time reversal invariance requires them to be the same. The minus sign arises because we are measuring the spin of the recoil particle rather than the scattered particle.

There is a standard notation for the various observables in nucleon-nucleon scattering experiments. Any expectation value of operators in the final state will involve scalar quantities of the form

$$\mathrm{Tr}(\underset{\approx}{\sigma}_s\, \underset{\approx}{\sigma}_n\, \underset{\approx}{S}\, \underset{\approx}{\sigma}_b\, \underset{\approx}{\sigma}_t\, \underset{\approx}{S}^\dagger) \equiv I(s\,r;bt)$$

where s,r refer to one axis of the helicity rest frame of the scattered (s) or recoil (r) particle, and b,t refer to the helicity rest frame of the beam (b) or target (t) particle. If an initial particle is unpolarized, or the spin of one of the final state particles is unobserved, the corresponding operator becomes $\underset{\approx}{\sigma}_0 = \underset{\approx}{1}$, the unit operator. For example, a polarized target experiment with the polarization normal to the scattering plane measures I(00;0y). There are 256 quantities I(sr;bt), but at a given energy and scattering angle only nine can be independent, since the five helicity amplitudes are determined to within an overall phase by nine scalar quantities. Thomas[11] has worked out the relations than must exist between the I(sr; bt)'s.

The following are conventional names for the various quantities measured in spin experiments:[9]

(a) No spins determined: $I(00;00)=I_o$, the differential cross section.

(b) One spin determined: $I(y0;00)=PI_o$, the polarization parameter. Parity conservation requires $I(x0;00)=I(z0;00)=0$. Time reversal invariance gives $I(y0;00)=I(00;y0)$.

(c) Two spins determined: $I(00;ij)=I_oC_{ij}$, the correlation tensor. Invariance requirements give $C_{xy}=C_{yx}=C_{zy}=C_{yz}=0$ and $C_{xz}=C_{zx}$. Also, $I(00;ij)=(-1)^{n_x} I(ij;00)$, where n_x is the number of indices which are x. C is measured when both the beam and target are polarized, or when the initial state is unpolarized and the spins of both final state particles are observed.

(d) Two spins observed: $I(j0;i0)=I_oD_{ij}$, the depolarization tensor. Invariance requirements give $D_{xy}=D_{yx}=D_{yz}=D_{zy}=0$ and $D_{xz}=-D_{zx}$. Also, $I(i0;j0)=I(0i;0j)$. D is measured when the beam is

polarized and the scattered particle's spin is measured, or (as is experimentally more feasible) the target is polarized and the recoil particle's spin is analysed.

(e) Two spins measured: $I(0j;i0)=I_0K_{ij}$, the polarization transfer tensor. Invariance requirements give $K_{xy}=K_{yx}=K_{yz}=K_{zy}=0$ and $K_{xz}=-K_{zx}$. Also, $I(j0;0i)=I(0j;i0)$. K is measured by analysing the spin of the recoil particle when the beam is polarized, or by measuring the spin of the scattered particle when the target is polarized.

Tensors have been defined for the case when three and four spins are measured, but we will not discuss these. I_0, P, and the independent elements of C, D, and K are given in table I-1 in terms of the helicity amplitudes. This table is taken from Fox[9]. Fox also discusses the three and four spin tensors.

In the 1950's Wolfenstein defined some of the possible observables in spin experiments and related them to a convenient coordinate system. His terminology is still often used, so we will discuss it briefly. Wolfenstein related the experimental observables to a coordinate system in the center of mass with unit vectors $\hat{K}$, $\hat{P}$, and $\hat{N}$ (see Fig. I-2) where

$$\hat{K} = (\underset{\sim}{k}_f-\underset{\sim}{k}_i)/|\underset{\sim}{k}_f-\underset{\sim}{k}_i|$$

$$\hat{P} = (\underset{\sim}{k}_f+\underset{\sim}{k}_i)/|\underset{\sim}{k}_f+\underset{\sim}{k}_i|$$

$$\hat{N} = \hat{P} \times \hat{K}$$

Here, $\underset{\sim}{k}_f$ is the scattered particle's momentum in the center of mass, and $\underset{\sim}{k}_i$ is the incident particle's momentum. From Fig. I-2, it is easy to

see that, non-relativistically,

(a) $\hat{P}$ is parallel to the momentum of the scattered particle in the lab,

(b) $\hat{P}$ is perpendicular to the direction of the recoil particle in the lab,

(c) $\hat{K}$ is perpendicular to the direction of the scattered particle in the lab, and

(d) $\hat{K}$ is antiparallel to the direction of the recoil particle in the lab.

In actual experiments, it is easiest to measure spins in the directions perpendicular to a particle's motion in the lab, so, in the non-relativistic limit, Wolfenstein's coordinate system is convenient for measurements in the lab. In practical (relativistic) experiments, a coordinate system is often defined in the lab for each particle with $\hat{\ell}$ along the particle's direction of motion, $\hat{n}$ perpendicular to the scattering plane, and $\hat{s} = \hat{n} \times \hat{\ell}$. (see Fig. I-3). The system for the target particle can be chosen to be the same as the beam. In the non-relativistic limit, this coordinate system is the same as the one defined by Wolfenstein if the following correspondences are made:

$$\hat{k}_i \rightarrow \hat{\ell}_{1,2}$$

$$\hat{N} \rightarrow \hat{n}_{1,2} \qquad \text{For the beam and target}$$

$$\hat{N} \times \hat{k}_i \rightarrow \hat{s}_{1,2}$$

$\hat{P} \rightarrow \hat{\ell}_3$

$\hat{K} \rightarrow \hat{s}_3$ For the scattered particle

$\hat{N} \rightarrow \hat{n}_3$

$\hat{K} \rightarrow -\hat{\ell}_4$

$\hat{P} \rightarrow \hat{s}_4$ For the recoil particle

$\hat{N} \rightarrow \hat{n}_4$

Quantities referred to the laboratory system are often given the notation, e.g., $I(00;ss)=C_{ss}$ (or in the non-relativistic case, $I(00;K\ P)=C_{KP}$), while the corresponding quantities referred to the helicity rest frames are $I(00;xx)=C_{xx}$. Table I-2 gives Wolfenstein's names for experimental quantities and what they correspond to in the laboratory systems just described. The parameters D, R, A, R', and A' are related to the depolarization tensor defined earlier. Also, C_{nn} and C_{ss} are related to the correlation tensor C. Note that, e.g., $C_{ss} \rightarrow C_{KP}$ in the non-relativistic limit, but $C_{nn} \rightarrow C_{NN}$ always, since the normal to the scattering plane is not changed by a Lorentz transformation. Wolfenstein's experimental quantities have been expressed in terms of the Wolfenstein parameters by several authors.[10]

Experimental quantities measured in the laboratory system can easily be related to quantities in the helicity rest frames of the particles. To do this, the components of $\hat{\ell}$, $\hat{s}$, and $\hat{n}$ in the helicity rest frame of each particle are needed. The relationships are[9] (see Fig. I-4)

$$\hat{\ell}_1 = \hat{z}_1 \qquad \hat{\ell}_2 = -\hat{z}_2$$

$$\hat{s}_1 = \hat{x}_1 \quad \text{for the beam} \qquad \hat{s}_2 = -\hat{x}_2 \quad \text{for the target}$$

$$\hat{n}_1 = \hat{y}_1 \qquad \hat{n}_2 = \hat{y}_2$$

$$\hat{\ell}_3 = -\sin\alpha_3\,\hat{x}_3 + \cos\alpha_3\,\hat{z}_3 \quad \text{for the scattered}$$

$$\hat{s}_3 = \cos\alpha_3\,\hat{x}_3 + \sin\alpha_3\,\hat{z}_3 \quad \text{particle}$$

$$\hat{n}_3 = \hat{y}_3$$

$$\hat{\ell}_4 = \sin\alpha_4\,\hat{x}_4 + \cos\alpha_4\,\hat{z}_4 \quad \text{for the recoil}$$

$$\hat{s}_4 = \cos\alpha_4\,\hat{x}_4 - \sin\alpha_4\,\hat{z}_4 \quad \text{particle}$$

$$\hat{n}_4 = \hat{y}_4$$

The angles α_3 and α_4 are defined in Fig. I-4. When the masses of all particles are equal (as in pp scattering), $\alpha_3 = \theta_{3lab}$ and $\alpha_4 = \theta_{4lab}$. As an example, suppose, for the case of pp scattering, the spin of the scattered particle is analysed along its direction $\hat{s}_3$ in the lab, and the beam is initially polarized in the $\hat{s}_1 = \hat{x}_1$ direction. Then the quantity measured is

$$I_o D_{ss} = I(s0;s0)$$

$$= I(\cos\theta_{3lab}\,\hat{x}_3 + \sin\theta_{3lab}\,\hat{z}_3\ 0;\hat{x}0)$$

$$= \cos\theta_{3lab}\,I(x0;x0) + \sin\theta_{3lab}\,I(z0;x0)$$

$$I_o D_{ss} = I_o\cos\theta_{3lab}\,D_{xx} + I_o\sin\theta_{3lab}\,D_{xz}.$$

5. Spin Analysis by Rescattering in Carbon

The quantity measured in E313 was $P = -I(0n;00)/I_o$ for pp elastic scattering. The incident beam and target were unpolarized, and the spin of the recoil proton was analyzed along the normal to the scattering

plane by rescattering it in a carbon block. The scattering of a proton on carbon (spin $\frac{1}{2}$ on spin 0) can be described using the same formalism used to describe pp scattering (spin $\frac{1}{2}$ on spin $\frac{1}{2}$). The scattering matrix for the scattering of a spin $\frac{1}{2}$ particle by a spin 0 particle is[10]

$$\underset{\approx}{S} = a\underset{\approx}{1} + b\underset{\approx}{\sigma}\cdot\hat{\underset{\sim}{N}}$$

where $\hat{N}$ is the normal to the scattering plane of the proton-carbon scatter. If the incoming proton has polarization $\underset{\sim}{P}$, its density matrix is $\rho_i = \frac{1}{2}(\underset{\approx}{1} + \underset{\sim}{P}\cdot\underset{\approx}{\sigma})$. Then the cross-section is

$$\frac{d\sigma}{d\Omega} = \frac{\mathrm{Tr}\,\rho_f}{\mathrm{Tr}\,\rho_i} = \frac{1}{2}\,\mathrm{Tr}(S\,\rho_i S^\dagger)$$

$$= \frac{1}{2}\,\mathrm{Tr}(\underset{\approx}{S}[\underset{\approx}{1} + \underset{\sim}{P}\cdot\underset{\approx}{\sigma}]\underset{\approx}{S}^\dagger)$$

$$= \frac{1}{2}\,\mathrm{Tr}(\underset{\approx}{S}\underset{\approx}{S}^\dagger) + \frac{1}{2}\,\mathrm{Tr}(\underset{\approx}{S}\,\underset{\sim}{P}\cdot\underset{\approx}{\sigma}\,\underset{\approx}{S}^\dagger) \quad .$$

Define the recoil proton's direction of motion as the z axis and the normal to the original scattering plane as the y axis. Then if the second scatter has angles θ and φ, the normal to the second scattering plane is $\hat{N} = (\sin\varphi, -\cos\varphi, 0)$. The cross section is given by

$$I(\theta) = \mathrm{Tr}\,(\underset{\approx}{S}\underset{\approx}{S}^\dagger) + \mathrm{Tr}\,(a\,\underset{\approx}{1} + b\underset{\approx}{\sigma}\cdot\underset{\sim}{N})\,(\underset{\sim}{P}\cdot\underset{\approx}{\sigma})\,(a^* + b^*\,\underset{\approx}{\sigma}\cdot\underset{\sim}{N})$$

$$= |a|^2 + |b|^2 + ab^*\,P\cos\varphi + ba^*\,P\cos\varphi$$

$$= |a|^2 + |b|^2 + 2\,\mathrm{Re}(ab^*\,P\cos\varphi) \quad ,$$

using the fact that parity conservation requires $\underset{\sim}{P} = P_y$ (polarization from the original scatter can only be normal to the original scattering plane).

Then

$I(\theta) = I_o + 2\,\mathrm{Re}(ab^*)\,P\cos\varphi$, where $I_o = |a|^2 + |b|^2$ is the cross section for scattering from an unpolarized beam. Our experimental method was to sum all scatters from $\varphi = \frac{-\pi}{2} \rightarrow \frac{\pi}{2}$ and to call those scatters "left". The scatters from $\varphi = \frac{\pi}{2} \rightarrow \frac{3\pi}{2}$ were called "right".

$$L = \int_{-\pi/2}^{\pi/2} [I_o + 2\,\mathrm{Re}(ab^*)P\cos\varphi]d\varphi = I_o\,\pi + 2\,\mathrm{Re}(ab^*)P$$

$$R = \int_{\pi/2}^{3\pi/2} [I_o + 2\,\mathrm{Re}(ab^*)P\cos\varphi]d\varphi = I_o\,\pi - 2\,\mathrm{Re}(ab^*)P$$

Then

$$L - R = I_o\,\pi + 2\,\mathrm{Re}\,ab^*\,P - I_o\,\pi + 2\,\mathrm{Re}\,ab^*P$$

$$= 4\,\mathrm{Re}\,ab^*P \qquad \text{and}$$

$$L + R = 2\,I_o\,\pi$$

The asymmetry ϵ is defined by

$$\epsilon = \frac{L-R}{L+R} = + \frac{4\,\mathrm{Re}\,ab^*\,P}{2\,I_o\,\pi} = AP$$

where A is the analyzing power of carbon. This expression is valid for a given polar angle θ. Our apparatus included a range of θ, so we effectively integrated this expression over θ. The working formula, then, for measuring P is

$$\epsilon = P_{recoil}/A = -\,P_{scatt}/A$$

P is normally defined as $\langle\sigma_y\rangle_f$ for the scattered particle. An extra minus sign arises in our expression for P because we observed the recoil proton rather than the scattered proton. The analyzing power A is a property of the carbon and of our particular geometry. It was determined

for our apparatus in a calibration run using the polarized beam at the Argonne ZGS[12].

Theoretical Models for pp Interactions

No complete theory of nucleon-nucleon interactions exists at this time--in fact, we are far from a theory which can calculate experimental quantities from first principles. The models that we do have provide forms to be used in fitting the data. There seem to be two major classes of models--optical-type models and Regge models. Optical models give predictions for the t-dependence of the polarization, but in general say nothing about the s-dependence. Regge models do give a definite form for the s-dependence.

6. Simple Regge Model

Regge theory is based on two main ideas: the generalization of the angular momentum ℓ to a complex variable, and the analyticity of the scattering amplitude as a function of s and t. The origins of Regge theory date back to the work of Watson[13] in 1918 and Sommerfeld[14] in 1949. They showed that it is possible to generalize the angular momentum to a complex variable. Then the partial wave expansion of the scattering amplitude can be expressed as an integral in the complex ℓ-plane (the Sommerfeld-Watson transformation). In 1959 Regge[15] showed that, in non-relativistic scattering theory and for a large class of potentials, the only singularities in the scattering amplitudes are simple poles. Then the amplitude can be expressed, using the Cauchy residue theorem, as a sum over the residues of the poles. These poles are called Regge poles; their position in the complex ℓ-plane moves with energy and traces

out the Regge tranjectories. Regge theory is rigorous only in the non-relativistic theory, but for the simple Regge theory, the conclusions are assumed to be true in the relativistic case as well. Many excellent discussions of Regge theory are given in the literature. See, for example, ref. 16. For completeness, a brief development of the theory is given here.

Consider the reaction $ab \to cd$. Define the invariant scattering amplitude A (ignoring spin for the moment):

$$\frac{d\sigma}{d\Omega} = \frac{4}{s} |A|^2$$

A is a function of the Mandelstam variables $s=(p_a + p_b)^2$ and $t=(p_a - p_b)^2$, and is assumed to be analytic except for isolated poles. The possible values of s and t for the physical process $ab \to cd$ are (assuming, for simplicity, that all masses are equal)

$$s \geq 4m^2$$

$$-4p^2 \leq t = -2p^2(1 - \cos\theta) \leq 0 \qquad \text{Region I}$$

where $p=(s/4-m^2)^{\frac{1}{2}}$ is the momentum of one of the particles in the center of mass. However, if A is an analytic function of s and t, it can be continued for values of s and t which do not correspond to the physical process $ab \to cd$. In particular, it can be continued to the region where

$$t \geq 4m^2$$

$$-4p^2 \leq s = -2p^2(1-\cos\theta_t) \leq 0, \text{ where now} \qquad \text{Region II}$$

$$p^2 = t/4-m^2 .$$

These values of s and t correspond to the physical region of the reaction $a\bar{c} \to \bar{b}d$, the crossed-channel or t-channel reaction. It is assumed that

the same amplitude, $A(s,t)$, describes both reactions, and that A can be analytically continued from one region to the other.

Now a standard partial wave decomposition of A can be done in region II:

$$A(s,t) = \sum_{\ell=0}^{\infty} (2\ell+1)\, A_\ell(t)\, P_\ell(\cos\theta_t).$$

The Sommerfeld-Watson transformation can be applied to the partial wave series to express A as an integral over α (α is used to denote complex ℓ).

$$A(s,t) = -\frac{1}{2i} \int_C \frac{d\alpha\, (2\alpha+1)\, A(\alpha,t)\, P_\alpha(\cos\theta_t)}{\sin \pi\alpha}$$

where the contour C is shown in Fig. I-5. The contour can be deformed as shown in Fig. I-6, and, if the only singularities are simple poles, the Cauchy residue theorem can be applied, and A can be expressed as:

$$A(s,t) = -\pi \sum_j \frac{\beta_j(t)\, (2\alpha_j+1)\, P_{\alpha_j}(\cos\theta_t)}{\sin \pi\alpha_j} + \int_{C',C''} \frac{d\alpha (2\alpha+1)\, A(\alpha,t)\, P_\alpha(\cos\theta_t)}{\sin \pi\alpha}$$

where $\beta_j(t)$ is the residue of the jth pole, and $\alpha_j(t)$ is the value of the angular momentum for which it occurs. The contours C' and C" are shown in Fig. I-6. It can be shown that the integral over the semicircle C" vanishes as the radius $\to \infty$.

Now the assumption of analyticity can be applied. This form of $A(s,t)$, although derived in the t-channel, is assumed to hold for the s-channel, where $s \geq 4m^2$ and $-4p^2 \leq t \leq 0$. We can now obtain an approximation for $A(s,t)$ in the limit $s \to \infty$. The generalized Legendre polynomials, $P_\alpha(z)$, have the behavior $P_\alpha(z) \to z^\alpha$ for $\mathrm{Re}\,\alpha > -\frac{1}{2}$ and $z \to \infty$. Consequently, the integral along C' goes as $(\cos\theta_t)^{-\frac{1}{2}+\epsilon} = [2s/(t-4m^2)]^{-\frac{1}{2}+\epsilon}$

which vanishes for $s \to \infty$ and $|t| < s$. Then only the residue term contributes to $A(s,t)$:

$$A(s,t) = \pi \sum_j \frac{\beta_j(t)\ (2\alpha_j+1)\ P_{\alpha_j}(\cos\ \theta_t)}{\sin\ \pi\alpha_j}$$

$$\cong \sum_j \frac{\beta_j(t)\ (2\alpha_j+1)\ (\cos\ \theta_t)^{\alpha_j}}{\sin\ \pi\alpha_j}$$

$$\cong \sum_j \frac{\beta_j(t)}{\sin\ \pi\alpha_j} \left(\frac{s}{s_o}\right)^{\alpha_j} \quad \text{for } s \to \infty.$$

The conventional scale factor, s_o, has been introduced, and the $(2\alpha_j+1)$ has been absorbed into $\beta_j(t)$. Each term in the sum corresponds to a pole or resonance in the t-channel. Fig. I-7 shows a Feynman diagram of the process believed to be occurring. The interaction $ab \to cd$ at high energy takes place through the exchange of a particle (Reggeon) in the t-channel. Stated simply, poles in the t-channel determine the high energy behavior of a reaction in the s-channel.

Regge theory makes no predictions about the forms of the residues, $\beta(t)$, or the trajectories, $\alpha(t)$. These parameters are adjusted to fit the data, and, hopefully, the same values will give good fits to several sets of data. One restriction on all trajectories, however, is that $\alpha(t = 0) \leq 1$ -- otherwise total cross sections would diverge for $s \to \infty$. The trajectory with $\alpha(t=0) = 1$ is called the Pomeron and is assumed to have the quantum numbers of the vacuum. $\beta(t)$ is generally taken to be real, and $\alpha(t)$ is believed to be real for $t < 0$.

One assumption usually made about the residue $\beta(t)$ is factorization. It is believed that, for the reaction $ab \to cd$, the residue can be written as $\beta = \beta_{arc}\,\beta_{brd}$ where r is the exchanged particle. Each factor corresponds to one vertex and is independent of the other vertex. (See Fig. I-7.) For example, if the reaction $ag \to ch$ were considered, the residue would be $\beta_{arc}\,\beta_{grh}$, where β_{arc} is the same as before, even though $\beta_{grh} \neq \beta_{brd}$.

In the discussion so far, the trajectories have been considered for the region $t < 0$. If a plot (called a Chew-Frautschi plot) of Re α vs. t is extended to $t > 0$, an interesting observation can be made.[17] For every other integral value of α(or half-integral for the case of baryons), the value of t corresponds to the square of the mass of a real particle whose spin is equal to Re α. All particles lying on a trajectory have the same quantum numbers except for spin. Trajectories are named for the lowest mass particle lying on them and are taken to have the same quantum numbers as that particle. They appear to be approximately linear with slope $\sim 1\ (\mathrm{GeV})^{-2}$. For a given reaction only certain trajectories can be exchanged, since quantum numbers must be conserved at each vertex.

The fact that particles occur only when α changes by two units rather than one leads to the idea of signature. To accommodate this experimental fact, a factor is introduced into the amplitude to cancel every other pole. For mesons the factor is $(1 \pm (-1)^{\alpha}) = (1 \pm e^{-i\pi\alpha})$, and the amplitude for a single pole becomes

$$A(s,t) = \beta(t)\left(\frac{s}{s_o}\right)^{\alpha(t)}\left[\frac{1 \pm e^{-i\pi\alpha}}{\sin \pi\alpha}\right] . \qquad (1)$$

The factor $(1 \pm e^{-i\pi\alpha})/\sin \pi\alpha$ is called the signature factor; the (+) sign corresponds to positive signature and the (-) sign to negative signature. In non-relativistic scattering, if an exchange potential is present, a Regge pole contributes only to odd or even partial waves. If the same property is assumed to be true in the relativistic case, A(s,t) would be written as

$$A(s,t) = \frac{\beta}{\sin \pi\alpha} [P_\alpha(\cos \theta_t) \pm P_\alpha(-\cos \theta_t)]$$

$$= \frac{\beta}{\sin \pi\alpha} \left(\frac{s}{s_o}\right)^\alpha [1 \pm (-1)^\alpha]$$

$$= \beta \left(\frac{s}{s_o}\right)^\alpha \left[\frac{1 \pm e^{-i\pi\alpha}}{\sin \pi\alpha}\right] ,$$

which also leads to the signature factor.

Spin is usually taken into account by assuming a form for each helicity amplitude like (1). The residues are factored, with the factor at each vertex being either flip of non-flip. For pp scattering the amplitudes for the exchange of a simple pole could be written:

$$\phi_1 = \phi_3 = \left(\frac{s}{s_o}\right)^\alpha \left[\frac{1 \pm e^{-i\pi\alpha}}{\sin \pi\alpha}\right] \eta^2$$

$$\phi_2 = \phi_4 = \left(\frac{s}{s_o}\right)^\alpha \left[\frac{1 \pm e^{-i\pi\alpha}}{\sin \pi\alpha}\right] \xi^2$$

$$\phi_5 = \left(\frac{s}{s_o}\right)^\alpha \left[\frac{1 \pm e^{-i\pi\alpha}}{\sin \pi\alpha}\right] \eta\, \xi$$

where $\eta(t)$ is the residue for non-flip coupling, and $\xi(t)$ is the residue for flip coupling at the vertex. Sometimes a factor $(-t)^{|\lambda-\lambda'|}$ is included, where $\lambda=\lambda_a-\lambda_b$ and $\lambda' = \lambda_c-\lambda_d$. This factor builds in the

correct angular momentum dependence as $t \to 0$.[18]

Regge theory has been used extensively to fit cross-section and polarization data for pp and other reactions. See for example, refs. 19,20. The simple Regge theory, using several trajectories, has had considerable success in fitting the data, but certainly not universal success.

Regge theory makes definite predictions for the s-dependence of the polarization, P. First of all, to obtain a non-zero polarization, it is necessary to exchange at least two Regge poles. Recall that

$$I_o P = -\mathrm{Im}\,(\phi_1 + \phi_2 + \phi_3 - \phi_4)\phi_5^*$$

Consider just the term $\phi_1\phi_5^*$, and assume that a single Reggeon with positive signature is exchanged. Then, using the forms for ϕ_1 and ϕ_5 given above,

$$\phi_1\phi_5^* = \pi^3\xi\left(\frac{s}{s_o}\right)^{2\alpha}\left[\frac{1 + e^{-i\pi\alpha}}{\sin \pi\alpha}\right]\left[\frac{1 + e^{-i\pi\alpha}}{\sin \pi\alpha}\right]^*$$

$$= \pi^3\xi\left(\frac{s}{s_o}\right)^{2\alpha}\left[\frac{2(1 + \cos \pi\alpha)}{\sin^2 \pi\alpha}\right]$$

which has no imaginary part! The same is true for all the other terms in P, so the polarization vanishes if only one Regge pole contributes to the process.

Now assume that two Regge poles contribute. Then ϕ_1 can be written as

$$\phi_1 = \left(\frac{s}{s_o}\right)^{\alpha_1}\left[\frac{1 + e^{-i\pi\alpha_1}}{\sin \pi\alpha_1}\right]\eta_1^2 + \left(\frac{s}{s_o}\right)^{\alpha_2}\left[\frac{1 + e^{-i\pi\alpha_2}}{\sin \pi\alpha_2}\right]\eta_2^2 ,$$

and likewise ϕ_5 can be written

$$\phi_5 = \left(\frac{s}{s_o}\right)^{\alpha_1}\left[\frac{1 + e^{-i\pi\alpha_1}}{\sin \pi\alpha_1}\right]\eta_1\xi_1 + \left(\frac{s}{s_o}\right)^{\alpha_2}\left[\frac{1 + e^{-i\pi\alpha_2}}{\sin \pi\alpha_2}\right]\eta_2\xi_2 .$$

Now interference can occur between the two Reggeons and P can be non-zero:

$$\phi_1\phi_5^* = \left(\frac{s}{s_o}\right)^{2\alpha_1} \eta_1^3\xi_1 \left[\frac{2 + 2\cos\pi\alpha_1}{\sin^2\pi\alpha_1}\right]$$

$$+ \left(\frac{s}{s_o}\right)^{\alpha_1+\alpha_2} \eta_1^2\eta_2\xi_2 \left[\frac{1 + e^{-i\pi\alpha_1} + e^{i\pi\alpha_2} + e^{-i\pi(\alpha_1-\alpha_2)}}{\sin\pi\alpha_1 \ \sin\pi\alpha_2}\right]$$

$$+ \left(\frac{s}{s_o}\right)^{\alpha_2+\alpha_1} \eta_2^2\eta_1\xi_1 \left[\frac{1 + e^{-i\pi\alpha_2} + e^{i\pi\alpha_1} + e^{-i\pi(\alpha_2-\alpha_1)}}{\sin\pi\alpha_1 \ \sin\pi\alpha_2}\right]$$

$$+ \left(\frac{s}{s_o}\right)^{2\alpha_2} \eta_2^3\xi_2 \left[\frac{2 + 2\cos\alpha_2}{\sin^2\pi\alpha_2}\right] .$$

This expression does have an imaginary part in the school and third terms:

$$\mathrm{Im}(\phi_1\phi_5^*) = \left(\frac{s}{s_o}\right)^{\alpha_1+\alpha_2} \eta_1^2\eta_2\xi_2 \ K + \left(\frac{s}{s_o}\right)^{\alpha_1+\alpha_2} \eta_2^2\eta_1\xi_1 \ K'$$

where K and K′ are factors involving $\alpha_1(t)$ and $\alpha_2(t)$ and are independent of s. We are interested in the s-dependence of P for $s \to \infty$. Again considering only the first term in P,

$$P \sim \frac{\mathrm{Im}(\phi_1\phi_5^*)}{I_o} \quad \text{where } I_o = |\phi_1|^2 + |\phi_2|^2 + |\phi_3|^2 + |\phi_4|^2 + 4|\phi_5|^2.$$

Then

$$P \sim \frac{K_1\left(\frac{s}{s_o}\right)^{\alpha_1+\alpha_2}}{K_2\left(\frac{s}{s_o}\right)^{2\alpha_1} + K_3\left(\frac{s}{s_o}\right)^{2\alpha_2} + K_4\left(\frac{s}{s_o}\right)^{\alpha_1+\alpha_2}}$$

where again the K's are factors that depend on t only. The pole with the largest value of α will determine the behavior of the denominator. This

will be the Pomeron, with $\alpha(t=0) = 1$. The other terms in the denominator can be neglected at high energy. Then

$$P \sim \left(\frac{s}{s_o}\right)^{\alpha_1+\alpha_2-2\alpha_1}$$

$$\sim \left(\frac{s}{s_o}\right)^{\alpha_2-\alpha_1}$$

Now, $(\alpha_2-\alpha_1) < 0$, since all other trajectories lie below the Pomeron. So the polarization dies off as some negative power of s. Thus standard Regge theory makes a definite (and discouraging) prediction for the polarization: $\underline{P \to 0 \text{ as } s \to \infty}$.

7. Modified Regge Theory: the Absorption Corrected Regge Model

When the simple Regge theory failed to fit certain data (such as polarization in $\pi^- p \to \pi^o n$), a number of modifications were tried with varying degrees of success. One of the most successful was the absorption correction to Regge amplitudes. A great deal of work has been done on this model by Kane and others at the University of Michigan.[21,22,23] Ref. 22 is an excellent and detailed discussion of the Michigan version of the absorption-corrected Regge theory. The model gives a definite prescription for calculating pp polarizations, as well as many other experimental quantities. The basic ideas of the model are briefly presented here.

Consider the reaction $ab \to cd$. If the Reggeon, r, being exchanged has non-vacuum quantum numbers, the form for each helicity amplitude is similar to that given by the simple Regge theory:

$$R^r(s,t) = (-t)^{n+x}\, \beta_{arc}\, \beta_{brd}\, \Gamma\left[\frac{j-\alpha_r(t)}{2}\right] \left(\frac{s}{s_o}\right)^{\alpha_r(t)} \exp\left[\frac{-i\pi(\alpha_r(t)-j)}{2}\right]$$

where $n + x = |\lambda_c-\lambda_a|+|\lambda_d-\lambda_b|$, j is the spin of the lowest-lying particle on the trajectory, and the β's are the factorized residues. The gamma function gives the amplitude poles at every <u>other</u> integral value of α, as required. The amplitudes can be expressed in impact parameter space by the transformation

$$R(s,b) = \frac{1}{2p^2} \int_0^\infty \sqrt{-t}\, d\sqrt{-t}\, R(s,t)\, J_n(b\sqrt{-t}) ,$$

where n is the net helicity flip. The inverse transformation is

$$R(s,t) = 2p^2 \int_0^\infty bdb\, R(s,b)\, J_n(b\sqrt{-t}) .$$

The model makes extensive use of the impact parameter representation and the transformations between b and t.

For vacuum quantum number exchange (the Pomeron), the amplitude is quite different. It is <u>not</u> an exchanged Regge pole. Rather, it is the complete amplitude corresponding to diffractive elastic scattering, and the arguments used to determine its form are very similar to those of optical models to be discussed later. Basically, hadrons are assumed to interact in terms of two components, a "central" component, and an "edge" or peripheral piece. Suppose the central portion is a black disk of radius R_c. Then the amplitude in impact parameter space would be $M_c(b) = \theta(R_c-b)$, where $\theta(x)$ is the step function

$$\theta(x) = 1 \quad \text{for } x > 0$$

$$\theta(x) = 0 \quad \text{for } x \leq 0$$

The distribution in t is given by

$$M_c(t) = 2p^2 \int_0^\infty bdb\, M(b)\, J_o(b\sqrt{-t})$$

$$= 2p^2\, R_c^2\, J_1(R_c\sqrt{-t})/R_c\sqrt{-t} \quad .$$

If the edge is a δ-function in impact parameter space at the radius R_e, $M_e(b) = R_e\, \delta(R_e - b)$, then the amplitude $M_e(t)$ would be

$$M_e(t) = 2p^2\, R_e^{\,2}\, J_o(R_e\sqrt{-t}) \ .$$

Of course, the central disk cannot really have a sharp boundary, and the edge piece is not a δ-function. The boundaries are spread out by multiplying the Bessel functions by exponentials.

The energy dependence of the Pomeron is determined by allowing the radius of both the central part and the peripheral part to increase with s. The radius of the edge is given the dependence $R_e^{\,2} \sim \ln(s)$, although no rigorous argument has been given for that choice. The central part is believed to increase more slowly with energy, so

$$R_c^{\,2} \sim R_{oc}^{\,2} + r_c^{\,2} \ln s,$$

where $R_{oc} \gg r_c$.

To guarantee that the Pomeran has even signature[22], the phase and energy are related by $s \to se^{-i\pi\alpha}$. That is, $(se^{-i\pi\alpha})$ is treated as a single variable.

All of these considerations together give a Pomeron of the form

$$P(s,t) = -is[A_c\, e^{B_c t}\, R_c^{\,2}\, J_1(R_c\sqrt{-t})/R_c\sqrt{-t}]$$

$$-is[A_e\, e^{B_e t}\, R_e^{\,2}\, J_o(R_e\sqrt{-t})]$$

where $R_c^2 = R_{oc}^2 + r_c(\ln s - i\pi/2)$ and $R_e^2 = R_{oe}^2(\ln s - i\pi/2)$.

In the absorption model, vacuum quantum number, diffractive processes can also flip helicities or change mass. (A specific mechanism by which this can occur is discussed later.) For this process only the peripheral part of the diffractive amplitude is used:

$$D_n(s,t) = -is[A_e\ e^{B_e t}\ R_e^2\ J_n(R_e^2\sqrt{-t})],$$

where n is the net helicity flip.

An important aspect of the Michigan model is the absorption correction to Reggeon exchange. The idea is, simply, that the initial and final state particles rescatter elastically off each other. Then the Reggeon amplitudes should be corrected for this elastic rescattering. The absorption prescription used is the method proposed by Sopkovich in 1962.[24] Each Regge amplitude in impact parameter space is modified by an effective S matrix:

$$M(s,b) = R(s,b)\ S_{eff}(s,b)$$

where S_{eff} is given by

$$S_{eff}(s,b) = 1 - i2p^2\ M_{eff}(s,b)/4\pi s.$$

$M_{eff}(s,t)$, the rescattering amplitude, has three contributions:

$$M_{eff}(s,t) = P(s,t) + M_f(s,t) + \Sigma(s,t)$$

Here $P(s,t)$ is the Pomeron amplitude defined earlier--this is the dominant contribution. The parameters in the Pomeron amplitude are determined from elastic cross section data, and the same form is used for the absorption. $M_f(s,t)$ is the contribution to elastic scattering from the exchange of the f-trajectory. $\Sigma(s,t)$ represents the contribution to the

absorption due to all the inelastic intermediate states. $M_{eff}(s,b)$ is obtained from $M_{eff}(s,t)$ by the appropriate transformation, the Reggeon amplitude $R(s,b)$ is then absorbed, and the absorbed amplitude is transformed back to the representation in t, giving the full Regge amplitude, $M(s,t)$. One interesting result of absorption is that, since the real and imaginary parts of an amplitude are absorbed differently their relative phase changes, and a single Regge exchange can give rise to a polarization.

Polarizations in pp scattering arise from two sources in this model. At low and intermediate energies, several Regge trajectories (ρ,ω,A_2) as well as the Pomeron will contribute to elastic scattering, and interference between them will lead to polarizations. But, as we have seen, this polarization will die off at higher energies.

Pumplin and Kane have discussed a process by which diffractive elastic scattering can flip helicities and lead to polarizations.[23] The process is two-pion exchange, as shown in Fig. I-8. The π can couple with a flip amplitude at one vertex and non-flip at the other, leading to a net helicity flip. Double flip amplitudes could arise if both protons dissociated, but such effects are assumed to be small. To calculate the polarization, it is necessary to know the flip/non-flip ratio for the process of Fig. I-8. Pumplin and Kane have calculated the ratio by numerical integration[23] and found it to be about .35. Now we can write down the non-flip and flip amplitudes for pp elastic scattering for this process:

$$M_{++} = is\, A_c\, R^{B_c t}\, J_1(R\sqrt{-t})/\sqrt{-t} + is\, A_e\, r^2\, e^{B_e t}\, J_o(r\sqrt{-t})$$

$$M_{+-} = is\, C\, A_e\, r^2\, e^{B_e t}\, J_1(r\sqrt{-t}), \text{ where}$$

$$R^2 = R_o^2 + R_1^2\,(\ln s - i\pi/2),$$

$$r^2 = r_o^2(\ln s - i\pi/2)$$

and C is the flip/non-flip ratio. The two non-flip amplitudes have been included together in M_{++}. The parameters A_e, B_e, etc. were determined from a fit to elastic cross section data, and the same parameters are assumed to hold in calculations of the polarization. Values given in ref. 23 are:

A_c=11.5 A_e=1.94 R_o^2=8.47 r_o^2=2.92

B_c=2.21 B_e=3.93 R_1^2=.33

This leads to very specific formulas for the amplitudes, and the polarization is easily calculated from

$$P = 2\ \mathrm{Im}(M_{++}\ M_{+-}^*)/[\ |M_{++}|^2 + |M_{+-}|^2\ ] .$$

The sign of the polarization is not determined because of ambiguity in $\pm\sqrt{R}$ where R is complex, but it can presumably be fixed by the low energy data. Two-pion exchange will continue to be important at high energy, so polarizations in pp elastic scattering (and other diffractive processes) should persist to very high energies. Polarizations calculated from ref. 23 are compared with our data in Chapter IV.

8. Optical Models

The general philosophy of optical models is quite different from that of Regge models. Optical models do not consider t-channel processes at all, but treat the interactions of hadrons as an s-channel process similar to the diffractive scattering of light from a physical object. Hadrons are assumed to be objects of finite size with certain mass distributions and opaqueness. When they interact, their mass distributions

overlap and absorption takes place. A number of optical models have been developed; we will discuss two, one due to Chu, Hendry and Abshire[25,26,27] and the second due to Durand and Halzen.[28].

The model of Chu, Hendry and Abshire has been quiet successful in fitting cross-section and polarization data for pp and other reactions below about 20 GeV/c.[26] In this model, the helicity amplitudes are expressed as functions of the impact parameter b. Recall that helicity amplitudes have the expansion[5] (assuming $\varphi = 0$):

$$\langle \lambda_c \lambda_d | S | \lambda_a \lambda_b \rangle = \tfrac{1}{2}p \sum_j (2j+1) \langle \lambda_c \lambda_d | S^j | \lambda_a \lambda_b \rangle \, d^j_{\lambda\lambda'}(\theta) \ ,$$

where $\lambda = \lambda_a - \lambda_b$, $\lambda' = \lambda_c - \lambda_d$ and S^j is the part of the S-matrix which acts on the jth partial wave. For the pp non-flip amplitudes, the expansion is

$$\phi_1 = \frac{1}{2p} \sum_j (2j+1) \, S_{++} \, d^j_{oo}(\theta) \ .$$

The d function has the Bessel function approximation (for large j and small θ)

$$d^j_{oo}(\theta) \cong J_o\left[(2j+1) \sin \frac{\theta}{2}\right] .$$

The impact parameter b is related to the angular momentum j approximately by

$$j + \tfrac{1}{2} \sim pb.$$

Also,

$$\sin \frac{\theta}{2} = \sqrt{-t}/2p \ .$$

Then

$$d^j_{oo}(\theta) \cong J_o(b\sqrt{-t})$$

The sum over j can be converted to an integral over b:

$$\phi_1 \approx \frac{1}{p} \int_0^\infty pbdb\ J_o(b\sqrt{-t})\ S^j_{++} \quad .$$

S^j_{++} is assumed to have two parts--a central absorptive disk,

$$S^j_{++} = ia_1 \qquad \text{for } b < R$$

$$= 0 \qquad \text{for } b > R \ ,$$

and a peripheral or edge part strongly peaked at R:

$$S^j_{++} = a_2\ \delta(b-R) \ .$$

Then the non-flip amplitude is

$$\phi_1 = ia_1 \int_0^\infty bdb\ J_o(R\sqrt{-t}) + a_2 \int_0^\infty bdb\ J_o(b\sqrt{-t})\delta(b-R)$$

$$= ia_1\ J_1(R\sqrt{-t})/R\sqrt{-t} \ + a_2\ R\ J_o(R\sqrt{-t}).$$

ϕ_3 has essentially the same form as ϕ_1.

For the single flip amplitude, ϕ_5, the expansion is

$$\phi_5 = \frac{1}{2p} \sum_j (2j+1)\ d^j_{01}(\theta)\ S^j_{+-}$$

Now S^j_{+-} is assumed to have only the peripheral part,

$$S^j_{+-} = a_3\ \delta(b-R)$$

The Bessel function approximation for $d^j_{01}(\theta)$ is

$$d^j_{01}(\theta) \cong J_1[(2j+1)\ \sin\frac{\theta}{2}\ ]$$

$$\cong J_1(b\sqrt{-t}) \ .$$

The sum over j can again be converted into an integral, and we have

$$\phi_5 = a_3 \int_0^\infty bdb\ J_1(b\sqrt{-t})\ \delta(b-R)$$

$$= a_3\ RJ_1(R\sqrt{-t}) \ .$$

Double flip amplitudes are assumed to be much smaller than single flip and are ignored. The result is a polarization of the form

$$P \sim [J_1(R\sqrt{-t})]^2/R\sqrt{-t}$$

Of course, the actual situation will not be represented by δ-functions and a disk with sharp edges, but this expression for P gives a general idea of the way P will behave. If the radii of the central and edge parts are the same, the polarization, as a function of t, will have double zeroes at the zeroes of J_1. If the radii are allowed to be different, P will have a single zero at the zeroes of $J_1(R\sqrt{-t})$ and $J_1(R'\sqrt{-t})$ and will probably go negative in between. This model gives no prediction for the energy dependence of the polarization.

The second optical model which will be briefly discussed is that of Durand and Halzen.[28] The basic assumption of the model is that the primary pp interaction is diffractive, and that spin effects enter only through a weak spin-orbit interaction. The eikonal approximation (a standard technique from optics) is used to obtain an expression for the scattering matrix S:

$$S = \frac{ip}{2\pi} \int [1-e^{-\chi(b)}]\, e^{-i\underset{\sim}{q}\cdot\underset{\sim}{b}}\, d^2b,$$

where $\underset{\sim}{q}$ is the momentum transfer, and $\underset{\sim}{b}$ is the impact parameter. The eikonal function $\chi(b)$, has two parts-a central, spin-independent term which gives the diffraction part of the interaction, and a term which gives the spin-orbit interaction:

$$\chi(\underset{\sim}{b}) = \chi_c(\underset{\sim}{b}) - i\,\chi_{LS}(\underset{\approx}{\sigma}_1 + \underset{\approx}{\sigma}_2)\cdot(\underset{\sim}{b} \times \hat{z}),$$

where $\hat{z}$ is along the direction of the particle's motion. χ_c is assumed to be real, χ_{LS} is real and positive for an attractive spin-orbit interaction, and $|\chi_{LS}| \ll |\chi_c|$. The evaluation of the integral (see ref. 28) leads to an expression for P in terms of the cross-section:

$$P\sigma \sim \chi_{LS}\, \sigma'$$

where $\sigma = \frac{d\sigma}{dt}$ and σ' is the derivative of $\frac{d\sigma}{dt}$ with respect to t. χ_{LS} is a parameter which is adjusted to fit the data. The model also gives

$$\sigma\, C_{nn} \sim \sigma\, K_{nn} \sim \chi^2_{LS}\, \sigma''.$$

If the model is valid, structure in $\frac{d\sigma}{dt}$ should be associated with structure in P. So in the dip region of $\frac{d\sigma}{dt}$ for pp scattering, one would expect to see a very interesting polarization. P should go though zero and change sign as $\frac{d\sigma}{dt}$ goes through the dip.

Table I-1

Experimental Observables in pp Scattering
in Terms of Helicity Amplitudes

Name	Helicity Amplitude Representation
I_o (Unpolarized cross section)	$\frac{1}{2}[\lvert\phi_1\rvert^2 + \lvert\phi_2\rvert^2 + \lvert\phi_3\rvert^2 + \lvert\phi_4\rvert^2 + 4\lvert\phi_5\rvert^2]$
I_oP (Polarization parameter)	$\mathrm{Im}\ \phi_5(\phi_1 + \phi_2 + \phi_3 - \phi_4)^*$
I_oC_{xx} (Spin correlation parameters)	$-\mathrm{Re}\ (\phi_2\phi_1^* + \phi_4\phi_3^*)$
I_oC_{yy}	$\mathrm{Re}[2\lvert\phi_5\rvert^2 + \phi_2\phi_1^* - \phi_4\phi_3^*]$
I_oC_{zz}	$\frac{1}{2}[\lvert\phi_1\rvert^2 + \lvert\phi_2\rvert^2 - \lvert\phi_3\rvert^2 - \lvert\phi_4\rvert^2]$
I_oC_{xz}	$\mathrm{Re}\ \phi_5(-\phi_1 - \phi_2 + \phi_3 - \phi_4)^*$
I_oD_{xx} (Depolarization parameter)	$\mathrm{Re}(\phi_3\phi_1^* + \phi_4\phi_2^*)$
I_oD_{yy}	$\mathrm{Re}[\phi_3\phi_1^* - \phi_4\phi_2^* + 2\lvert\phi_5\rvert^2]$
I_oD_{zz}	$\frac{1}{2}[\lvert\phi_1\rvert^2 - \lvert\phi_2\rvert^2 + \lvert\phi_3\rvert^2 - \lvert\phi_4\rvert^2]$
I_oD_{xz}	$\mathrm{Re}\ \phi_5(-\phi_1 + \phi_2 - \phi_3 - \phi_4)^*$
I_oK_{xx} (Polarization transfer parameters)	$-\mathrm{Re}(\phi_3\phi_2^* + \phi_4\phi_1^*)$
I_oK_{yy}	$\mathrm{Re}[\phi_3\phi_2^* - \phi_4\phi_1^* + 2\lvert\phi_5\rvert^*]$
I_oK_{zz}	$\frac{1}{2}[\lvert\phi_1\rvert^2 - \lvert\phi_2\rvert^2 - \lvert\phi_3\rvert^2 + \lvert\phi_4\rvert^2]$
I_oK_{xz}	$\mathrm{Re}\ \phi_5(-\phi_1 + \phi_2 + \phi_3 + \phi_4)^*$

These quantities are referred to the helicity rest frames of the particles, as described in section I-4.

Table I-2

Wolfenstein's Experimental Observables and their Relativistic Generalizations.

$I_o = I(00;00)$

$I_oP = I(\hat{N}0;00) \rightarrow I(\hat{n}0;00)$

$I_oD = I(\hat{N}0;\hat{N}0) \rightarrow I(\hat{n}0;n0)$

$I_oR = I(\hat{K}0;\hat{N} \times \hat{k}_i 0) \rightarrow I(\hat{s}0;\hat{s}0)$

$I_oA = I(\hat{K}0;\hat{k}_i 0) \rightarrow I(\hat{s}0;\hat{\ell}0)$

$I_oR' = I(\hat{P}0;\hat{N} \times \hat{k}_i 0) \rightarrow I(\hat{\ell}0;\hat{s}0)$

$I_oA' = I(\hat{P}0;\hat{k}_i 0) \rightarrow I(\hat{\ell}0;\hat{\ell}0)$

$I_oC_{NN} = I(\hat{N}\hat{N};00) \rightarrow I(\hat{n}\hat{n};00)$

$I_oC_{KP} = I(\hat{K}\hat{P};00) \rightarrow I(\hat{s}\hat{s};00)$

The vectors $\hat{K}$, $\hat{N}$, $\hat{P}$, $\hat{n}$, etc., are defined in section I-4.

CHAPTER I FIGURES

Figure I-1. The helicity rest frames are defined in the center of mass coordinate system for the interaction $12 \to 34$. Each particle has its z axis along its direction of motion in the center of mass; the y axis is normal to the scattering plane, and x = y x z.

Figure I-2. The coordinate system defined by Wolfenstein to describe experimental observables. k_i and k_f are the incident and final momenta of particle 1 in the center of mass, $K = (k_f - k_i)/|\underset{\sim}{k}_f - \underset{\sim}{k}_i|$, and $P = (k_f + k_i)/|\underset{\sim}{k}_f + \underset{\sim}{k}_i|$. The normal to the scattering plane is out of the paper.

Figure I-3. The laboratory coordinate system used in relativistic spin experiments. Each particle has its own system with along the particle's direction of motion, n normal to the scattering plane, and s = n x . The target particle, which is at rest in the lab is given the same system as the beam.

Figure I-4. The relationship of laboratory coordinate systems to center of mass helicity rest frames. In the non-relativistic limit, or when the masses of all particles are equal,

Figure I-5. Contour for the Sommerfeld-Watson transformation. The contour encloses the positive real axis but excludes any poles in the amplitude A(t).

Figure I-6. The contour of Figure I-5 deformed to convert the integral of the Sommerfeld-Watson transformation into a sum over the residues of the poles in A(t). The line C must pass to the right of Re $= -\frac{1}{2}$.

Figure I-7. The exchange of a Reggeon r in the t-channel of the reaction ab cd. Associated with the vertex of particles a, r, and c is the factorized residue β_{arc}. The residue β_{brd} is associated with the vertex of particles b, r, and d.

Figure I-8. The two pion exchange process of reference 23. Particle a dissociates into c plus a pion, the pion interacts with b via Pomeron exchange, and the pion is reabsorbed by particle a.

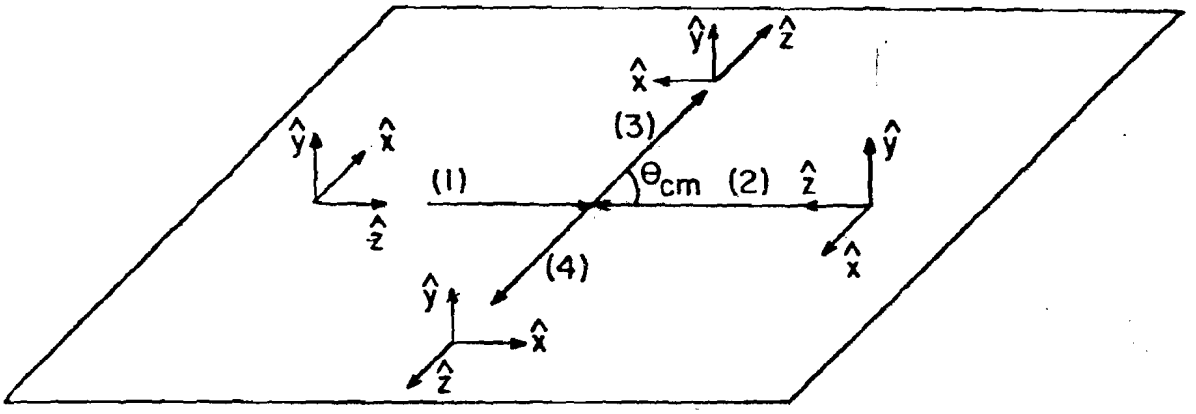

Figure I-1

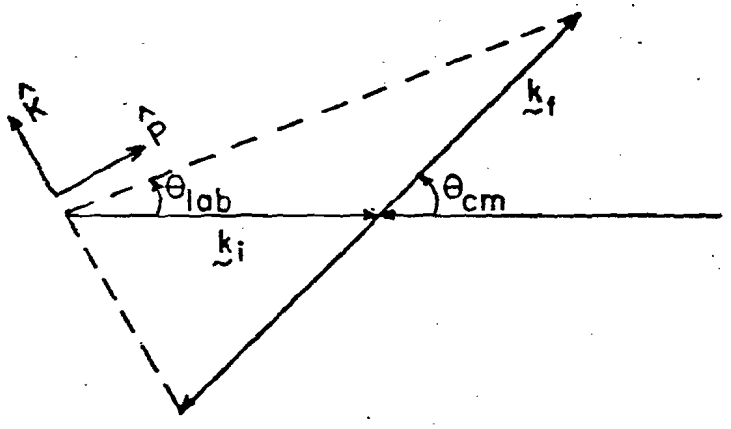

Figure I-2

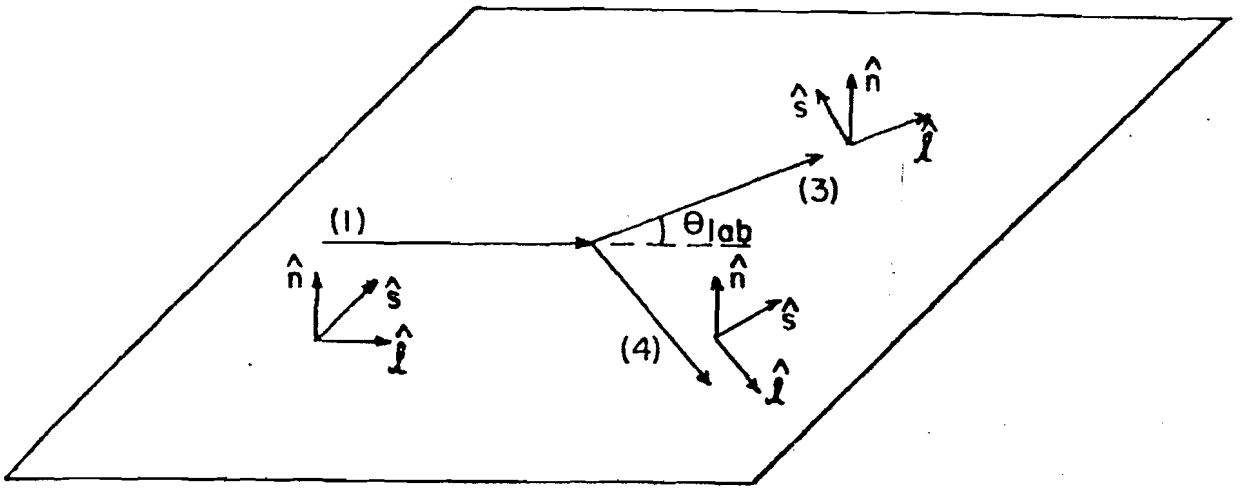

Figure I-3

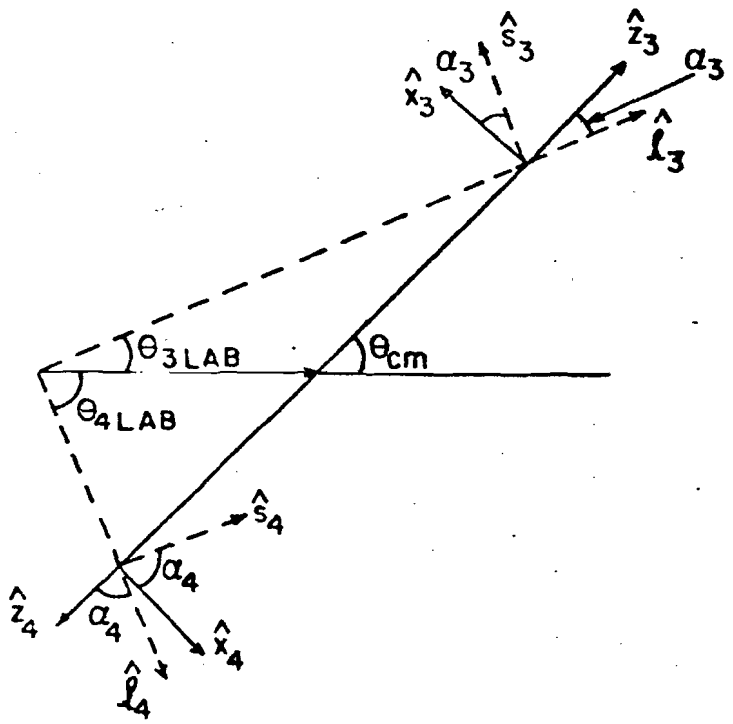

Figure I-4

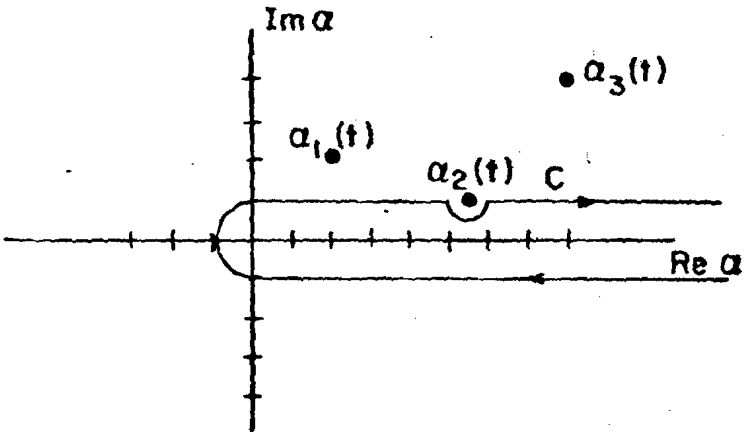

Figure I-5

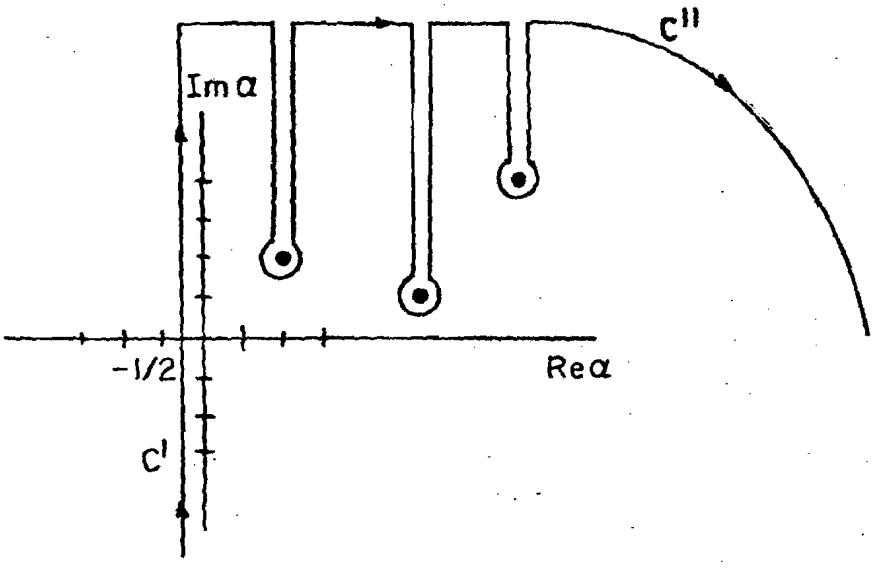

Figure I-6

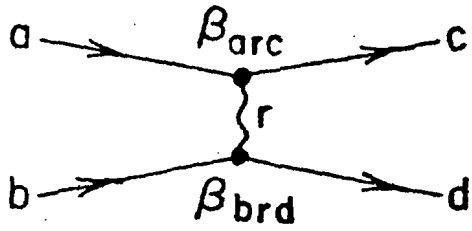

Figure I-7

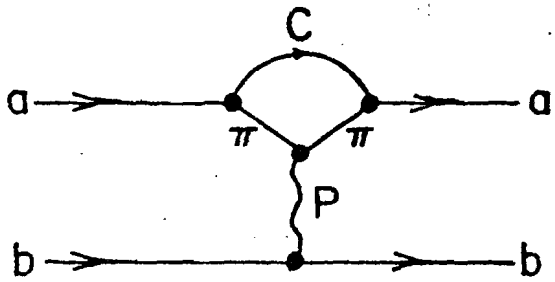

Figure I-8

CHAPTER I REFERENCES

1. L. Wolfenstein and J. Ashkin, Phys. Rev., 85, 947 (1952).

2. L. Wolfenstein, Phys. Rev., 96, 1654 (1954).

3. H. P. Stapp, Phys. Rev., 103, 425 (1956).

4. S. M. Bilenkii, L. I. Lapidus, and R. M. Ryndin, Soviet Physics JETP, 24, 593 (1967).

5. M. Jacob and G. C. Wick, Annals of Physics, 7, 404 (1959).

6. M. Perl, High Energy Hadron Physics, John Wiley and Sons, New York, 1974, p. 228.

7. M. L. Goldberger, M. T. Grisaru, S. W. MacDowell, and D. Y. Wong, Phys. Rev., 120, 2250 (1960).

8. U. Fano, Reviews of Modern Physics, 29, 74 (1957).

9. G. Fox, unpublished supplement to G. Fox and C. Quigg, Annual Rev. of Nuc. Science, 23, 219 (1973).

10. M. H. MacGregor, M. J. Moravcsik, and H. P. Stapp, Annual Rev. of Nuc. Science, 10, 291 (1960).

11. G. H. Thomas, "Nucleon-Nucleon Scattering Experiments in the Relativistic Region and Possible Tests of the Long Range Pion Exchange", Ph. D. thesis, University of California at Los Angeles, 1969.

12. G. W. Bryant, H. A. Neal, and D. R. Rust, "Proton-Carbon Analyzing Power Measurements for Proton Kinetic Energies between .150 GeV and .840 GeV", Indiana University Internal Report, COO-2009-102.

13. G. N. Watson, Proc. Roy. Soc, 95, 83 (1918).

14. A. Sommerfeld, Partial Differential Equiations in Physics, Academic Press, New York, 1949, p. 282.

15. T. Regge, Nuovo Cimento, 14, 951 (1959).

16. P. D. B. Collins and E. J. Squires, Regge Poles in Particle Physics, Springer Tracts in Modern Physics, vol. 45, Springer, New York, 1968.

17. G. F. Chew and S. C. Frautschi, Phys. Rev. Letters, 7, 394 (1960).

18. Perl, p. 422.

19. R. J. N. Phillips and W. Rarita, Phys. Rev., 139, B1336 (1965).

20. D. M. Austin et. al., Phys. Rev., D2, 2613 (1970).

21. B. J. Hartley and G. L. Kane, Nuc. Phys., B57, 157 (1973).

22. G. L. Kane and A. Seidl, Rev. of Modern Phys., 48, 309 (1976).

23. J. Pumplin and G. L. Kane, Phys. Rev., D11, 1183 (1975).

24. N. J. Sopkovich, Nuovo Cimento, 26, 186 (1962).

25. S. Y. Chu and A. W. Hendry, Phys. Rev. Letters, 25, 313 (1970).

26. T. Y. Cheng, S. Y. Chu, and A. W. Hendry, Phys. Rev., D7, 86 (1973).

27. G. W. Abshire, "Polarization in Proton-Proton Scattering at 5.15, 7.0, and 12.33 GeV/c", Ph. D. thesis, Indiana University, 1974.

28. L. Durand and F. Halzen, Nuc. Phys., B104, 317 (1976).

CHAPTER II

DESCRIPTION OF APPARATUS

This experiment was done at the Internal Target Area (ITA) of the Fermi National Accelerator Laboratory. The experimental apparatus used consisted of two fairly distinct devices--the ITA Large Angle Recoil Spectrometer (including the gas jet target), and the E313 polarimeter. Protons in the accelerator's main ring interacted with a spray of hydrogen gas from the gas jet target. The momentum and production angle of the recoiling proton was measured by the spectrometer. Located directly behind the spectrometer was the E313 polarimeter, which measured the polarization of the recoil proton by double scattering it in a carbon block. The spectrometer was a joint effort of ITA, E198A (a collaboration of the University of Rochester, Rutgers University, and Imperial College of London), and E313 (Indiana University). The polarimeter was constructed by Indiana University. Fig. II-1 shows the target, the spectrometer, and the polarimeter. Fig. II-2 is a more detailed view of the polarimeter.

This chapter begins with a brief description of the spectrometer and the polarimeter. Then each element of both devices is described in detail. Finally, items common to both--the fast logic and the method of data acquisition--are discussed.

General Description of Spectrometer and Polarimeter

Interactions occurred when a jet of hydrogen gas from the gas jet target was sprayed into the circulating proton beam in the accelerator's

main ring. The recoil protons were focussed by a quadrupole doublet. (Q1and Q2 in Fig. II-1) Momentum analysis was accomplished by a dipole magnet which bent on-momentum particles through 25°. A series of multi-wire proportional chambers (SPC1-11 in Fig. II-1) and hodoscopes (H1-4 in Fig. II-1) determined the trajectories of the particles. Several scintillation counters (S1-4), as well as a fast wire-or of one of the multiwire proportional chambers (MWPC), were available to trigger the system. To minimize Coulomb scattering, the protons travelled through vacuum or helium filled pipes whenever possible.

The momentum acceptance of the spectrometer was $\pm$ 5%, and the resolution in missing mass squared was about 150 $(\mathrm{MeV}/c^2)^2$. The spectrometer pivoted under the target from 33.5° to 80° in the lab (as measured from the incident beam direction). This corresponded to a t range of -8. to -.1 $(\mathrm{GeV}/c)^2$. The spectrometer could be remotely moved over about one-fourth of its angular range. An access in the main ring was required to move from one "region" to another. The spectrometer's position could be remotely read from a tape mounted on the floor underneath it.

The E313 polarimeter (see Fig. II-2) was located directly behind the spectrometer. The polarization of the recoil proton was determined by double scattering the protons in a carbon block (C in Fig. II-2) and measuring the asymmetry. (See section I-5). The particles' trajectories in both the horizontal and vertical planes were measured by MWPC's

before and after the carbon block (PC1-8). Two hodoscope planes (HX and HY) were used to resolve ambiguities in track reconstruction in the chambers. Two scintillation counters (T1 and T2) triggered the system. A calorimeter consisting of three large scintillators (R1-3), with variable thicknesses of steel sandwiched between them as absorbers, gave a rough energy measurement of the double scattered particles and could be included in the trigger to increase the relative number of elastics in the sample. A hardware preprossessor was used to eliminate a large fraction of the uninteresting events which scattered less than 6° in the carbon. The entire apparatus could be rotated 180° about the beam axis; as will be described in detail in Chapter III, this was important in minimizing systematic asymmetries.

The Spectrometer

1. The Gas Jet Target

The gas jet target used in this experiment was one of three located at the ITA. Fig. II-3 shows a schematic of the target. It was built by E198A and ITA; the nozzle was supplied by Los Alamos.

When the jet was pulsed, a jet of hydrogen (or possibly other) gas at about 10 atmospheres pressure was sprayed through the .003" nozzle directly into the circulating beam. The expansion of the gas cooled it to about 100°K when it entered the beam. Ater interactions had occurred, it was important to remove the gas from the main ring as soon as possible, so as not to interfere with the operation of the accelerator. This jet was a non-cryogenic, or "warm" jet, that is, the gas was removed by pumping rather than by freezing with liquid helium. Most of the gas

(about 85%) passed through the beam and into an inverted mylar cone located about 2" below the jet. The cone led to a 1 m^3 buffer volume. The gas was then at a low enough pressure so that two 10" oil diffusion pumps could evacuate the area. In addition, two other 10" pumps, one upstream and one downstream of the jet, pumped excess gas out of the main ring. To prevent more gas from seeping into the beam pipe after the jet was over, the nozzle was pumped from behind by a mechanical pump.

Some of the typical operating parameters are as follows. The density of the jet was about 10^{-7} g/cm^3 and could be varied by changing the pressure of the hydrogen gas at the nozzle. The width of the jet was about 6 mm FWHM, and the length along the beam direction was 1 cm. The length of the pulse could be varied from 20 ms up to any desired length. The jet's density and duration were limited in practice by the amount it interferred with the accelerator's normal operation. For a typical beam burst of 10^{13} protons, the luminosity of the jet was $\sim .5 \times 10^{34}$. It could be pulsed at any point during the beam's acceleration, allowing us to select any incident beam momentum from 10-400 GeV/c. Also, at least five jets per beam pulse were possible, allowing us to sample five energy ranges simulatneously. Normally, we ran with three to five jet pulses per beam burst, each 100-200 ms long. For a typical acceleration rate of 125 GeV/c per second, each jet pulse would then cover a range of beam momenta 12-25 GeV/c wide.

2. Magnets

The beam of recoiling protons was focussed by a superconducting

quadrupole doublet (Q1 and Q2 in Fig. II-1). For this experiment, the quads increased the effective solid angle by about a factor of 40. The magnets were designed to provide a parallel-to-point focus at the first proportional chamber, that is, all particles produced at the same lab angle were focussed to the same point at the first chamber (SPC1 in Fig. II-1). Then a measurement of position at SPC1 corresponded to a measurement of production angle at the target.

A superconducting dipole magnet provided momentum analysis. On-momentum particles were bent through 25°. During construction of the spectrometer, the dipole was mapped using a Hall probe. The field was found to vary no more than ± 3% both horizontally and vertically across the width and heighth of the magnet. However, the dipole was found to have large fringe fields which produced some unusual focussing properties in both the horizontal and vertical planes. This necessitated using some second and third order matrix elements in the momentum analysis. All three magnets were on loan from the Lawrence Berkeley Laboratory. Some parameters for both the quads and the dipole can be found in Table II-1.

3. Spectrometer Chambers, Hodoscopes, and Trigger Counters

A series of MWPC's, hodoscopes, and trigger counters was used to detect the recoiling protons and measure their momentum and production angle, (see Fig. II-1). Details of their dimensions and positions can be found in Table II-2. All chambers had wire spacings of 1.3 mm. The gas used was the standard "magic gas" mixture, 20% isobutane, about .4% freon, and the balance argon.

The first set of chambers (SPC1-3 in Fig. II-1) was located about 760 cm from the target. It contained three wire planes, two measuring the horizontal coordinate (x), and one measuring the vertical (y). In the x-planes the wires were staggered by $\frac{1}{2}$ wire spacing to increase the resolution. The "parallel-to-point" focus of the quads occurred at this set of chambers, so that a position measurement in x here corresponded to a measurement of the production angle. A similar set of chambers (SPC4-6) was located about 75 cm downstream. Three hodoscopes (H1-2 and H3) were located between the two sets of chambers and were used to resolve ambiguities in track reconstruction. Also, located between the two sets of chambers were two trigger counters, S1 and S2. Another proportional wire plane SPC7 was located immediately in front of the dipole. A fast wire-or of all the wires in this plane was available as part of the trigger. However, timing problems limited its usefulness. Two more wire planes (SPC8-9) were located immediately after the dipole. About 250 cm further downstream were located two "crossed wire" chambers (SPC10-11) with the wires tilted $\pm 15^{\circ}$ from the vertical. All of the MWPC's were used in the momentum reconstruction. One more hodoscope plane (H4) and one more trigger counter (S4) were located behind the last set of chambers. Our normal trigger for the spectrometer (which we called TR) was S1·S2 or S1·S2·S4. Under normal running conditions, there was almost no difference between these two triggers, and S4 was usually omitted. An EVENT, then, was an AND of the spectrometer trigger (TR) and the polarimeter trigger (TP).

Chamber Readout

Both E198A and E313 read out the spectrometer chambers. The amplifier circuit for the E198A readout is shown in Fig. II-4. The negative signal from the chamber wire triggered the 74L04 pre-amplifier. (The 74L04 is actually a TTL inverter which was made to operate as a low gain amplifier with the use of negative feedback.) The positive signal from the 74L04 then went into the negative input of the 72810L, a high-gain TTL amplifier. The amplified negative signal was then converted to ECL levels, and the signal was fed into a MC1035, an ECL line driver. The output of the line driver went to the E198A trailer. E313 teed off the signal from the MC1035 as shown.

The circuit following the tee is shown in Fig. II-5. A constant -1.3 V on the positive input of the 710 comparator set the threshold--whenever the negative input was at a voltage lower than -1.3 v, the amplifier was triggered. The quiescent input to the 710 from the MC1035 was -.8 V. When a signal appeared on a wire, the input switched to -1.6 V, which crossed the threshold and triggered the amplifier. The 710 saturated at +3 V, and the signal lasted from 100-200 ns. The sequence of signals is shown in Fig. II-6.

The amplified signal from each wire was fed in parallel into one bit of a shift register. The integrated circuit used for the shift register was a 4012, a four fit TTL shift register. The pin configuration of this chip and a section of a larger shift register is shown in Fig. II-7. When a spectrometer event (TR) occurred, the state

of each wire at that time was loaded in parallel into the shift register. If the event was acceptable (that is, a polarimeter trigger was also present), the information was shifted out serially into a SAC system. When the readout began, a series of scalars in the SAC system began counting at a rate set by a 20 MHz clock. The chamber information was shifted out synchronously by the same clock at a rate eight times slower. Each "hit" in a chamber stopped a scalar; the scalar reading then indicated which wire had been hit. These scalar readings were recorded for each event. There were four scalars for each chamber; if more wires were hit, the additional ones were lost and a spark overflow bit was set. Events which had the spark overflow bit set were disregarded in the analysis, since chamber information had been lost. These events were a small fraction of the total, however (about 1%).

4. Minimization of Coulomb Scattering

At low $|t|$ values, the energy of the recoil proton is quite small (at $t = -.3$, the kinetic energy is 160 MeV). Coulomb scattering can be a problem at these energies. To minimize this effect, the protons travelled through vacuum or helium filled pipes wherever possible. The main ring vacuum was extended up to the first quadrupole magnet; after the second quad, the particles travelled through a helium filled pipe up to the first set of proportional chambers. After the second set of chambers, the protons again travelled through a helium filled pipe which extended up to the dipole magnet. Another helium pipe was located between the chambers directly behind the dipole and the crossed wire chambers.

5. Beam Conditions and Monitor

A typical beam pulse in the main ring varied in intensity from about 5×10^{12} to 2×10^{13} protons. Beam was injected into the main ring from the booster at 8.89 GeV/c. The rate of acceleration after injection was typically 125 GeV/c per second. The flat top, which was normally at 400 GeV/c, lasted about two seconds. The accelerator's cycle time varied from about 10-15 seconds. We had one running period with unusual beam parameters--a 100 GeV/c "front proch", which lasted two seconds, and a 200 GeV/c flat top, which also lasted two seconds. The cycle time was nine seconds for this mode of operation.

The beam intensity was monitored by a solid state silicon detector located near the target at 85.5° in the lab, as measured from the beam direction. The thickness of the detector was 1500 microns, and the area was 25 mm^2. The monitor was located in such a way that essentially all the protons it saw were elastic.

The Polarimeter

6. Carbon Block

A carbon block (C in Fig. II-2) served as the spin analyser for the protons. For $|t|$ values greater than .3 $(GeV/c)^2$, a two inch thick block was used. For $|t|$ values less than .3, a one-half inch block was used. The thicker block gave a larger percentage of useful double scatters at the higher energies, but at lower energies it absorbed too many of the protons. The analysing power of the blocks was measured using the polarized proton beam at Argonne National Laboratory's ZGS.[4] (This calibration will be discussed in Chapter III.) The carbon could be

remotely moved in and out of the apparatus to allow for "straight through" runs as well as regular data runs. The straight through information was used to check the alignment and efficiency of the chambers and hodoscopes.

7. Polarimeter Chambers, Hodoscopes, and Trigger Counters

Four MWPC's (PC1-4 in Fig. II-2) were located in front of the carbon block to measure the incoming angle of the protons in both the horizontal and vertical planes. Four more chambers (PC5-8) were behind the carbon to measure the angle of the scattered protons. All of the chambers had 2 mm wire spacing. The gas usedwas the standard "magic gas" mixture--20% isobutane, .4% freon, and the balance argon. Table II-3 has details of the dimensions and positions for the chambers, trigger counters, and hodoscopes.

Two scintillation counter hodoscope planes (HX and HY in Fig. II-2) were located after the last proportional chamber. They measured both the horizontal and vertical coordinates and were useful in resolving ambiguities in track reconstruction in the chambers. There were two trigger counters--the first (T1), was located before the first chamber, and the second (T2), was located between PC2 and PC3. A polarimeter trigger (which we called TP) consisted of T1·T2.

Chamber Readout

The amplifier circuit for a single wire of the polarimeter chambers is shown in Fig. II-8. The input bias current of the 710 comparator was about 10 μa. The negative input of the amplifier in the quiescent state was -10 mV, and the positive input was at a constant -15 mV. The difference in these two (-5 mV) set the threshold. A negative signal

from the chamber wire of 5 mV or greater would cross the threshold and trigger the amplifier. (A typical pulse from a chamber wire was about 20 mv.) The output of the amplifier was +3 volts and lasted 100-200 ns.

The outputs of the 710's were fed in parallel into a shift register. When a polarimeter event (TP) occurred, the state of each wire was latched into the shift register. If the event was acceptable, the shift registers were read out in series through the SAC system, just as for the spectrometer chambers.

8. Polarimeter Computer

Only protons which double scattered in the carbon into an angular region of 6° -22° were useful for determining the asymmetry. Outside of this region, the analysing power of carbon becomes small, that is, it does not differentiate well between spin states. However, only about 1-2% of all protons passing through the carbon double scattered into this region. A unique feature of the E313 polarimeter was the "polarimeter computer", a hardware preprocessor which was designed to eliminate at least some of the uninteresting straight-through events. The polarimeter computer could be used in the trigger, or the status of the tests could be used only to tag events. The polarimeter computer proved essential to our data taking--it increased the fraction of useful double scatters by about a factor of 20.

The polarimeter computer used information from the proportional chambers to make tests on the events. The outputs of the chamber shift registers were OR'd together in pairs and fed into separate shift registers used only by the polarimeter computer. When an event

occurred, these shift registers were latched into the same state as the chamber shift registers. Then three separate tests were made on the event through a series of hard-wired logic gates. If any one of the tests failed, the processing was stopped and a reset signal was sent to the fast logic. All three tests were completed in about 2 μ sec. The horizontal and vertical planes were treated identically in all tests.

Upstream Test

All of the chambers upstream of the carbon block were required to have at least one "hit", and the particle was required to enter the polarimeter reasonably parallel to the nominal beam direction in both the horizontal and vertical planes. The allowed deviation from the nominal beam direction could be chosen to be $\pm$ 13 mr, $\pm$ 26 mr, or $\pm$ 39 mr. Once acceptable upstream tracks were found, predictions were made in both planes for the position of an unscattered particle in the rear chambers.

Straight-Through Test

Using the predicted positions of straight-throughs from the upstream test, the polarimeter computer searched for a track in the downstream chambers which agreed with them. Each prediction corresponded to a certain bit of the shift register of each downstream chamber. The polarimeter computer looked for a "hit" within a certain (adjustable) tolerance on either side of that bit. The tolerance was chosen so that scatters of 6° or less would be identified as straight-throughs. If a straight-through track was found in both planes, the event failed. If a straight through was seen in only one plane, the event passed.

Scatter Test

If the event passed the first two tests, a third test was made to determine if a good double scatter had occurred. The polarimeter computer looked for tracks in the rear chambers which corresponded to a scatter of 6° - 22° away from the predicted straight-through position. If such a track was found in either plane, the event passed. If no such track was found, it failed.

Any or all of these tests could be included in the trigger. The tests were sequential, that is, it would not make sense to require the second test without the first, or the third test without the first two. If the polarimeter computer was in the trigger, when the required tests had been passed, a polarimeter computer EVENT signal was generated which went to the computer and the SAC system and initiated the data readout. If the polarimeter computer was in the trigger and one of the required tests failed, a reset signal was sent to the fast logic and another event could be accepted. If the polarimeter computer was not in the trigger, all of the tests were still made, but a PC EVENT signal was generated regardless of the status of the tests. The status of each test was tagged for each event, whether or not the polarimeter computer was in the trigger.

9. Range Counter

Some fraction of the protons scattered inelastically in the carbon. In fact, sometimes more than one particle could be observed emerging from the carbon block. Such inelastic events were not useful in measuring the

asymmetry, since the analysing power of carbon is small for such events. The range counter provided a method of determining which double scatters were extremely inelastic. Three large scintillators (R1, R2 and R3 in Fig. II-2) were located behind the hodoscope planes. The dimensions of the scintillators were 76 cm x 76 cm x 1.05 cm. Sandwiched between them was varying amounts of steel. The correct amount of steel was placed between R1 and R2 so that a proton which elastically scattered in the carbon would pass through, but those that had lost more than about 30-40 Mev would be ranged out. Additional steel between R2 and R3 ranged out the elastic protons. An elastic signal, then, would be $R1 \cdot R2 \cdot \overline{R3}$. For each event, analog signals from the range counters were analysed by ADC's, and a tag bit was set. This provided information about a particle's energy, as well as which counters it reached. R3 and $\overline{R3}$ were available for the trigger, although in practice including them created problems. Such large scintillators could easily have variations in efficiency in different regions due to, for example, variations in the scintillator itself, placement of the phototubes, or differences in timing across the scintillator because of its large size. Including them in the trigger could create an instrumental asymmetry. Such an asymmetry should "rotate out", (see section 10 of this chapter), but we avoided any instrumental biases whenever possible. For most of our data taking, the range counter information was recorded for each event, but was not included in the trigger.

10. Polarimeter Rotation

Since the polarization we were measuring was expected to be small (at least according to some predictions), it was important to guard against instrumental asymmetries. A number of effects could lead to such asymmetries. For example, a slight difference in the efficiency between left and right in the chambers or hodoscopes could give a difference between the number of observed left and right scatters. It was also found through a Monte Carlo study that "phasing" of the wires in the chambers (that is, wires not being exactly lined up with respect to each other) could also give a small asymmetry. To avoid this problem, the polarimeter was designed to rotate 180° about the beam axis, and equal amounts of data were taken at each orientation. Then the instrumental asymmetries would average out, and only the true asymmetry due to the proton's polarization would be measured. The polarimeter was remotely rotated from our trailer. A TV camera monitored the progress of the rotation and viewed precision levels which indicated when the polarimeter had reached the correct position. A remotely controlled relay then locked the polarimeter into place. Orientations were changed about every 30K-60K triggers, or about every one or two hours.

11. Fast Logic

The fast logic for the experiment was located in four places--on the polarimeter, on the spectrometer, on a relay rack beside the polarimeter, and in our trailer. Diagrams of the fast logic are shown in Figs. II-9 through II-12. Each figure corresponds to one of the four locations. All logic units used standard NIM signals: -.75 V for TRUE, and ground for FALSE.

Logic on the Polarimeter

Three units were located on the polarimeter and rotated with it. A 621 BL quad discriminator was used to discriminate pulses from the trigger counters (T1 and T2). One output went through a coincidence unit (622), also on the polarimeter, to form the STROBE. The STROBE signal went through a fanout (F344) to all of the polarimeter chambers. This signal was used to latch the chamber shift registers before the final decision was made whether or not to keep the event. Other outputs from the T1 and T2 discriminators went to the relay rack beside the polarimeter to form the polarimeter trigger (TP), and to the trailer to be scaled.

Logic on the Spectrometer

The logic on the spectrometer was similar to that on the polarimeter. The trigger counters S1 and S2 were discriminated there and formed the STROBE for the spectrometer chambers. The STROBE was then fanned out to the chambers. Other outputs of the S1 and S2 discriminators were used to form the spectrometer trigger (TR) on the relay rack beside the polarimeter.

Logic Beside the Polarimeter

The third location of the fast logic was a relay rack beside the polarimeter. TP, TR and EVENT were formed here, using 365ALP remote coincidence units. The 365ALP's could be remotely controlled to be 1, 2, 3 or 4-fold coincidences. Also, any of the four inputs could be switched in or out of the coincidences at any time. The polarimeter trigger, TP, was usually T1·T2, although signals from the range counters could be included. The spectrometer trigger, TR, was formed by S1·S2.

TR then went through a remote delay box into the EVENT coincidence. Different spectrometer angles corresponded to different proton momenta, and therefore different timing between TR and TP. The remote delay box allowed us to adjust the delay whenever necessary. EVENT was normally TR·TP, although S4, the last spectrometer trigger counter, and a fast wire-or from one of the spectrometer MWPC's could be included.

EVENT set the HOLD flip-flop (a364ALP), which was used in several places. HOLD was used to inhibit TP, TR and the STROBE coincidences until the current event could be processed. It was fed into all the chamber strobe lines and overlapped the STROBE signal, so that the shift registers remained latched until they could be read out. HOLD also went to the polarimeter computer and was the signal for processing to begin. The flip-flop was reset either by the polarimeter computer, if the event did not pass the required tests, or by the computer, after the data had been read in.

Signals from all three range counters were fanned out (428 linear fanout) on the relay rack and went from there to the ADC's in the trailer and to dicriminators (621). The discriminated signals could then be included in the trigger.

Logic in the Trailer

The last location for the fast logic was our trailer. EVENT, TP, and TR all came to the trailer from the spectrometer room and were rediscriminated there. EVENT was used to gate the polarimeter hodoscopes and the last spectrometer hodoscope. TR, gated by EVENT, latched the

first three spectrometer hodoscopes. The hodoscope tagging units used were LRS2340A (for the polarimeter hodoscopes) and CR116 (for the spectrometer hodoscopes). EVENT was also used to gate the analog-to-digital converters used for the range counters.

The time of flight measurement was made using a LRS2228 time-to-digital converter. The time measured was the length of time for the particle to travel from the first spectrometer trigger counter, S1, to the first polarimeter trigger counter, T1. TR, gated by EVENT, was used as the start pulse. A delayed TP was the stop pulse. For our normal trigger (except at t = -1.0) the timing difference between protons and pions was so great that both could not satisfy the trigger at the same time. The TOF spectrum was usually a clean, single peak. When the trigger was adjusted so that both pions and protons were able to satisfy it, two distinct peaks could be seen.

A number of quantities were scaled. EVENT, TR, TP and the monitor counts each had four scalars--one for each jet burst and one for the total. T1 and T2 were scaled separately. Polarimeter computer events were scaled, as well as rejects, that is, events which did not pass the required polarimeter computer tests. The T1, T2 and monitor scalars were inhibited by HOLD, so that they did not continue to count between beam bursts and while an event was being processed. The number of beam pulses were also scaled.

12. Data Acquisition and Monitoring

A PDP-15 computer was used on-line to control the data taking and monitor the experiment. When an event occurred, an interrupt was generated, the experiment was gated off, and the computer immediately began reading the information for that event into the buffer. All the

information except the chamber hits were read into CAMAC units; the chamber information was read into a SAC system. The CAMAC units were then read out via a CAMAC-SAC interface through the SAC system and into the computer. The time required to read in an event was about 500 μ sec. Up to 51 events were stored in the buffer before all the information was written onto magnetic tape. Later on the experiment, more core was obtained for the PDP-15, so that up to 201 events could be stored before writing them onto tape. The first word of every event was a "key word", or fixed word, to check that all the information was being read in correctly. The second word was the "B-dot" scalar, a machine scalar which was proportional to the current in the main ring magnets and indicated the incident beam momentum for each event. There were two other scalars, one which counted "events in this buffer", and one which counted total events. Other information for each event included the time of flight measurement, the ADC measurement from each range counter, and tags for the polarimeter computer tests. Of course, all the MWPC and hodoscope information was read in for each event. Other scalars (such as TP, TR, EVENT, etc.) were read in every buffer, that is, about every 50 events. After the data acquisition was complete, a reset signal was sent to all the fast logic, and another event could be accepted.

Between events, various calculations (such as chamber efficiencies) were made, and a number of histograms were built. Histograms which could be displayed on a CRT included chamber and hodoscope distributions, the time of flight distribution, the carbon double scattering distribution, the bend angle through the magnet, and the analog signals from the range

counters. The events could be monitored on the CRT with the "view display", a scale drawing of all the chambers and hodoscopes with their hit distributions displayed for each event. A raw data dump for each event was also available.

Various error conditions could be detected by the computer, and, if the error was serious enough, an alarm was sounded. A very serious error (such as the high voltage on a chamber tripping off, or running off the end of the magnetic tape) would stop the data taking until the error was corrected.

A second PDP-15 computer was available off-line for rapid analysis of data tapes. This preliminary analysis was useful in monitoring the progress of the experiment and discovering problems.

Table II-1

Magnet Parameters

Parameter	Quadrupoles	Dipole
Maximum Field Strength	2.36 kgauss/cm	40 kgauss
Length	176.3 cm	135.4 cm
Magnetic Length	63.2 cm (each)	81.9 cm
Current at Rated Strength	664 amp	597 amp
Excitation Slope	3.56 gauss/cm-amp	61.8 gauss/amp
Integral Excitation Slope	225 gauss/amp	5590 gauss-cm/amp

Table II-2

Spectrometer, Proportional Chambers, Hodoscopes, and Trigger Counters

Proportional Chambers

Plane	Number of Wires	Wire Spacing (mm)	Coordinates Measured*	Distance along Beam Line** (cm)	Vertical Dimension (cm)	Horizontal Dimension (cm)
SPC1	80	1.3	X	749.0	15.2	10.2
SPC2	80	1.3	X	749.8	15.2	10.2
SPC3	120	1.3	Y	750.8	15.2	10.2
SPC4	80	1.3	X	855.5	15.2	10.2
SPC5	80	1.3	X	856.2	15.2	10.2
SPC6	120	1.3	Y	854.5	15.2	10.2
SPC7	80	1.3	X	1160.7	15.2	10.2
SPC8	80	1.3	X	1340.4	15.2	10.2
SPC9	96	1.3	Y	1339.3	15.2	10.2
SPC10	150	1.3	U(+15°)	1573.8	15.2	30.5
SPC11	150	1.3	V(-15°)	1583.4	15.2	30.5

Hodoscopes

Plane	Number of Elements	Coordinate Measured*	Vertical Dimension (cm)	Horizontal Dimension (cm)	Distance among Beam Line** (cm)
H1	12	X	15.2	.85	764.8
H2	12	Y	1.0	15.2	824.3
H3	12	X	15.2	.85	824.3
H4	20	X	20.3	3.37	1161.4

Trigger Counters

Counter	Vertical Dimension (cm)	Horizontal Dimension (cm)	Distance among Beam Line (cm)
S1	20.3	11.4	773.7
S2	15.2	10.2	829.6
S3	20.3	40.6	1617.7

* X is the horizontal coordinate; Y is the vertical coordinate
** As measured from the target

Table II-3

Polarimeter Proportional Chambers, Hodoscopes and Trigger Counters.

Proportional Chambers

Plane	Number of wires	Wire spacing (mm)	Coordinate measured *	Distance along beam line** (cm)	Vertical dimension (cm)	Horizontal dimension (cm)
PC1	90	2	Y	-1.20	17.8	17.8
PC2	90	2	X	1.09	17.8	17.8
PC3	90	2	Y	29.34	17.8	17.8
PC4	90	2	X	31.61	17.8	17.8
PC5	150	2	Y	44.55	30.5	30.5
PC6	150	2	X	46.89	30.5	30.5
PC7	210	2	Y	59.52	45.7	45.7
PC8	210	2	X	62.40	45.7	45.7

Hodoscopes

Plane	Number of elements	Coordinate measured *	Distance along beam line ** (cm)	Vertical dimension (cm)	Horizontal dimension (cm)
HX	12	X	77.5	30.5	5.1
HY	12	Y	83.2	5.1	30.5

Trigger Counters

Counter	Vertical dimension (cm)	Horizontal dimension (cm)	Distance along beam line** (cm)
T1	15.2	15.2	-7.6
T2	15.2	15.2	7.6

* X is the horizontal coordinate; Y is the vertical coordinate.

** Distances measured from an arbitrary origin within the polarimeter. The origin was chosen to be the center of the plate used to mount the first two chambers.

CHAPTER II FIGURES

Figure II-1. The Internal Target Area Spectrometer. Recoil protons from pp interactions in the accelerator's main ring are focussed by the quadrupole doublet Q1 and Q2. An array of multiwire proportional chambers (SPC1-11), hodoscopes (H1-H4), and trigger counters (S1, S2, and S4) track the particles through the spectrometer. The dipole bends on-momentum particles through 25°. The polarimeter, located at the end of the spectrometer, analyzes the spin of the recoil proton.

Figure II-2. The polarimeter. The protons are rescattered in a carbon block (C). Multiwire proportional chambers upstream and downstream of the carbon (PC1-8) measure the incoming and outgoing trajectories of the particles. T1 and T2 are trigger counters. The hodoscopes (HX and HY) help resolve ambiguities in track reconstruction in the chambers. Three large scintillators, R1, R2, and R3, with varying amounts of steel sandwiched in between, form the calorimeter or range counter.

Figure II-3. The gas jet target. Hydrogen gas is sprayed from the .003" nozzle into the accelerator's main ring. Most of the gas passes into the buffer volume where two 10" diffusion pumps evacuate it. Additional 10" pumps both upstream and downstream of the target also help remove the gas.

Figure II-4. E198A amplifier circuit for the spectrometer chambers. The circuit is described in the text.

Figure II-5. Amplifier circuit for the spectrometer chambers following the MC1035 line driver of Figure II-4.

Figure II-6. Sequence of signals generated by a particle passing through a chamber. A pulse of about -20mV appears on the wire, producing a -1.6V signal at the output of the E198A amplifier circuit. This triggers the E313 amplifier, which has an output signal of +3V, 100-200 ns long.

Figure II-7. Section of a shift register used in chamber readout. The integrated circuit used is a 4012, a four bit shift register. Chamber wires (W1-W12) are fed in parallel into each bit of the shift register. When the MODE and LOAD lines are high (+5V), the state of each chamber wire is latched into the shift register and appears at the outputs (Q1-Q12). Then the MODE line goes low (ground), and the information is shifted out serially by the SHIFT pulse, a 2.5 MHz clock. The small numbers indicate pin numbers on the 4012.

Figure II-8. Amplifier circuit for polarimeter chambers. The 710 amplifier is triggered by a signal from a chamber wire, giving an output pulse of +3V.

Figure II-9. Fast logic located on the polarimeter. See text for a description of individual elements of the fast logic.

Figure II-10. Fast logic located on the spectrometer.

Figure II-11. Fast logic located on a relay rack in the spectrometer room.

Figure II-12. Fast logic located in the experimental trailer.

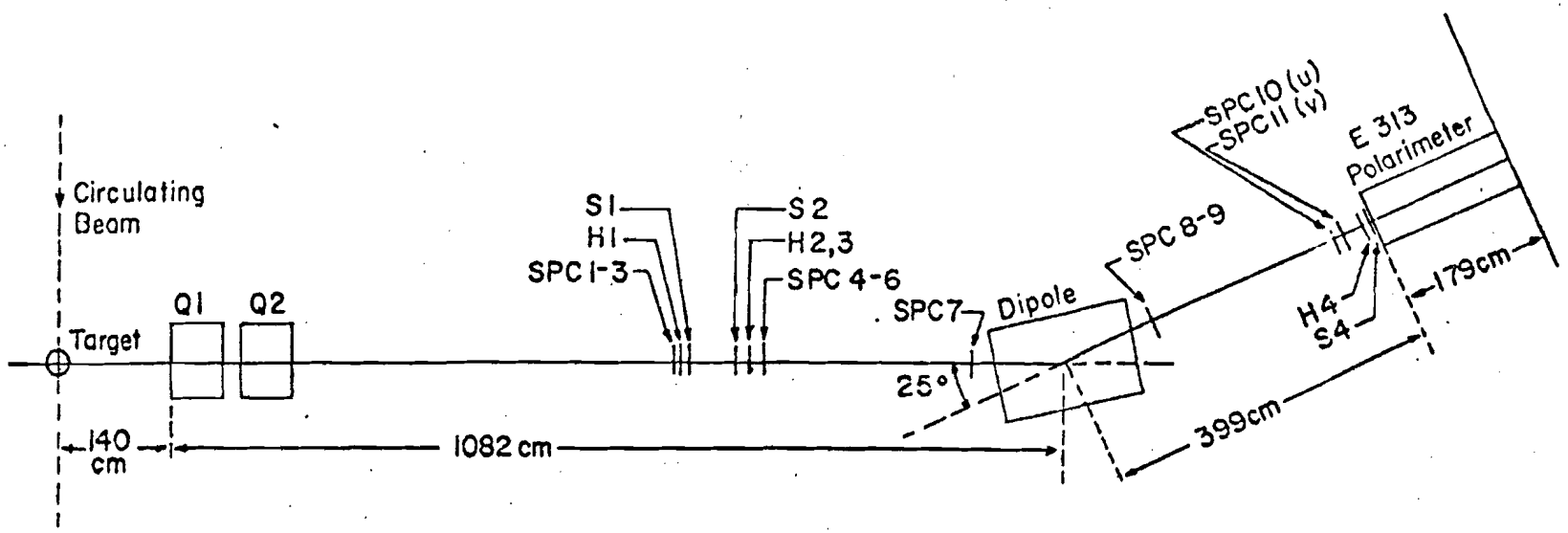

INTERNAL TARGET SPECTROMETER

Figure II-1

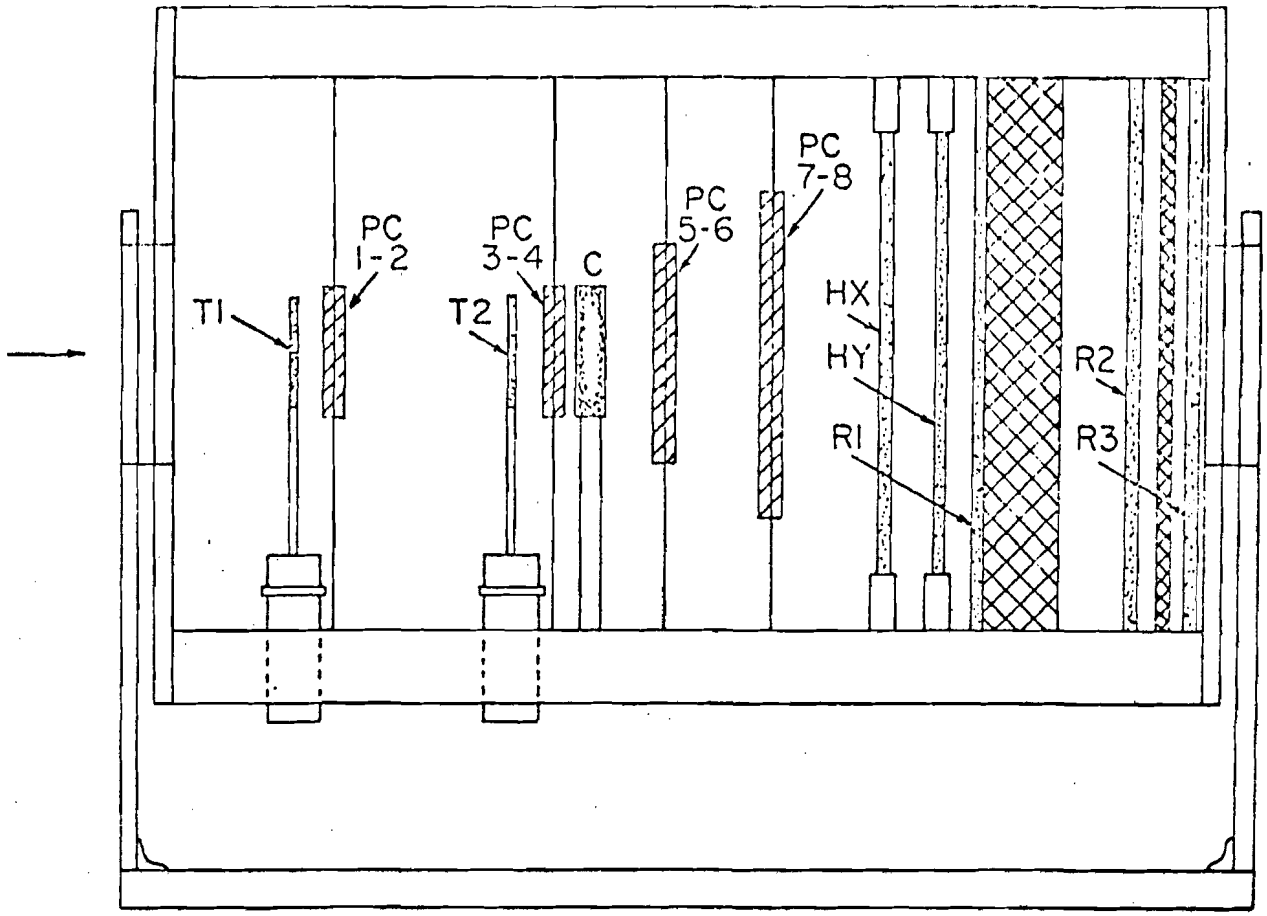

POLARIMETER LAYOUT

proportional chambers
range steel
scintillation counters
carbon block

Figure II-2

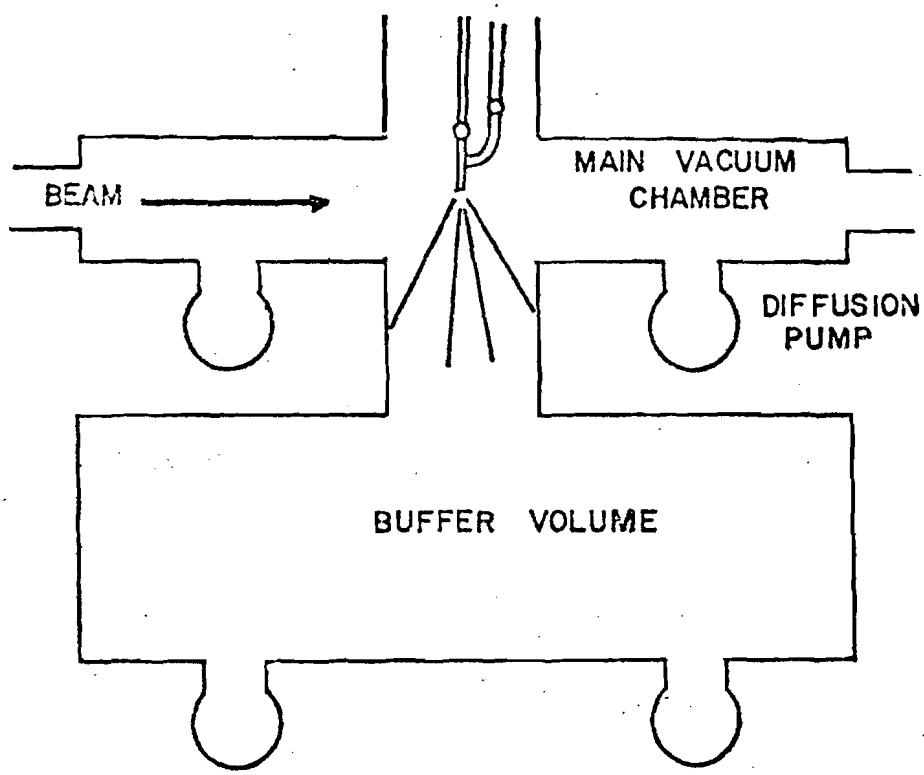

Figure II-3

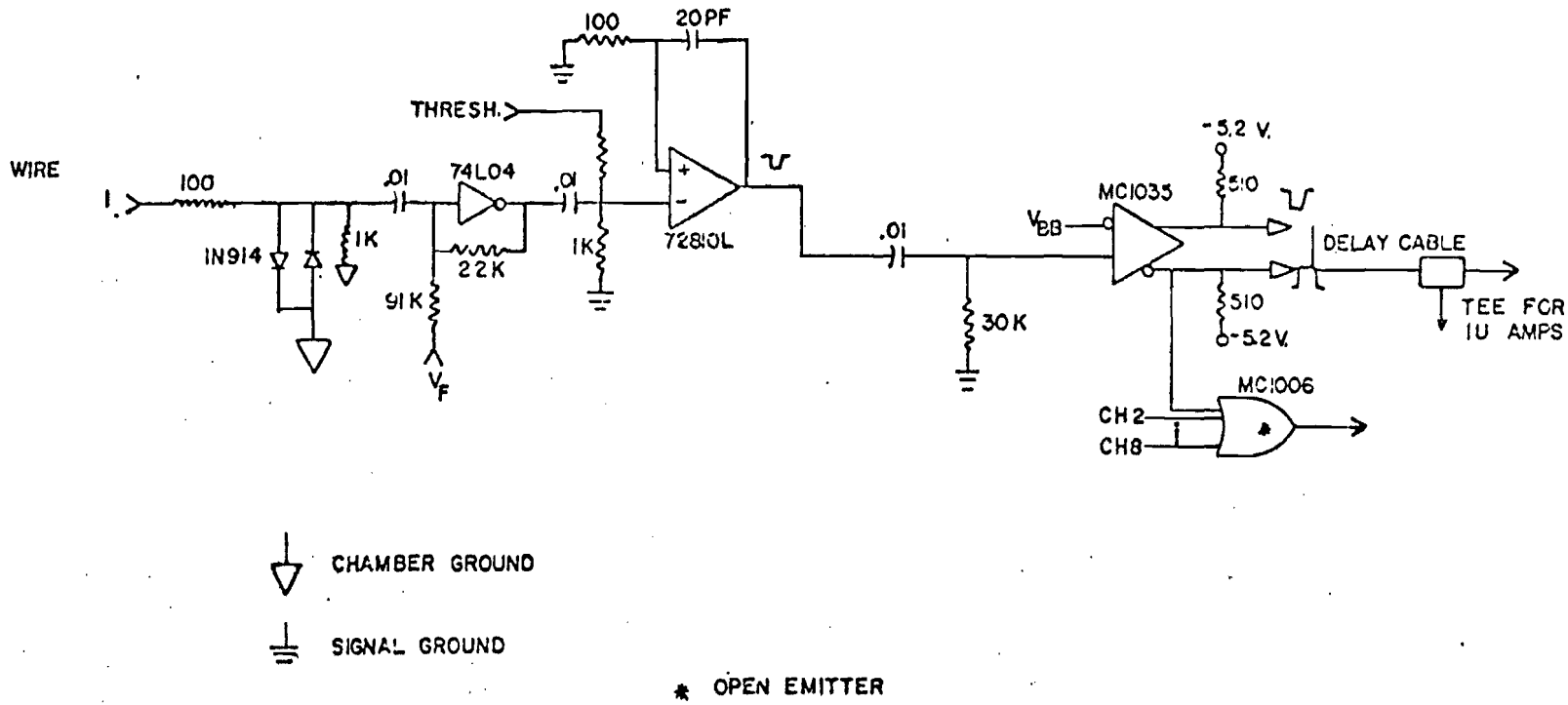
WIRE
100
IN914
1K
.01
74L04
22K
91K
V_F
THRESH.
.01
1K
100
20PF
72810L
.01
30K
V_{BB}
MC1035
-5.2 V.
510
510
-5.2V.
DELAY CABLE
TEE FOR
IU AMPS
MC1006
CH2
CH8
CHAMBER GROUND
SIGNAL GROUND
* OPEN EMITTER

Figure II-4

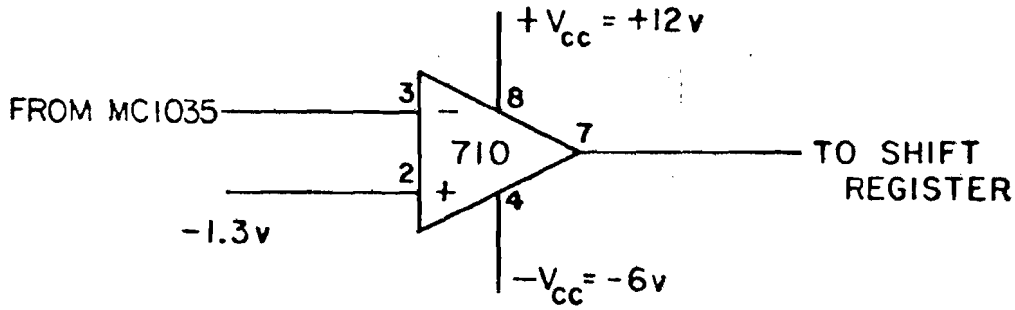

Figure II-5

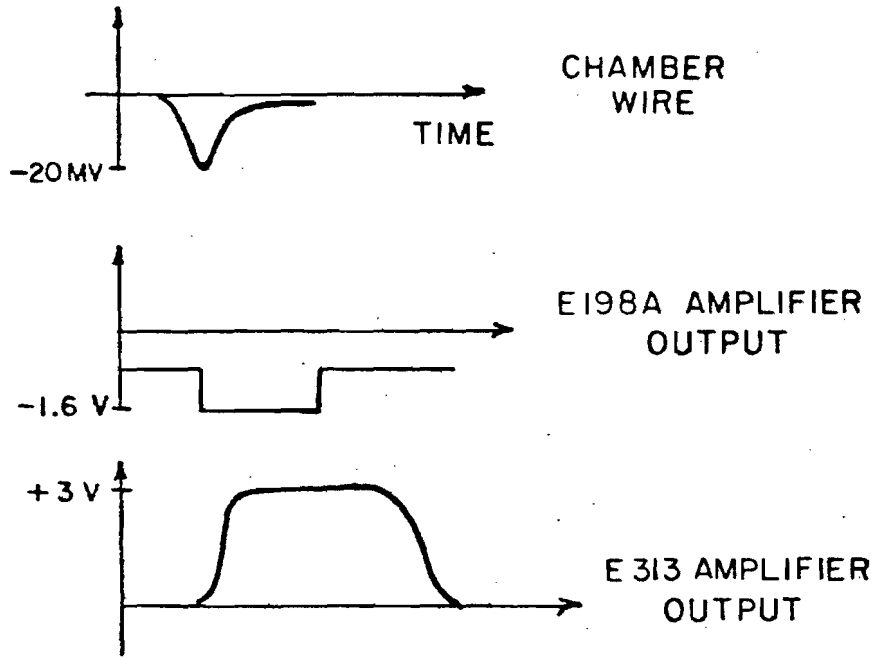

Figure II-6

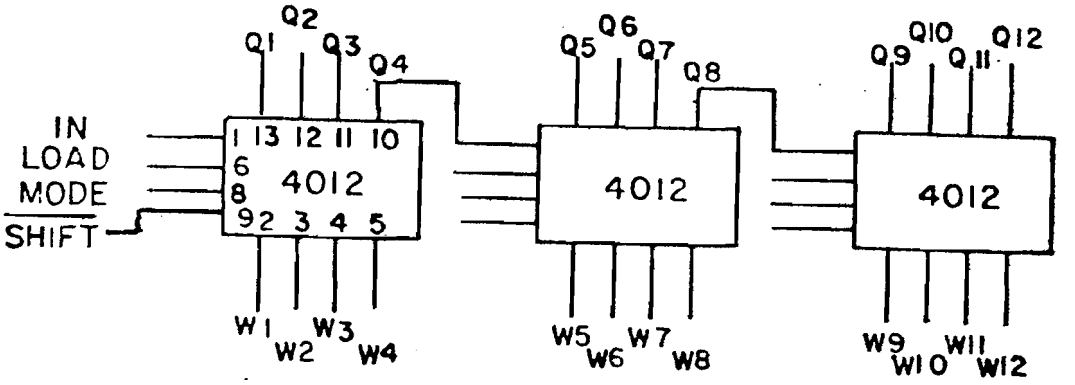

Figure II-7

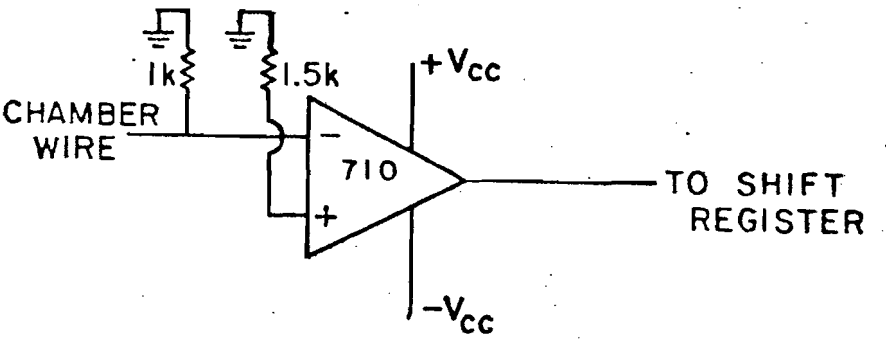

Figure II-8

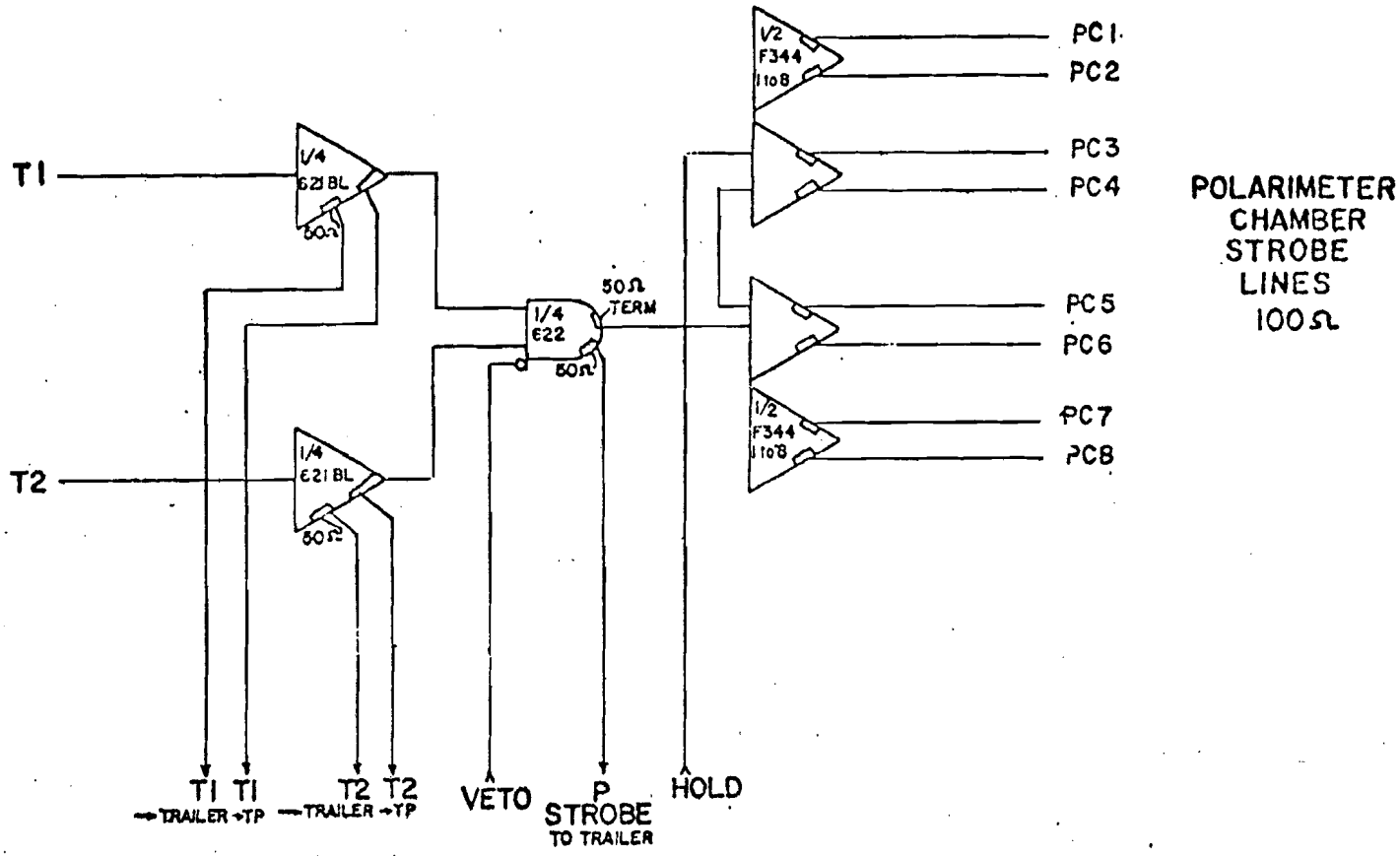

FAST LOGIC ON THE POLARIMETER

Figure II-9

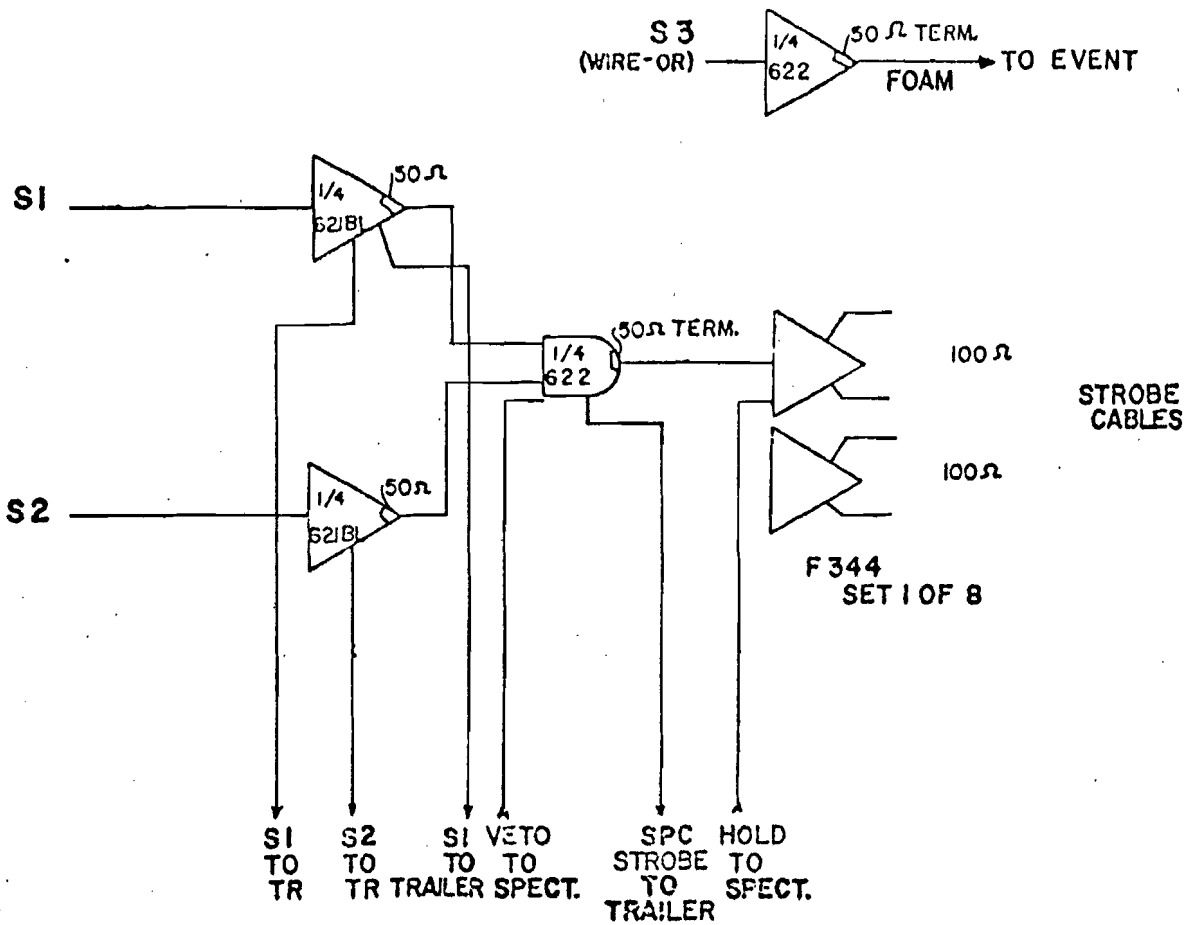

FAST LOGIC ON SPECTROMETER

Figure II-10

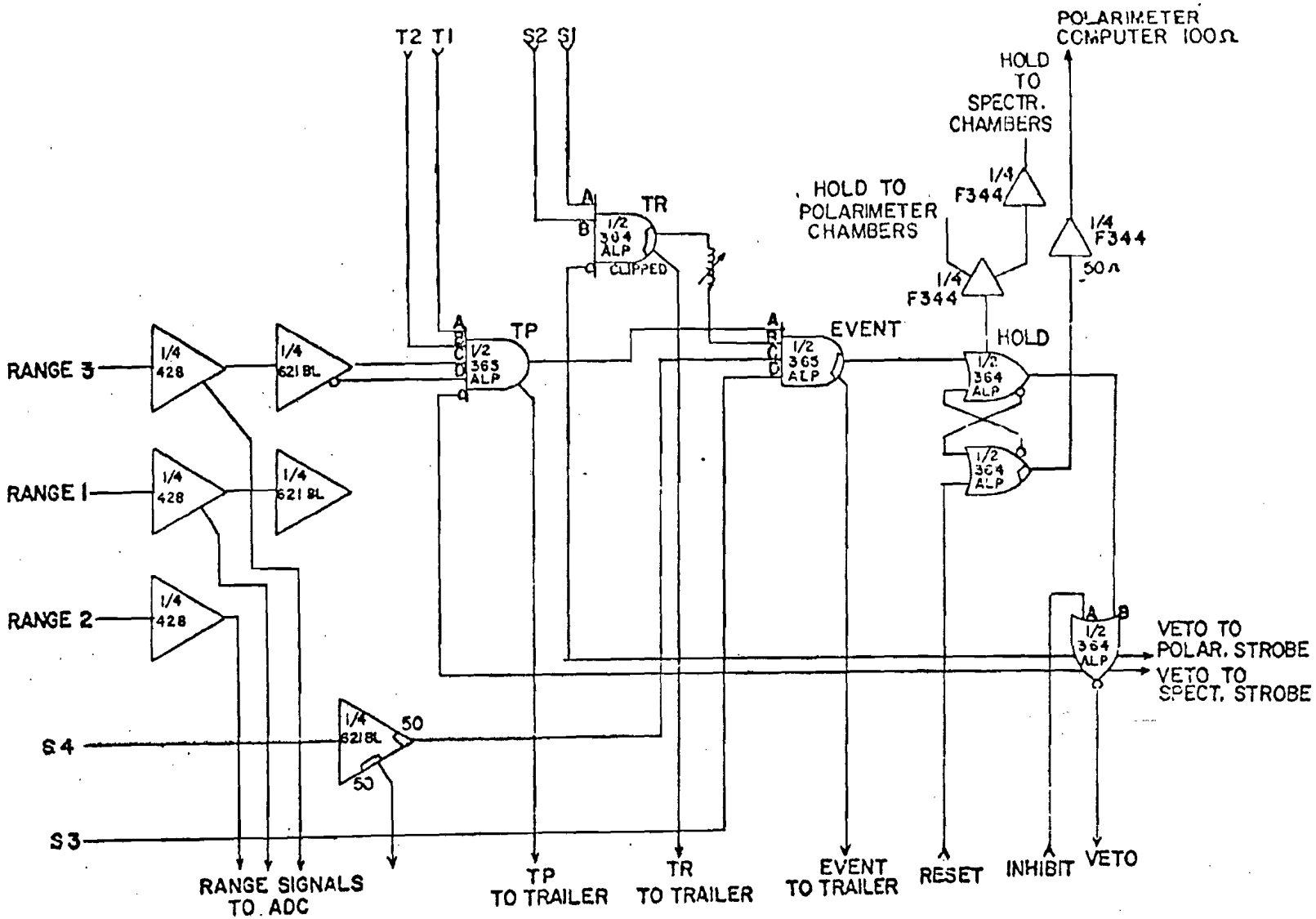

LOGIC IN DOWNSTAIRS RELAY RACK

Figure II-11

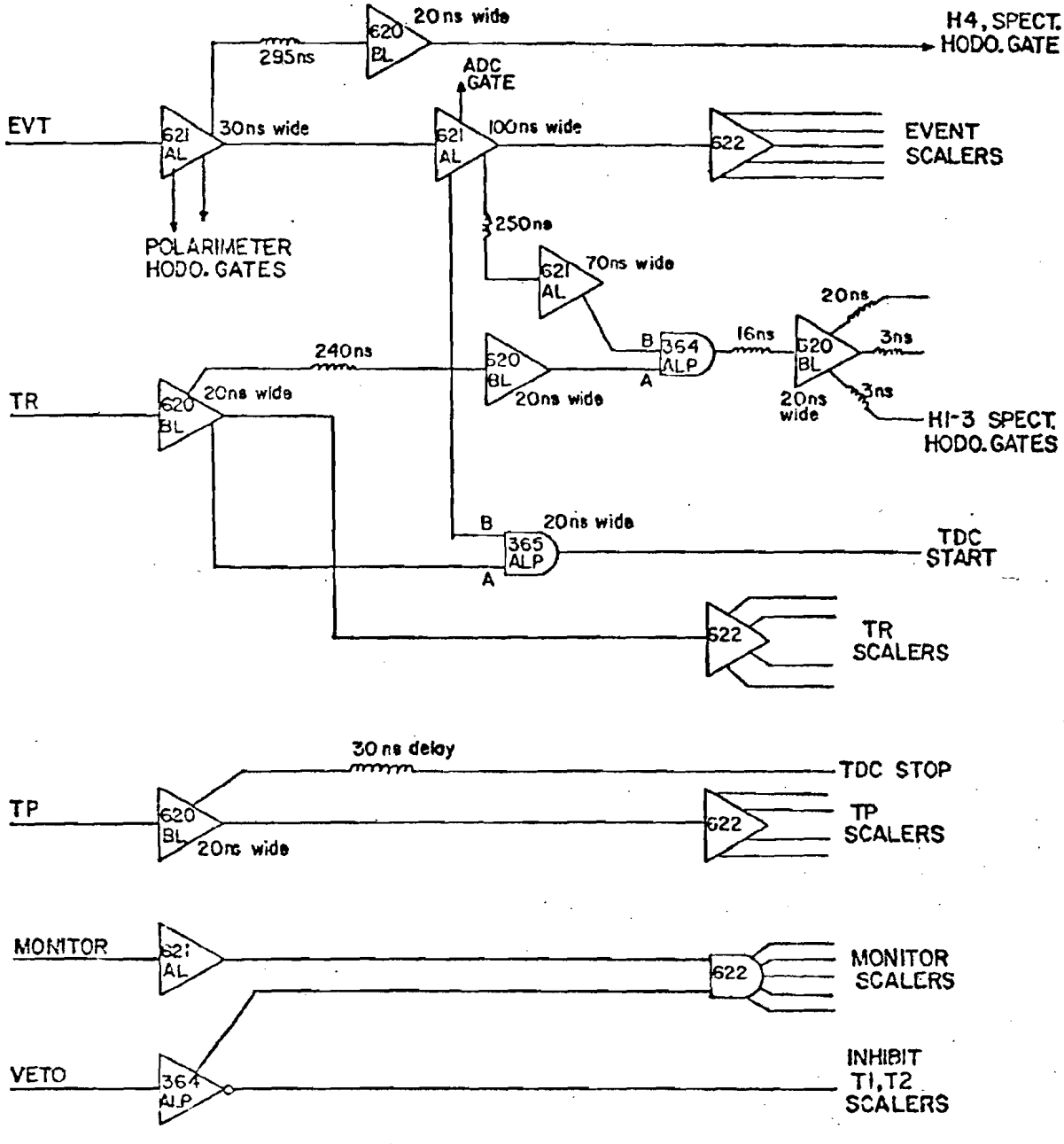

LOGIC FOR HODOS, ADC, TDC, SCALERS

Figure II-12

CHAPTER II REFERENCES

1. P. Mantsch and F. Turkot, "Feasibility Study of a Gas Jet Target with Liquid Helium for Use in the Main Ring", Fermilab Technical Memo, TM-582, June 6, 1975.

2. P. Mantsch and F. Turkot, "Design of a Gas Jet Target Operating at Ambient Temperature in the Main Ring", Fermilab Technical Memo, TM-586, June 18, 1975.

3. S. Gray, "Polarization in Elastic Scattering at High Energies", High Energy Physics with Polarized Beams and Targets, AIP Conference Proceedings, No. 35, American Institute of Physics, New York, 1976, p. 145.

4. G.W. Bryant, H.A. Neal and D.R. Rust, Proton-Carbon Analyzing Power Measurements for Proton Kinetic Energies between .150 Gev and .440 Gev, Indiana University Internal Report COO-2009-102.

CHAPTER III

ANALYSIS

Several computers were used in the data analysis. Most of the heavy "number crunching" was done on Indiana University's CDC 6600 and CYBER 172 system. During the data taking, an off line PDP 15 was used for fast preliminary analysis. The Fermilab DEC 10 and two CDC 6600's were also used for program development and a first look at some of the data. The preliminary analysis of the first t=-.3 data was done on the γ5 computer at the physics department at Indiana University.

Three passes were made through the data (not counting the preliminary analysis.) The first pass wrote data summary tapes (DST's) and printed out interesting histograms, chamber and hodoscope efficiencies, and the asymmetries for elastic protons in each energy range. The second pass read the DST's, calculated more detailed chamber and hodoscope efficiency distributions, and determined the asymmetries for each jet for various cuts. This information was saved on magnetic tape for later use. The third pass used calculations from the second pass to make corrections for chamber inefficiency. A few other corrections were also made in the third pass, and the final asymmetries were calculated. For the higher energy jets, a correction for inelastic contamination of the elastic signal was also necessary.

1. Preliminary Analysis

An off-line PDP 15 was used to analyze the data tapes immediately after they were written. This enabled us to quickly find and correct

problems with our apparatus. Chamber and hodoscope efficiencies, as well as the performance of the TDC, the ADC's, and the B-dot scalar (which was used to determine the beam momentum) were monitored. From the preliminary analysis it was observed that the center of the elastic peak moved across the appartus as the beam momentum increased. This, of course, was not surprizing, since the dipole bent the lower momentum particles through larger angles. The PDP 15 analysis enable us to determine the proper magnet settings so that the second jet was centered as well as possible in the apparatus. Although the other jets were then not centered, this seemed to be the best compromise.

2. Alignment

Since the chamber wires were not exactly lined up with respect to each other, it was necessary to correct for the offset. At the beginning of each data run, a few thousand straight through events were recorded, and these were later used to align the chambers. The x chambers (which measured the horizontal coordinate) and the y chambers (which measured the vertical coordinate) were treated separately. To determine the alignment parameters, particles were tracked through all four chambers. The positions of "hits" in the two middle chambers were predicted from hits in the front and back chambers, and the difference between the predicted and measured positions was averaged for a few thousand events. This average was then used to correct the position measurement in the middle chambers. The alignment parameters were very stable over periods of several months. In fact, the only time a change was observed was when a chamber was removed for repair and then replaced. A typical alignment correction was $\frac{1}{4}$ wire spacing; the largest correction ever needed was about $\frac{1}{2}$ wire spacing. The calculation of the alignment correction was done primarily

on the PDP 15.

3. Writing the DST's

The DST's were written almost entirely on the CYBER 172 system at Indiana University (which, at the time the analysis was done, was separate from the CDC 6600). For each raw data tape, a header record was written which contained the run number (which was also the date), certain analysis parameters, and the polarimeter orientation. (We called the two orientations, somewhat arbitrarily, 0° and 180°.) Data was stored on the DST's event-by-event, but in a much more compact form than on the raw data tapes. We were quite cautious in writing the DST's, and only a few classes of events were eliminated. Information retained for each event included: all of the chamber information (stored as wire numbers), hodoscope tags, the B-dot scalar, the ADC's for the range counters, the TOF measurement, and the beam monitor. Certain calculated quantities were also included: the missing mass squared, the projected scattering angle in the carbon block in both planes, and the vertex distributions. If an event was not successfully reconstructed, it was still written onto the DST, and default values for the calculated quantities were used.

In addition to writing data summary tapes, the first pass analysis printed out histograms for various interesting distributions. The histograms included: the missing mass squared, the B-dot scalar, the TOF, scattering angles in the carbon block, and vertex distributions in the carbon. The histograms were useful in determining where various cuts should be made, particularly in the missing mass distributions.

Chamber and hodoscope efficiencies and the asymmetries for each energy range were also calculated and printed out.

During the writing of the DST's, runs which had no chance of being analyzed were eliminated (such as runs in which a vital chamber was not operating). Certain other problems, such as a failure of the B-dot scalar for several runs, were corrected. All of the data was put in a standard format, which greatly simplified further analysis. Four or five raw data tapes could be written onto one DST. All of our data was compressed into 76 DST's, plus three DST's of pion data.

The DST writing program consisted of two independent sections. The first used information from the spectrometer chambers and hodoscopes to calculate the missing mass and determine if the event was elastic. The second calculated the double scattering distribution in the carbon block and added up the total number of left and right scatters for each jet. Before any of these calculations could be done, it was necessary to read in the information from the data tapes and convert the SAC scalar readings and hodoscopes tags into coordinates in space.

The spectrometer analysis routine calculated the momentum by tracking the particles through the dipole. Standard beam transport equations were used. A six component vector, $(x_1, x_2, x_3, x_4, x_5, x_6)$, was defined for several values of z (z was the distance along the beam line from the target). The components x_1 and x_3 were the positions in the horizontal and vertical planes respectively; x_2 and x_4 were the angles in those planes,

$$x_2 = \frac{d\,x_1}{dz}$$

$$x_4 = \frac{d\,x_3}{dz} \quad .$$

x_5 was a parameter which described "bunching" of the particles in the beam and did not enter into our calculations. x_6 was $\delta p/p$, the desired quantity. Passage though the dipole was described by an equation of the form

$$x_i' = A_j x_j + B_{ij} x_i x_j + C_{ijk} x_i x_j x_k + \dots ,$$

where x_i' was the coordinate after the magnet, and the x_j's were the coordinates before the magnet. This equation, at least to second order, can easily be solved for $x_6=\delta p/p$ if x_1, x_2, x_3, and x_4 are known before and after the magnet. The matrix elements A_j, B_{ij}, and C_{ijk} were determined by mapping the dipole field. Although some of the third order matrix elements were available, it was found that the second order calculation was sufficient.

The momentum was actually calculated two ways--"forward" though the magnet, and "backward". For the forward calculation, the chamber directly in front of the magnet was used. For the backward calculation, the chambers directly behind the magnet were used. For both cases, chambers further upstream and downstream of the magnet were needed. Usually it was possible to calculate the momentum both ways--then the average of the two was used. Using both methods, the momentum could be calculated for about 75-80% of all events.

In order to calculate the missing mass, the production angle as well as the momentum was needed. Recall from Chapter II that the quadropole magnets were designed to give a "parallel-to-point" focus at the first set of MWPC's. So a measurement of position there was almost

a direct measure of the production angle. Momentum-dependent corrections to the angle were made after the momentum was calculated.

The data consisted of events taken for energy ranges centered at beam momenta of 22 GeV/c, 45 GeV/c, 75 GeV/c, 110 GeV/c, and 175 GeV/c for t=-.3, t=-.6, t=-.8, and t=-1.0. A small amount of data for t=-.3 with a beam momentum of 200 GeV/c was also taken. Figs. III-1 and III-2 show a typical distribution of the B-dot scalar for data with five jets and three jets, respectively. The different energy ranges can be clearly seen. Figs. III-3 through III-26 show the distribution of (missing mass)^2 - (proton mass)^2 for each energy range and t value. For the lowest jet, essentially all of the events were elastic. As the beam momentum increased, the number of inelastics increased. At the higher energies, and especially for the higher $|t|$ values, there was considerable inelastic contamination under the elastic peak. This necessitated a correction to the final result, which will be discussed later. For t=-1.0 and a beam momentum of 175 GeV/c, no elastic peak was visible at all. This point was not included in our final data sample. Also shown in the figures are the time of flight distributions for each t value. The distributions in all cases are very clean. A pion peak can be seen in the t=-1.0 data, but it was well separated from the proton peak and could easily be excluded.

Reconstruction in the polarimeter was independent of the spectrometer. A coordinate system was defined in space such that $\hat{z}$ was along the beam direction, y was up, and x=y x z. This system was fixed in space and

did not rotate with the polarimeter. Reconstructions in the x-z plane and the y-z plane were done independently.

A fairly simple algorithm was used to sort out spurious chamber hits and reconstruct particle tracks. Trajectories were calculated both upstream and downstream of the carbon block for all combinations of chamber hits. Then these tracks were projected along the z-axis to the center of the carbon block. The difference in the upstream and downstream projected x-(or y-) coordinates was required to fall within a certain tolerance for a track to be accepted. In the original version of the filtering program, that tolerance was a constant for all tracks. In a later, improved version, the tolerance depended on the scattering angle (larger angles being given a larger tolerance). If more than one track was found which linked up in the carbon, the event was rejected as non-reconstructable, since there was no way of knowing which track to choose. Once the trajectories into and out of the carbon were known for both planes, all pertinent quantities could be calculated. These included the polar scattering angle (θ), the azimuthal angle (φ), the projected scattering angles in both planes, θ_x and θ_y, and the vertex distributions. For each reconstructed event, a tag bit was set which indicated whether or not a hodoscope element had fired which agreed with the downstream track.

The first pass analysis yielded several pieces of information. The asymmetries were calculated for each run and were added up by hand to give a "first pass" answer for the polarization. The histograms were used to determine where various cuts should be placed. Also,

the calculated efficiencies showed that a few of the polarimeter chambers and hodoscopes (the last y chamber in particular) sometimes showed regions of inefficiency.

4. First Analysis of the DST's.

Chamber or hodoscope inefficiencies could be a serious problem in a double scattering experiment, since one measures small differences in the number of left and right scatters. Although rotation of the polarimeter should cancel out the instrumental asymmetry, complete cancellation would not occur for all jets because events were not centered in the apparatus for all jets. Also, the efficiencies were not constant in time and were not always the same for the two orientations of the polarimeter. Even though chamber inefficiencies were a problem for only a small amount of the data, and the crucial x chambers were unaffected, it was decided that the best solution was to correct the number of left and right scatters by the chamber efficiencies. In the first pass through the DST's, detailed chamber efficiency distributions were calculated for the four downstream polarimeter chambers. (The efficiency of the upstream chambers didn't matter, since only the downstream chambers could give an instrumental asymmetry.) Each downstream chamber was divided into a 12 x 12 array, and the efficiency for each section was calculated using the upstream chambers, the hodoscopes, and the other downstream chambers. These efficiencies were saved on magnetic tape for later use.

In addition to calculating the efficiencies, the first analysis of the DST's calculated the asymmetry for the normal data sample and

also for a number of specialized cuts. These asymmetries were also saved for each DST and were added up for all runs. The specialized cuts led to some interesting observations and one correction, which will be discussed later. Another observation made during this stage of the analysis was the strong correlation between position in the front x chamber and the incoming angle. This correlation was not suprizing at all--it is just due to the particles passing through the dipole.

5. Problems and Corrections

One observation made from the specialized cuts of the first DST analysis was that the asymmetry varied as a function of position across the first x chamber. This effect was believed to be due (at least in part) to events we called "vees"--events with two prongs emerging from the carbon block. Ordinarily, such events were thrown out, because two tracks were reconstructed. But if the event occurred, say, on the left side of chamber X1, the left arm of the vee might be lost off the edge of the apparatus (see Fig. III-27a). Then the event would be reconstructed as a right scatter, and the left side of the chamber would accumulate more right scatters. Likewise, the right side of the chamber would have more left scatters, and the effect would be the same for the two orientations of the polarimeter. (This was exactly the effect observed). For a well-centered beam, the effect would cancel--but our events were not well centered for all jets. The solution was to keep the smaller angle arm of the vees. Then, for an event on the left side of the chamber, when the larger angle arm scattered left and was lost off the edge of the apparatus, a right scatter was observed. When the

larger angle arm scattered right, the corresponding small angle track was counted as a left scatter, and no bias was introduced. (See Fig. III-27b). It was found, after the polarimeter reconstruction program was modified to find vees, that the maximum percentage of vees in our data was about 3% (at t=-1.0), and smaller for the other t values.

While the second pass analysis was in progress, several other independent tests were made, one of which led to another correction. For small angle scatters (less than 2-3°), the average scattering angle in x (θ_{av}) should always be zero (since carbon has zero analyzing power for small angle scatters.) Several long tapes of straight through data were analyzed to see of this was the case. It was found that, although θ_{av} was zero when averaged for all incoming angles, it was not zero when calculated for a small range of values of the incoming angle (AINX). θ_{av} and AINX were found to be related approximately linearly over the range of incoming angles the apparatus accepted (about ± 30 mr). (See Fig. III-28). θ_{av} ranged from about + .1° to -.1°. The effect was the same for both orientations of the polarimeter--the slope of the lines was the same, although the intercept was slightly different. A Monte Carlo study of the problem indicated that this effect was due to a sensitive interplay between the incoming angle, the discreteness of the chamber wires, the chamber alignment, and the spacing in z between the chambers. The problem was corrected by forcing θ_{av} to be zero by shifting the observed scattering angle in x, θ_x, by an amount which depended on the value of AINX for that event. The idea was that, when the true scattering angle was θ_x, the chambers measured

an angle $\theta_x + \epsilon$. The error could be corrected simply by subtracting ϵ.

The "θ_{av} vs. AINX" correction led to another embellishment of the analysis. An expanded histogram of θ_x showed that the distribution was very discrete, with sharp spikes and no events in between. This was due, of course, to the discreteness of the chamber wires. If the value of θ_x was shifted by a certain amount, even if that amount was small, the 6° cut used for calculating the asymmetry could cross one of the spikes and perhaps lead to a large change in the asymmetry. This seemed like an undesirable occurrance, so we decided to smooth out the θ_x distribution (and in fact, all of our distributions) by "randomizing" the wire positions, When a wire fires, all that is really known about the particle's position is that is passed through a sensitive region surrounding the wire. A reasonable estimate of that region was made (about 80% of the wire spacing), and, instead of using the actual coordinate of the wire, the particle was placed randomly somewhere in the sensitive region. The effect on some of the distributions (particularly the incoming angle) was striking. Figs. III-29 through III-60 show both randomized and unrandomized distributions of the polar and azimuthal scattering angles, the projected scattering angles in both planes, the reconstructed vertex, and the incoming angle. The distributions are shown for t=-.8 (with the 2" carbon block) and t=-.3 (with the .5" carbon block). The other t values had distributions very similar to those of t=-.8.

6. Effect of the Polarimeter Computer

Of the figures presented in the last section, the histograms of θ, θ_x, and θ_y are of particular interest. These distributions were made with no software cuts at all--only the hardware cuts of the polarimeter computer. Without the polarimeter computer in the trigger, almost all events would be straight throughs, and the plots of θ, θ_x, and θ_y would be sharp spikes at 0°. Scatters at large angles would be a small background compared to the peak. Figs. III-61 and III-62 show histograms of θ and θ_x for a run which did not have the polarimeter computer in the trigger. The difference is striking and emphasizes the importance of eliminating the straight through events. The polarimeter computer required a scatter between (approximately) 6° and 22° in either x or y. Events in the small angle region of θ_x had a scatter in y greater than 6°, and vice versa. The actual hardware cuts were not exactly at 6° and 22°, but a few degrees away, so that we were certain the angular region used to calculate the asymmetry was unaffected. The action of the polarimeter computer can perhaps best be seen in the scatter plot of Fig. III-63. The cut made was very nearly a square in the θ_x vs. θ_y plane. The polarimeter computer was not completely efficient, however, and some events slipped into the region which, ideally, should have no events.

The θ, θ_x, and θ_y histograms for t=-.3 and t=-.8 are similar but not identical. The difference comes from two sources, First of all, there is a real difference in the shape of the proton-carbon cross section for different proton momenta. Secondly, the action of the polarimeter computer was somewhat different in the two cases, since

the cuts and tolerances were different for the 2" carbon block and the .5" block.

7. Background

With the dipole off and the jet pulsing, our trigger rate was very low--only one or two events per beam pulse without the polarimeter computer, and essentially nothing with the polarimeter computer in the trigger. However, there were a large number of particles entering the polarimeter at steep negative angles--these were particles which were coming from the target, but around the dipole. Also, upstream of our target was another gas jet target which bombarded the polarimeter with particles when it was pulsed. Such particles were a potential source of background. They could never travel completely through the spectrometer, but they could cause confusion in reconstruction in the polarimeter. Suppose the "real" proton went through the spectrometer as it should, entered the polarimeter, and then stopped in the carbon. (Stopping in the carbon was not uncommon, especially at the lower t values.) If a background particle passed through the back polarimeter chambers close enough in time to the real event, it could be mistaken for the real proton. Almost all such "events" would appear to be right scatters in the carbon. To eliminate them, we required, first of all, that the upstream and downstream tracks link up in the carbon to within fairly tight tolerances. We also required a good reconstruction in both the x and y planes, and we made fairly tight cuts on the vertex distribution. Requiring the hodoscopes in the reconstruction should also help eliminate background because of

their stricter timing requirements. It was found that requiring the hodoscopes made no difference, which indicates that essentially all of this type of background was being eliminated. The hodoscopes were not required in the final data sample. To eliminate other possible sources of background, a tight cut was made on the TOF distribution, and every event was required to track all the way through the spectrometer and reconstruct in missing mass.

8. Third Pass Analysis

All of the corrections discussed above were incorporated into the final analysis of the DST's. The efficiency correction was done by incrementing the total number of left or right scatters by 1/EFF rather than 1 whenever a scatter was observed. Here EFF is the product of all pertinent chamber efficiencies. The correction for θ_{av} was done by shifting the calculated value of θ_x for each event by an amount which depended on the value of AINX for that event. These two corrections never shifted the asymmetries for x scatters by more than half of a standard deviation. However, the efficiency correction had a three standard deviation effect on the asymmetry in y for t=-1.0, which was the t value most affected by chamber inefficiencies. The fact that the corrected y asymmetries, even for t=-1.0, were zero within statistical errors gave us confidence that the efficiency correction was doing the right thing.

Cuts were carefully placed to assure that the data sample was as clean as possible. A cut was made for AINX at ± 25 mr. Outside of this

region our knowledge of the θ_{av} correction was not good. Cuts were also placed in the TOF distribution and the z-vertex distribution. The vertex cut was made slightly outside the physical dimensions of the carbon block, since the resolution and the randomization of the wires spread the distribution.

The asymmetries were calculated for each energy range and for up to ten bins in missing mass. The first bin corresponded to elastics. The other bins were the same width as the first, but were progressively higher in missing mass. This allowed us to plot the asymmetry as a function of missing mass and make a correction for inelastic contamination of the elastic signal. All of the asymmetries were savedfor each DST and were added up for all runs.

9. Consistency Checks

Several consistency checks were made on the data. First of all, a data point was taken at a beam momentum of 22 GeV/c for each t value. These results could then be checked with existing data, and in all cases our results were found to be in good agreement with previous results. About a million pion triggers were taken, and the asymmetry of these events was found to be zero within the statistical error of .3%. Another check was the asymmetry in the y plane, the "up-down" asymmetry. Parity conservation, of course, requires this to be zero, since the proton can be polarized only normal to the original scattering plane. After all corrections had been made, the y asymmetries for all t values came out to be zero within the statistical errors. A final check was the comparison of results for the two polarimeter orientations. All the asymmetries were calculated for 0° and 180°

separately. A large difference in the two results would indicate a large instrumental asymmetry of some kind. For almost all the data points the 0° and 180° results agreed within one standard deviation. No points were more than $1\frac{1}{2}$ standard deviations apart. The final asymmetry used to calculate the polarization was the weighted average of the 0° and 180° results.

10. Carbon Analyzing Power

The calculated asymmetries must be divided by the analyzing power of carbon to obtain the polarization. The analyzing power (A), was measured in a calibration run using the polarized beam at the Argonne ZGS[1]. The projected scattering angle in the horizontal plane (θ_x) was measured with a series of MWPC's. Scatters into the angular region of 6°-22° were used to calculate the asymmetry,

$$\epsilon = (L-R)/(L + R) ,$$

where L is the total number of left scatters, and R is the number of right scatters. Then, since the beam polarization was known, A was easily calculated from $P=\epsilon/A$. A typical value for the beam polarization was 70-80%. Instrumental asymmetries were averaged out by reversing the beam polarization periodically. It should be noted that, since the calibration was done for the angular region 6°-22°, the asymmetries calculated in the experiment had to be over the same region.

The analyzing power was measured for five different values of the kinetic energy of the incident proton. Data was taken for two values of incident beam momentum: .815 GeV/c, and 1.0 GeV/c. Other values of kinetic energy were obtained by passing the beam through carbon degraders

of varying thicknesses. Table III-1 gives the measured values of A for each value of the kinetic energy. Fig. III-64 is a plot of analyzing power vs. kinetic energy. A fit was made to the five data points; this fit is also given in Table III-1. Results from this calibration are in good agreement with previous measurements of A.[2]

11. Correction for Inelastic Contamination

From the missing mass histograms, (Fig. III-3 through III-20) it is clear that, for the higher $|t|$ values and the higher energies, inelastic contamination under the elastic peak was a problem. See, for example, $t = -.8$ $(GeV/c)^2$ and $p_{beam} = 110$ GeV/c or 175 GeV/c. A correction was necessary for this contamination for the three highest energy points at all t values except $t = -.3$, where essentially all events were elastic.

The per cent contamination was estimated by hand-drawn curves to both the elastic peaks and the background. The half of the peak lowest in missing mass was assumed to be free of background and to represent the true shape. The peak was assumed to be symmetric and was extrapolated into the region which contained both elastics and background. Then the shape of the background could be determined and, using the known position of the missing mass cut, the per cent of inelastics within the cut was estimated. For $t = -.6$ the contamination was less than 10% in all cases; for $t = -.8$ the contamination was 17-18% for the three higher energy jets. Even though the higher energies had greater background, the cut in missing mass was further into the elastic peak, so the amount of contamination within the cut was about the same. At $t = -1.0$ and $p_{beam} = 75$, the contamination was about 17%, and the $p_{beam} = 100$ it was about 23%. At

$t = -1.0$ and $p_{beam} = 175$, no elastic peak could be separated at all, and this point was not included in our final results.

In making the correction, it was assumed that the elastics had zero polarization. The polarization for the inelastics was calculated for bins in missing mass different from the elastics (see section IV-3), and was found, for the most part, to be consistent with zero. There was a general trend toward positive polarizations for higher missing mass, but the points closest to the elastic peak were very nearly zero in most cases and were assumed to be zero for purposes of the correction.

The inelastic correction changed the results by less than one-fourth of a standard deviation for all points except $t = -1.0$ and $p_{beam} = 110$. For that point, the result was changed by a little less than one half of a standard deviation, and the estimated error was increased slightly to account for error in the correction.

Table III-1

Analyzing Power of Carbon

Kinetic Energy (GeV)	A	ΔA	A_{fit}
.154	.2344	.0110	.2348
.239	.2897	.0083	.2877
.261	.2740	.0122	.2788
.345	.2236	.0110	.2228
.433	.1839	.0123	.1841

$$A_{fit} = -.77889 + 13.19184T - 56.82162T^2 + 99.952507T^3 - 62.87229T^4$$

T = Kinetic Energy

CHAPTER III FIGURES

Figure III-1. Distribution of beam momenta for a typical sample of events. Five energy ranges, corresponding to five pulses of the gas jet target, can be clearly seen. Units are GeV/c.

Figure III-2. Distribution of beam momenta when only three jet pulses were used.

Figure III-3. Distribution of $(\text{missing mass})^2 - (\text{proton mass})^2$ in units of $(\text{GeV}/c^2)^2$ for $t = -.3\ (\text{GeV}/c)^2$ and $p_{beam} = 20$ GeV/c.

Figure III-4. Missing mass distribution for $t = -.3$ and $p_{beam} = 45$ GeV/c.

Figure III-5. Missing mass distribution for $t = -.3$ and $p_{beam} = 75$ GeV/c.

Figure III-6. Missing mass distribution for $t = -.3$ and $p_{beam} = 110$ GeV/c.

Figure III-7. Missing mass distribution for $t = -.3$ and $p_{beam} = 175$ GeV/c.

Figure III-8. Time of flight distribution for $t = -.3$. Units are tenths of nanoseconds.

Figure III-9. Missing mass distribution for $t = -.6$ and $p_{beam} = 22$ GeV/c.

Figure III-10. Missing mass distribution for $t = -.6$ and $p_{beam} = 45$ GeV/c.

Figure III-11. Missing mass distribution for $t = -.6$ and $p_{beam} = 75$ GeV/c.

Figure III-12. Missing mass distribution for $t = -.6$ and $p_{beam} = 110$ GeV/c.

Figure III-13. Missing mass distribution for $t = -.6$ and $p_{beam} = 175$ GeV/c.

Figure III-14. Time of flight distribution for $t = -.6$, in tenths of nanoseconds.

Figure III-15. Missing mass distribution for t = -.8 and p_{beam} = 22 GeV/c.

Figure III-16. Missing mass distribution for t = -.8 and p_{beam} = 45 GeV/c.

Figure III-17. Missing mass distribution for t = -.8 and p_{beam} = 75 GeV/c.

Figure III-18. Missing mass distribution for t = -.8 and p_{beam} = 110 GeV/c.

Figure III-19. Missing mass distribution for t = -.8 and p_{beam} = 175 GeV/c.

Figure III-20. Time of flight distribution for t = -.8, in tenths of nanoseconds.

Figure III-21. Missing mass distribution for t = -1.0 and p_{beam} = 22 GeV/c.

Figure III-22. Missing mass distribution for t = -1.0 and p_{beam} = 45 GeV/c.

Figure III-23. Missing mass distribution for t = -1.0 and p_{beam} = 75 GeV/c.

Figure III-24. Missing mass distribution for t = -1.0 and p_{beam} = 110 GeV/c.

Figure III-25. Missing mass distribution for t = -1.0 and p_{beam} = 175 GeV/c.

Figure III-26. Time of flight distribution for t = -1.0. Note the small pion peak to the left of the proton peak.

Figure III-27. The "vee" correction. Problems arise in the analysis when more than one particle emerges from the carbon block. If the larger angle track is lost off the edge of the apparatus (27a), a right scatter is recorded. If the larger angle track scatters right, both tracks are seen, and the ambiguity causes the event to be rejected (27b). An experimental bias is created if events occur predominately on one side of the apparatus. The solution is to count the small angel arm whenever a vee is observed. Then in 27b, a left scatter is recorded to balance the right scatter of 27a.

Figure III-28. The AINX vs. θ_{av} correction. AINX is the incoming angle of the beam (in milliradians) in the horizontal (x) direction. θ_{av} is the average angle in degrees for small angle scatters ($\pm 1^{o}$) for polarimeter computer out runs. Ideally $\theta_{av} = 0$. However, it was found that θ_{av} and AINX were related almost linearly over the range of incoming angles accepted by the apparatus. This necessitated a correction to the measured scattering angle, as described in the text.

Figure III-29. Polar scattering angle in the .5" carbon block for t = -.3. Units are degrees.

Figure III-30. Same as Figure III-29, with the wire positions "randomized" as discussed in the text. This distribution was changed very little by randomization.

Figure III-31. Azimuthal scattering angle in the carbon block for t = -.3. Units are degrees.

Figure III-32. Same as Figure III-31, but with the wire positions randomized. This distribution is noticably smoothed as a result of randomization.

Figure III-33. Carbon scattering angle projected into the horizontal (x) plane for t = -.3. Units are degrees.

Figure III-34. Same as Figure III-33, but randomized and therefore much smoother.

Figure III-35. Carbon scattering angle in degrees projected into the vertical (y) plane for t = -.3.

Figure III-36. Same as Figure III-35, but randomized.

Figure III-37. Z-position of the vertex for the scatter in the carbon block, as calculated in the x-plane. Z is along the beam direction, and x is the horizontal direction. The edges of the .5" block can be clearly seen. Units are inches from the first polarimeter chamber.

Figure III-38. Same as Figure III-37, but randomized. The vertex distribution was smoothed and somewhat spread out by randomization.

Figure III-39. X-position of the carbon vertex. The edges of the carbon block at ± 3" can be clearly seen. Units are inches from the center of the polarimeter.

Figure III-40. Same as Figure III-39, but randomized.

Figure III-41. Incoming angle of the beam in the horizontal plane for t = -.3, in milliradians. An angle of 0 mr corresponds to normal incidence. The distribution is very granular because of the discreteness of the chamber wires.

Figure III-42. Same as Figure III-41, but randomized. The effect of randomization was striking for this distribution--the granularity completely disappeared.

Figure III-43. Incoming angle of the beam in the vertical plane for t = -.3, in milliradians.

Figure III-44. Same as Figure III-43, but randomized. Again the randomization had a striking effect on the distribution.

Figure III-45. Polar scattering angle in the carbon for t = -.8 and the 2" block. Units are degrees.

Figure III-46. Same as Figure III-45, but randomized.

Figure III-47. Azimuthal scattering angle in the carbon for t = -.8, in degrees.

Figure III-48. Same as Figure III-47, but randomized.

Figure III-49. Scattering angle in the carbon projected into the horizontal (x) plane for t = -.8, in degrees.

Figure III-50. Same as Figure III-49, but randomized.

Figure III-51. Scattering angle in the carbon projected into the vertical (y) plane for t = -.8, in degrees.

Figure III-52. Same as Figure III-51, but randomized.

Figure III-53. Z-position of the vertex in the carbon as calculated in the horizontal plane. The edges of the 2" block can be clearly seen. Units are inches from the first polarimeter chamber.

Figure III-54. Same as Figure III-53, but randomized.

Figure III-55. X-position of the carbon vertex. The edges of the block can be clearly seen. Units are inches from the center of the polarimeter.

Figure III-56. Same as Figure III-55, but randomized.

Figure III-57. Incoming angle of the beam in the horizontal plane, in milliradians. 0 mr corresponds to normal incidence. The granularity of the distribution is due to the discreteness of the chamber wires.

Figure III-58. Same as Figure III-57, but randomized.

Figure III-59. Incoming angle if the beam in the vertical plane in milliradians.

Figure III-60. Same as Figure III-59, but randomized.

Figure III-61. Polar scattering angle in the carbon when the polarimeter computer was not in the trigger. Almost all events were "straight throughs", i. e., events which did not scatter in the carbon or scattered at very small angles.

Figure III-62. Carbon scattering angle projected into the x plane, again without the polarimeter computer in the trigger.

Figure III-63. Scatter plot showing the effect of the polarimeter computer. The polarimeter computer required a scatter greater than about 4° in either the horizontal (x) or vertical (y) plane, effectively making a square cut in the θ_x vs. θ_y plane. This plot was made with no software cuts, only the hardware cuts of the polarimeter computer.

Figure III-64. Analyzing power of carbon.

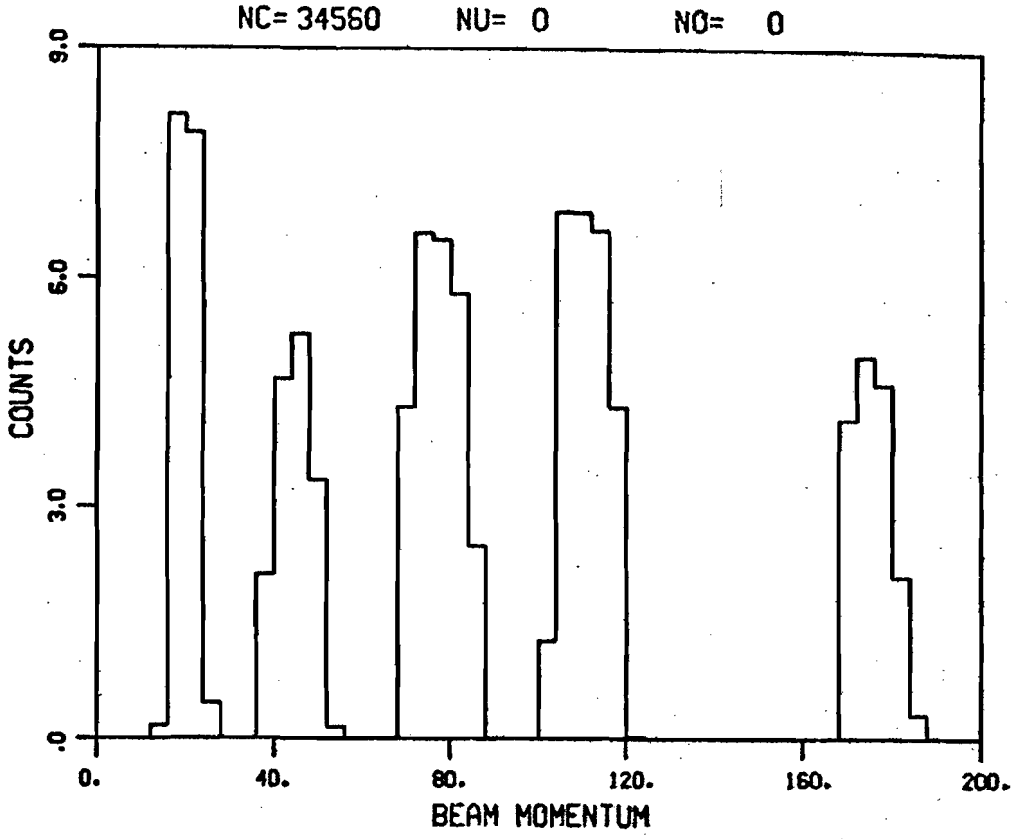

Figure III-1

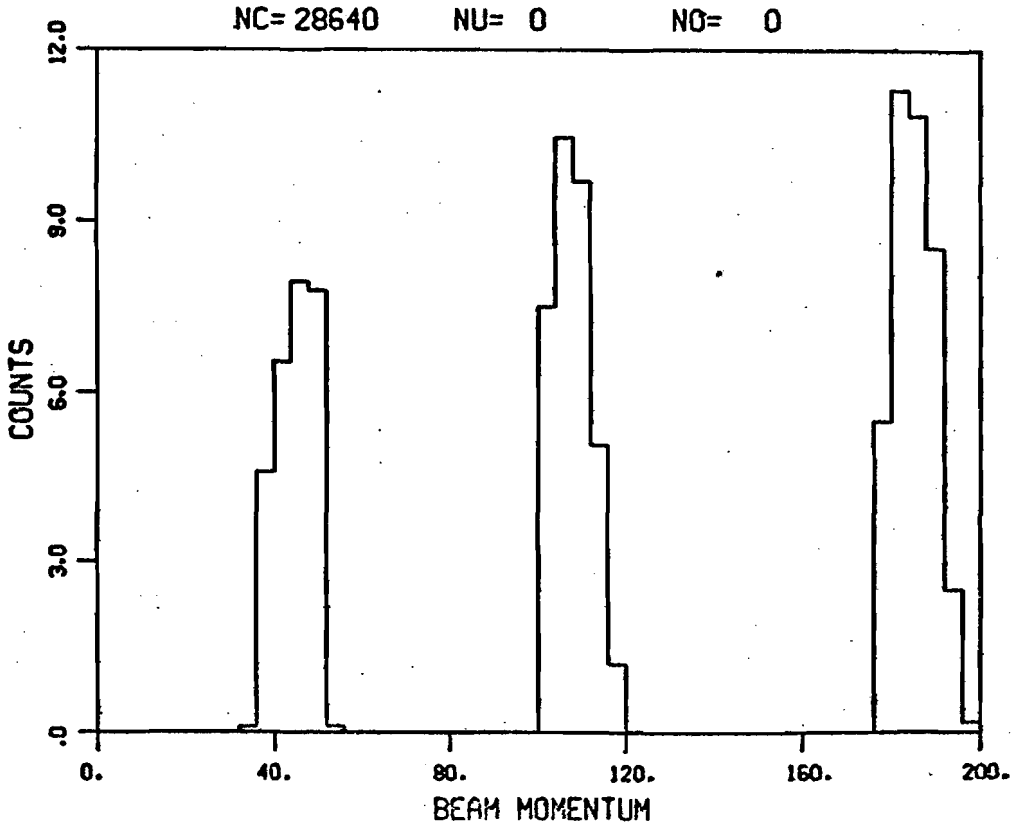

Figure III-2

T = -.3

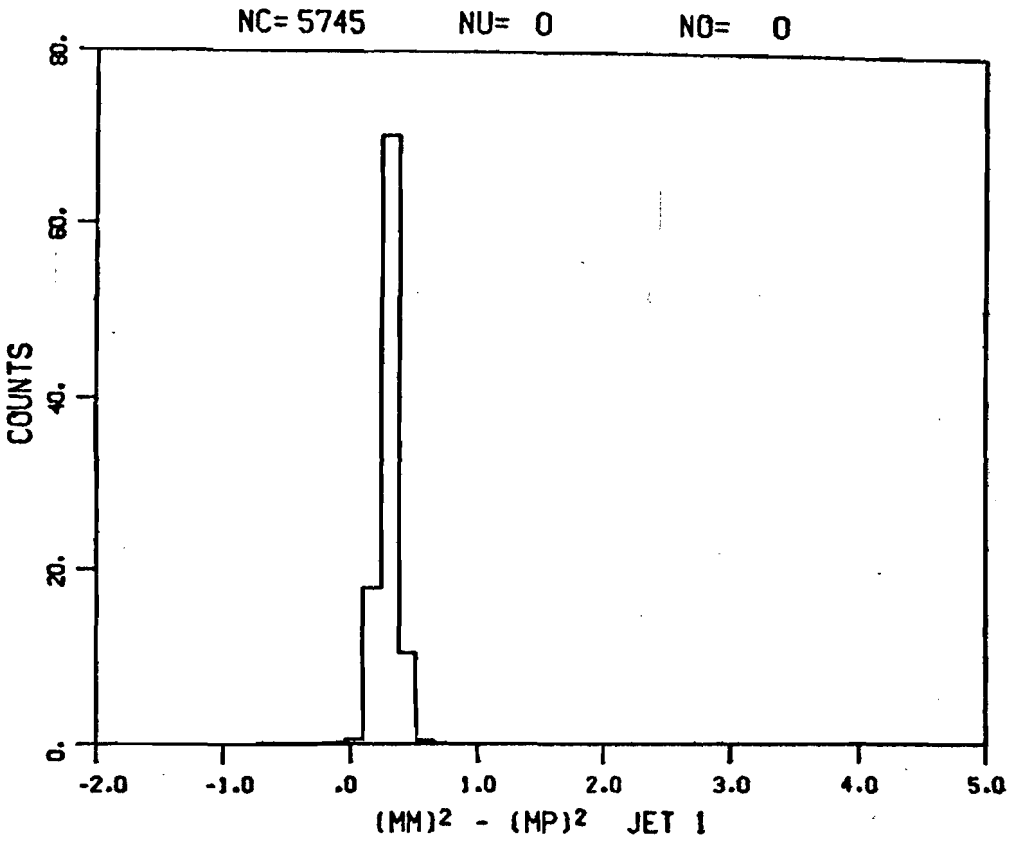

Figure III-3

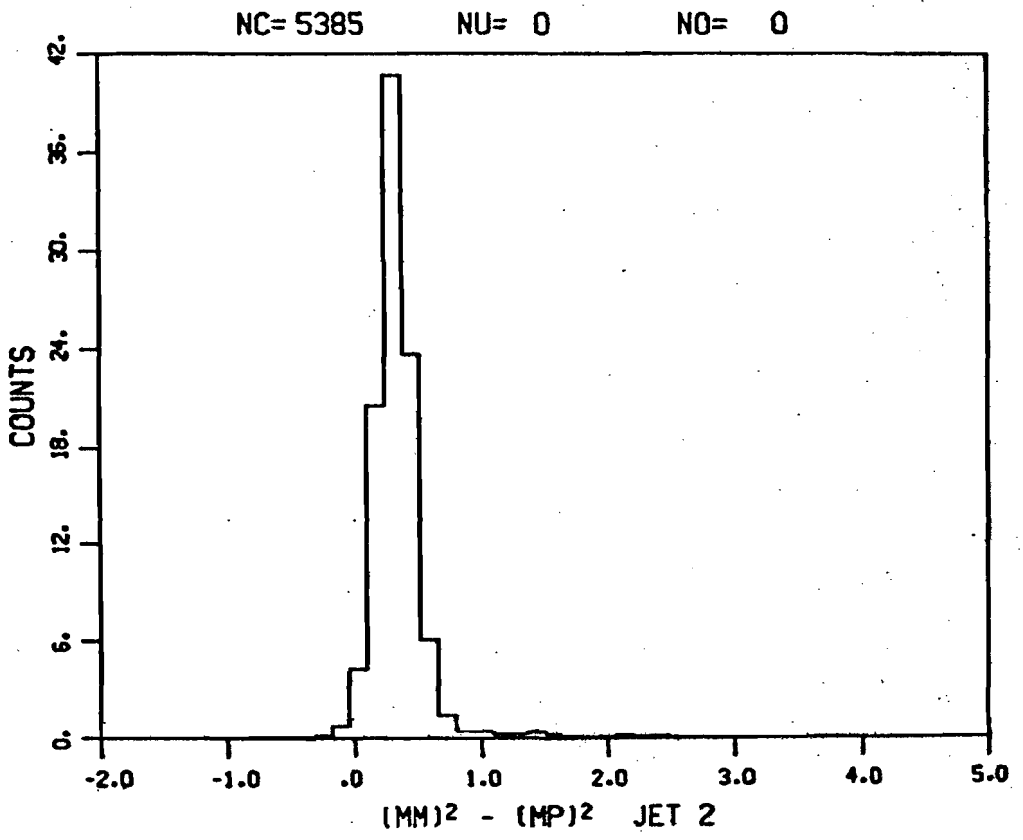

Figure III-4

T = -.3

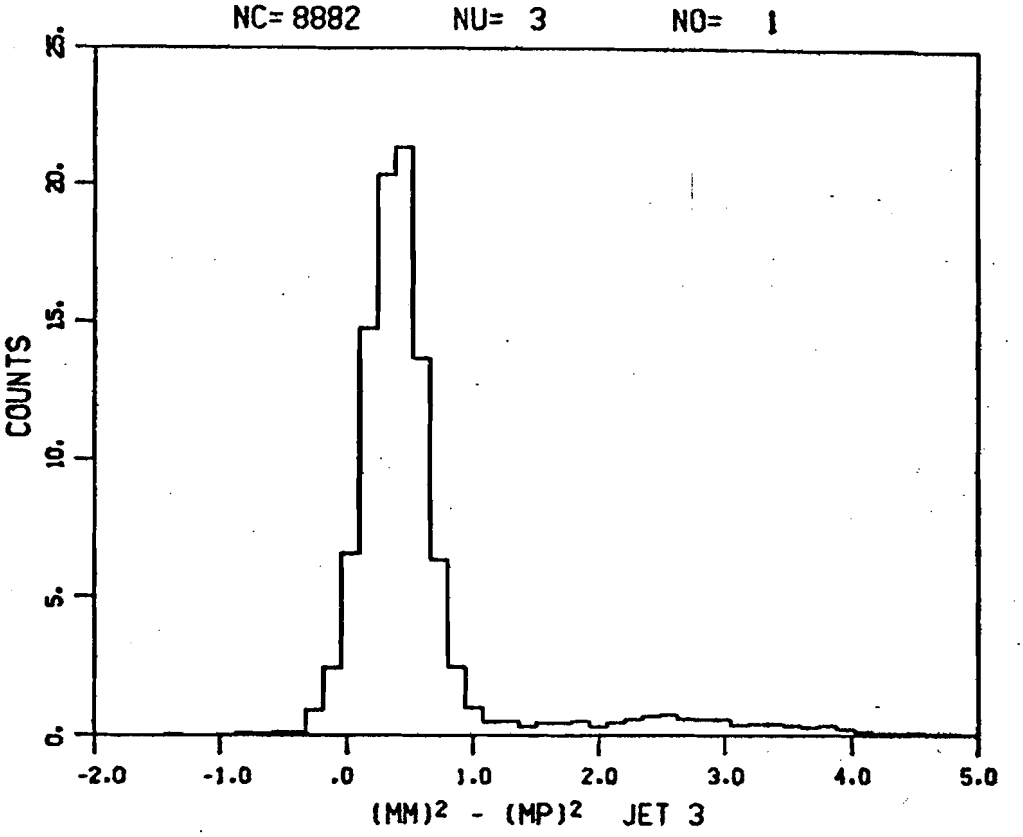

Figure III-5

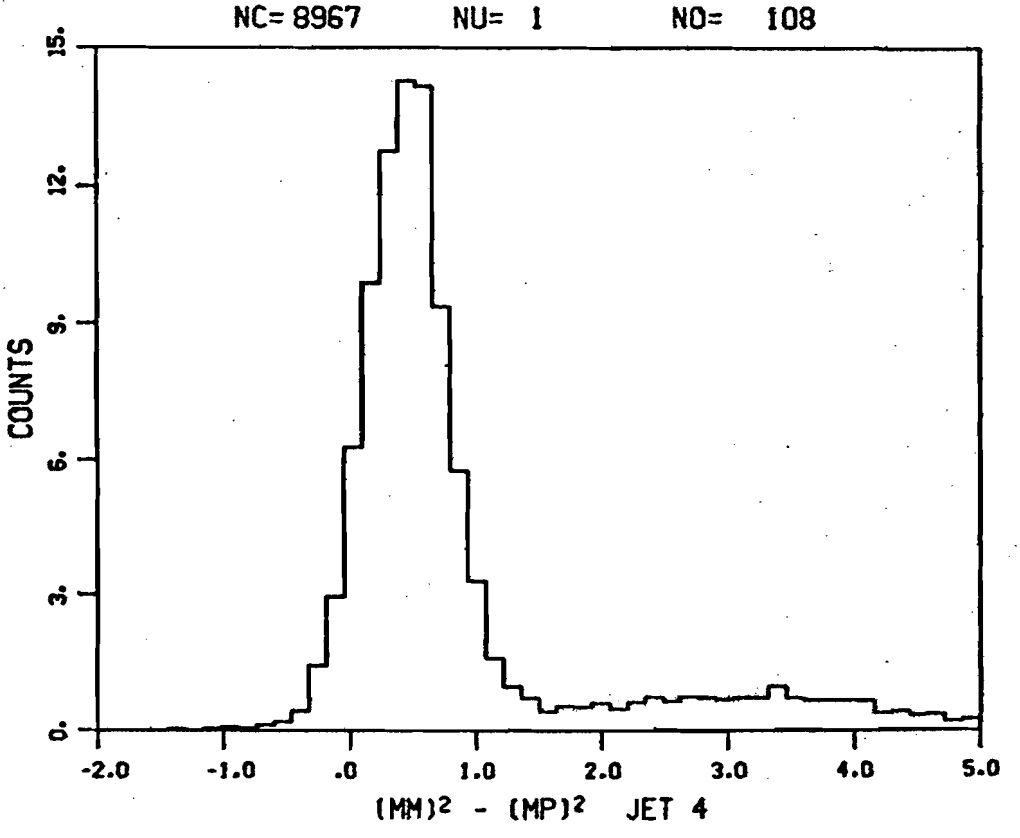

Figure III-6

T = -.3

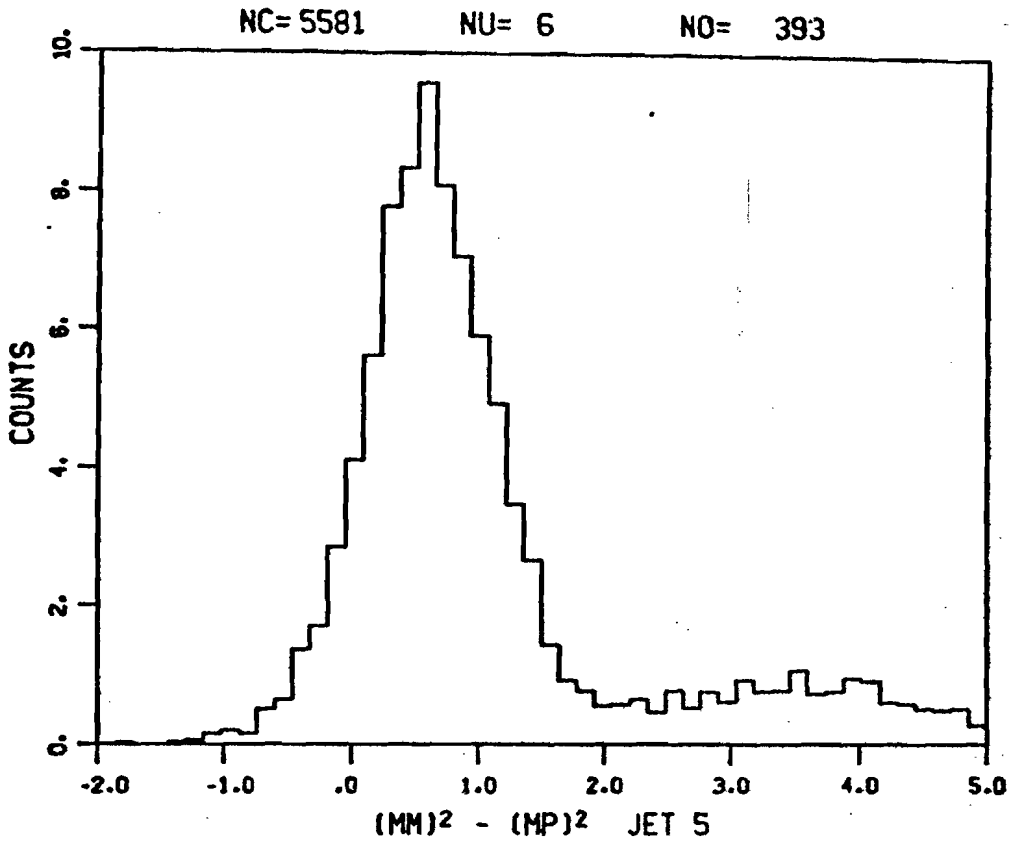

Figure III-7

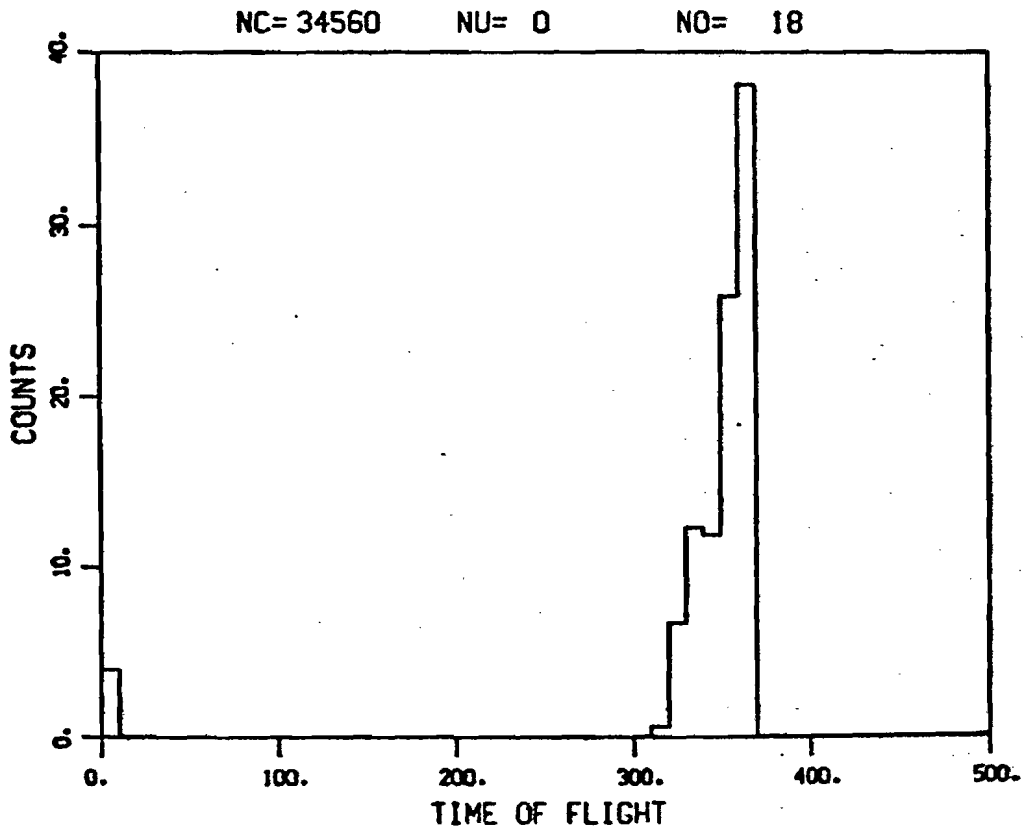

Figure III-8

T = -.6

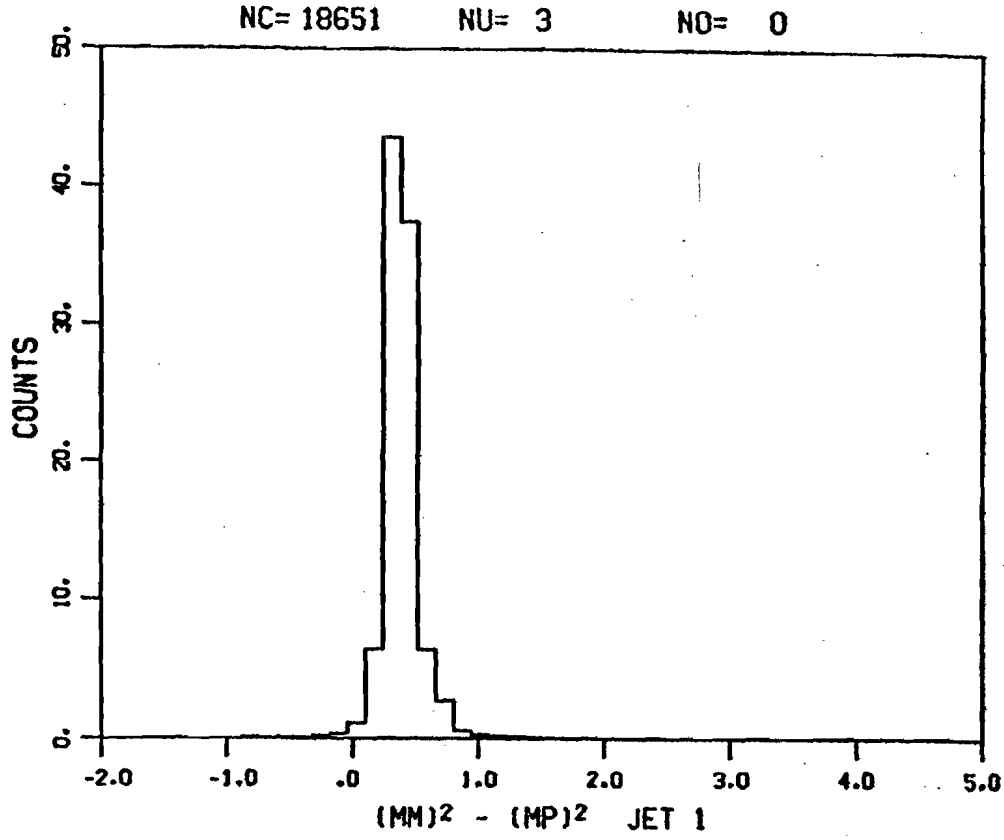

Figure III-9

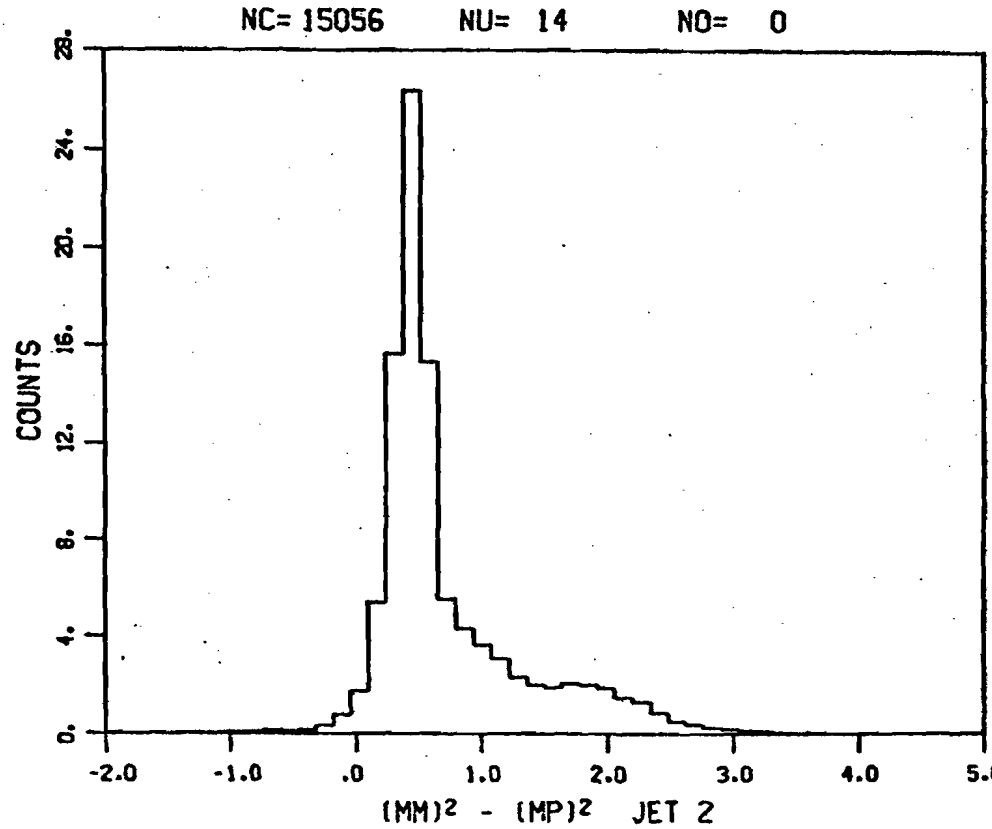

Figure III-10

T = -.6

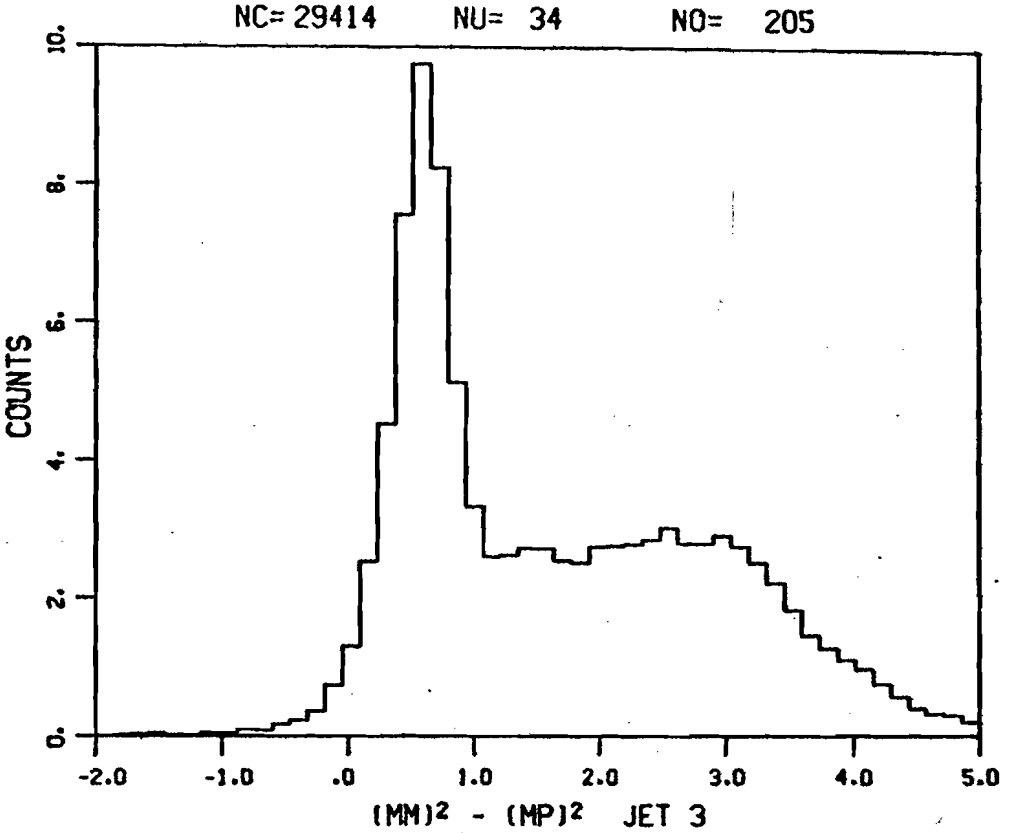

Figure III-11

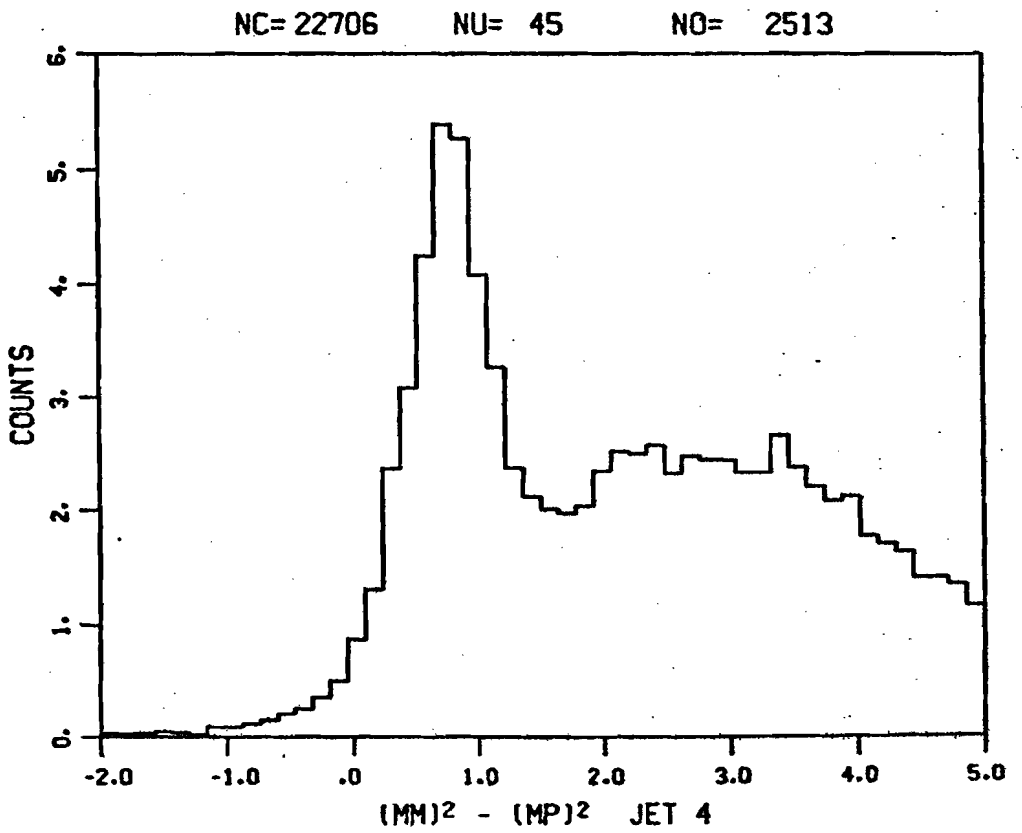

Figure III-12

T = -.6

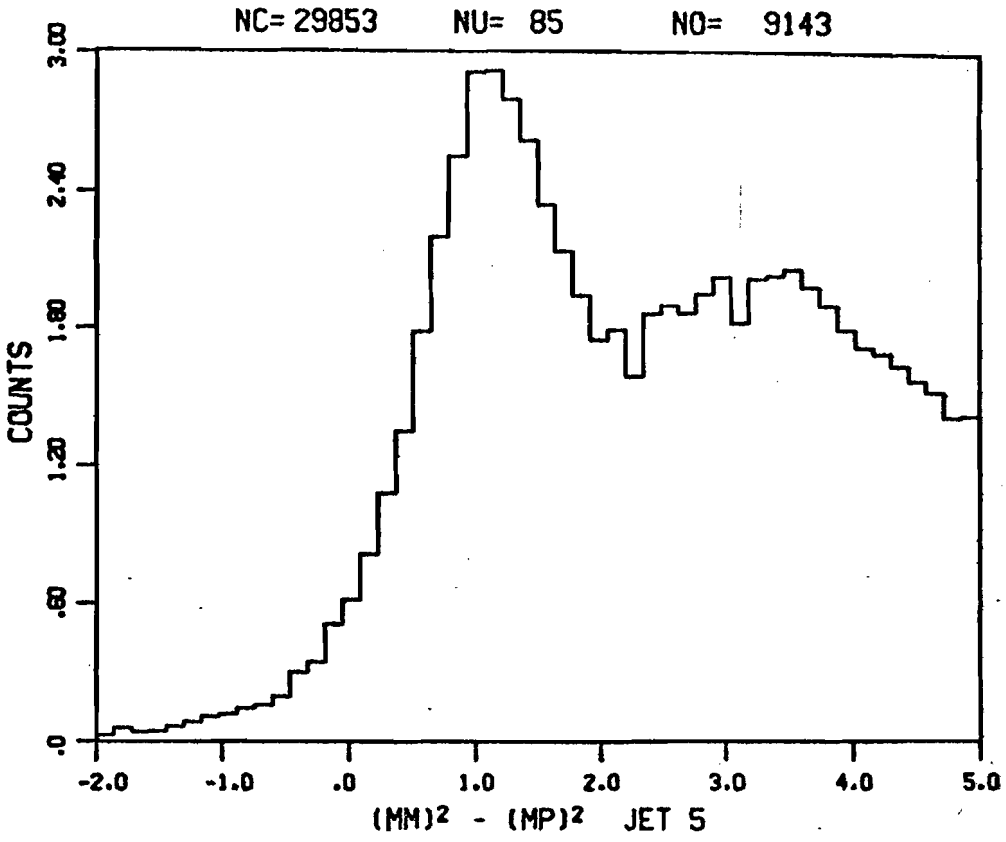

Figure III-13

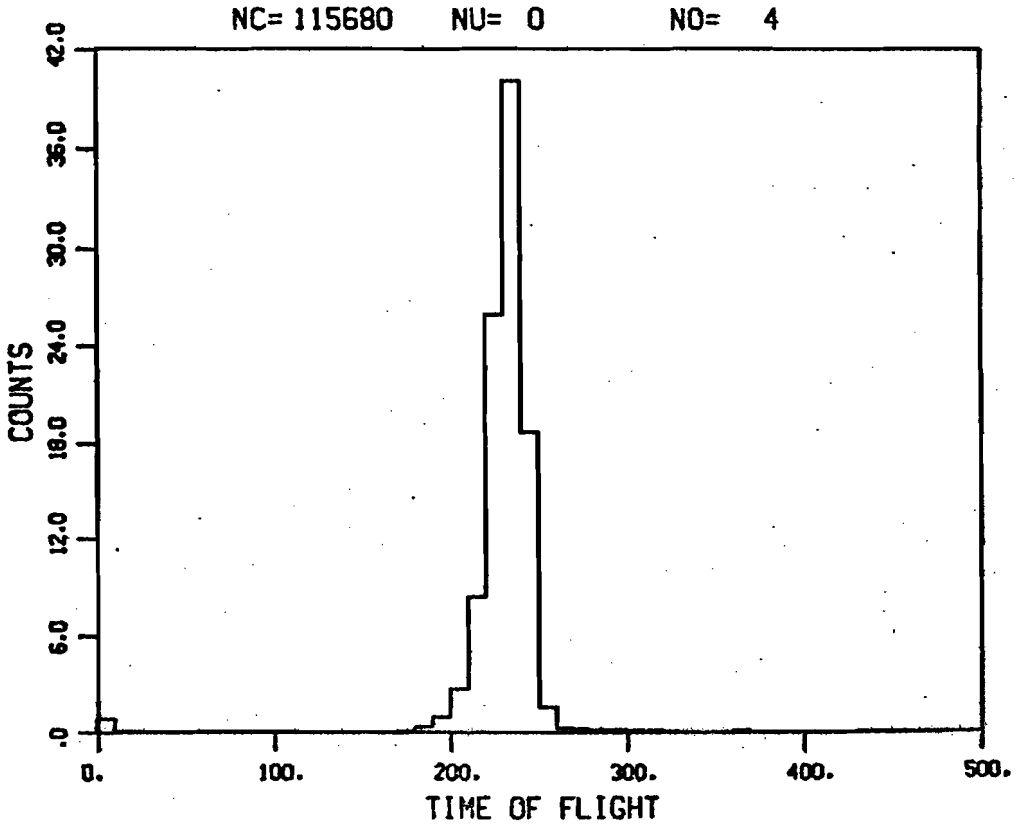

Figure III-14

T = -.8

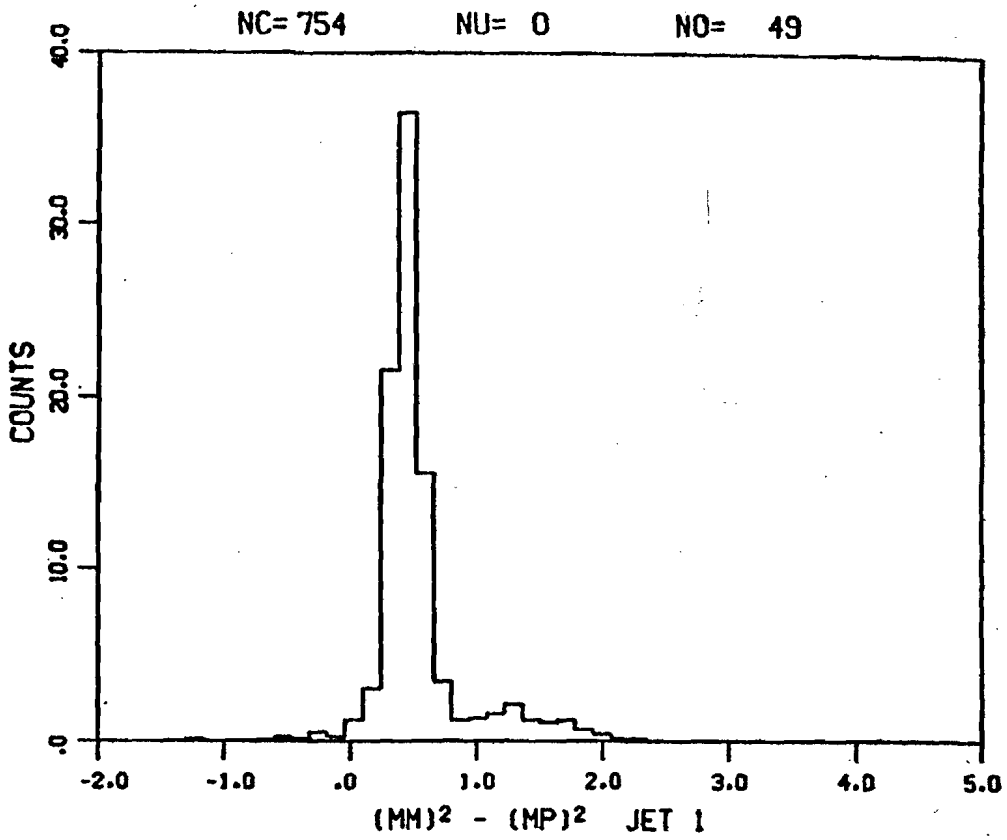

Figure III-15

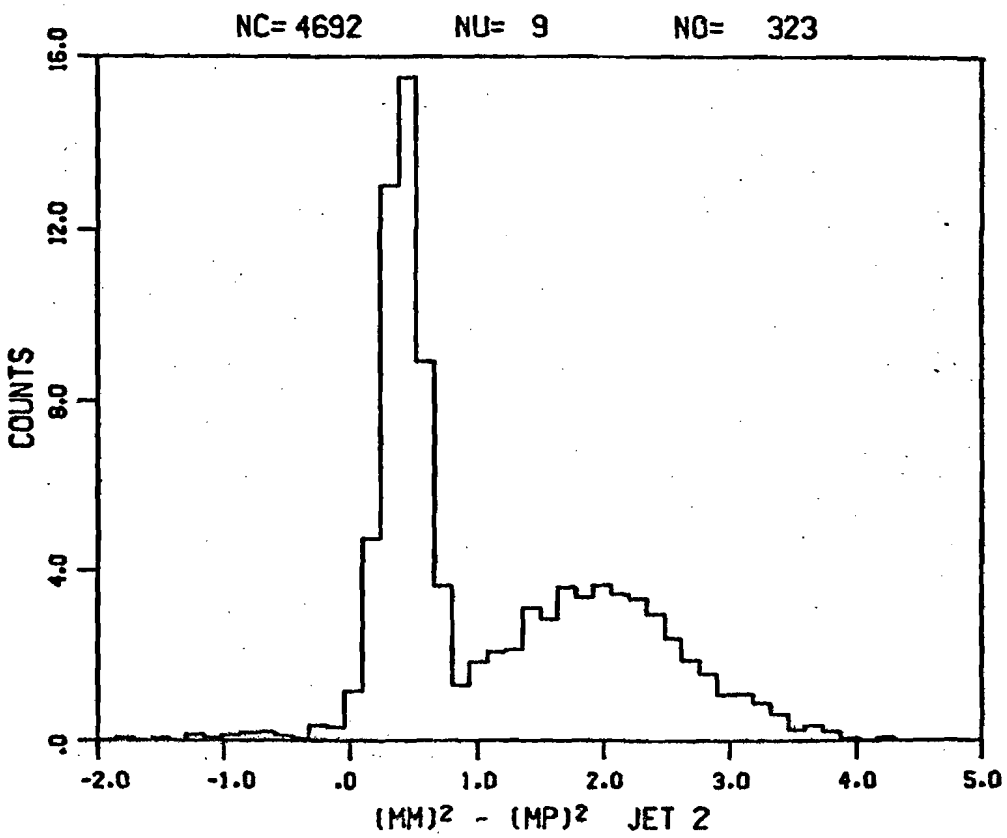

Figure III-16

T = -.8

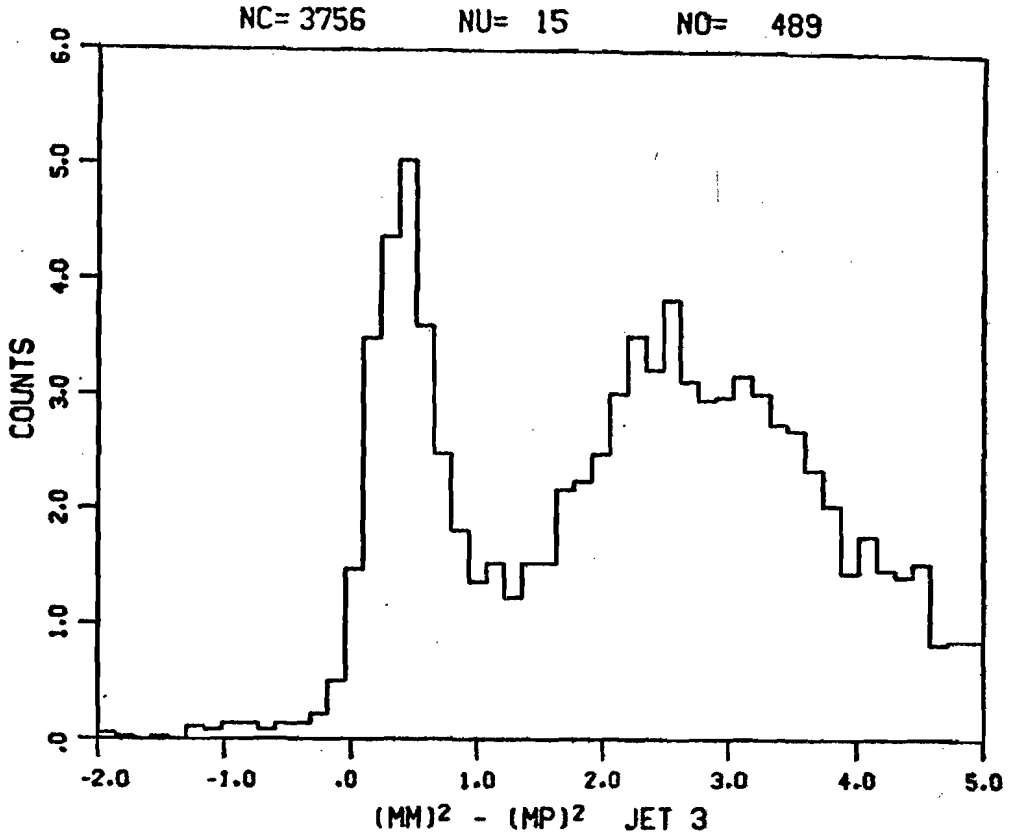

Figure III-17

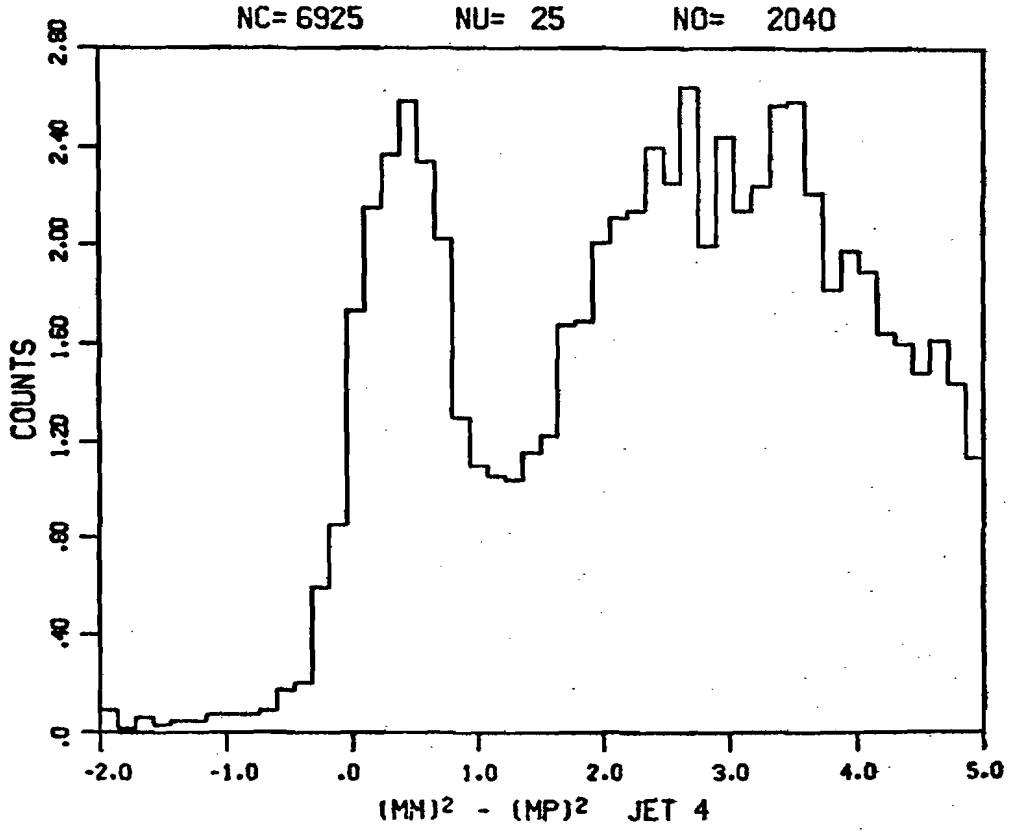

Figure III-18

T = -.8

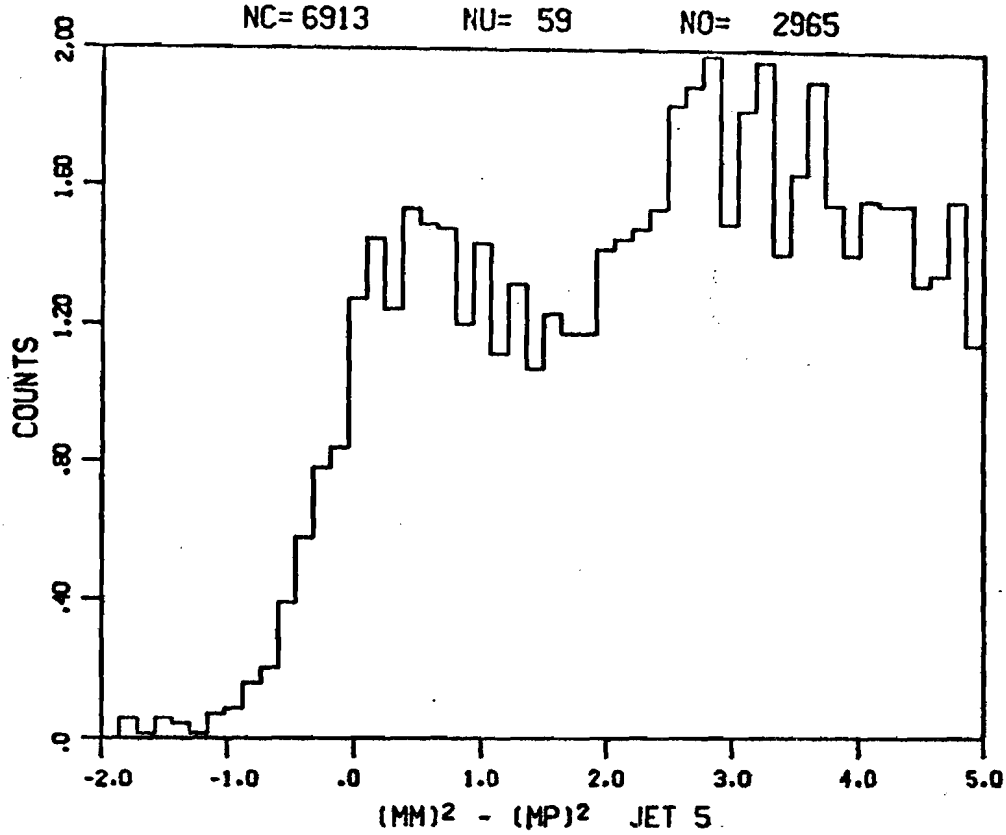

Figure III-19

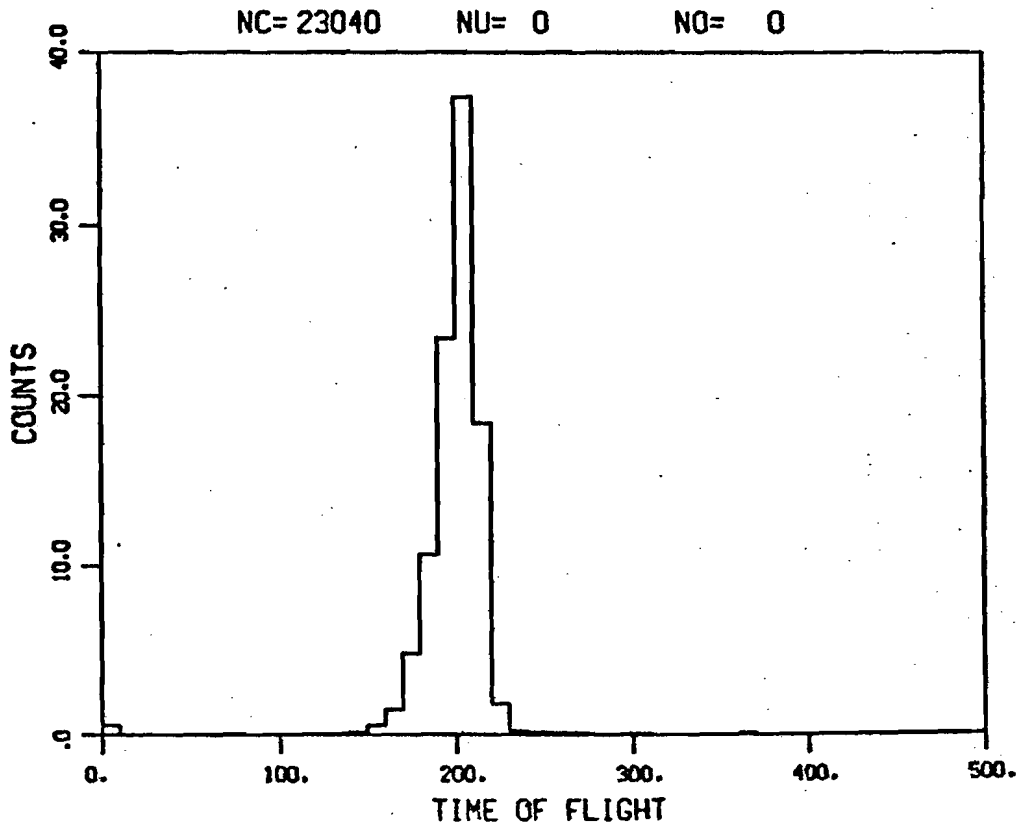

Figure III-20

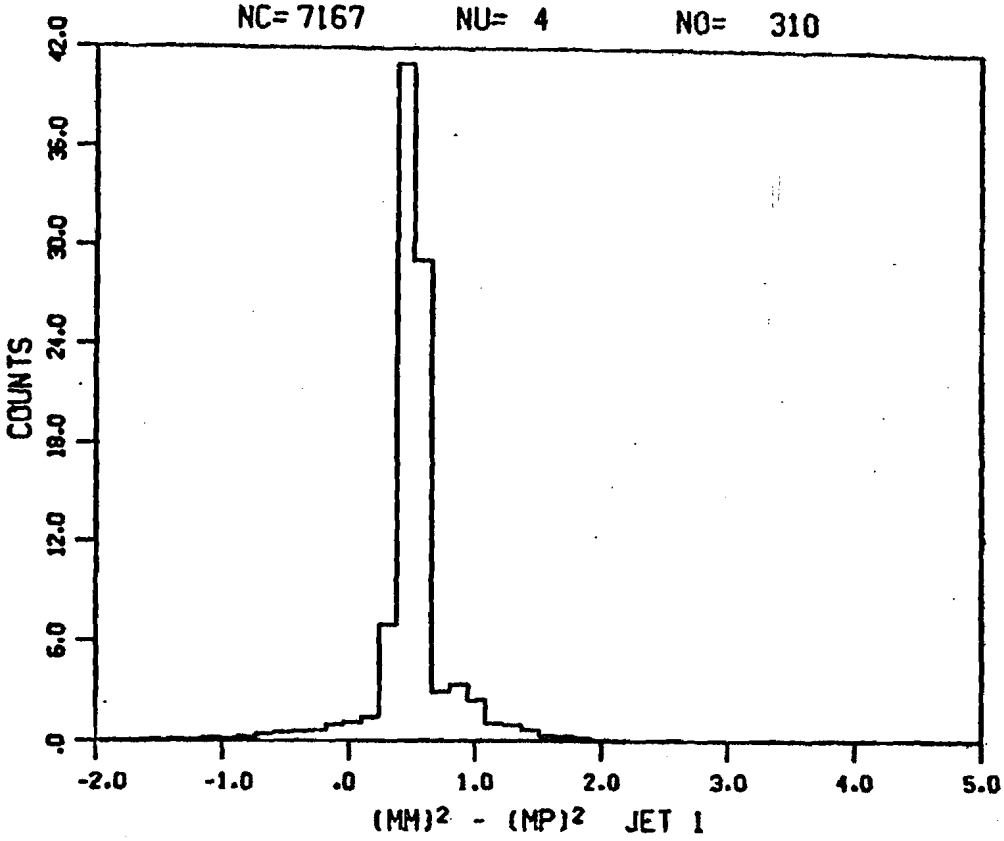

Figure III-21

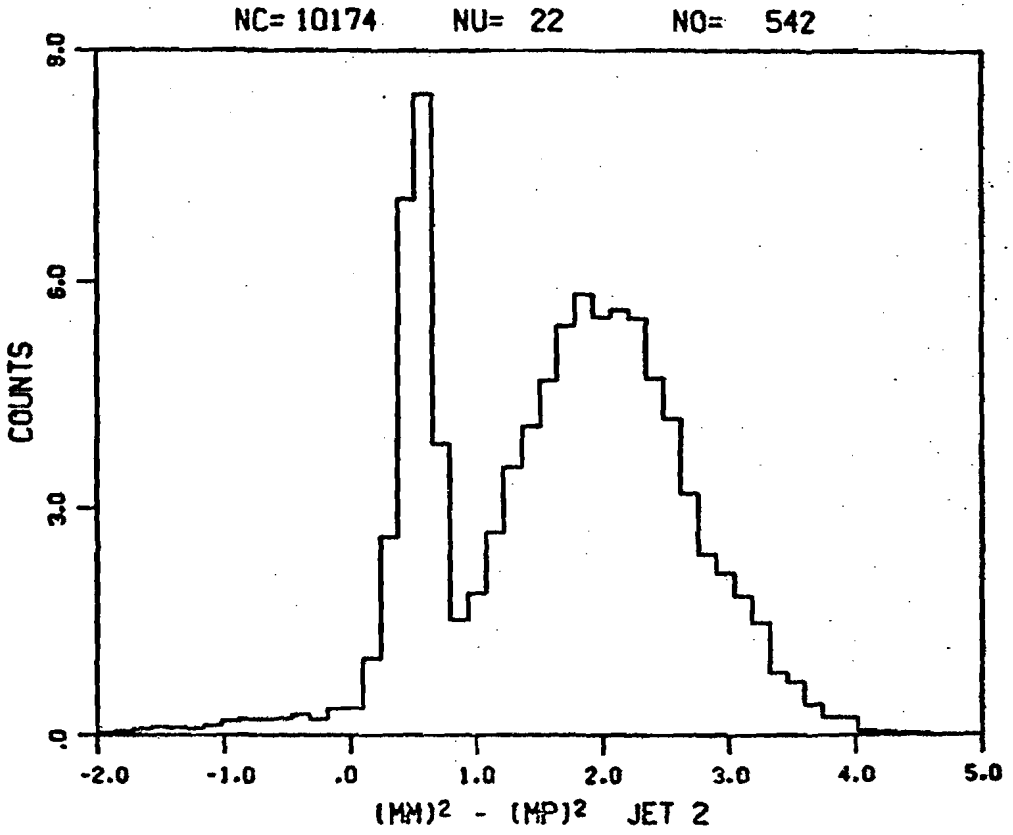

Figure III-22

T = -1.0

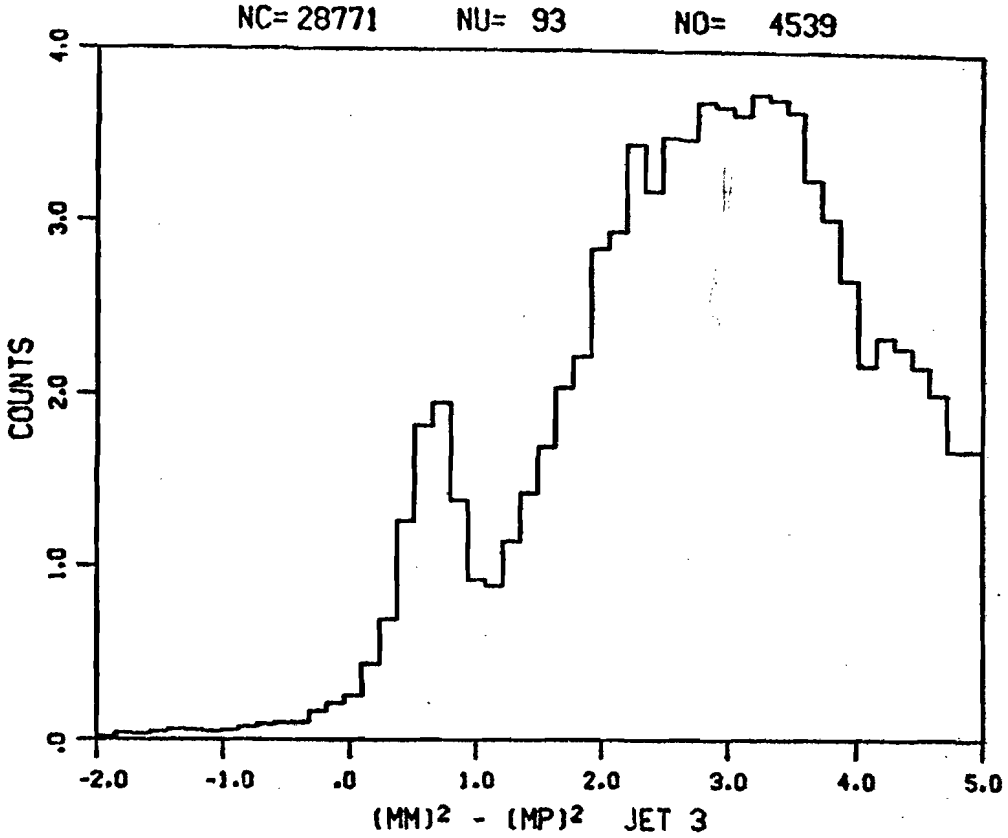

Figure III-23

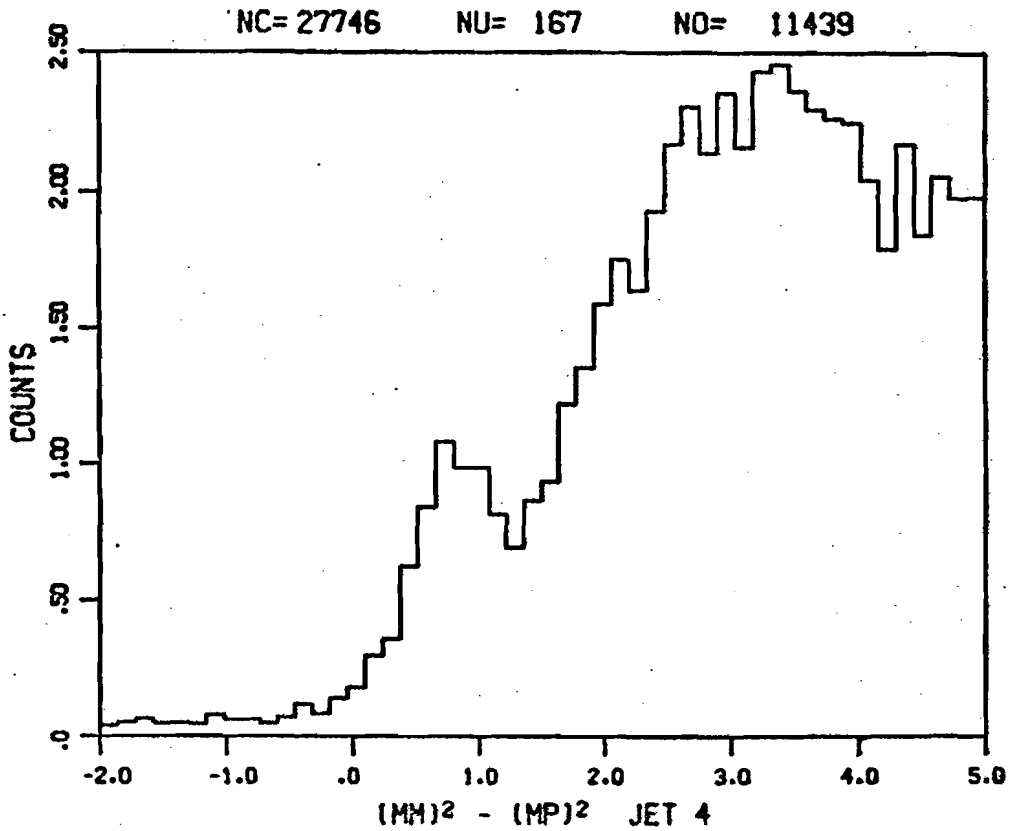

Figure III-24

T = -1.0

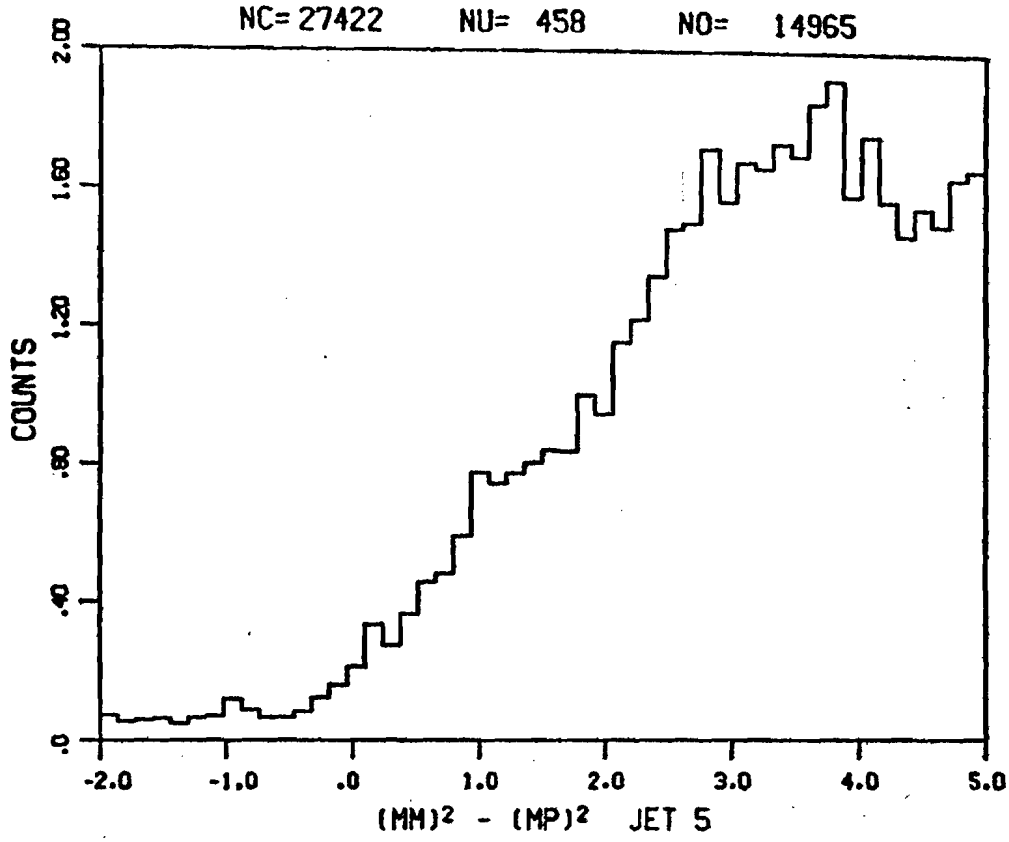

Figure III-25

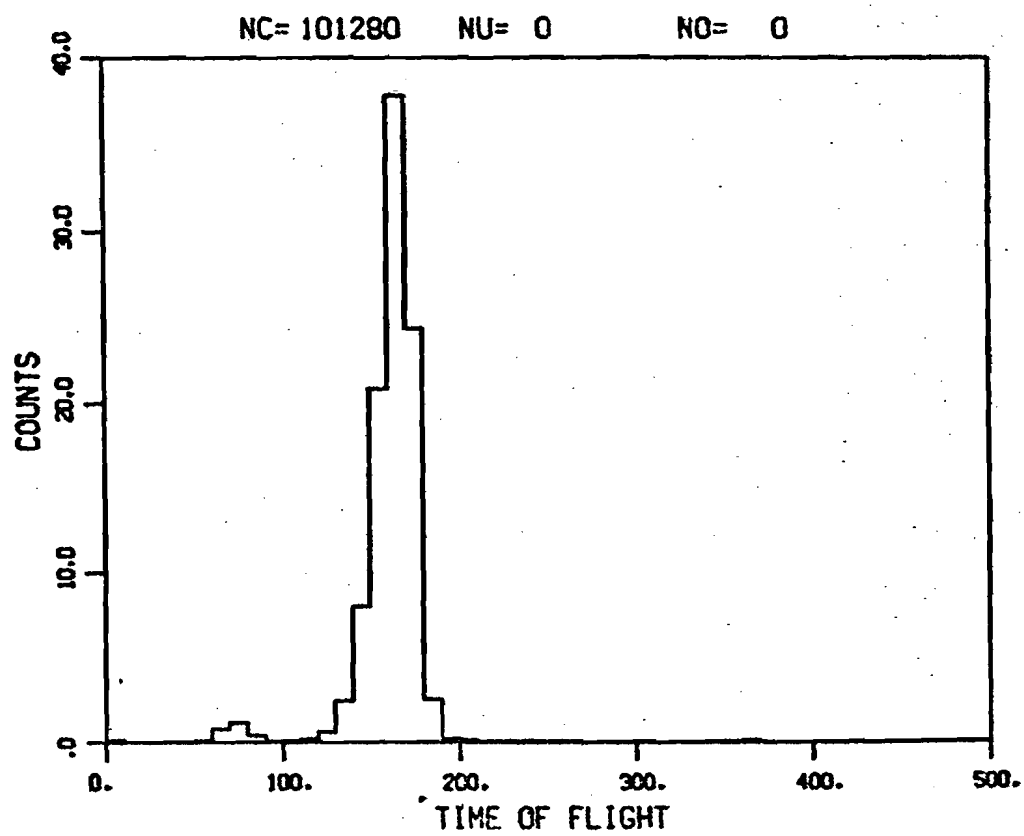

Figure III-26

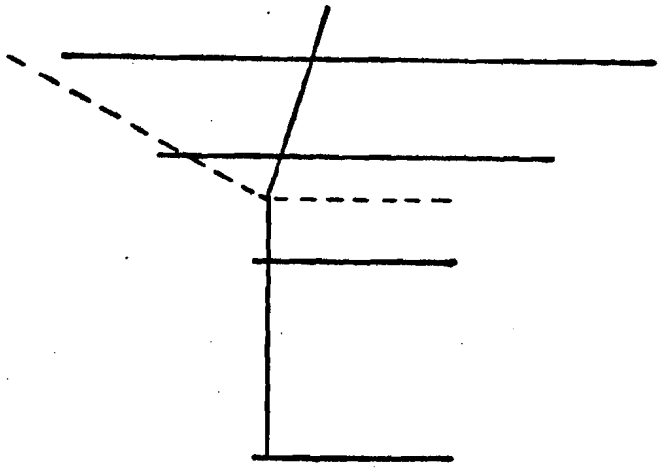

Figure III-27a

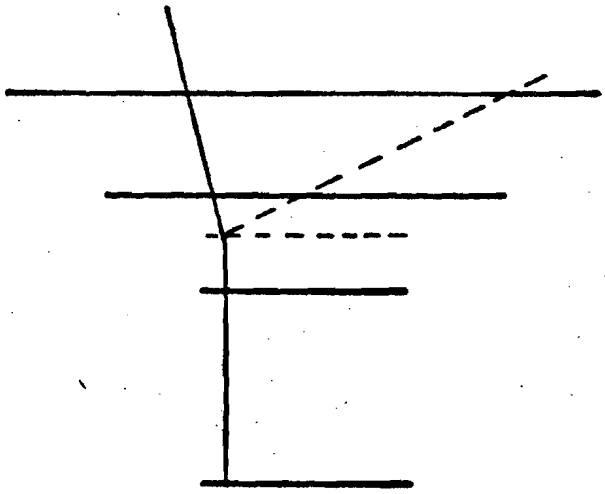

Figure III-27b

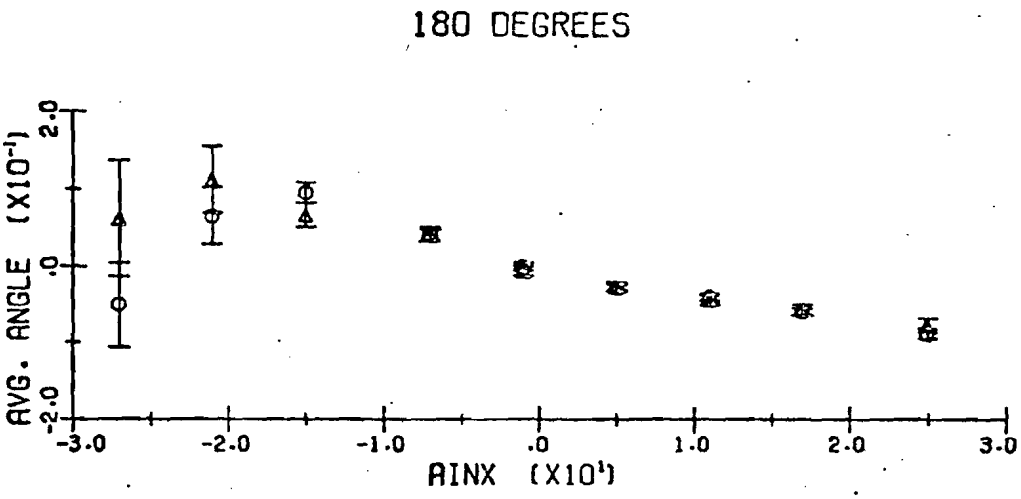

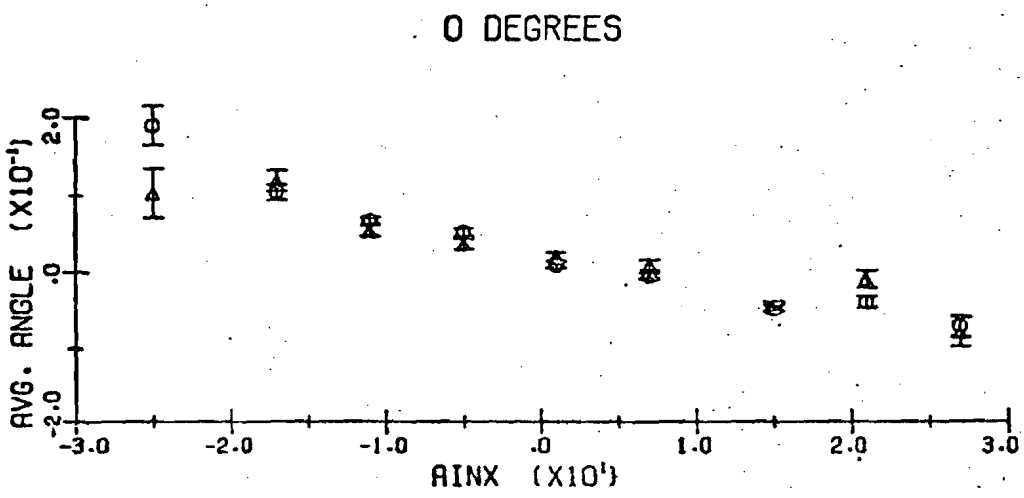

Figure III-28

T = -.3

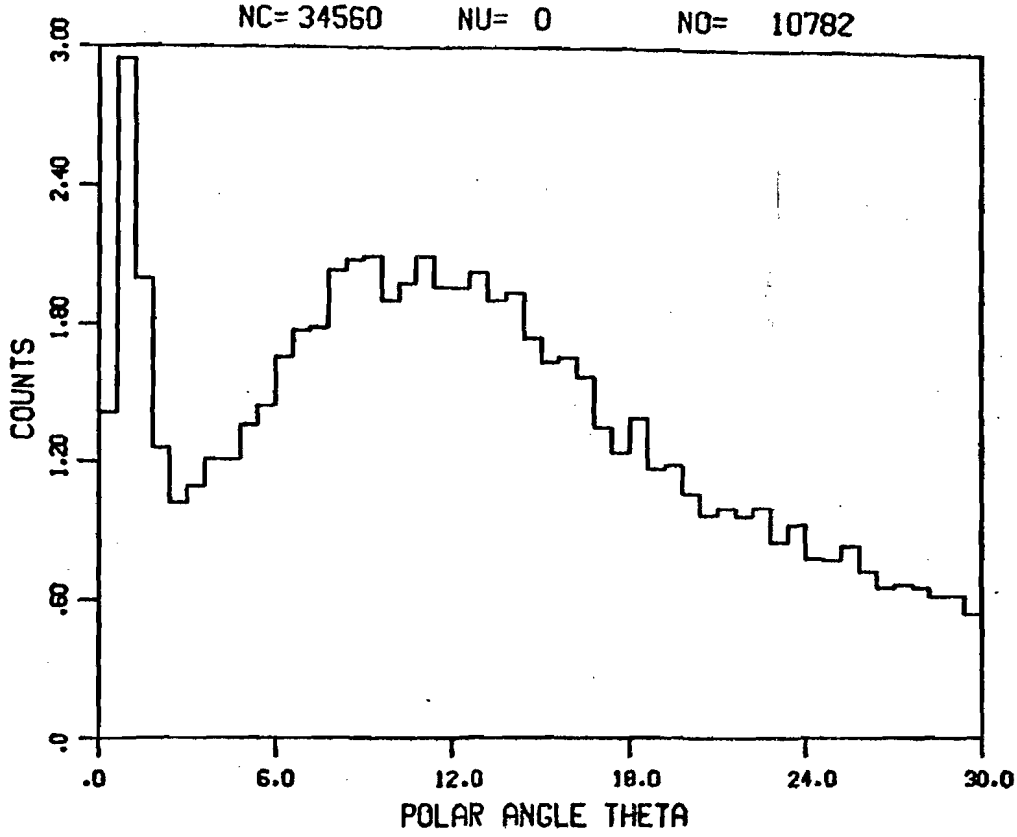

Figure III-29

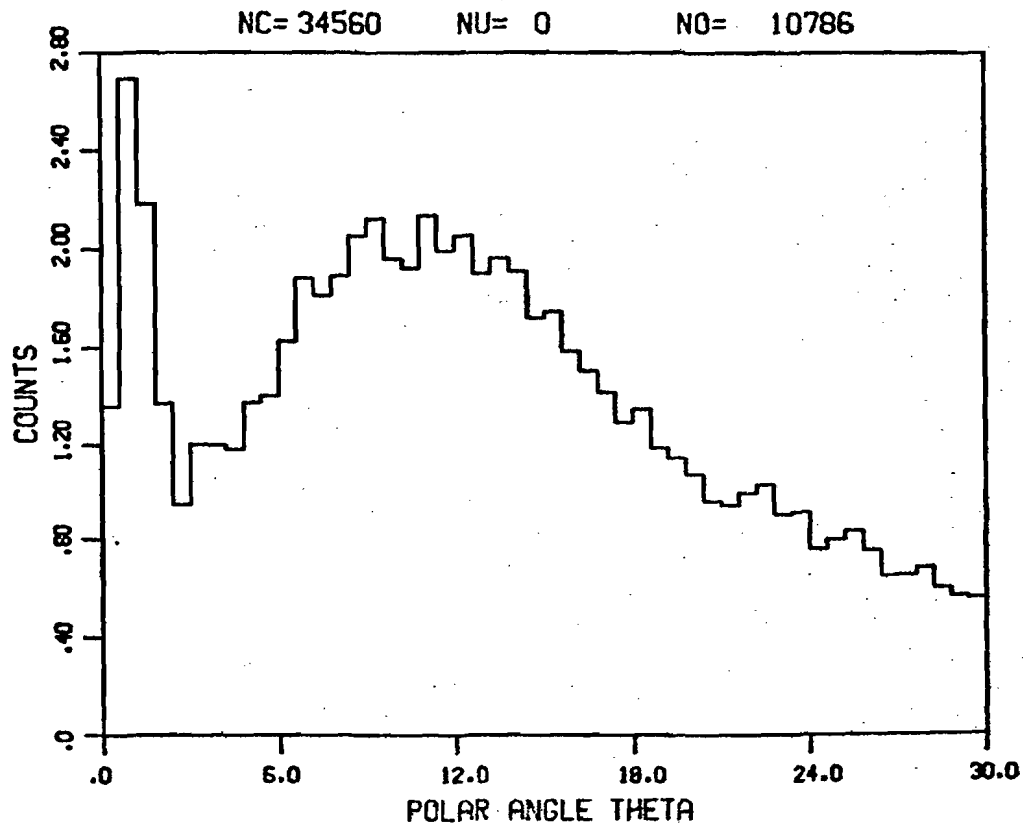

Figure III-30

T = -.3

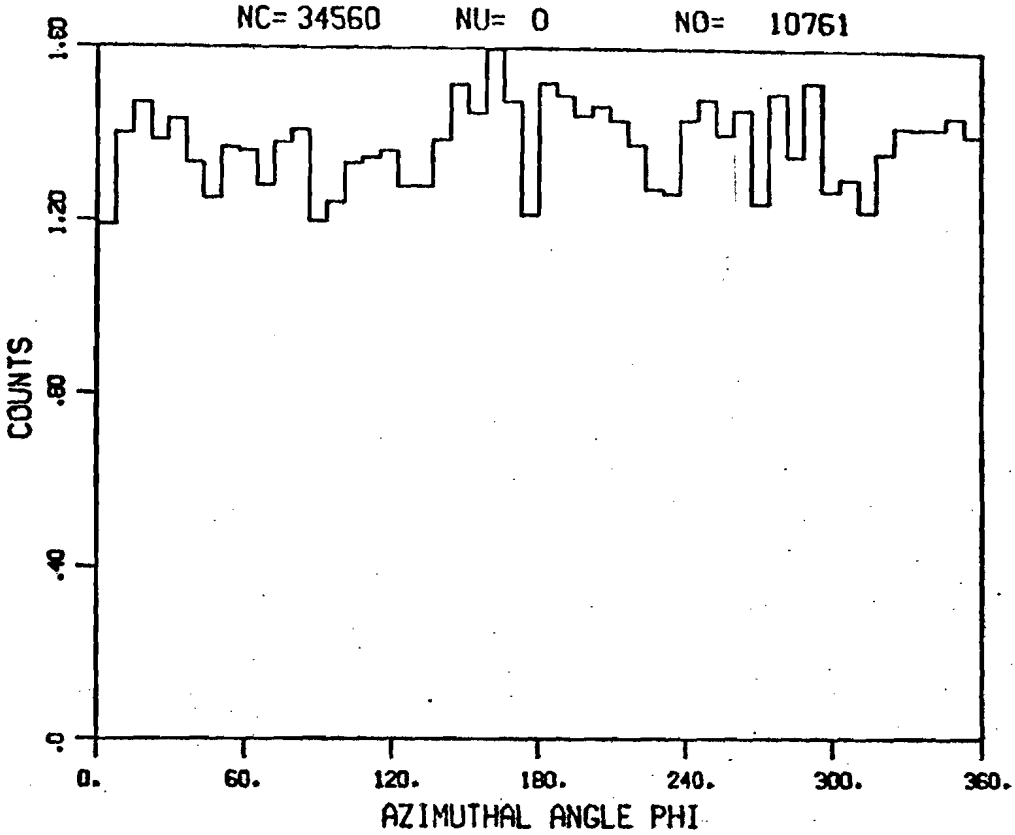

Figure III-31

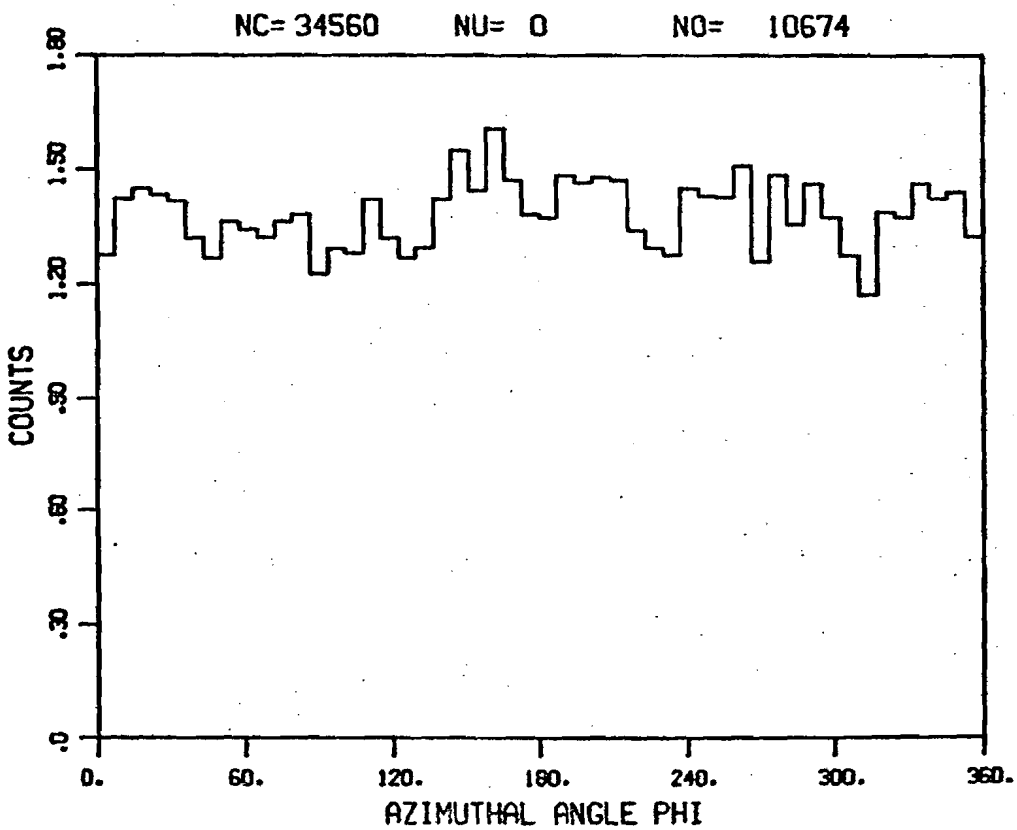

Figure III-32

T = -.3

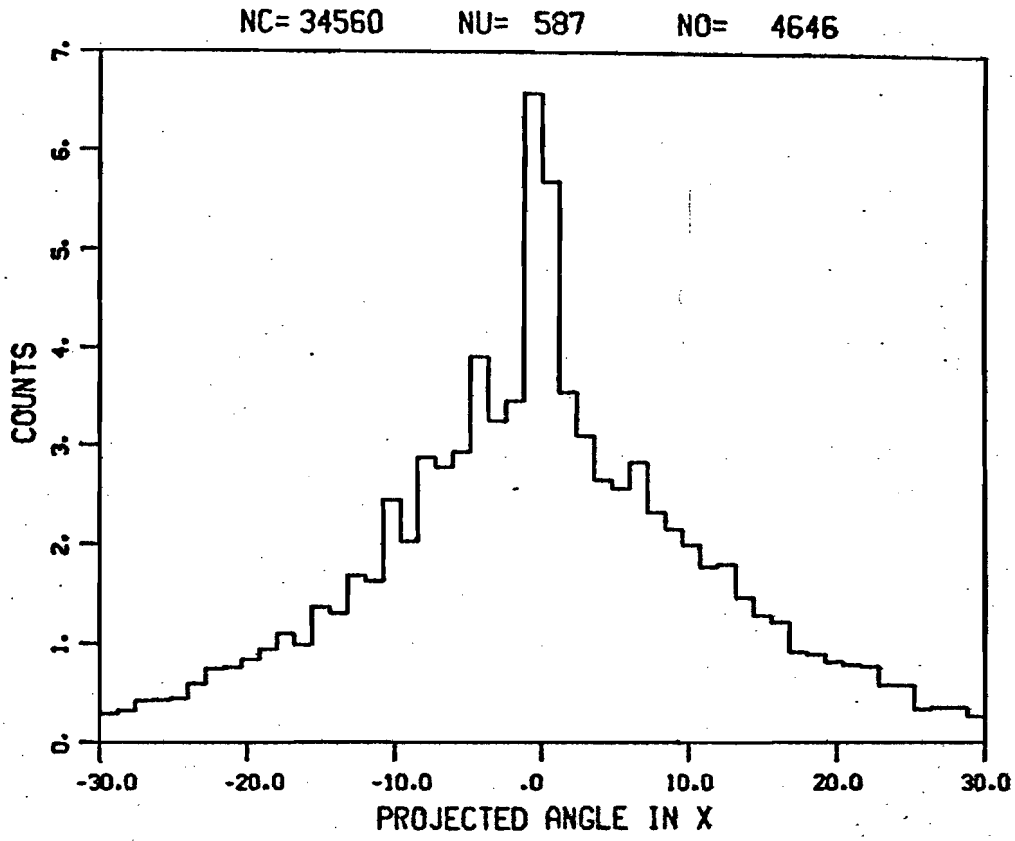

Figure III-33

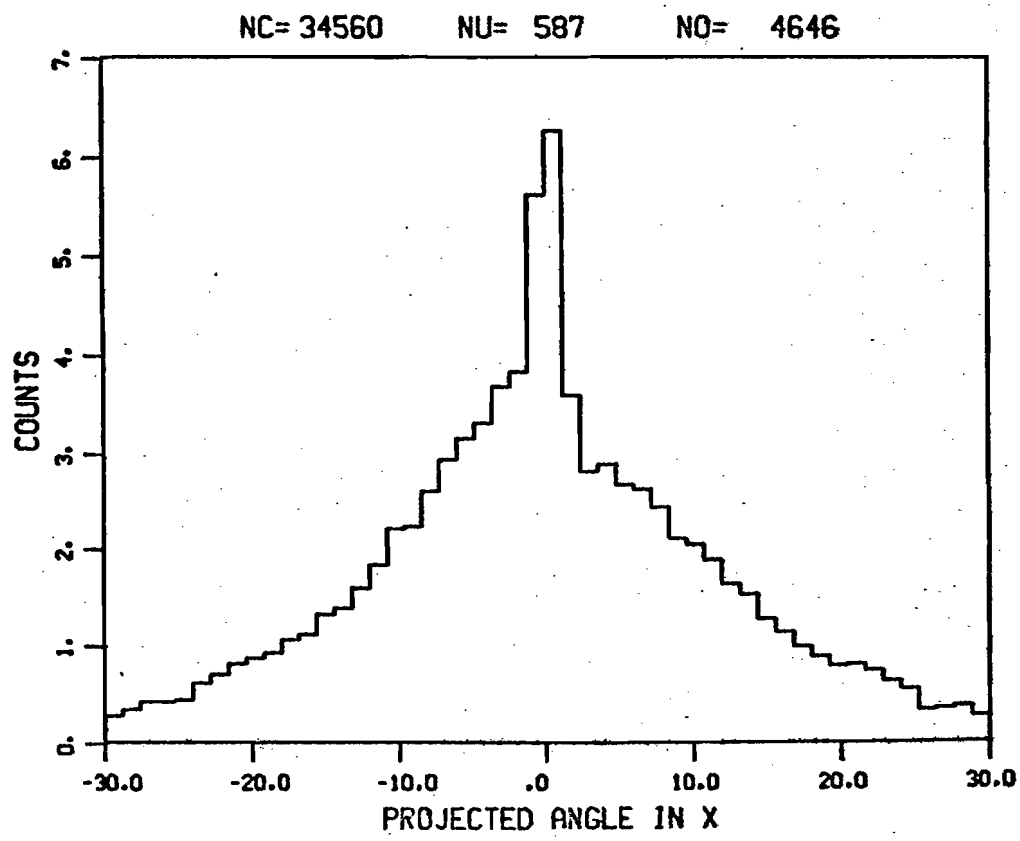

Figure III-34

T = -.3

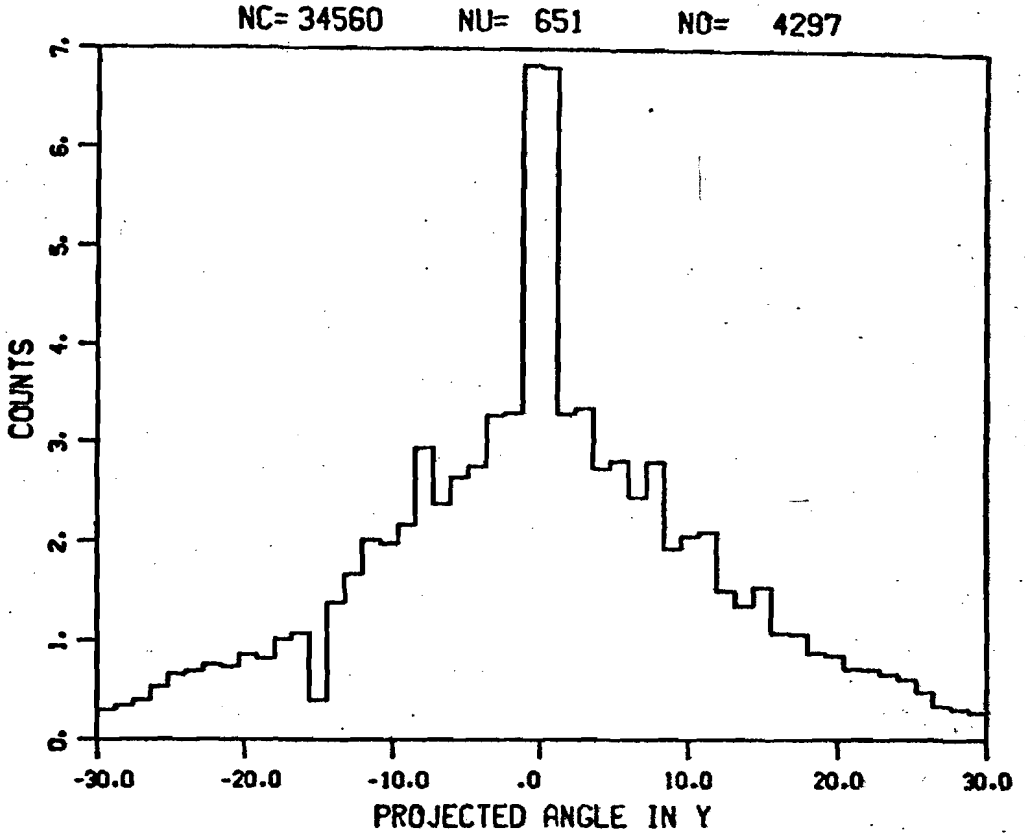

Figure III-35

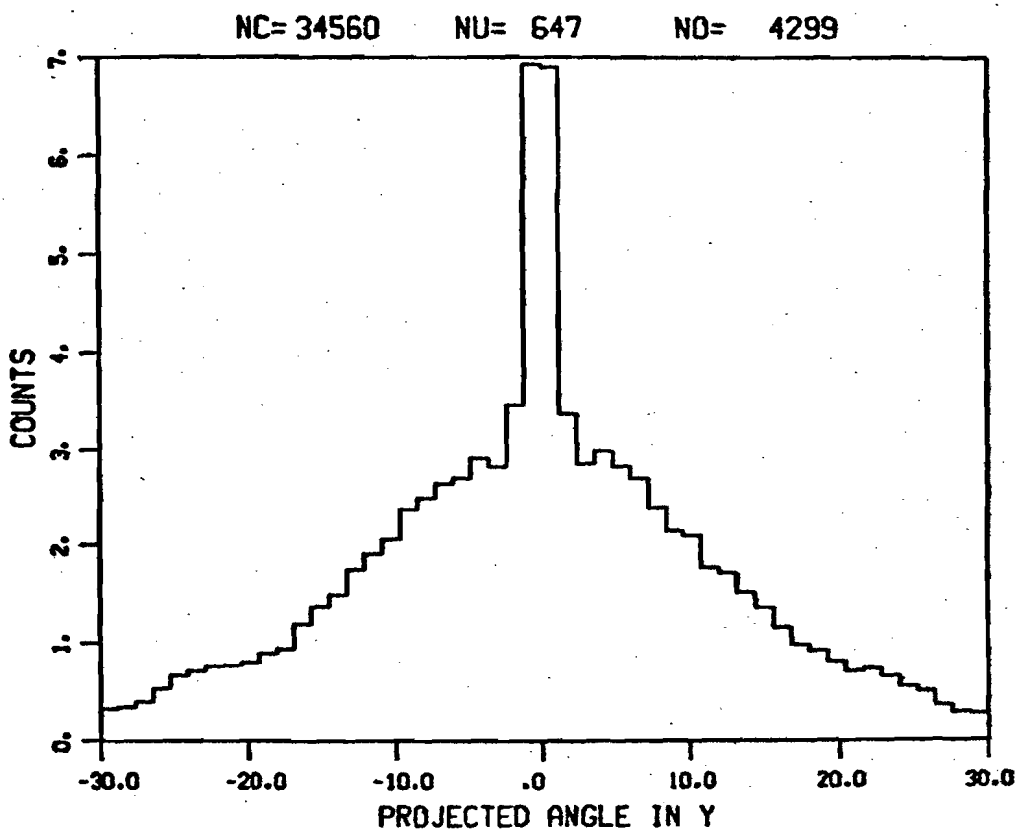

Figure III-36

T = -.3

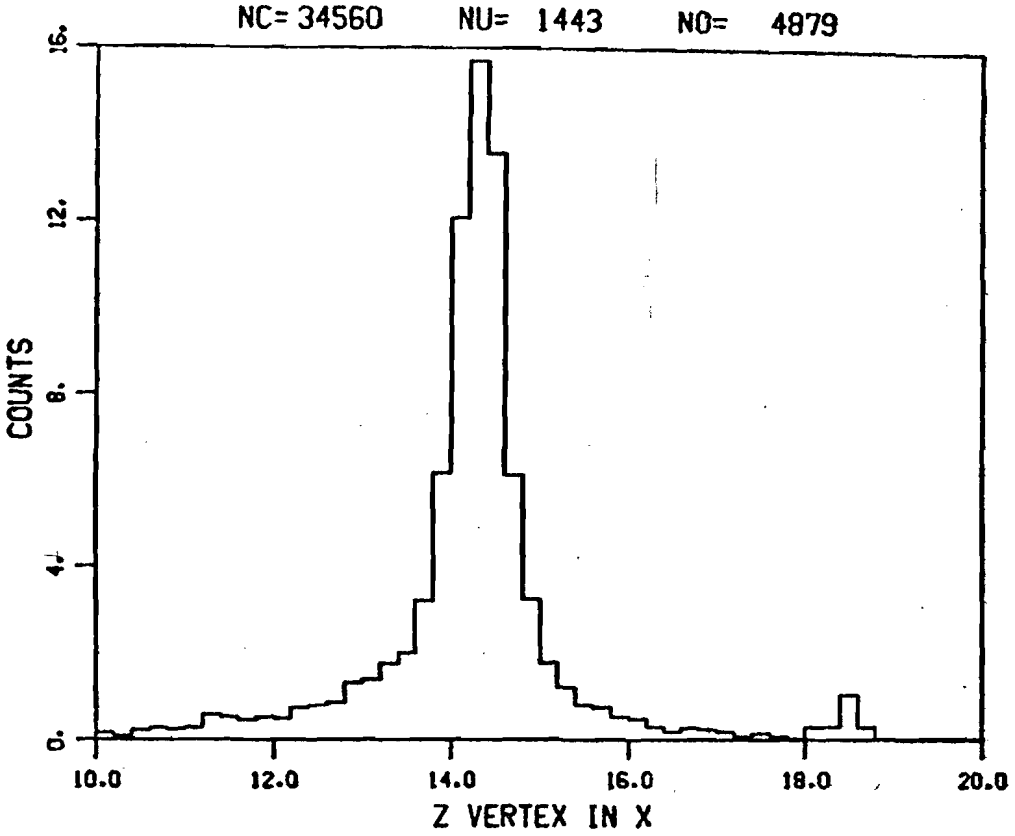

Figure III-37

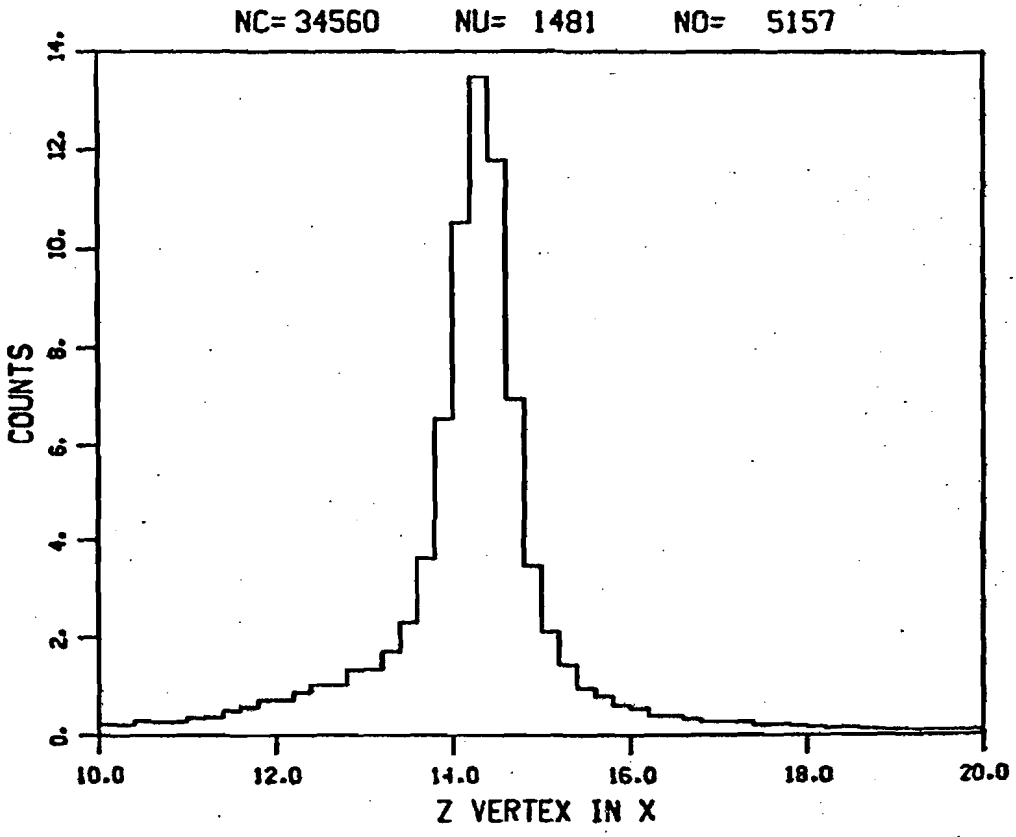

Figure III-38

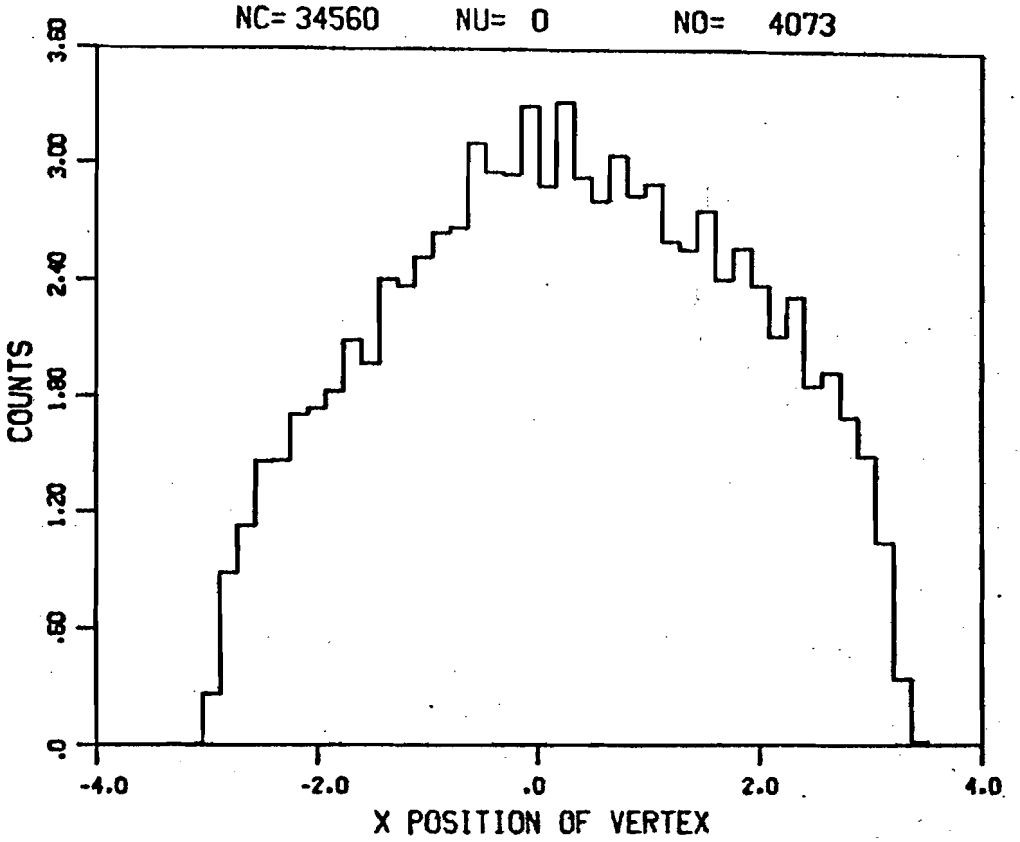

Figure III-39

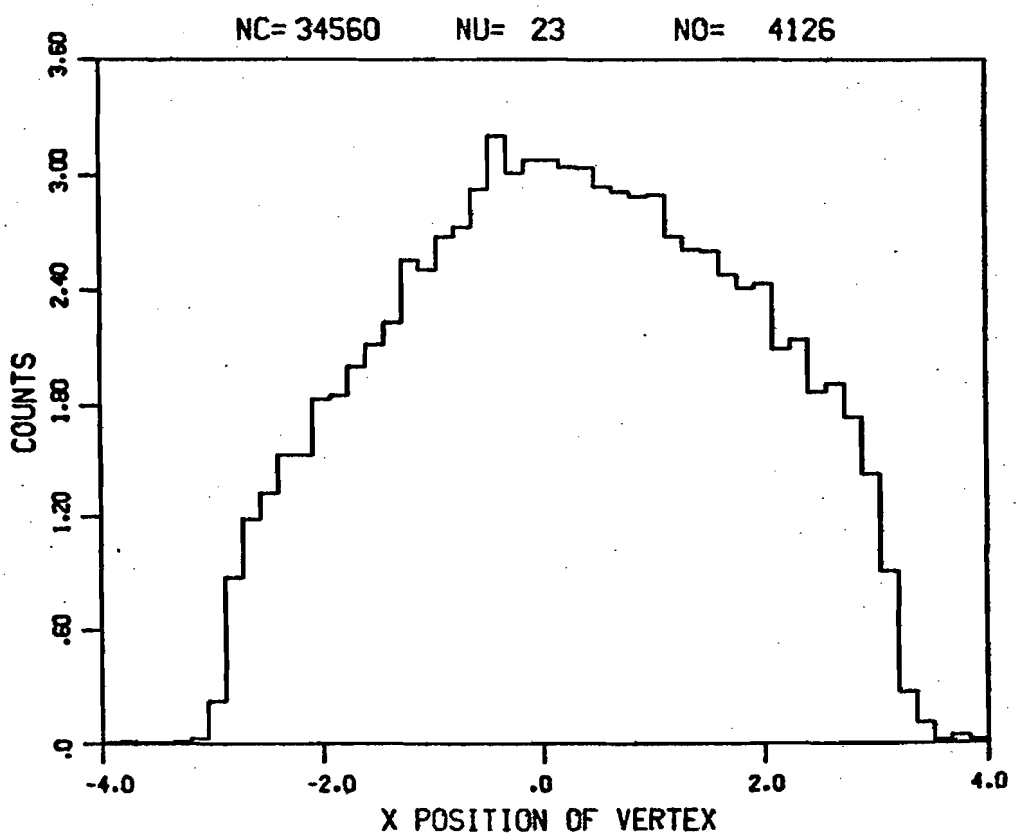

Figure III-40

T = -.3

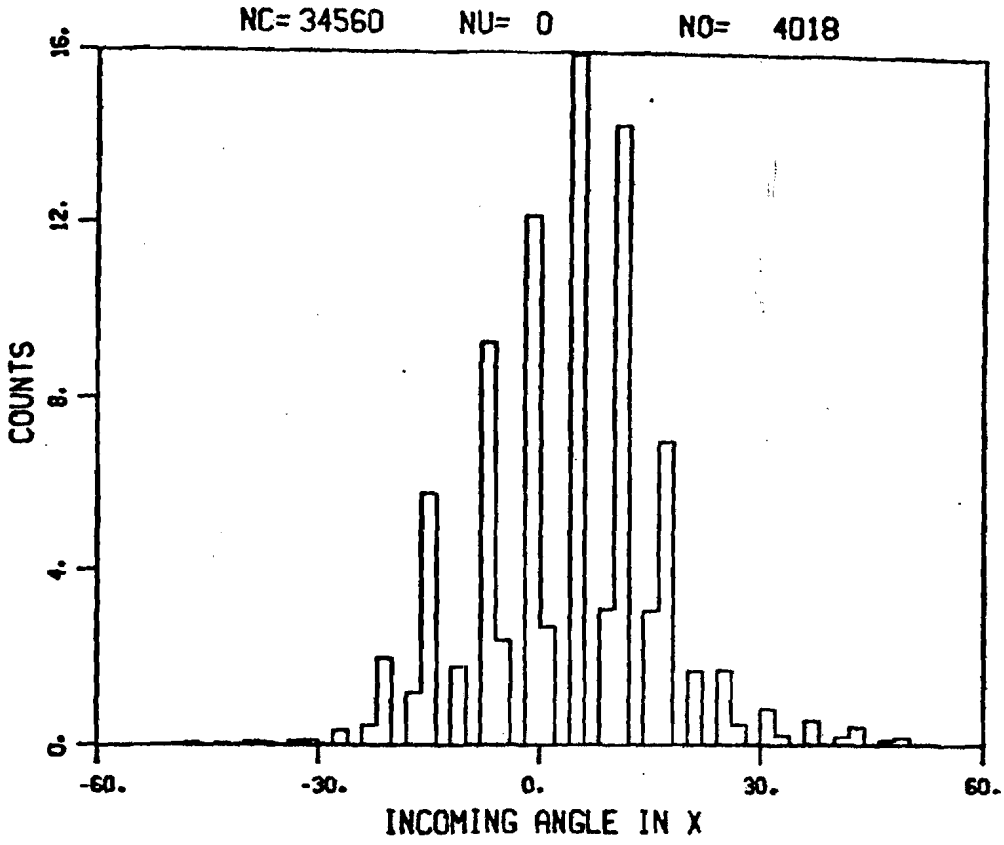

Figure III-41

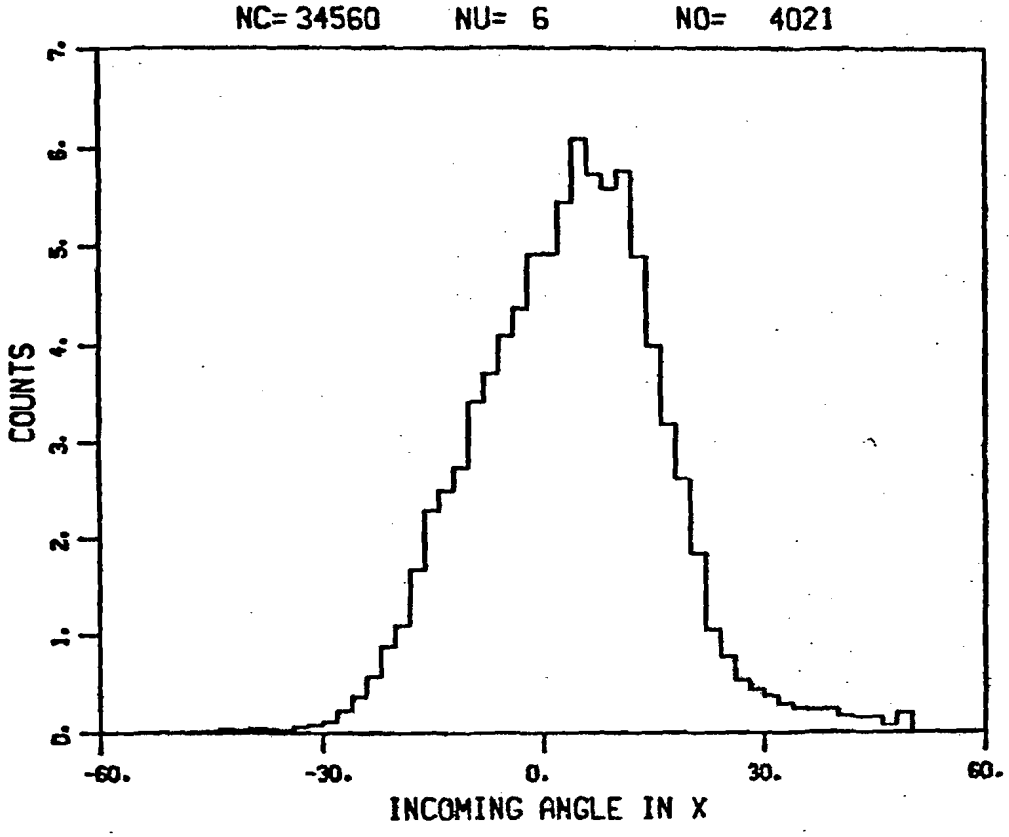

Figure III-42

T = -.3

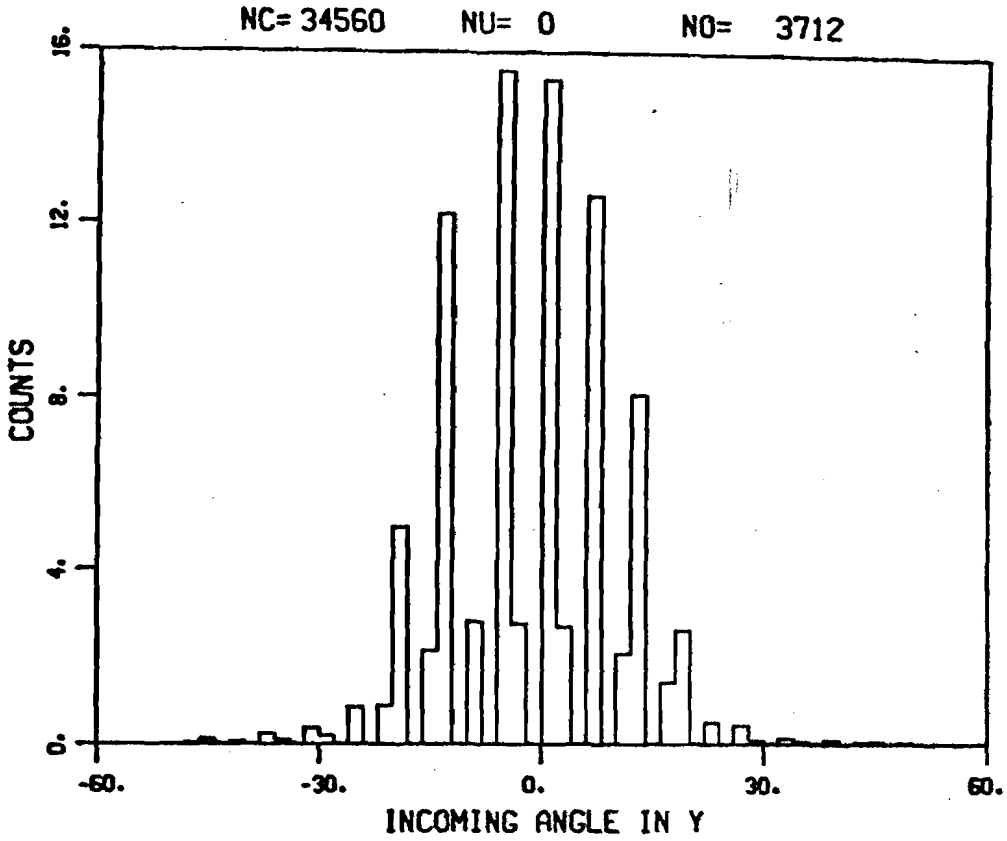

Figure III-43

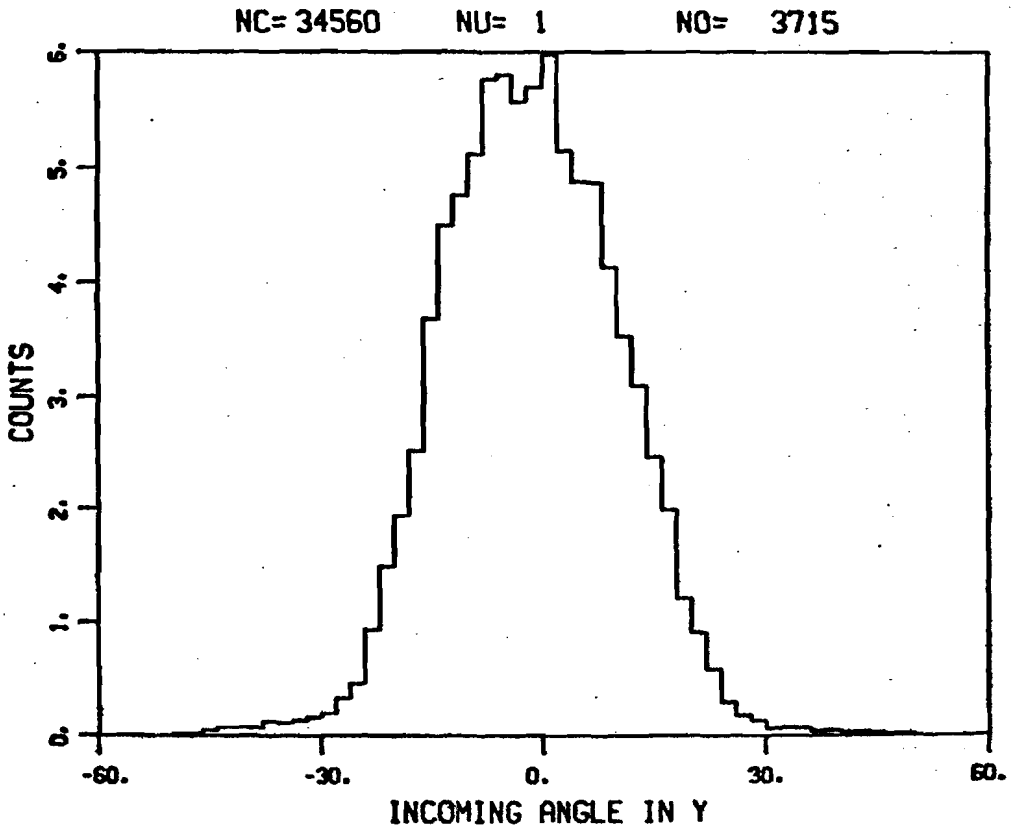

Figure III-44

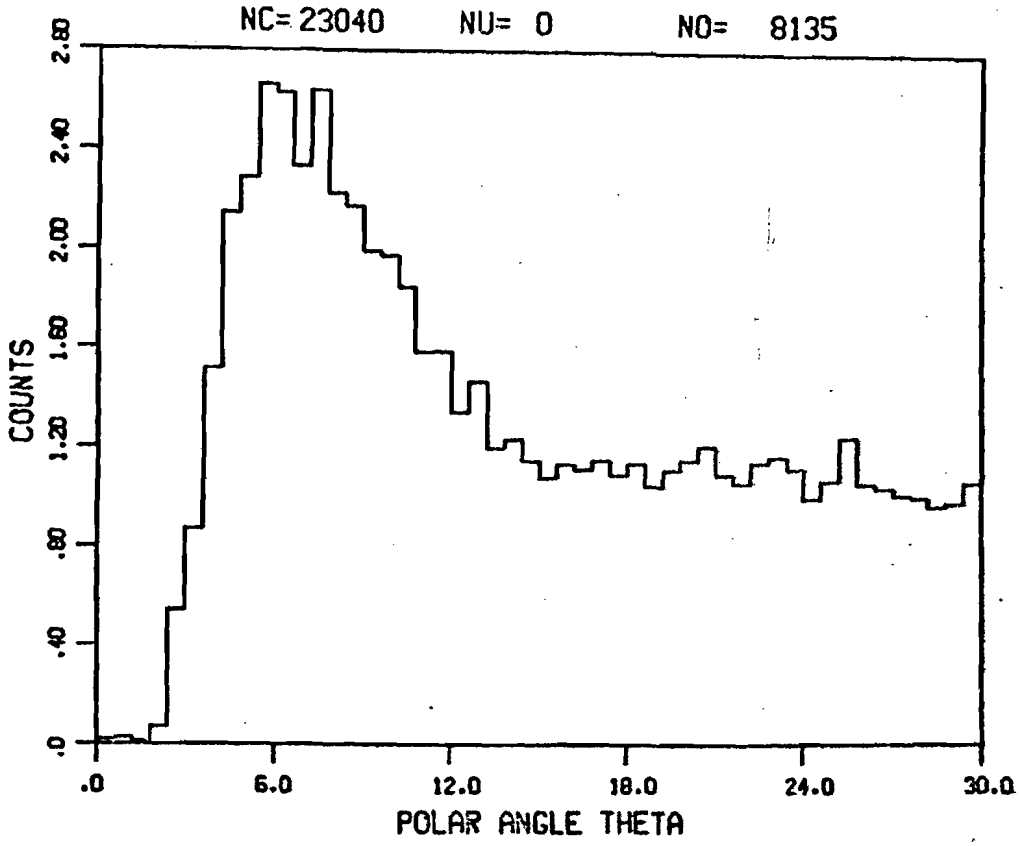

Figure III-45

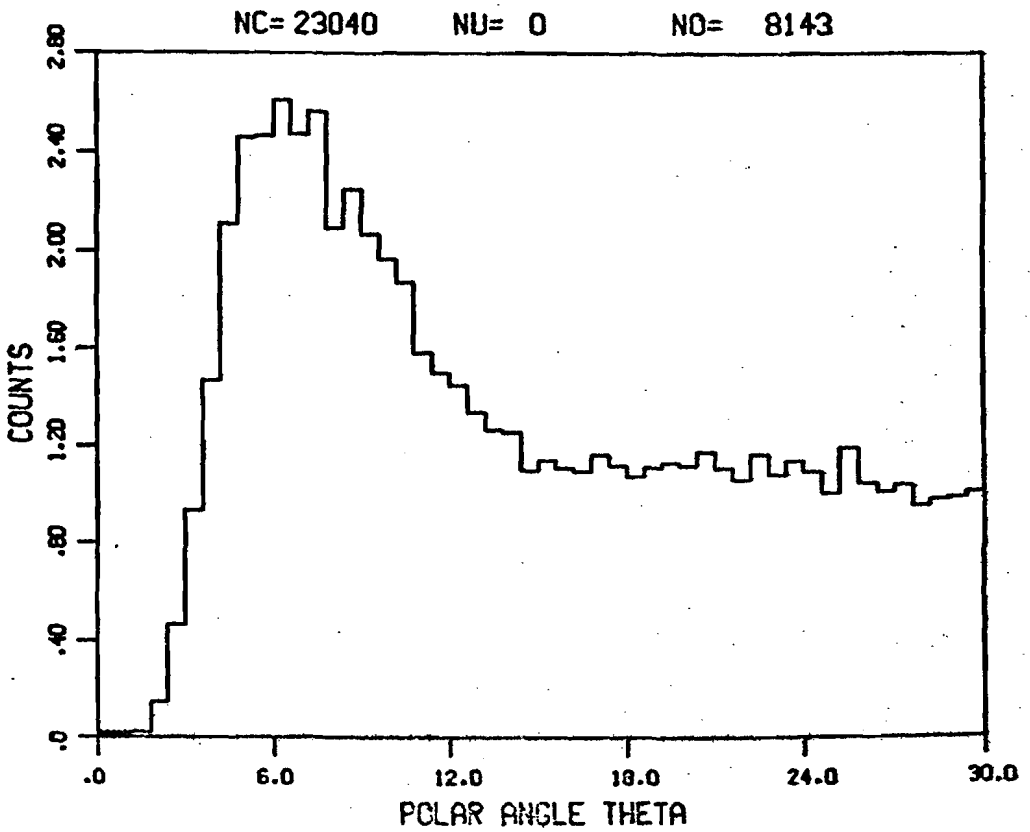

Figure III-46

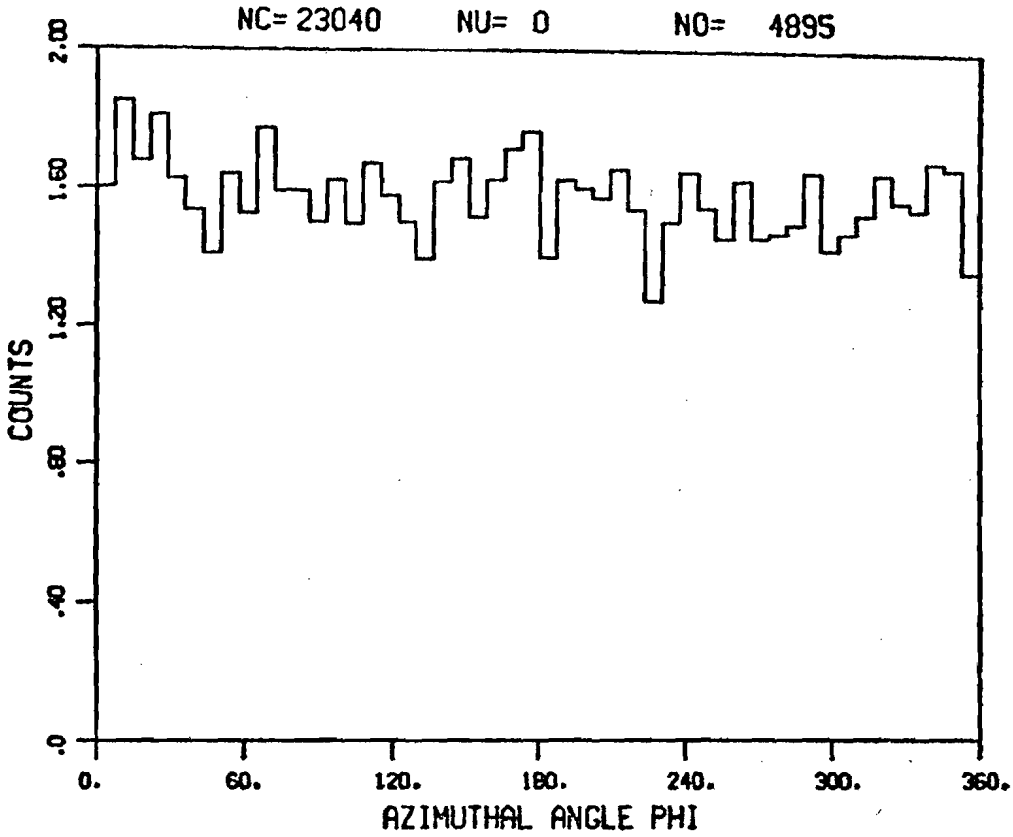

Figure III-47

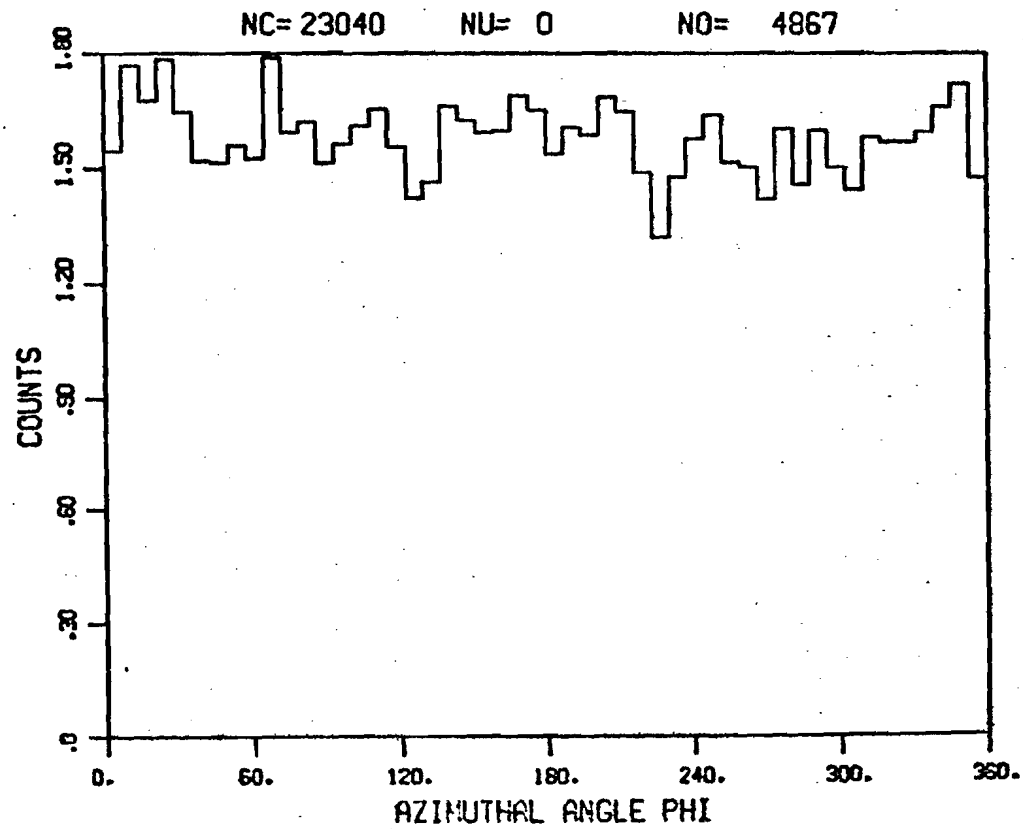

Figure III-48

T = -.8

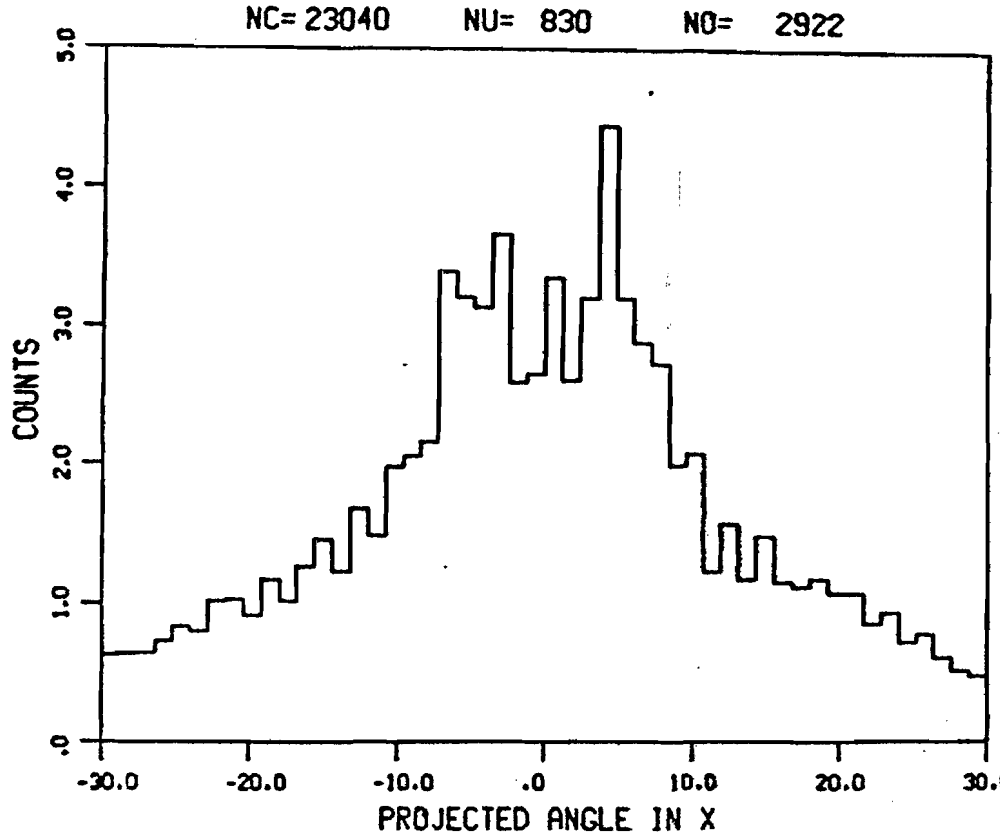

Figure III-49

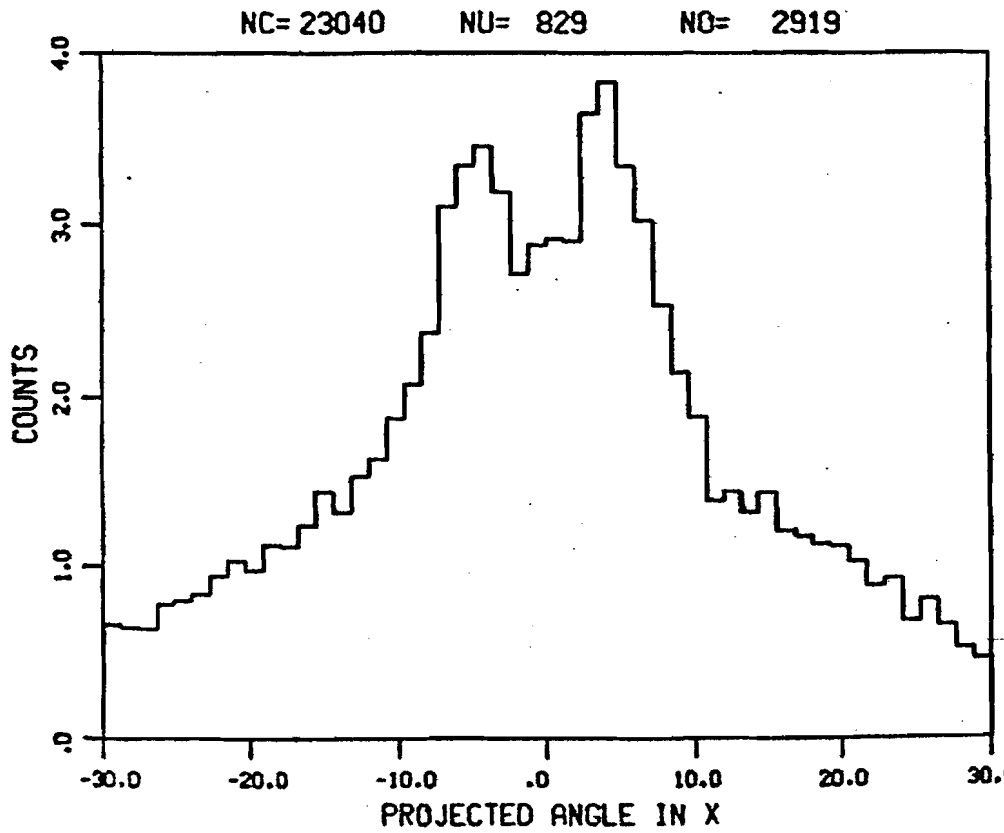

Figure III-50

T = -.8

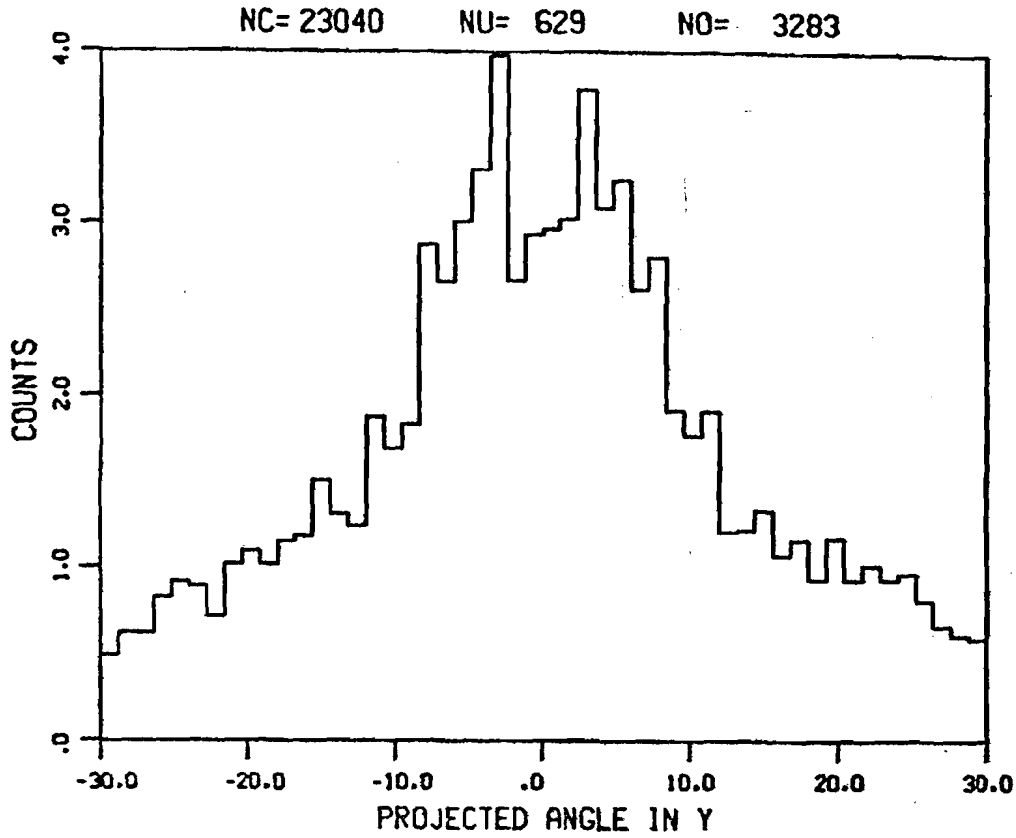

Figure III-51

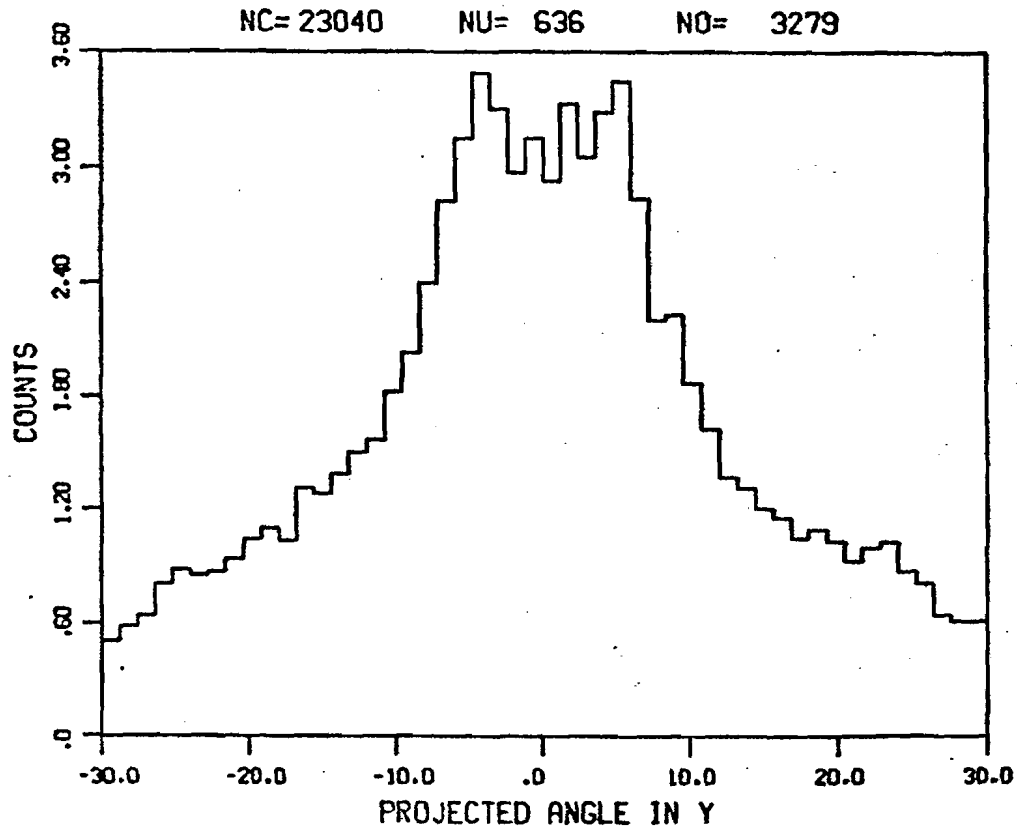

Figure III-52

T = -.8

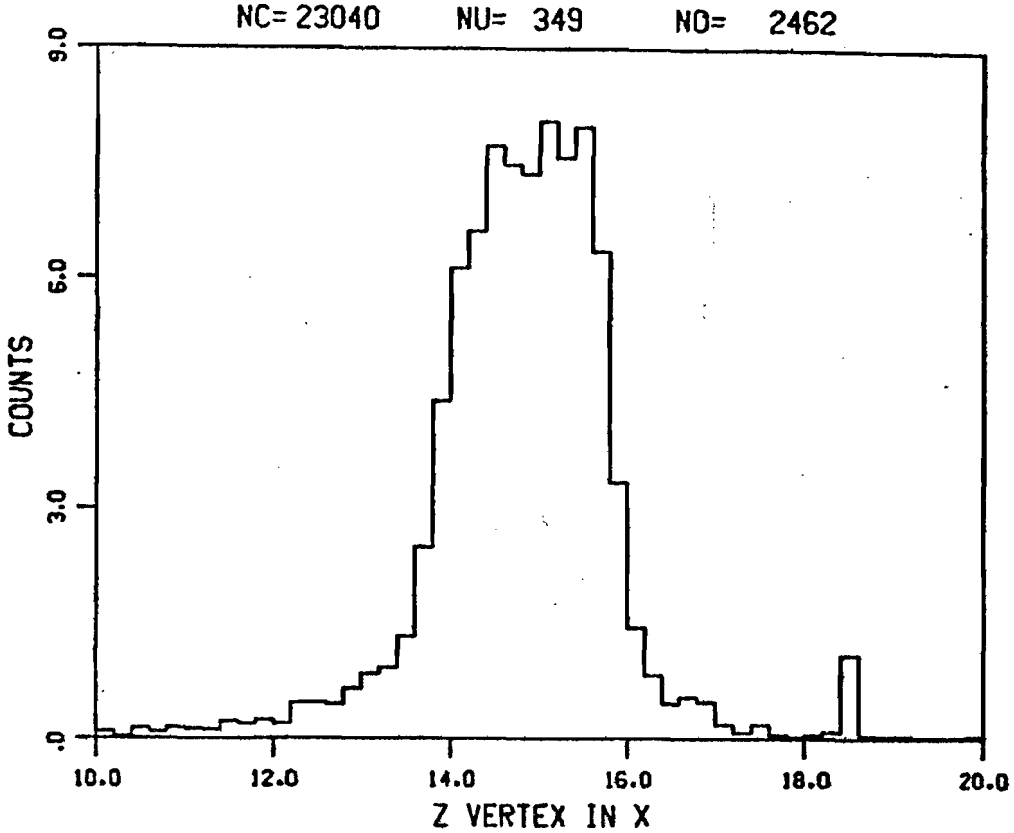

Figure III-53

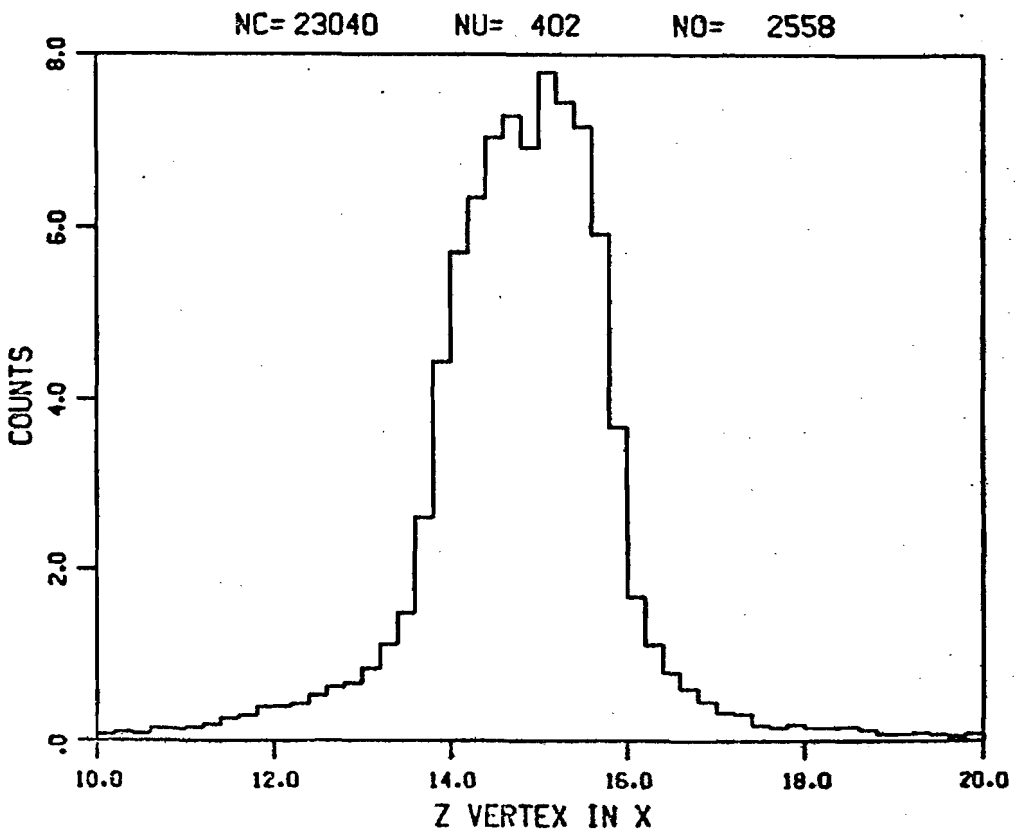

Figure III-54

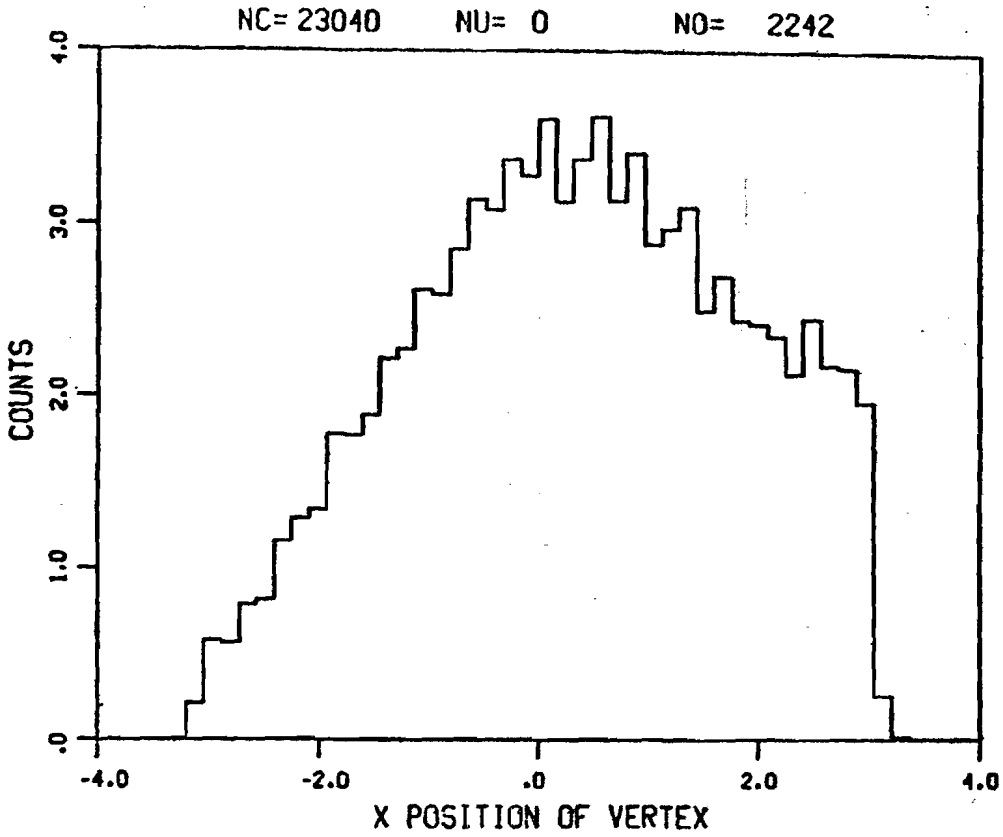

Figure III-55

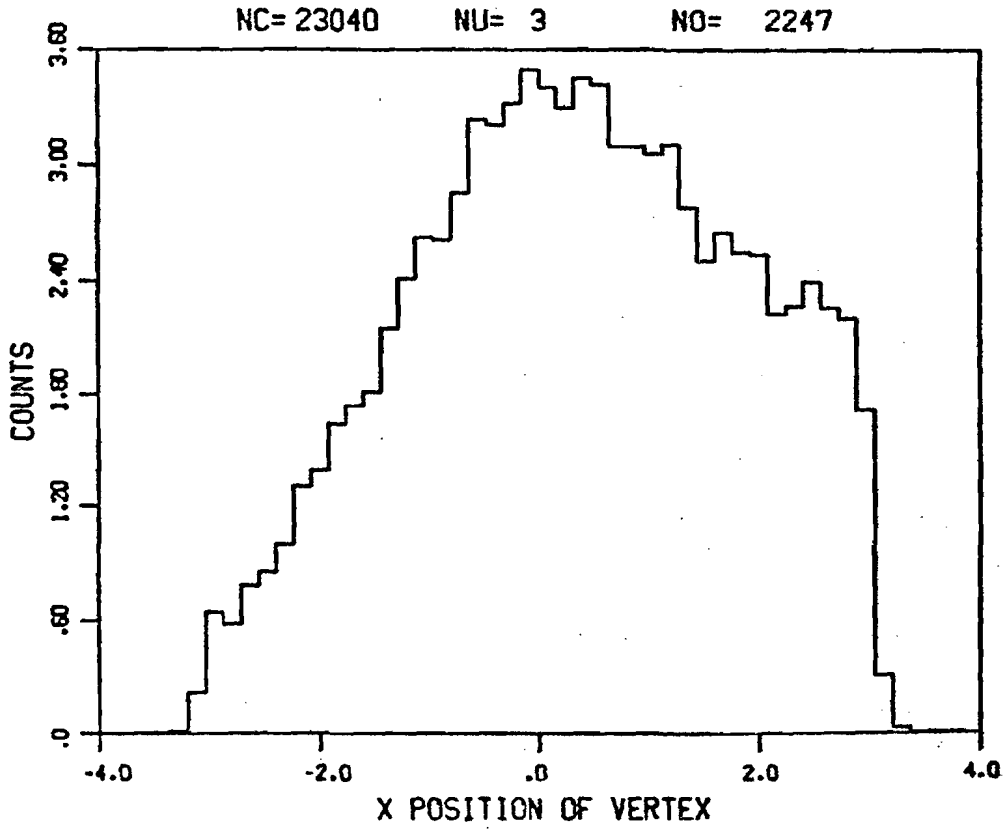

Figure III-56

T = -.8

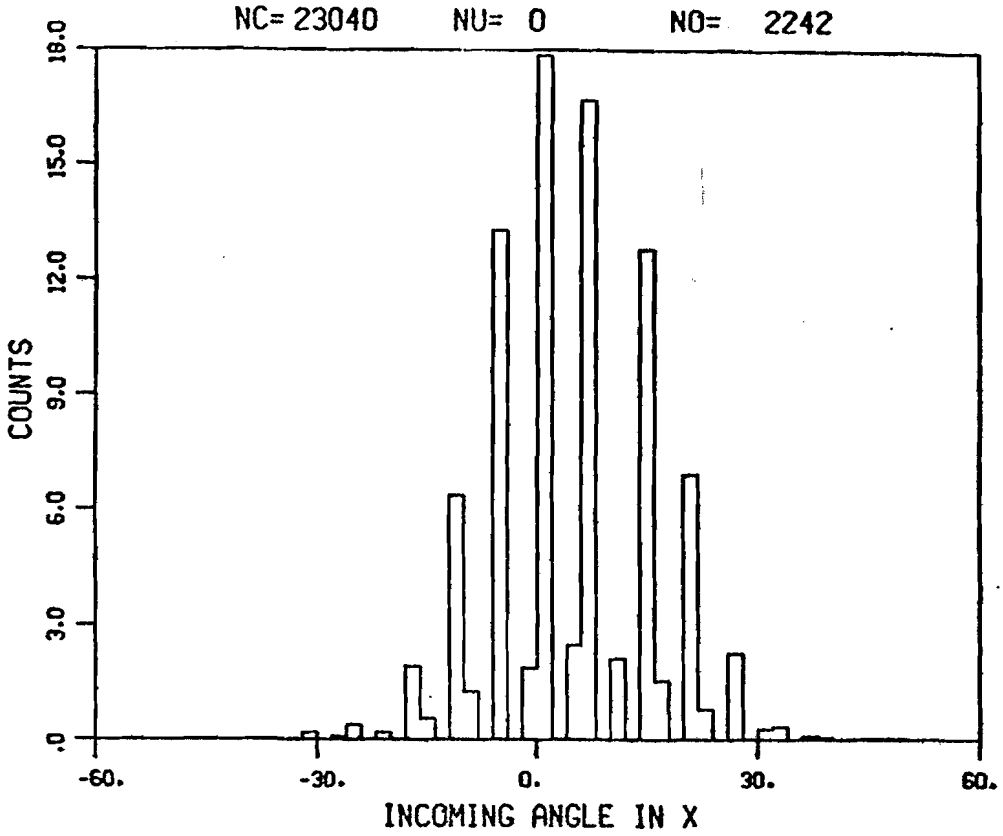

Figure III-57

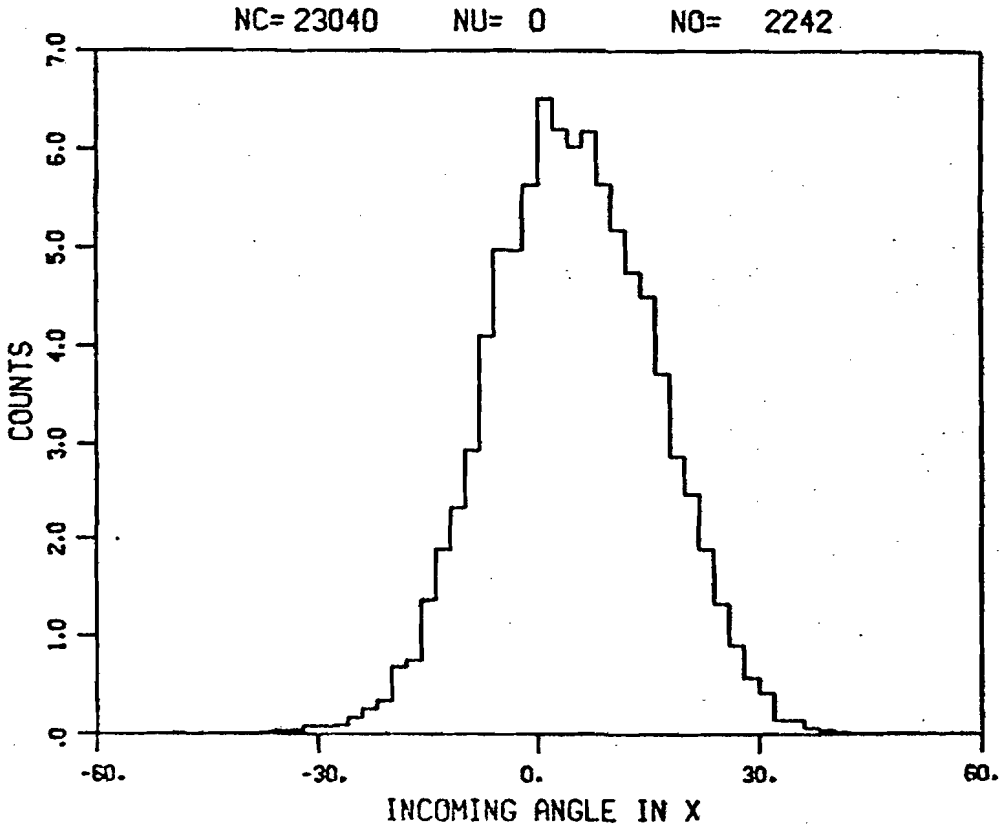

Figure III-58

T = -.8

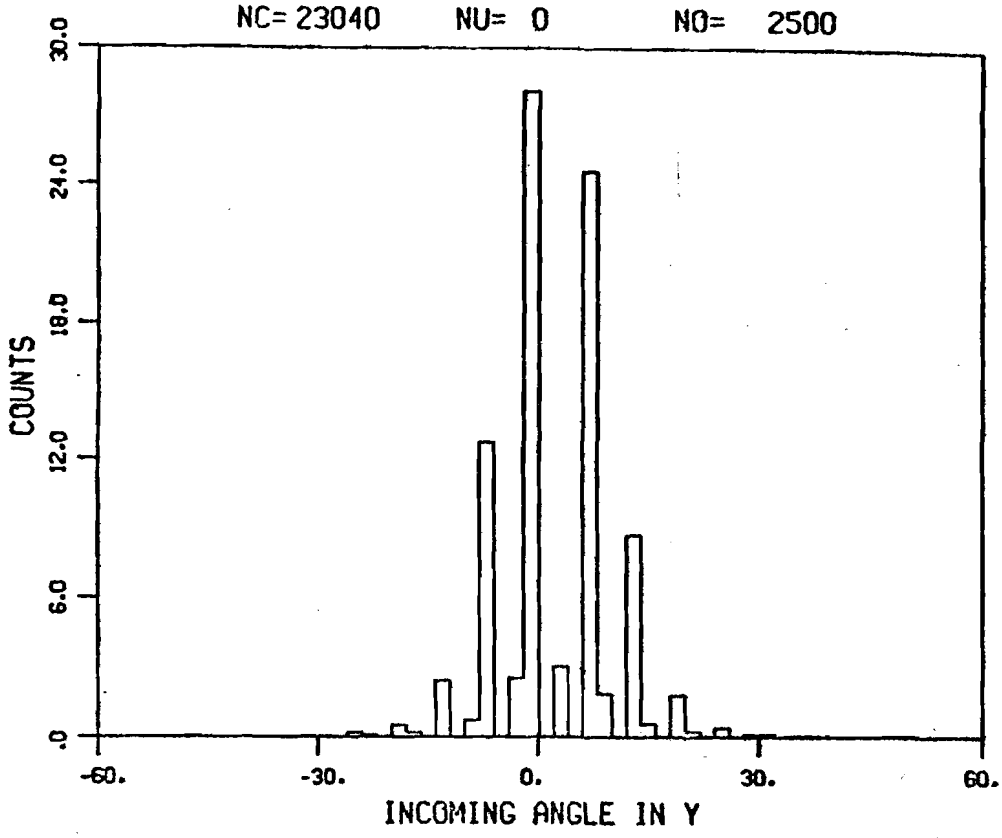

Figure III-59

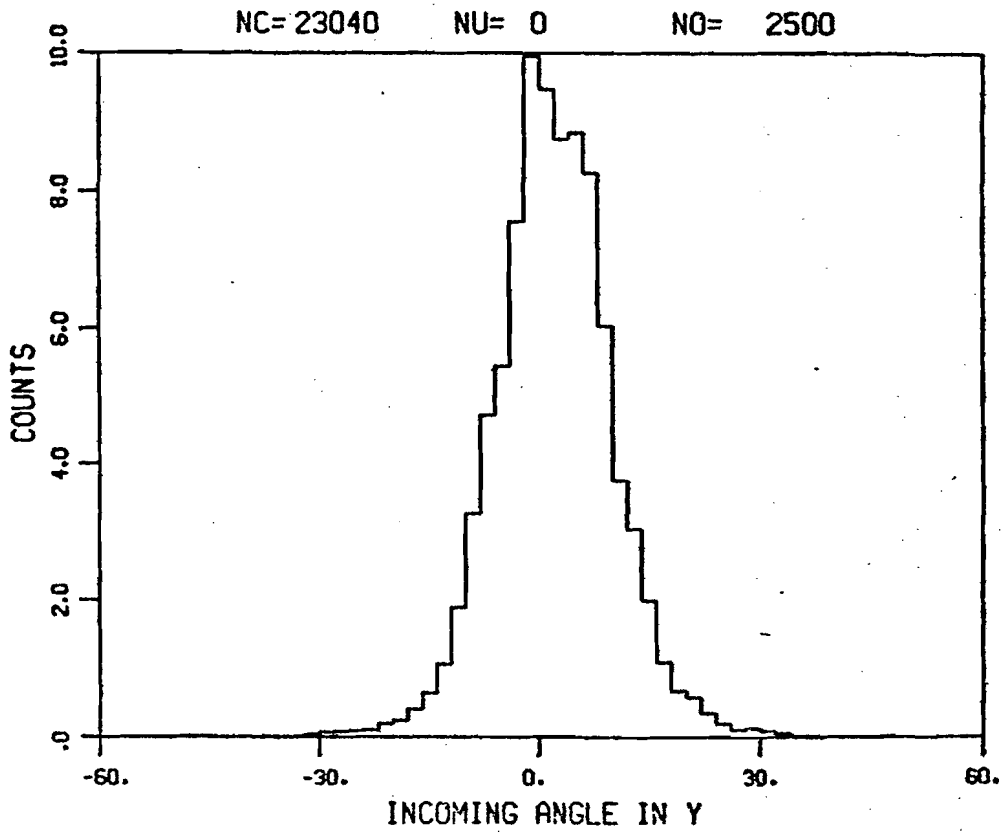

Figure III-60

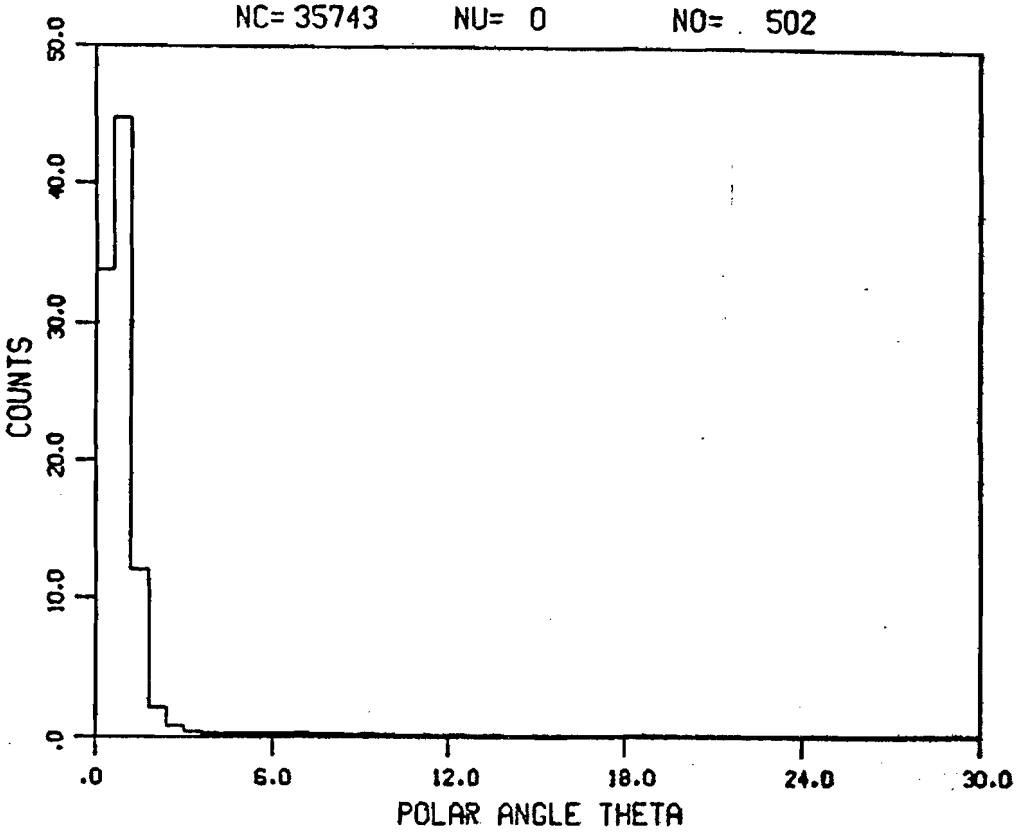

Figure III-61

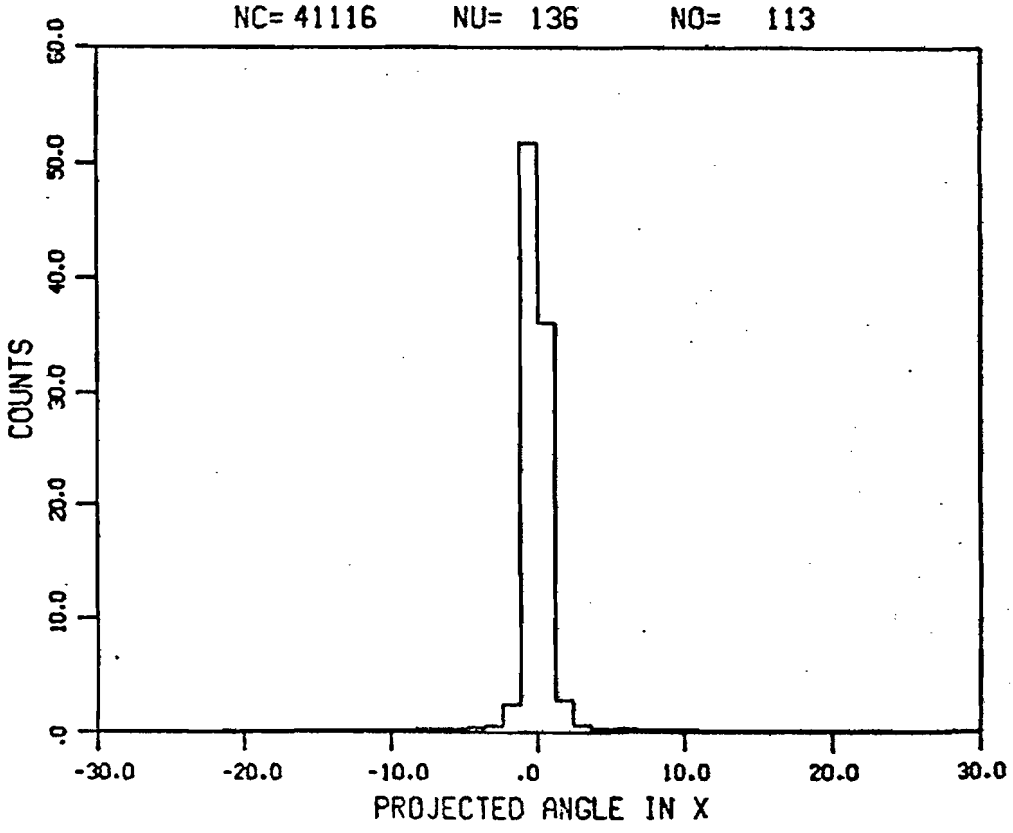

Figure III-62

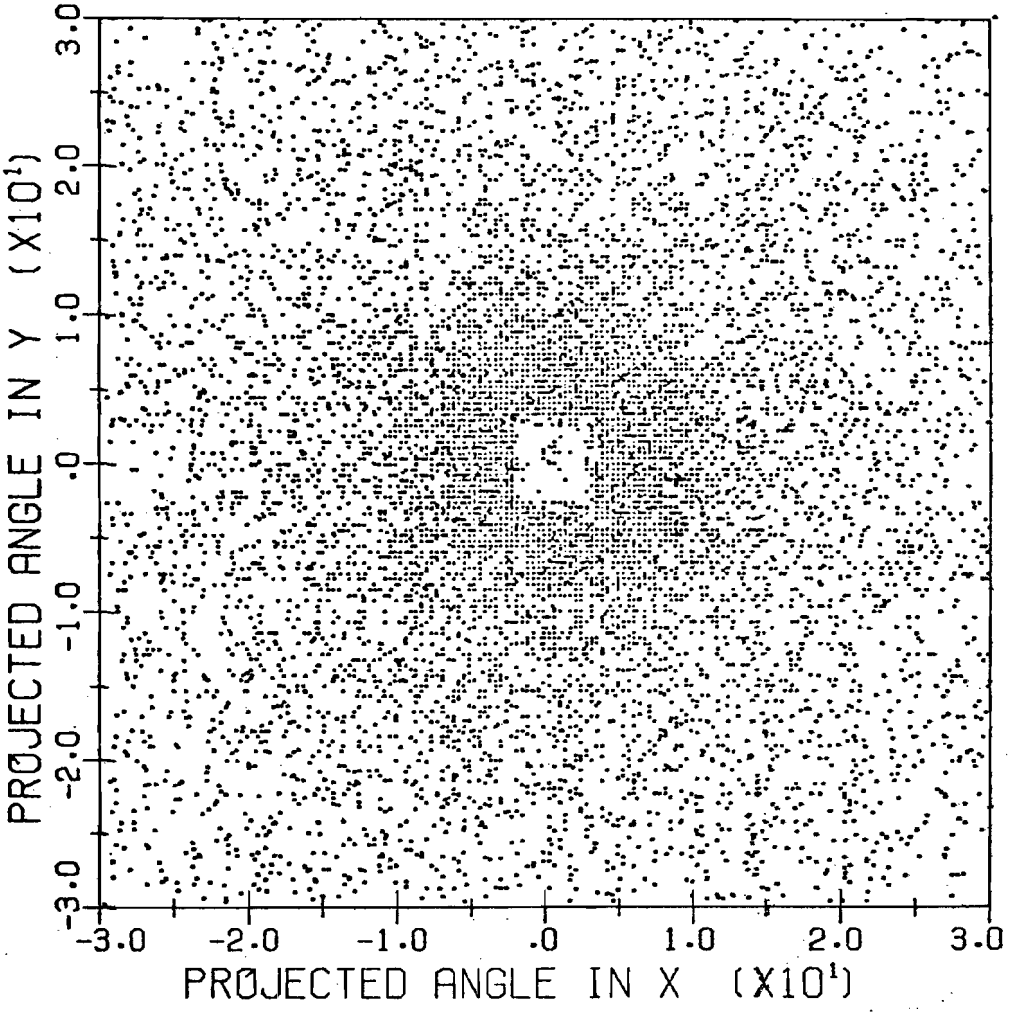

Figure III-63

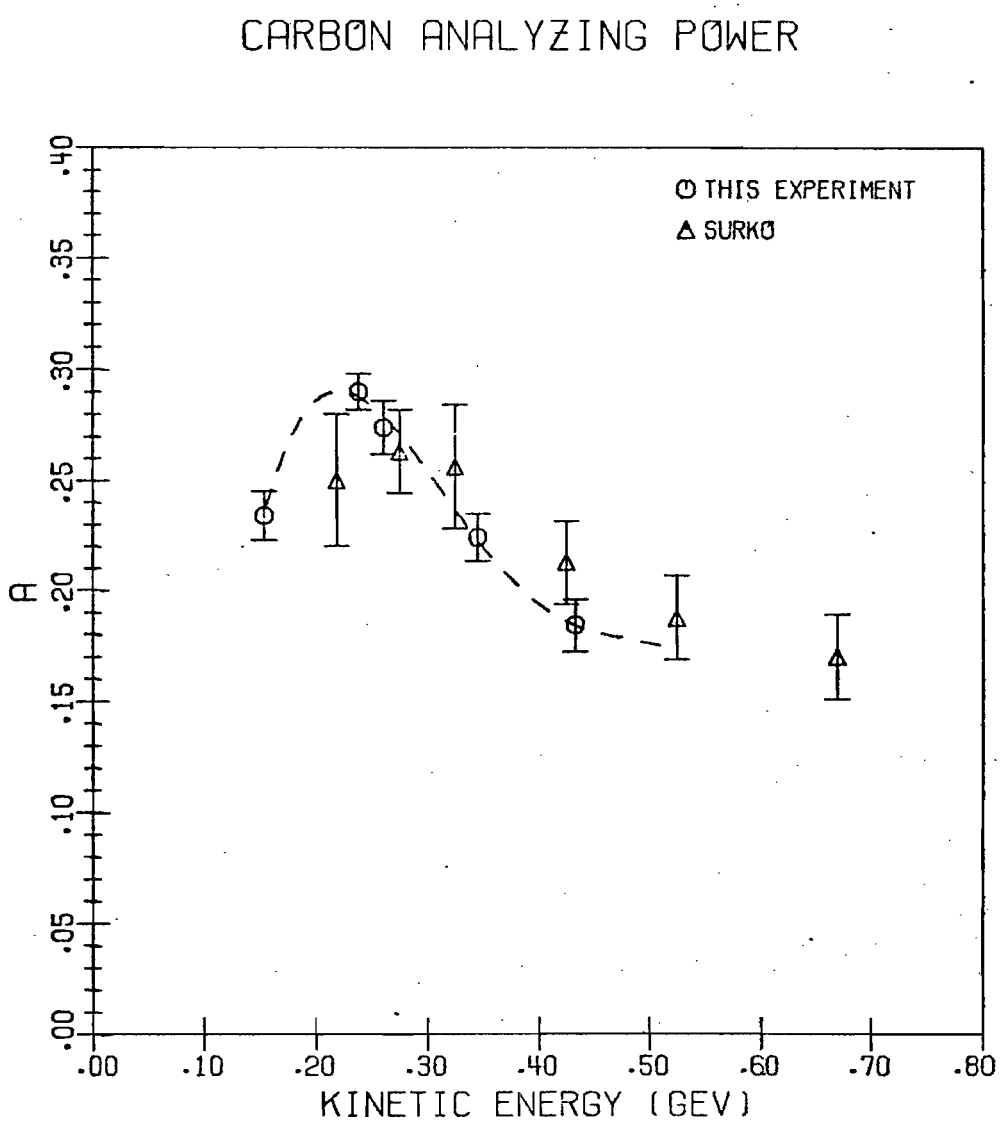

Figure III-64

CHAPTER III REFERENCES

1. G. W. Bryant, H. A. Neal, and D. R. Rust, "Proton-Carbon Analyzing Power Measurements for Proton Kinetic Energies between .150 GeV and .440 GeV", Indiana University Internal Report COO-2009-102.

2. P. Surko, University of California Internal Report, UCRL-19451.

CHAPTER IV

RESULTS

1. Discussion of the Data

The polarization of proton-proton elastic scattering was measured as a function of s for t values of -.3, -.6, -.8 and -1.0 $(GeV/c)^2$. Data for all t values covered a range of beam momenta from 20 to 175 GeV/c. The measured polarization results are shown in Figures IV-1 through IV-4. Shown also are several other experimental results; the dashed line indicates the theoretical prediction of Pumplin and Kane[7]. The corresponding tabulated results are given in Table IV-1. The estimated errors shown are statistical, except for one point at t = 1.0 and s = 210 $(GeV/c)^2$; the estimated error for this point has been increased slightly to account for error in the correction for inelastic contamination. The general behavior of P vs. s is quite similar at all t values,

At t = -.3, (Fig. IV-1) the polarization falls from large positive values at low energies to near zero by $s \cong 210$ $(GeV/c)^2$. However, at higher energies it appears that the polarization begins to rise again. More data would be needed for $s > 200$ $(GeV/c)^2$ to confirm this. Our result at s = 40 agrees well with $s \cong 35$ results of Borghini et. al.[3]; there is also good agreement between our result and that of Gaidot et al.[6] at s = 86.

At t = -.6, (Fig. IV-2) the shape of the P vs. s plot is very similar to that of t = -.3. The polarization starts out large and positive at low energies and falls quickly with increasing energy. However, unlike the t = -.3 result, between s = 50 and s = 70 the polarization becomes

slightly negative and remains a few percent negative at least up to $s \cong 210$. By $s = 330$ the polarization appears to be rising again, but because of the statistical errors it is not clear if P remains a few percent negative or approaches zero. Again our results are in good agreement with other experimental results between $s = 43$ and $s = 83$.

At $t = -.8$, (Fig. IV-3) the pattern is again quite similar to the results at $t = -.3$ and $t = -.6$. From a fairly large positive value at low energy the polarization falls to zero by about $s = 47$ $(GeV/c)^2$ and becomes negative. P remains a few percent negative up to $s = 145$ and perhaps rises again as the energy increases. As in the case of $t = -.6$, because of statistical errors it is not clear if P remains negative or returns to zero. Once again there is good agreement between our results and those of other experiments.

At $t = -1.0$ (Fig. IV-4) the pattern at low energies is repeated: P is positive and fairly large at low energy and falls with increasing energy. The situation at $s = 86$ $(GeV/c)^2$, however, is not clear. There is some discrepancy between the result of this experiment, which is about +.14 and the data of Gaidot et. al. which is about -.08. The experimental error estimates for both points are large, however. More data would be needed to clear up the confusion. At both $s = 145$ and $s = 210$ the polarization was measured to be large and negative, about -.15. Unfortunately, the error estimates are also large, but the data certainly indicates that the polarization is negative at these energies and may be quite large. There is no point at $s = 330$ $(GeV/c)^2$ for $t = -1.0$ because it was not possible to separate the elastic events from the inelastic background.

2. Discussion of Models

The standard Regge theory cannot accommodate polarizations which, for fixed t, change sign as s increases. The Regge model predicts

$$P \sim A \left(\frac{s}{s_0}\right)^{\alpha}$$

where A and α depend only on t and $\alpha < 0$. If the polarization is positive for low energies this form of s-dependence predicts that the polarization should remain positive and fall to zero as $s \to \infty$. But for all t values except t = -.3, P was found to change sign with increasing s. Even at t = -.3, P seems to be increasing again at high energies, which is also in disagreement with Regge theory.

The modified Regge theory of Kane and others (see section I-7), however, does predict negative polarizations and non-zero polarizations at high energies. The dashed line in Figures IV-1 through IV-4 indicates the prediction for high energy polarizations from the two-pion exchange model of Pumplin and Kane[7]. The prediction does not fit the data particularly well. At t = -.3 the predicted polarization is too high, except perhaps at the highest energy. At the other t values the predicted polarizations become negative but continue to increase in magnitude with increasing energy, while the experimental results appear to level off and perhaps begin to rise. Also the predicted positions of the cross-overs are not right, except for t = -.8. However, the model <u>does</u> predict the observed change in sign of the polarization and the non-zero polarization at high energies.

The optical models discussed in Chapter I do not give specific forms for the s-dependence of the polarizations, so no real comparison can

be made. However, one point is worth noting. The Durand-Halzen[8] model predicts large and rapidly changing polarizations in the region of the dip in $d\sigma/dt$, since their model predicts

$$P\sigma \sim \chi\sigma'.$$

At higher energies, the dip moves into lower $|t|$ values (at $s = 500\ (\mathrm{GeV}/c)^2$ the dip occurs at $t = -1.4$) - perhaps the negative polarization that develops at high energy is indicative of the effects of the dip region beginning to affect the polarization. The fact that P was largest at $t = -1.0$, which is closest to the dip, supports this argument. However, P becomes negative by $s = 86$ at $t = -.6$ and $t = -.8$, which is still far from the dip both in t and in s.

3. Polarization as a Function of Missing Mass in Inelastic Events

It is perhaps reasonable to expect that, for inelastic events, the polarization might be a continuous function of the missing mass. Since the data contained a considerable number of inelastic events, their polarization was also calculated. These results are shown in Figures IV-5 through IV-16. For each t value (except $t = -.3$) are each energy range (except $p_{beam} = 20$ GeV/c) the polarization is plotted as a function of $(\text{missing mass})^2 - (\text{proton mass})^2$. The first point corresponds to the elastic events; the other points represent bins in $(\text{missing mass})^2$ which are the same width as the elastic peak. Since the $t = -.3$ data was almost purely elastic, it was not possible to calculate inelastic polarizations for this t value. Also the data at $p_{beam} = 20$ GeV/c for each t value was essentially purely elastic so no inelastic polarizations were calculated for this energy range.

For the most part, the inelastic data was consistent with a polarization of zero. However, there does seem to be a general trend - as the missing mass increases, the polarization seems to become more positive, and, at higher missing masses, may turn over and start to become negative again. There is a sign convention which should be mentioned. In pp elastic scattering, it is conventional to define the polarization as the expectation value of the spin for the scattered particle. Since this experiment measured the spin of the recoil proton, the results were multiplied by -1 to be consistent with the conventional definition of P. The results for the inelastic polarizations presented here have also been multiplied by -1, so that the first bin in missing mass, which represents the elastic data, corresponds to the conventional definition of P for elastic events.

4. Conclusions

The results are among the first polarization measurements above beam momenta of 17.5 GeV/c, and represent the first systematic study of fixed-t energy dependence of the polarization at high energies. The polarization was found to be non-zero at high energies, and, in fact, to change sign with increasing energy for all t values except t = -.3. This contradicts predictions of standard Regge theory, although modified Regge theories seem to predict some of the qualitative features of the data.

The general shape of the P vs. s curve seems to be the same for all t values. The polarization starts out positive at low energies, falls with increasing energy, and may start to rise again at the highest

energies measured. For all t values except $t = -.3$, P was found to become negative between about $s = 50$ and $s = 70$ $(GeV)^2$. Except at $t = -1.0$, the magnitude of the measured polarizations was small (less than .05). Large values of $|P|$ were measured at $t = -1.0$, but the estimated errors are also large.

Many questions remain unanswered. Does the polarization start to rise above $s = 200$ $(GeV/c)^2$, or does it level off? What happens at higher energies for $t = -1.0$? Does P become even more negative for $|t|$ values greater than 1.0? High $|t|$, high energy polarization experiments are difficult, but the situation is intriguing. Additional experiments in this area could give interesting and unexpected results.

Table IV-1

Polarization Results for pp Elastic Scattering

t $(GeV/c)^2$	p_{beam} (GeV/c)	s $(GeV/c)^2$	Polarization
-.3	20 ± 6	39	.058 ± .015
	45 ± 8	86	.011 ± .016
	77 ± 10	147	.020 ± .013
	110 ± 10	209	.003 ± .013
	176 ± 12	333	.035 ± .014
	205 ± 15	387	.026 ± .056
-.6	22 ± 6	43	.029 ± .014
	43 ± 10	83	-.029 ± .017
	75 ± 12	143	-.014 ± .015
	110 ± 10	209	-.035 ± .017
	176 ± 12	333	-.003 ± .018
-.8	21 ± 6	41	.038 ± .026
	45 ± 8	86	-.042 ± .018
	76 ± 10	145	-.014 ± .015
	110 ± 10	209	-.035 ± .017
	176 ± 8	333	-.021 ± .021
-1.0	22 ± 6	43	.025 ± .052
	44 ± 10	85	.144 ± .073
	76 ± 12	145	-.158 ± .072
	110 ± 10	209	-.150 ± .099

CHAPTER IV FIGURES

Figure IV-1. Polarization results for pp elastic scattering at $t = -.3\ (GeV/c)^2$. The dashed line in this and the next three figures represents the prediction for high energy pp polarizations of Pumplin and Kane (Ref. 7).

Figure IV-2. Polarization results for pp elastic scattering at $t = -.6\ (GeV/c)^2$.

Figure IV-3. Polarization results for $t = -.8\ (GeV/c)^2$.

Figure IV-4. Polarization results for $t = -1.0\ (GeV/c)^2$.

Figure IV-5. Polarization as a function of $(\text{missing mass})^2 - (\text{proton mass})^2$ for $t = -.6\ (GeV/c)^2$ and $p_{beam} = 45$ GeV/c. The first point represents elastics: $(\text{missing mass})^2 - (\text{proton mass})^2 = 0$. Other points represent inelastic events divided into missing mass bins the same width as the elastic peak.

Figure IV-6. Polarization as a function of $(\text{missing mass})^2$ for $t = -.6\ (GeV/c)^2$ and $p_{beam} = 75$ GeV/c.

Figure IV-7. Polarization as a function of $(\text{missing mass})^2$ for $t = -.6$ and $p_{beam} = 110$ GeV/c.

Figure IV-8. Polarization as a function of $(\text{missing mass})^2$ for $t = -.6$ and $p_{beam} = 175$ GeV/c.

Figure IV-9. Polarization as a function of $(\text{missing mass})^2$ for $t = -.8$ and $p_{beam} = 45$ GeV/c.

Figure IV-10. Polarization as a function of $(\text{missing mass})^2$ for $t = -.8$ and $p_{beam} = 75$ GeV/c.

Figure IV-11. Polarization as a function of $(\text{missing mass})^2$ for $t = -.8$ and $p_{beam} = 110$ GeV/c.

Figure IV-12. Polarization as a function of (missing mass)^2 for t = -.8 and p_{beam} = 175 GeV/c.

Figure IV-13. Polarization as a function of (missing mass)^2 for t = -1.0 and p_{beam} = 45 GeV/c.

Figure IV-14. Polarization as a function of (missing mass)^2 for t = -1.0 and p_{beam} = 75 GeV/c.

Figure IV-15. Polarization as a function of (missing mass)^2 for t = -1.0 and p_{beam} = 110 GeV/c.

Figure IV-16. Polarization as a function of (missing mass)^2 for t = -1.0 and p_{beam} = 175 GeV/c.

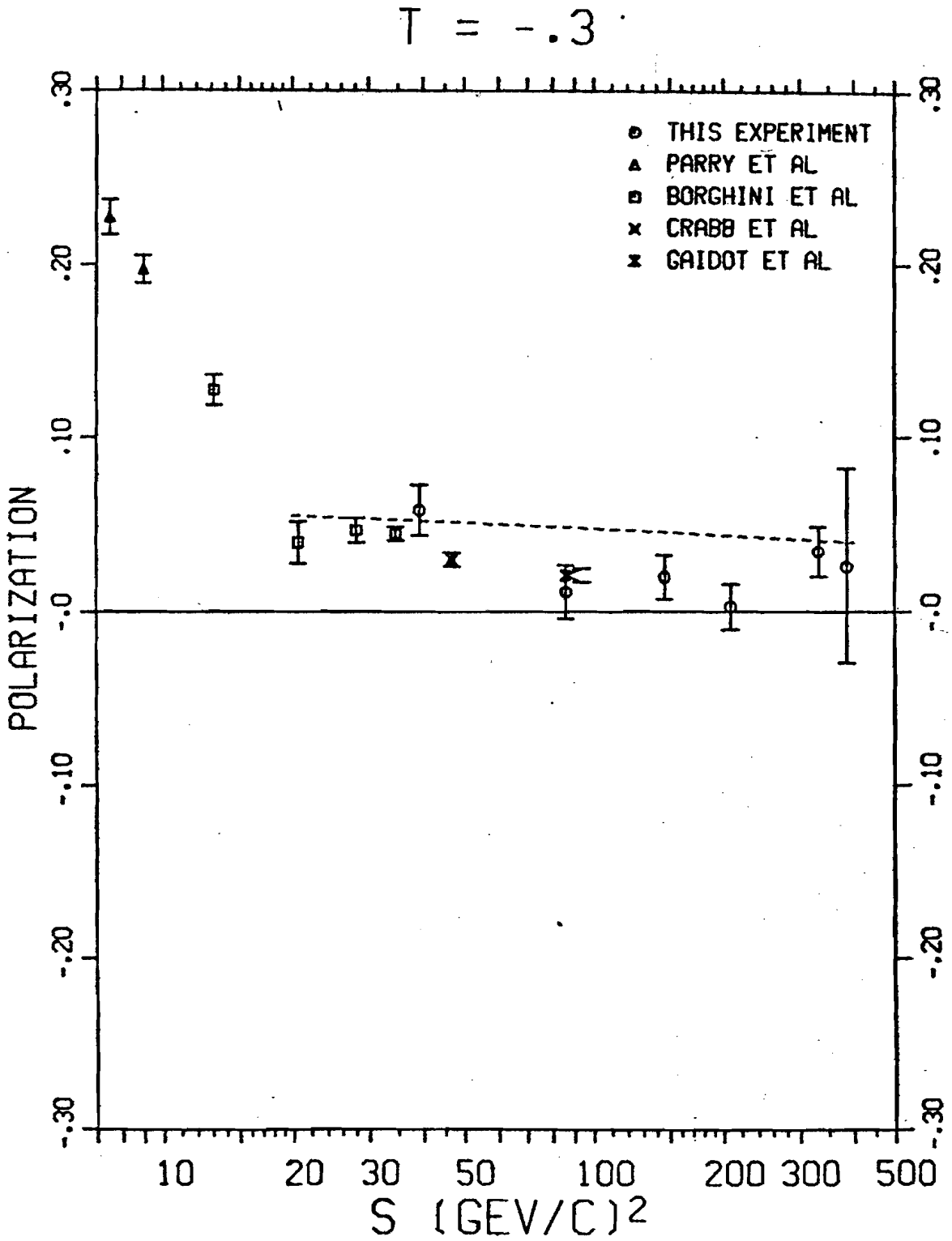
T = -.3
THIS EXPERIMENT
PARRY ET AL
BORGHINI ET AL
CRABB ET AL
GAIDOT ET AL
POLARIZATION
.30
.20
.10
-.0
-.10
-.20
-.30
10
20
30
50
100
200
300
500
S (GEV/C)2

Figure IV-1

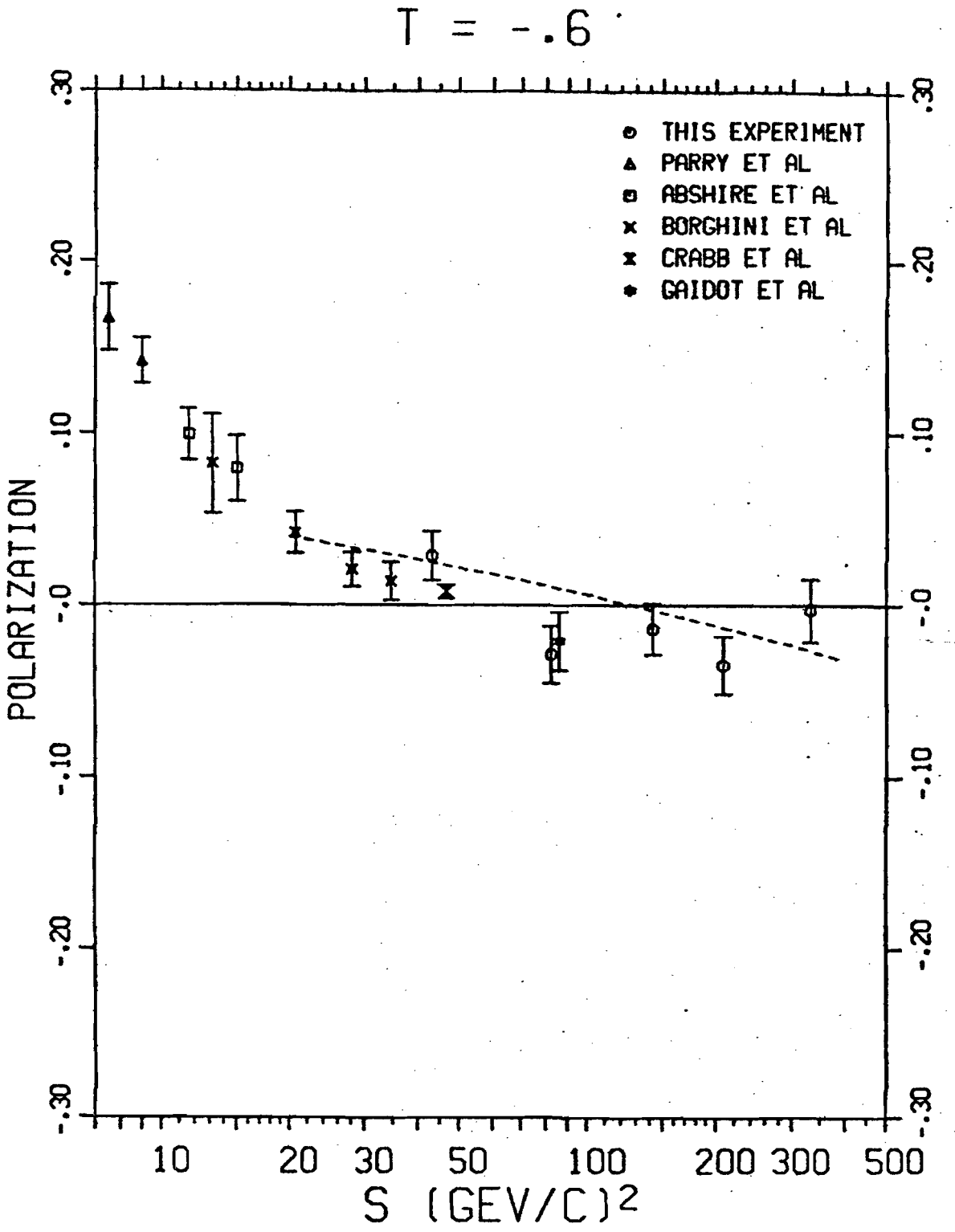
T = -.6
THIS EXPERIMENT
PARRY ET AL
ABSHIRE ET AL
BORGHINI ET AL
CRABB ET AL
GAIDOT ET AL
POLARIZATION
.30
.20
.10
-.0
-.10
-.20
-.30
10
20
30
50
100
200
300
500
S (GEV/C)2

Figure IV-2

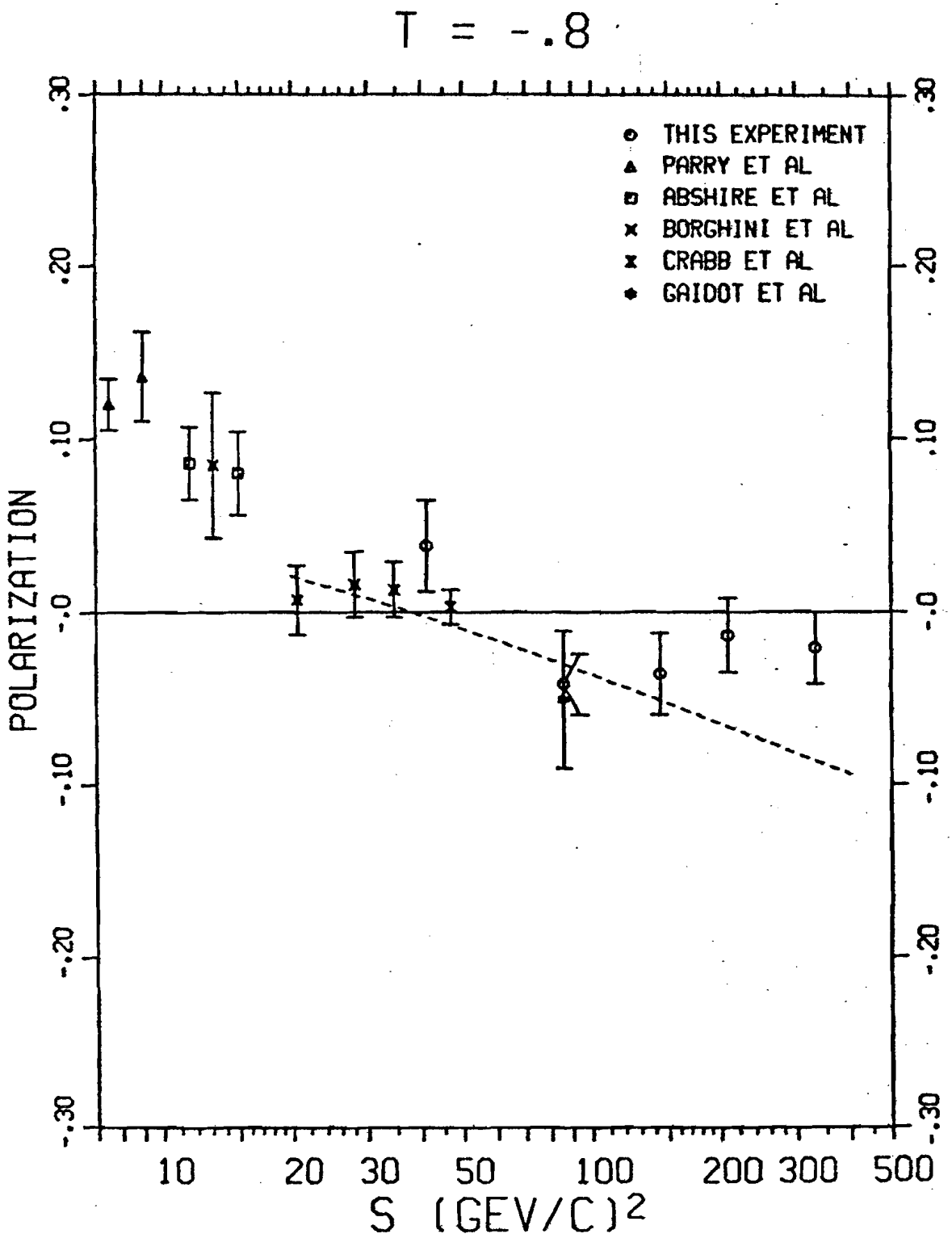
T = -.8
THIS EXPERIMENT
PARRY ET AL
ABSHIRE ET AL
BORGHINI ET AL
CRABB ET AL
GAIDOT ET AL
POLARIZATION
.30
.20
.10
-.0
-.10
-.20
-.30
10
20
30
50
100
200
300
500
S (GEV/C)2

Figure IV-3

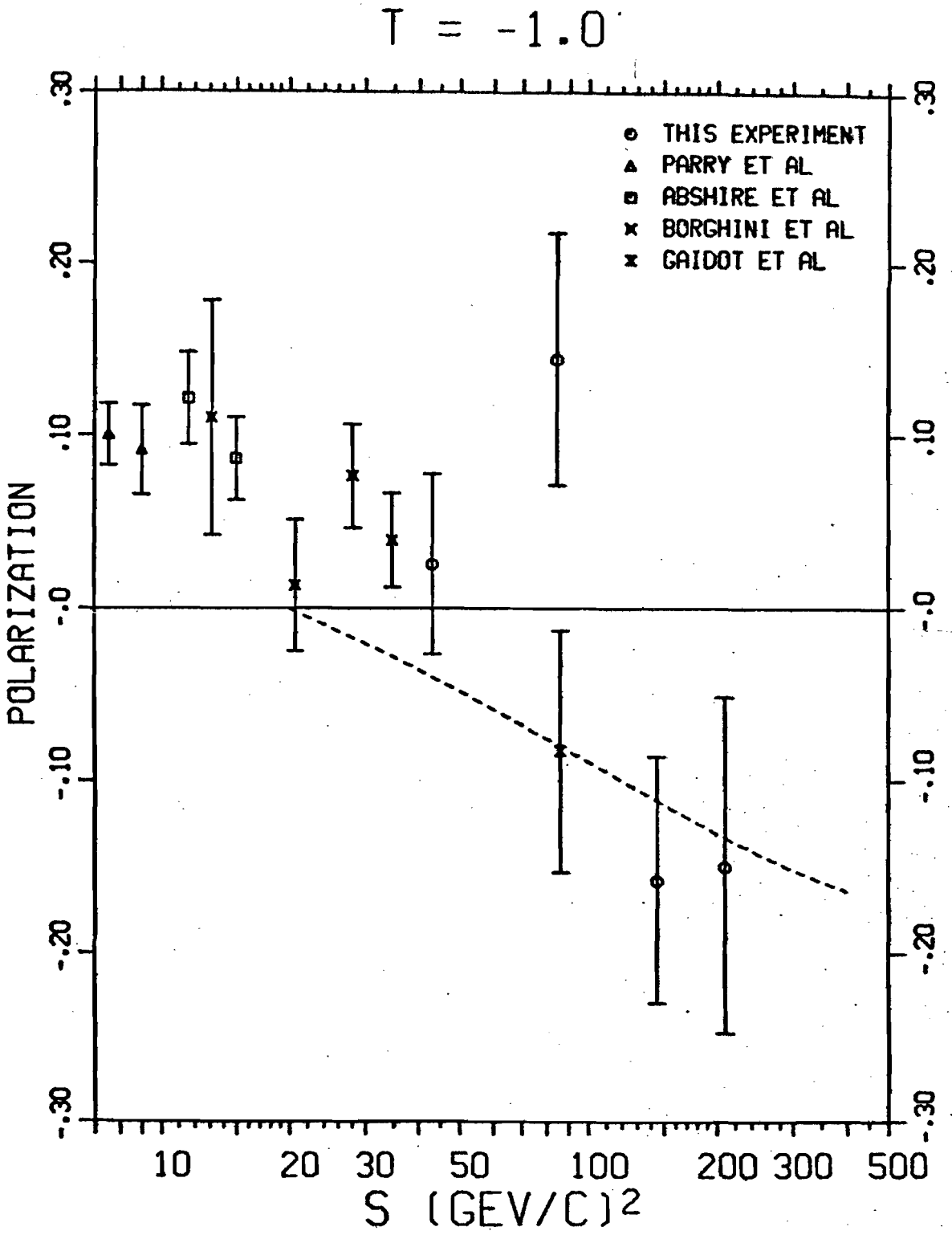
T = -1.0
THIS EXPERIMENT
PARRY ET AL
ABSHIRE ET AL
BORGHINI ET AL
GAIDOT ET AL
POLARIZATION
.30
.20
.10
-.0
-.10
-.20
-.30
10
20
30
50
100
200
300
500
S (GEV/C)2

Figure IV-4

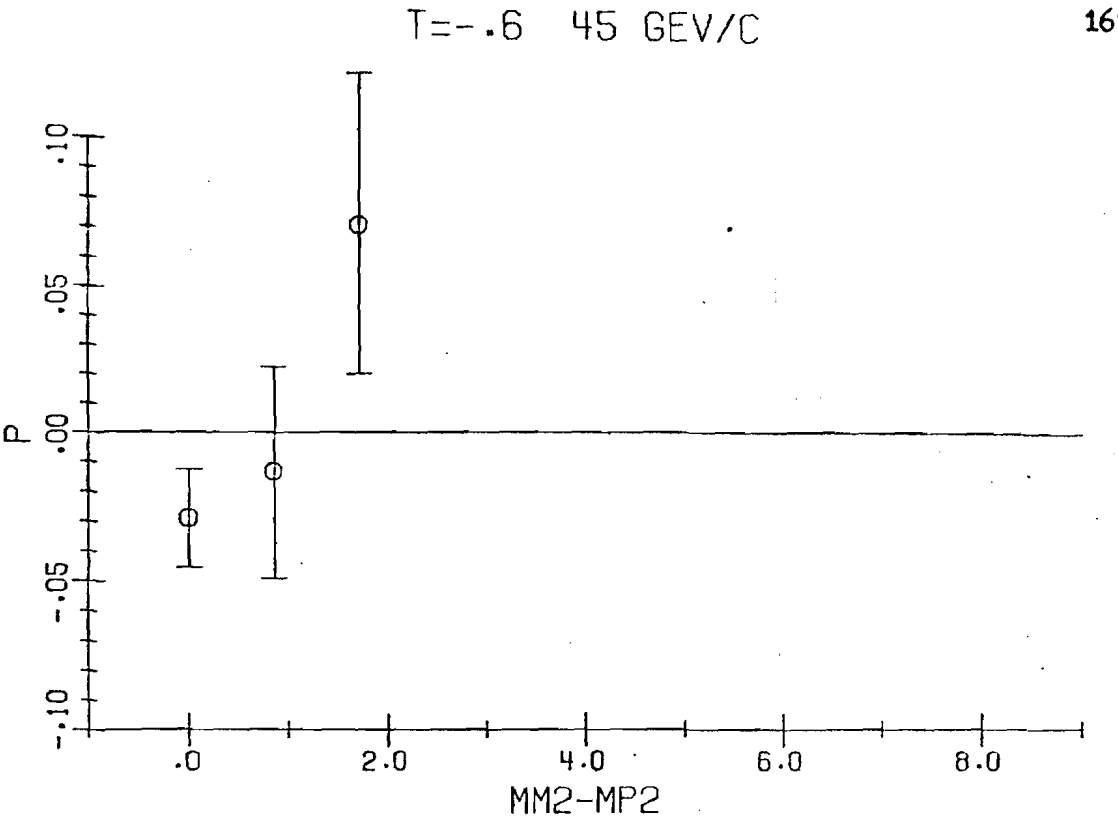

Figure IV-5

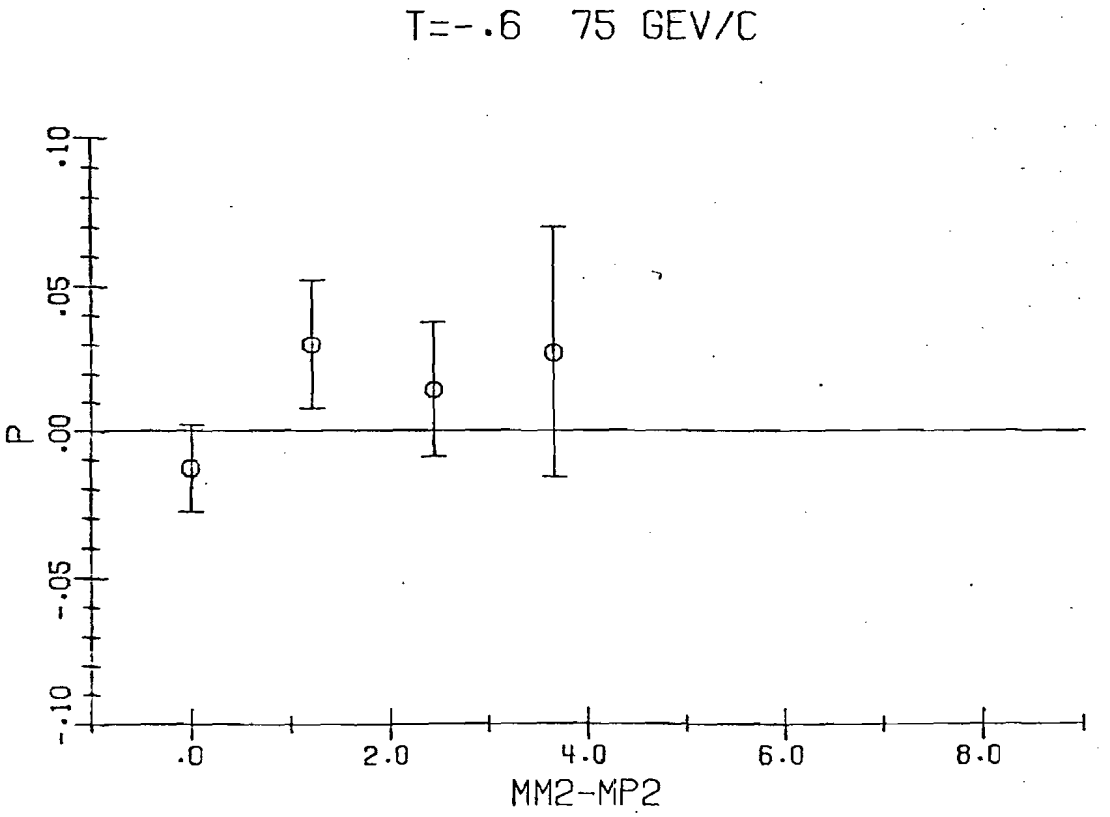

Figure IV-6

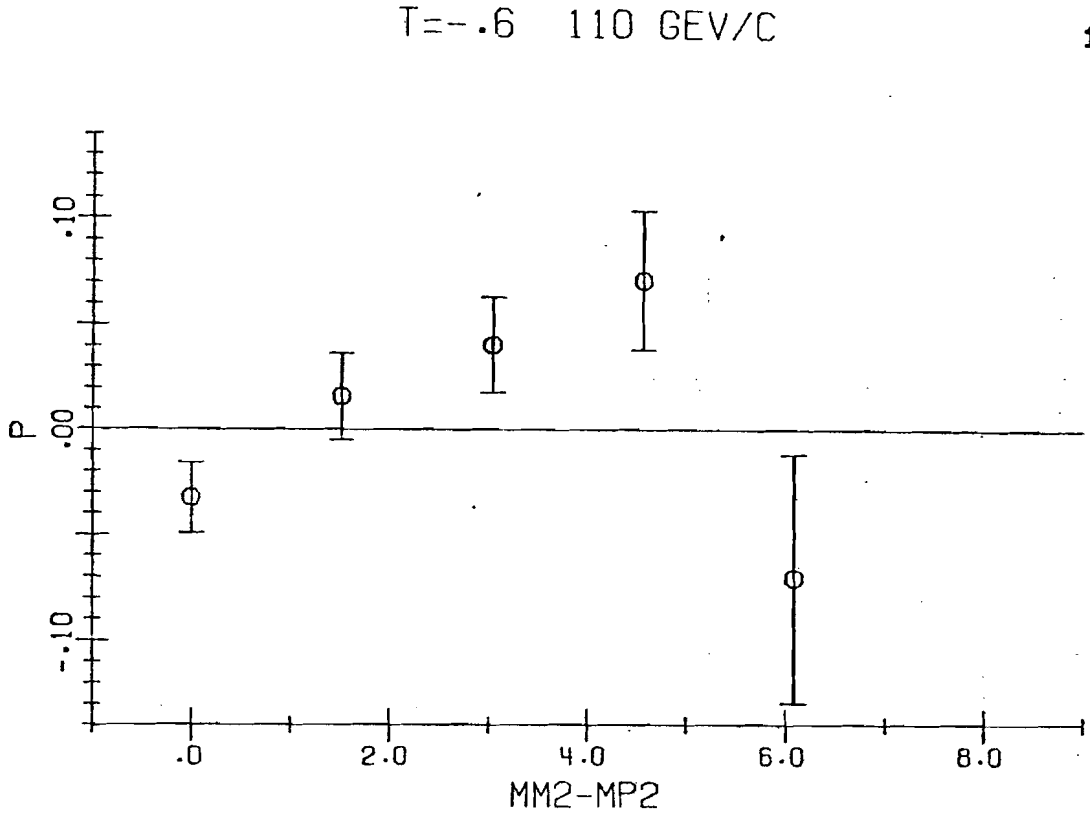

Figure IV-7

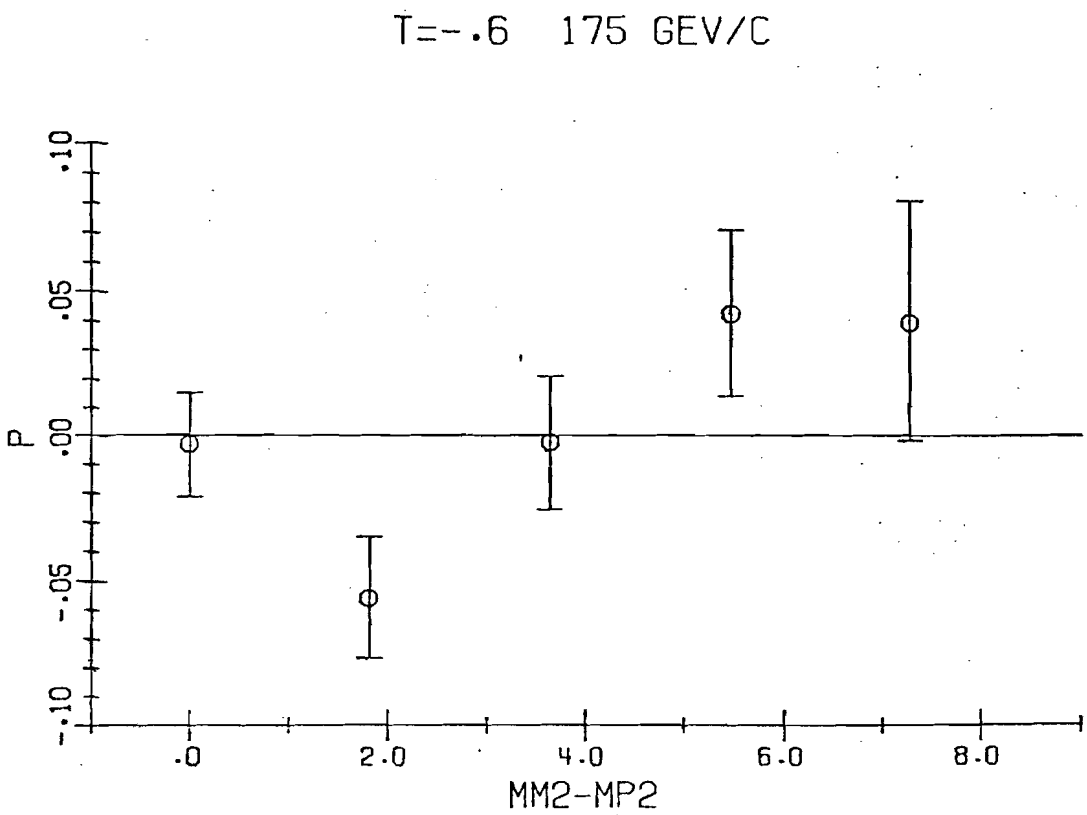

Figure IV-8

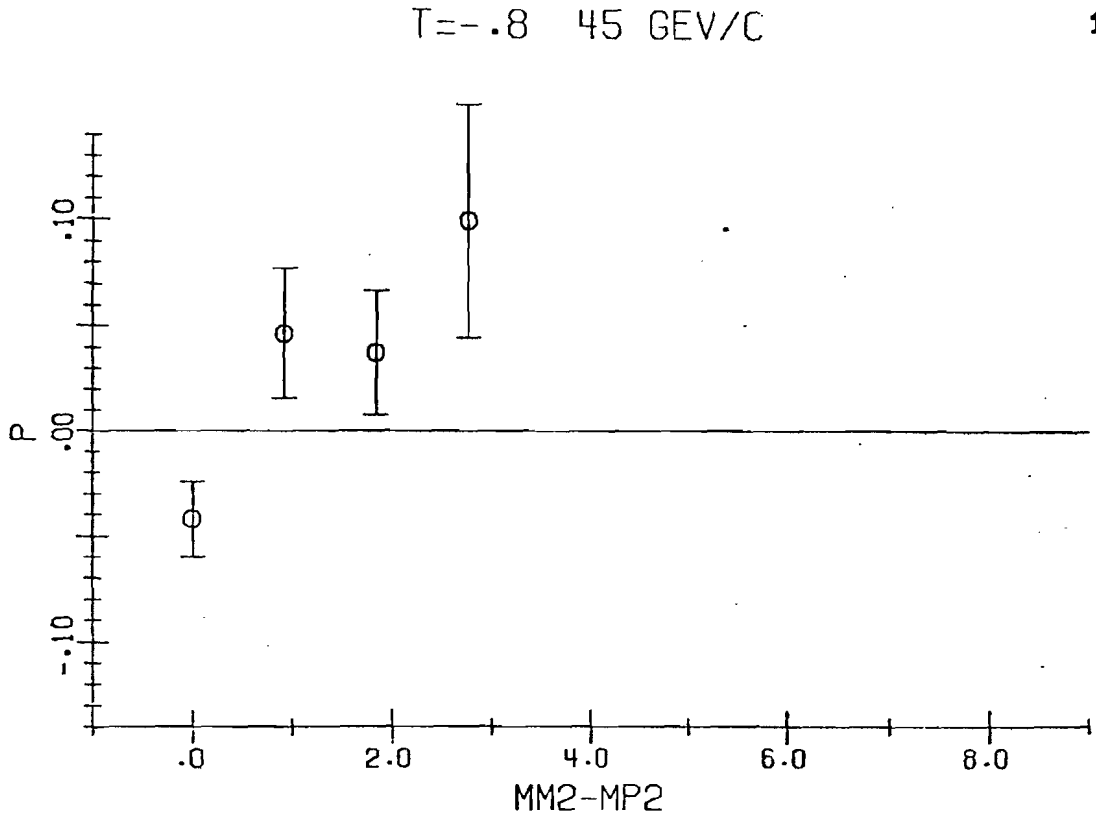

Figure IV-9

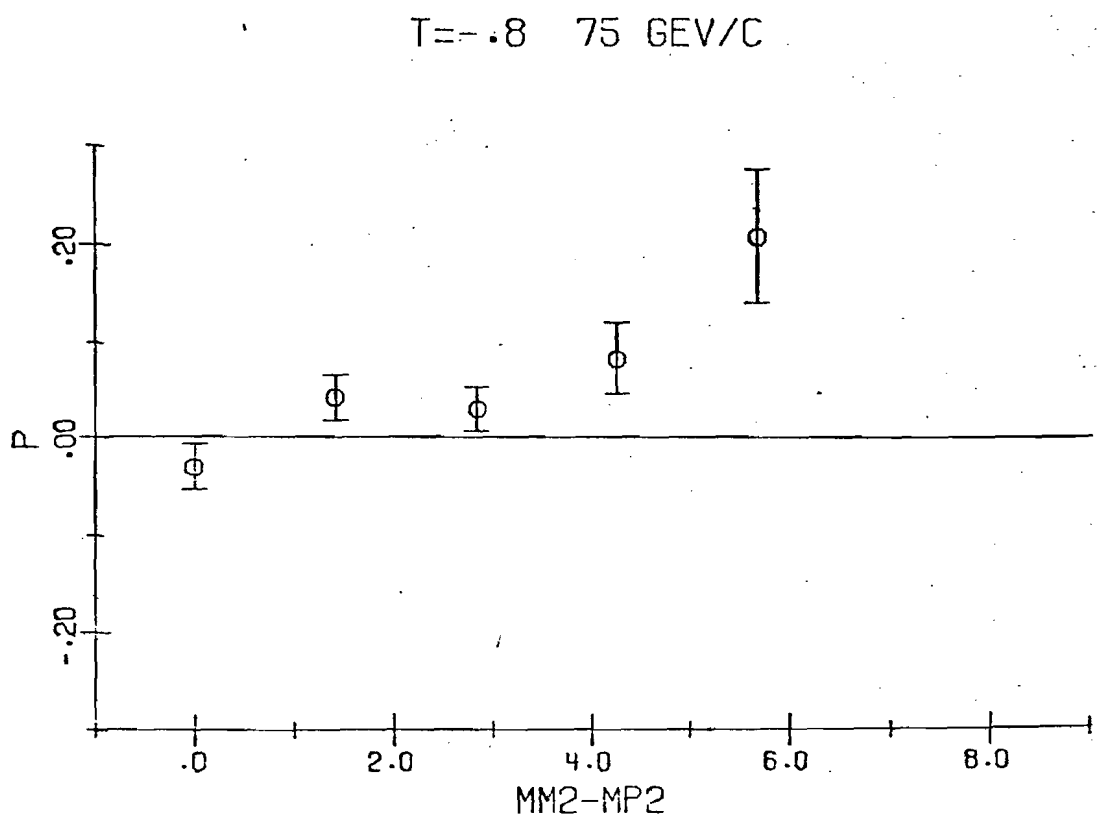

Figure IV-10

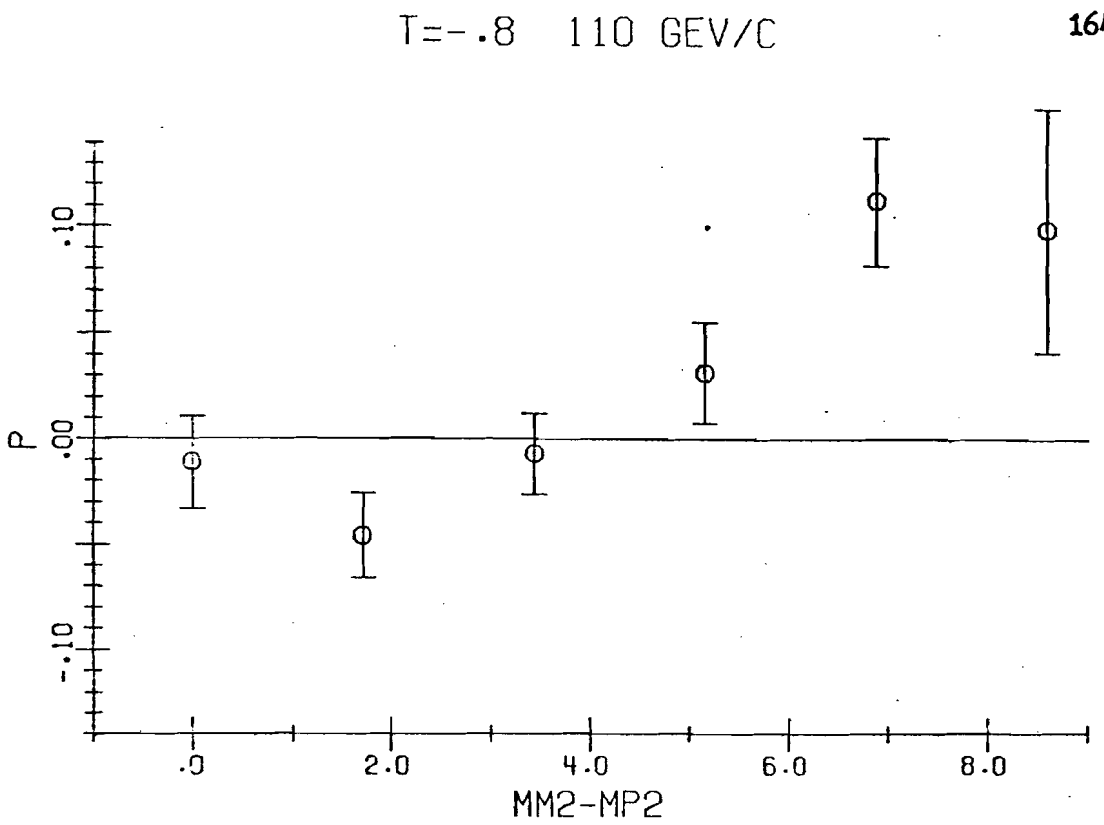

Figure IV-11

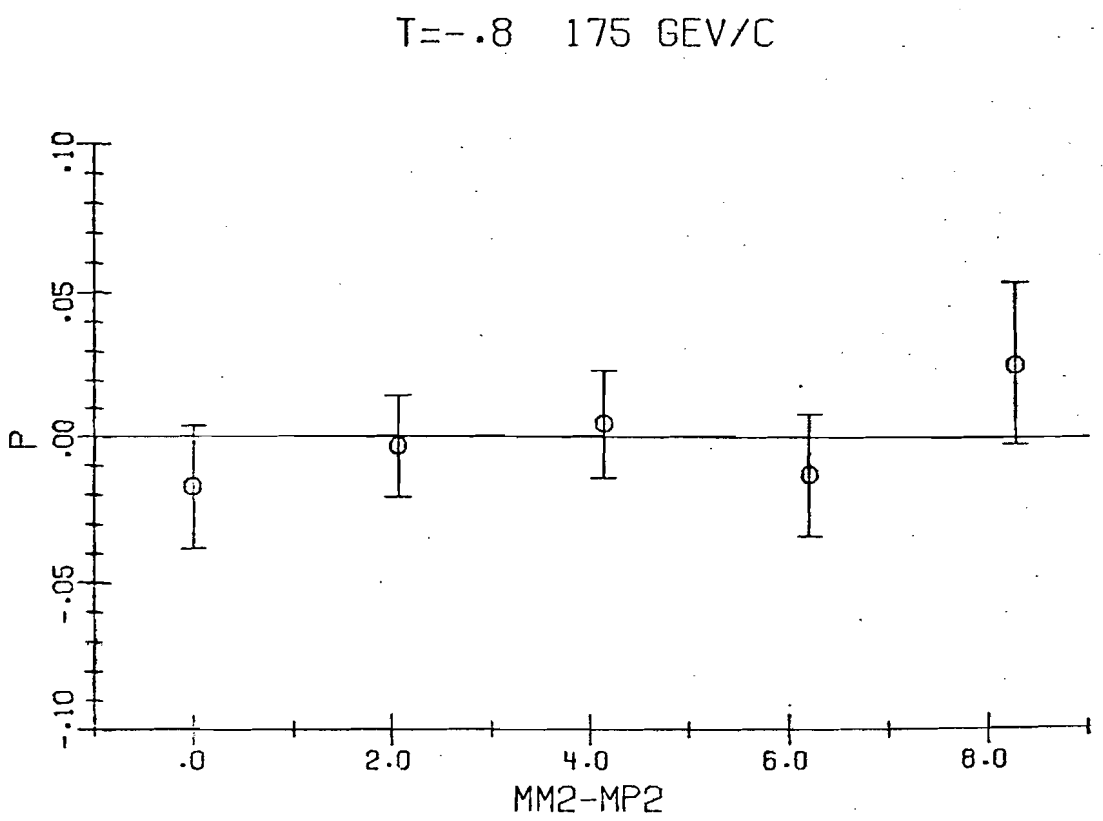

Figure IV-12

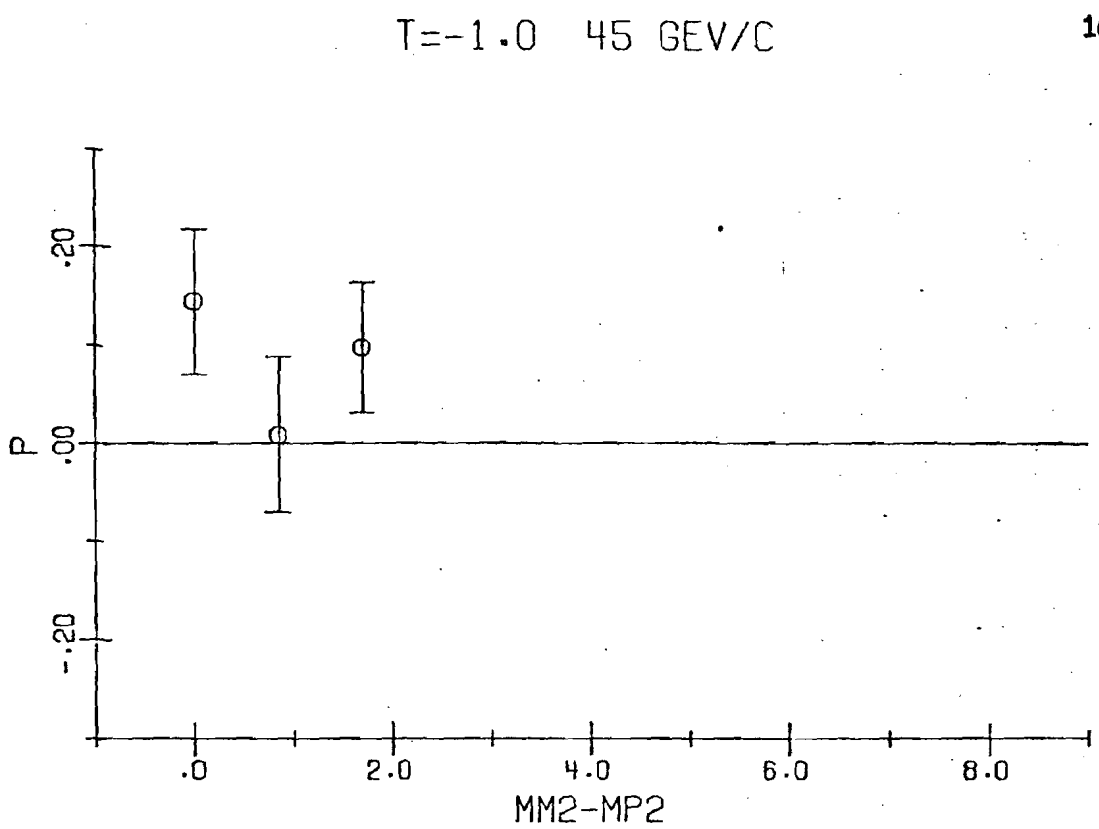

Figure IV-13

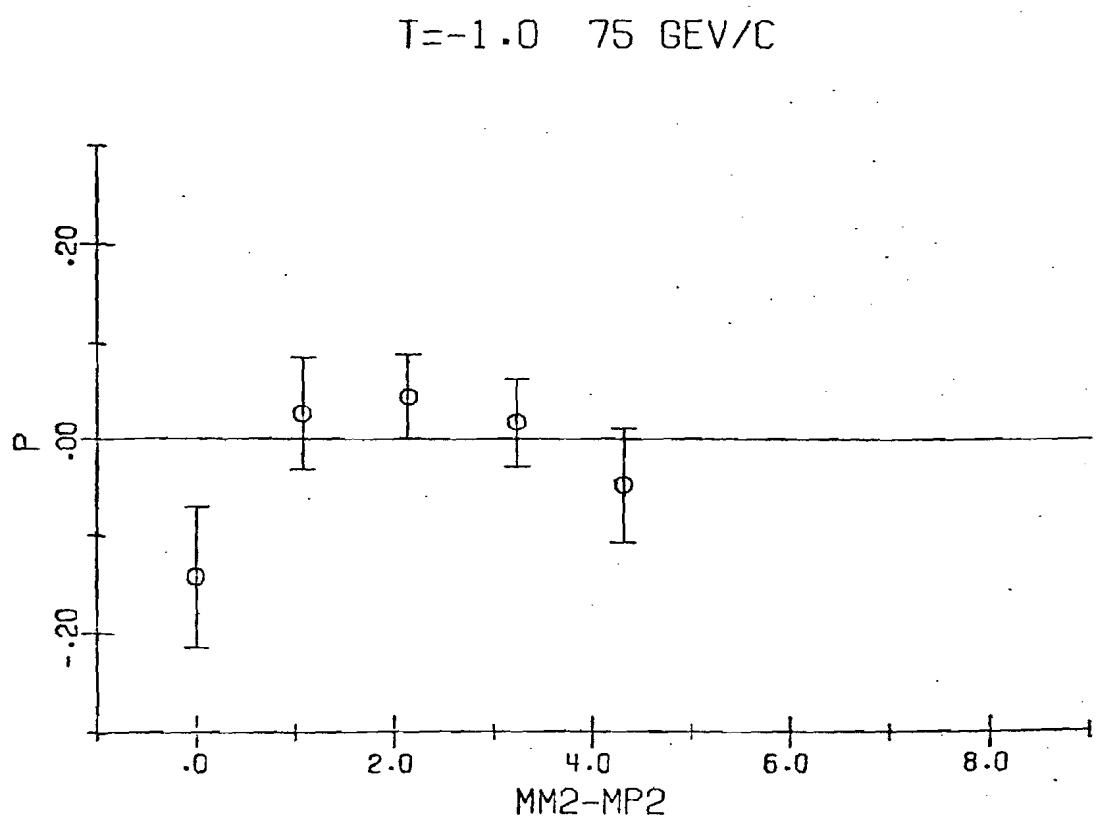

Figure IV-14

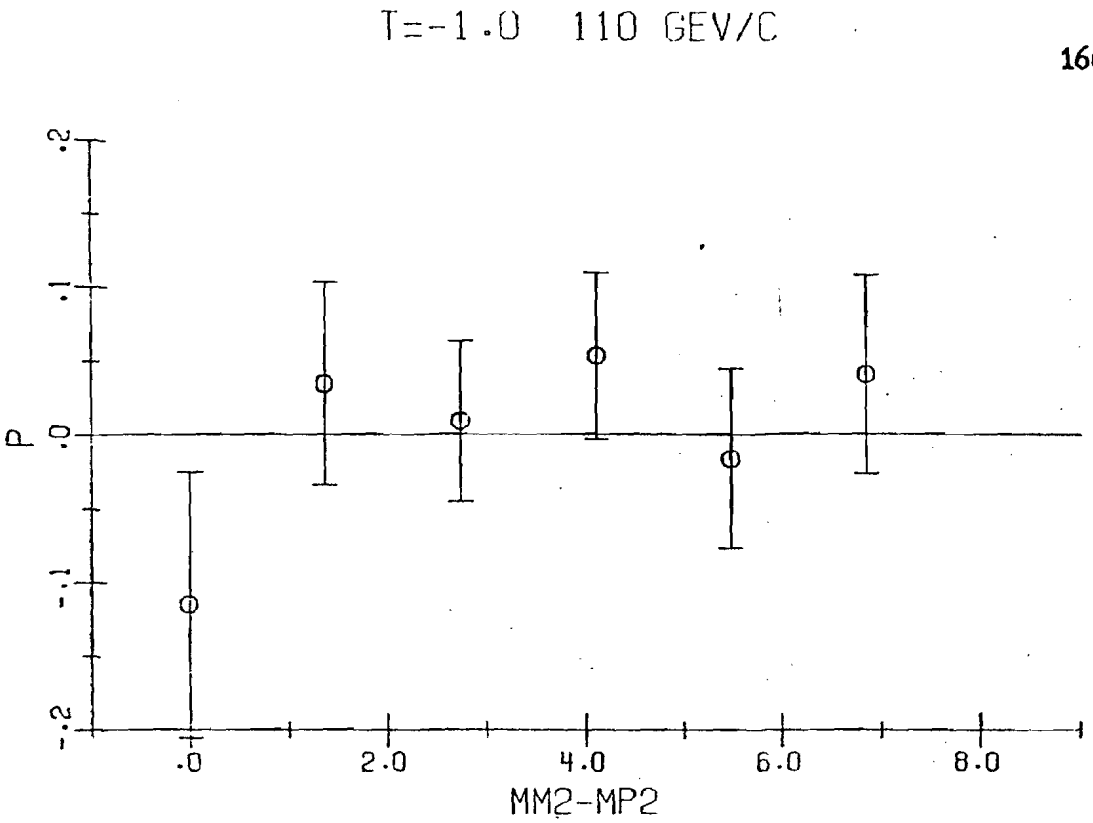

Figure IV-15

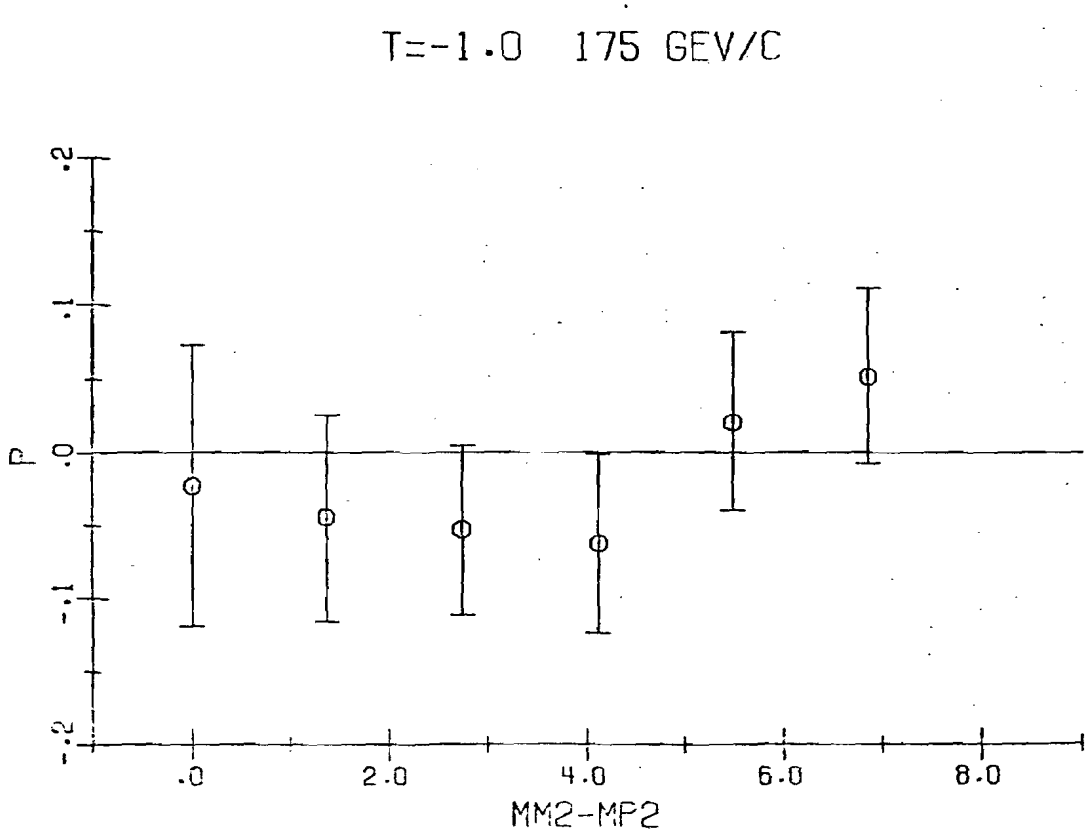

Figure IV-16

CHAPTER IV REFERENCES

1. J. H. Parry et. al., Phys. Rev., D8, 45 (1973).

2. M. Borghini et. al., Phys. Letters, 31B, 405 (1970).

3. M. Borghini et. al., Phys. Letters, 36B, 501 (1971).

4. G. W. Abshire et. al., Phys. Rev. Letters, 32, 1261 (1974).

5. D. G. Crabb, "Measurement of the Polarization Parameter in PP Elastic Scattering at 24 GeV/c", High Energy Physics with Polarized Beams and Targets, AIP Conference Proceedings, No. 35, American Institute of Physics, New York, 1975, p. 120.

6. A. Gaidot et. al., Phys. Letters, 61B, 103 (1976).

7. J. Pumplin and G. Kane, Phys. Rev., D11, 1183 (1975).

8. L. Durand and F. Halzen, Nuc. Phys., B104, 317 (1976).

VITA

Name:	Marjorie Diane Blasius Corcoran
Place of Birth:	Dayton, Ohio
Education:	B. S. in Physics, 1972 University of Dayton